Molecular Dynamics Simulations of Clay-Oil-Brine Interfaces: Understanding Low-Salinity Enhanced Oil Recovery

UNDERWOOD, THOMAS,RICHARD

Molecular Dynamics Simulations of Clay-Oil-Brine Interfaces: Understanding Low-Salinity Enhanced Oil Recovery

Thomas Underwood

A Thesis Presented for the Degree of
Doctor of Philosophy

Department of Earth Sciences
University of Durham
England

May 2017

Dedicated to

My family and friends.

Molecular Dynamics Simulations of Clay-Oil-Brine Interfaces: Understanding Low-Salinity Enhanced Oil Recovery

Thomas Underwood

Submitted for the degree of Doctor of Philosophy
May 2017

Abstract

In an age of increasing energy demand it is clear that we must utilise our energy resources as efficiently as possible. Current oil extraction methods only recover in the region of a third of the oil in a reservoir. Presently oil is recovered through primary methods (pressure differentials) and secondary methods (water-flooding). However, it has been shown that incremental oil recovery beyond secondary methods can be achieved via using water floods of decreased salinity. The aim of this research is to bring clarity to the fundamental mechanisms behind low-salinity enhanced oil recovery (EOR), a technique where sea water, partially desalinated, is used to push increasing amounts of crude oil from existing, and future, oil reservoirs, increasing the reservoir lifetime and overall production. In this thesis, the key mechanisms driving low-salinity EOR have been examined with atomic resolution using classical molecular dynamics (MD) simulations. Simulations have focussed on modelling the three-phase properties of clays (montmorillonite and kaolinite) with model oil compounds (containing decane, decanoic acid and decanamine) at varying salt concentrations of brines (NaCl and $CaCl_2$). The key result presents that clay minerals play an important role in the phenomenon of low-salinity EOR. The oil-wettability of a clay mineral surface is dictated by several factors, including: (a) the surface charge density of the mineral; (b) the nature of the charge balancing cation (monovalent vs divalent); (c) the amount of polar components within the oil phase; (d) the salt concentration of the surrounding flood.

Declaration

The work in this thesis is based on research carried out in the Layered Mineral Group, the Department of Earth Sciences, Durham, England. No part of this thesis has been submitted elsewhere for any other degree or qualification. It is all my own work unless referenced to the contrary in the text.

Acknowledgements

To all my friends and family, colleagues and acquaintances. I would like to thank you all for helping me get to the end of my PhD.

To Bia, who has been the foremost supportive figure during this period. To all my friends from Ustinov. Taras, Elise, Tom, Elena, Jenine, Cahir, Fienke, and countless others. My life has been enriched by getting to know you all. To the guys at 214, you were some of the best, most fun housemates I could ever have ask for. Adam, Fienke, Ben, Edward, Liz; it was a pleasure to spend two years with you. We had some of the most ridiculous parties, and the annual trips to Amsterdam will always be cherished. To Adam, for the mumbles we done did speak. To all the friends I have made along the way. From Friday night football, a weekly ritual that has been with me since Year 9 (long may it continue); to dance outings in Newcastle.

To my primary supervisor, Chris, who has enabled me to explore the science that interests me the most. Who has always been there when needed, and who has always been a friend foremost. To Valentina, who spent an inordinate amount of time listening to my drunken scientific (and non-scientific) rambles. To Rikan, for helping my geology throughout. To Pablo, Hala Madrid! To all those within the group at Durham. I thank you all.

To my family, Mum, Dad and Alice. To Grandma and Grandad. To the Adams and the Freestones and the Underwoods. You have been the constant in my life. The backbone. I thank you all for the support, not just during the PhD, but in all the times beforehand. Here is to new adventures!

Contents

List of Figures

List of Tables

Chapter 1

Introduction

Global energy demand is increasing year on year. Annual energy consumption is predicted to increase 48% by the year 2040, compared to levels of consumption in 2012. The International Energy Agency forecasts that energy expenditure from **all** sources (fossil, renewable and nuclear) is expected to grow between 2016 and 2040[1], as shown in Figure 1.1.

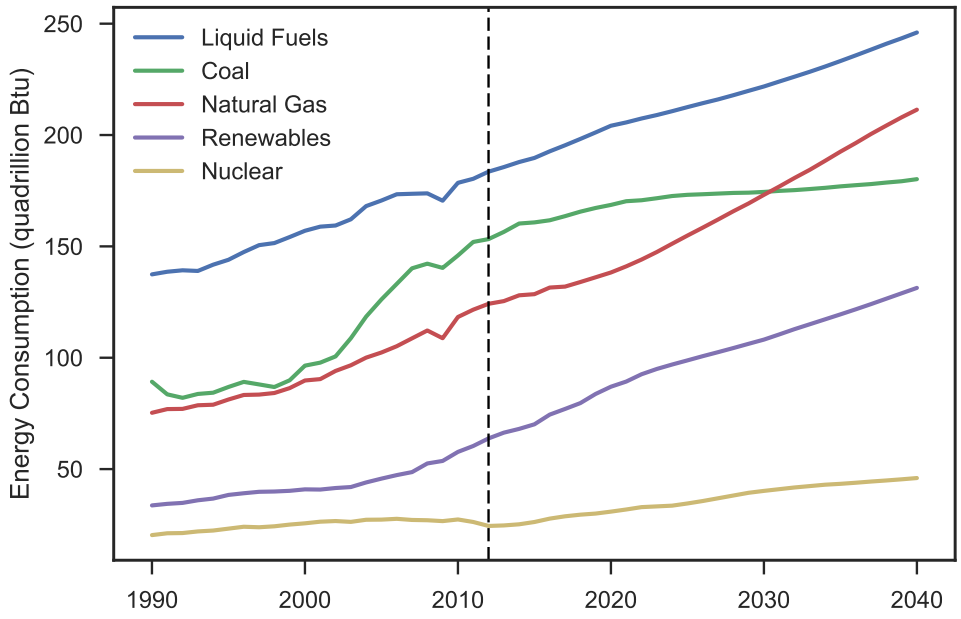

Figure 1.1: The global energy consumption by source from 1990 to 2040. Historical data (left of vertical dotted line) and projected trends (right of vertical dotted line). Data have been extracted from the IEA *Internation Energy Outlook 2016*[1]. Units are in Btu (British thermal units), where 1 Btu $\approx$ 1.054 kJ.

Concerns about the environmental impact of fossil fuels will see an increase in the energy produced from renewable sources. However, combustible fuels will remain the largest contributor to total global energy consumption for the foreseeable future. Fossil fuels are predicted to provide 78% of the world's total energy consumption in 2040, with petroleum and other liquid-based fuels notably providing the largest share. The majority of this consumption will occur in the transportation sector, where petroleum based engines will remain the standard[1]. Now, more so than ever, it is becoming increasingly important to optimise oil extraction rates, as the demand in liquid-fuel is unlikely to waver over the next half century.

Over the past fifty years the oil industry has improved the efficacy of its extraction techniques, in some cases extracting up to 50% of the original oil in place (OOIP) from a reservoir, up from a recovery rate of typically 30% in the 1970s[2,3]. This is due to an increased understanding in the geology surrounding the reservoir environment, as well as the physical and chemical processes occurring during extraction. Yet, whilst extraction rates have improved, at least half of the OOIP remains currently unavailable to supply the world energy markets. That is, at least half of all petroleum remains locked away within reservoirs around the world.

Current oil extraction procedure follows a three-step process. Upon drilling into a reservoir, a *primary flood* of oil is produced due to the inherent pressure difference between the surface and the reservoir. This pressure gradient can produce approximately 5-10% of the OOIP, before the reservoir pressure equilibrates with the surface[4].

Beyond this, *secondary recovery* increases the production lifetime of a reservoir by displacing the OOIP with an injected flooding-fluid/gas. This technique, also known as water-flooding for a water-based injection, once again increases the pressure within the reservoir. The secondary flood process can extract a further 20-25% of the OOIP from a reservoir[5].

Tertiary recovery, also known as enhanced oil recovery (EOR), is any additional technique beyond secondary recovery. It is achieved by modulating the chemistry of the fluid/gas used in a secondary flood. This causes a change in the wettability of the reservoir rock, releasing yet more previously unobtainable oil from the reservoir.

Whilst the aim of EOR is to increase oil extraction rates as much as possible, in reality, such techniques can only procure an additional few percent of the OOIP over a secondary water-flood[6].

Currently, the most common EOR techniques are either thermal based, such as steam injection and *in situ* combustion; or chemical based, such as CO_2 injection or polymer/surfactant floods[6]. One particularly compelling technique is low-salinity enhanced oil recovery, whereby the amount of recoverable OOIP can be increased upon flushing a reservoir with a flooding fluid with a lower salinity[6,7], see Figure 1.2.

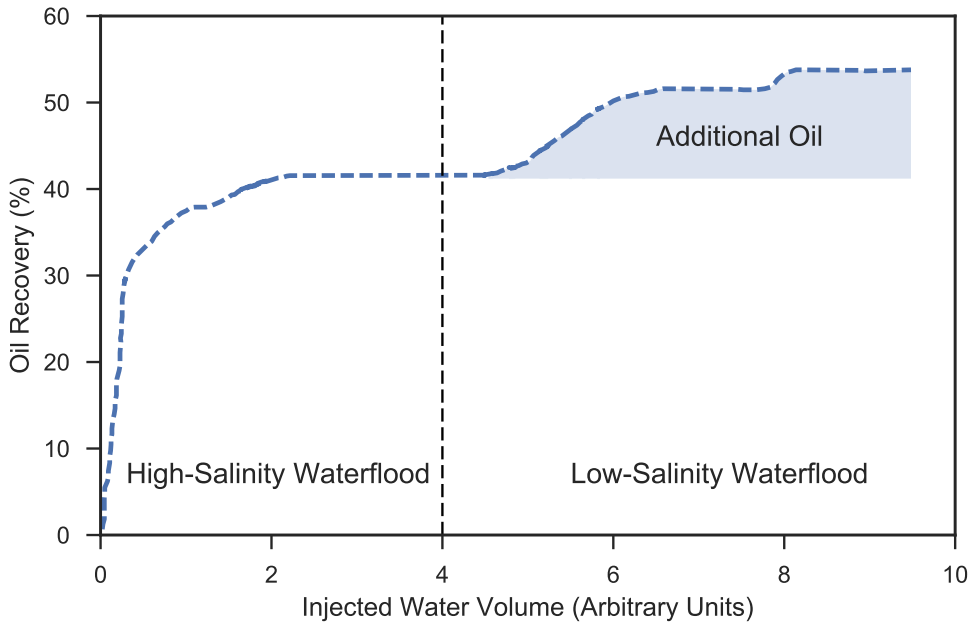

Figure 1.2: The increase in oil output during a low salinity flood. The shaded region integrates to give the total additional oil produced after introducing a low-salinity water-flood at injected volume $V = 4$ (arbitrary units). Image adapted from *GE Power: Water and Process Technologies* online resources[7].

This technique has numerable advantages over other EOR technologies. It is sustainable, cheap, the low-salinity injection water can be produced *in situ*, and the process is comparatively environmentally friendly[8]. Industrial interest in the technique has significantly increased in the past twenty years, however, one problem remains. Namely, there has been no scientific consensus on how the process truly works[9].

1.1 Low-Salinity Enhanced Oil Recovery

The history of low-salinity EOR can be traced back almost 60 years. In 1959, Martin *et al.* noted that an injection of diluted seawater into the Maracaibo basin, Venezuela, led to incremental improvements in oil recovery[10]. Their findings were expanded upon in 1967 by Bernard *et al.* who systematically studied the salinity effects in controlled core-flooding experiments[11]. Significant potential for enhanced oil recovery was found when the sodium chloride (NaCl) concentration of the flooding fluid dropped sequentially from 15% to 0.1% (mass percentage)[11].

More recently, several key criteria have been observed linking the chemical environment of the reservoir and the chemical composition of the low-salinity flood to the efficacy of the low-salinity water-flood. Current understanding states that the low-salinity enhanced oil recovery phenomenon depends on several key conditions:

- *The salinity and ionic composition of the flooding fluid.*
  Webb *et al.*[12] and Jerauld *et al.*[13] noted that optimal oil extraction rates occurred when the total dissolved ionic solids were reduced to less than 5000 ppm (n.b. seawater has approximately 35000 ppm total dissolved ionic solids). Morrow *et al.*[14] also noted that different brine compositions correlated directly with the amount of oil recovered. Yildiz *et al.*[15] saw that oil extraction rates were significantly improved upon reducing the overall divalent cation concentration in the water-flood, compared to reducing monovalent cation concentrations solely. These results present that the ionic composition (the ratio of divalent cations to monovalent cations) of a water-flood is just as important as the overall salinity of the water-flood.

- *The presence of clay minerals in the reservoir.*
  Clay minerals are widely present in the pores of sandstone reservoirs, where they form surface coatings upon the underlying quartz. These minerals are thought to interact significantly with the oil in the reservoir, and therefore play a determining role in the overall wettability of the rock[16,17]. Sandstone reservoirs are considered more viable for low-salinity EOR compared to carbonate reservoirs, as they contain more clay mineral content[18].

- *The presence of polar components in the recovered oil.*

  Zhang *et al.*[19] have noted that refined oils, stripped of polar oil components, do not present incremental oil recovery rates at lower salinities compared to oils containing polar groups. It has been argued that the polar functional groups interact primarily with the clay minerals present within the reservoir, whereby the clay can tether the oil to the reservoir rock (acting like a link in a chain), reducing the tendency of the oil to be released from the surface[20]. It has also been argued that the polar components in the oil act as natural surfactants and directly alter the wettability of the three-phase rock-oil-brine system[21,22].

1.1.1 Mechanisms of Low-Salinity Enhanced Oil Recovery

To date, studies have proposed more than 17 separate mechanisms by which a low-salinity water flood can enhance oil recovery. These are explained in some detail in the review by Sheng[9]. Some of the more frequently cited mechanisms are highlighted in Table 1.1.

Table 1.1: A selection of mechanisms proposed to explain the low-salinity enhanced oil recovery phenomenon. Generally, each mechanism can be categorised into one of two classes, either fines migration (FM) or wettability alteration (WA).

Mechanism	Class	Original Source
Fines mobilisation	FM	Tang and Morrow (1999)[16]
Release of mixed-wet particles	FM	Buckley and Morrow (2011)[23]
Salinity induced pH changes	WA	McGuire *et al.* (2005)[6]
Multicomponent ionic exchange	WA	Lager *et al.* (2008)[24]
Electric double layer expansion	WA	Ligthelm *et al.* (2009)[25]
Salting-in effects	WA	RezaeiDoust *et al.* (2009)[26]
Osmotic pressure effects	WA	Buckley and Morrow (2011)[23]

Many of these 17 mechanisms share similar features and can be categorised into two separate phenomenological classes (also indicated in Table 1.1):

(a) *Increasing oil output due to fines (cf. clay particles) migration.* Upon flushing the reservoir with a low-salinity flooding fluid, oil-bearing clay particles are released from the reservoir surface and carry the oil downstream[9].

(b) *Increasing oil output due to wettability alteration.* The introduction of a low-salinity flooding fluid into the three-phase rock-oil-brine interface directly alters the interfacial properties of the system. This makes the reservoir increasingly water-wet, releasing more oil, as shown in Figure 1.3.

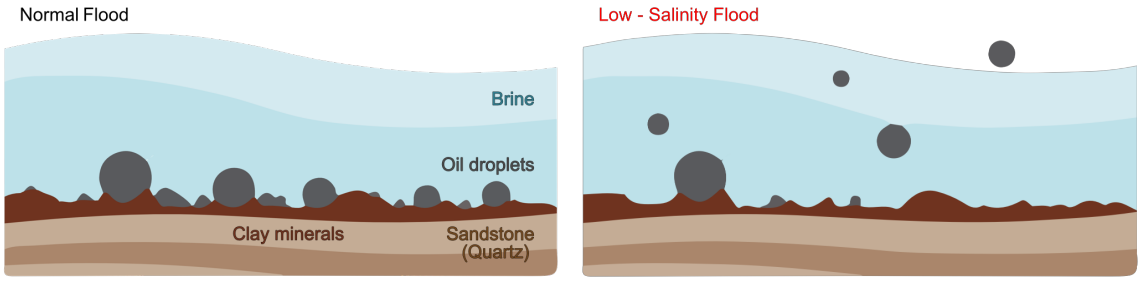

Figure 1.3: A schematic of the wettability change at the clay-oil-brine interface. The wettability is changed from a traditional water-flood (left) to a low-salinity water-flood (right), releasing previously unobtainable oil.

The mechanisms described by fines mobility can explain why the presence of clay minerals in the reservoir is important, but cannot describe why the salt composition and polar component concentration play a role in low-salinity EOR. The release of initially surface-bound clay minerals explains why certain clays are produced alongside the oil during a low-salinity flood. Notably, kaolinite particles (see Chapter 5 for a full introduction) are frequently displaced during a low-salinity flood, and are therefore released from the reservoir alongside the oil[16].

Conversely, the wettability alteration mechanisms explain why the chemical composition of the oil and the brine are linked to the potential for low-salinity EOR, but cannot explain the correlation between oil recovery and clay content in the resulting oil.

In summary, it appears as though both phenomenological classes occur during a low-salinity enhanced oil recovery flood, as neither one alone can explain all the requirements noted for a low-salinity flood. Ultimately, both phenomena are likely to be simultaneously responsible. The question then becomes: can we truly understand each phenomenon, and if so, can we utilise our understanding to further optimise oil extraction rates through low-salinity enhanced oil recovery?

1.1.2 Understanding Low-Salinity Enhanced Oil Recovery

Recently, scientists have begun to use a wide variety of techniques to help further our understanding of low-salinity enhanced oil recovery. Geological approaches have used core-flooding experiments to determine the conditions and relationships relevant for a low-salinity water-flood[27]. This, however, does not provide a complete picture of the physics and chemistry dictating the low-salinity effect. Rather it just informs upon the empirical end results. Beyond this, techniques such as scanning electron microscopy (SEM) and environmental scanning electron microscopy (ESEM) can provide information about the migration of clays by examining the state of a reservoir rock prior to, and post, water-flooding, as well as information about the wettability of a mineral surface by examining the contact angle of brine on the surface[27]. Again, this provides empirical information about the mechanisms at play, but does not provide a complete picture of the low-salinity EOR phenomenon.

Ultimately, the understanding of wettability alteration is a surface chemistry problem, which can only be explored using techniques of finer and finer detail. Atomic force microscopy (AFM) is a promising approach that has been used to provide information about the wettability alteration of a mineral surface at various brine compositions and ionic strengths[28]. Furthermore, computational techniques such as density functional theory and classical molecular dynamics are being increasingly used to understand the phenomenon of low-salinity enhanced oil recovery at an atomic resolution, see Figure 1.4. For this reason, these techniques seem ideally placed to interpret the low-salinity phenomenon at the nanoscale.

Density functional theory (DFT) is a computation technique based upon the principles of quantum mechanics (QM). The method explicitly includes electron interactions, and is able to model reaction mechanisms between clay, oil and brine. Recently, DFT simulations have become a useful tool to model the interaction of simple organic molecules on reservoir surfaces, for example the adsorption of oil-relevant monomers on clay surfaces[29] and upon carbonates[30]. That noted, the complexity of composition and structure of most clay minerals and the sheer number of interactions involved in low-salinity EOR often rules out the use of QM methods with their restricted time- and length-scales.

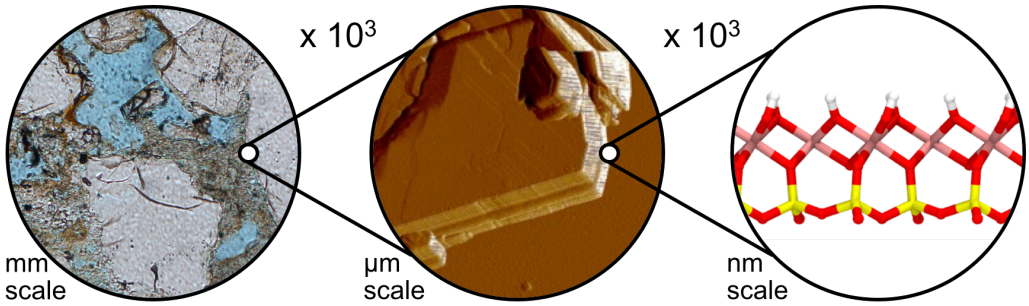

Figure 1.4: The scales of research examining low-salinity EOR. Optical microscope image (left) of a sandstone core presenting a composition of large quartz grains (silver), pore water (blue) and clay minerals between quartz grains (grey and brown). Atomic force microscope image of clay grains stacked upon each other (centre), and the atomic structure of a single clay layer (right). ESEM and AFM images have been taken from unpublished work by R. Kareem and P. Cubillas.

In contrast, classical atomistic molecular dynamics (MD) can probe the mechanisms of low-salinity enhanced oil recovery at notably larger time- and length-scales. Atomistic molecular dynamics simulations treat atoms as spheres, intramolecularly bonded to one another via a set of springs. Compared to DFT, this simpler approach dramatically increases both the length-scale and time-scale that can be simulated. The main disadvantage of classical MD simulations is the lack of bond breaking and bond formation, hence chemical reactions are impossible to model using classical MD without the use of specialist parameter sets (such as ReaxFF[31]). A comprehensive overview of the techniques and implementations of classical molecular dynamics is presented in the work of Cramer[32] and Frenkel & Smit[33].

Due to its potential to unravel physical processes with molecular resolution, classical MD is becoming one of the key techniques used to model clay systems. Historically, computational studies have been restricted to understanding the structural and mechanical (*i.e.* bulk) properties of clay minerals. Such examinations have been highlighted in the review article by Greenwell *et al.*[34]. Similarly, the large-scale structural properties of clay minerals have been examined by Suter *et al.*[35]. Only recently have the models begun to see use in understanding the interfacial properties of clay surfaces, as highlighted in the article by Greathouse *et al.*[36]. In particular, the interface between clay and oil has rarely been discerned using classical MD. This forms the key objective of this thesis.

1.2 Thesis Objectives

This thesis is a computational study into the phenomenon of low-salinity enhanced oil recovery. Interactions between clay mineral surfaces, model oil compounds, and brine solutions have been modelled using classical atomistic molecular dynamics. The emphasis of this study is on understanding the dominant factors controlling low-salinity EOR at an atomic level, by using MD simulations to further our understanding of the technique. The main objectives of the thesis are:

1. To understand the role that clay particles play in low-salinity EOR at an atomic level, and to understand how different clays interact with oil.
   As to examine the work of Tang and Morrow[16], who state that clay minerals play an important role in the phenomenon of low-salinity EOR.

2. To understand the role of salt concentration and ionic composition in low-salinity EOR. Whether the distinction between monovalent and divalent cation (primarily Na^+ or Ca^{2+}) is important in determining the oil-clay interactions.
   To determine the 'salinity' component of low-salinity EOR; and to determine whether an ion exchange mechanism is important for low-salinity EOR, as proposed by Lager et al.[24]

3. To interpret the role of oil composition for oil-clay interactions. To understand how different functional groups (carboxylic acid, primary amines) alter the behaviour of alkanes at the oil-clay interface.
   To examine the role of polar functional groups in low-salinity EOR, as observed by Zhang et al.[19].

4. To probe how useful MD simulations can be to help us interpret surface wetting and wettability alterations at the atomic level.

1.3 Thesis Outline

With these aims in mind, the thesis is broken down into several chapters. Each chapter is self-contained and is presented in an article-style format. Each chapter has been written with forethought of being submitted for publication in the future (Chapters 2 and 6), or has already been published in peer-reviewed journals (Chapters 3, 4 and 5). A brief description of each chapter follows:

Chapter 2: Understanding Oil/Brine/Oil-Brine Interfaces: Validation of Force Fields and the Role of NaCl Concentration.

This chapter is currently being finalised for submission. The chapter introduces the concept of using atomistic simulations to model the interfacial properties of different liquid phases. The presented work focusses solely on the liquid-vapour and liquid-liquid interfaces of alkanes and NaCl electrolytes. This chapter trials various force fields in an attempt to interpret their applicability to model more complex (three-phase) systems. It is shown that the most commonly used models of water frequently underestimate the absolute surface tension of water, however, their variation with salt concentration generally agrees with the experimental measurements. The surface tensions of alkanes are in agreement with experiment for various force fields, and the water-alkane interfacial tensions also agree with experimental trends. All parameters utilised in later chapters are validated and are shown to accurately reproduce the alkane-brine interfacial tension as a function of NaCl concentration.

Chapter 3: Montmorillonite-Organic Interactions under Varying Salinity. This chapter has previously been published in its presented form in the Journal of Physical Chemistry C:

Thomas Underwood, Valentina Erastova, Pablo Cubillas & H. Chris Greenwell.

Molecular Dynamics Simulations of Montmorillonite-Organic Interactions under Varying Salinity: An Insight into Enhanced Oil Recovery.

J. Phys. Chem. C, 2015, 119 (13), pages: 7282-7294, DOI: 10.1021/acs.jpcc.5b0055

The main aim of this chapter is to interpret the phenomenon of low-salinity EOR at the surface of montmorillonite, a highly-charged clay. The chapter has an in-depth breakdown of the potential mechanisms driving wettability alteration at clay surfaces. The MD simulations examine a mixture of decane and decanoic acid at various NaCl concentrations with Na^{+}- and Ca^{2+}- charge-balanced montmorillonite. The results present that expansion of the electric double layer (a concept introduced in detail in Chapter 3) is not able to fully explain the effects of low-salinity enhanced oil recovery. The pH surrounding a clay's basal surface, and hence the protonation and charge of acid molecules, is determined to be one of the more dominant effects. Furthermore, it is shown that the presence of calcium cations can drastically alter the oil wettability of a clay mineral surface. Replacing all divalent cations with monovalent cations dramatically increases the water wettability of a clay surface.

Chapter 4: The Hofmeister Series for Montmorillonite.

This chapter was invited for publication in a special issue of *Clay and Clay Minerals*. It has previously been published in its presented form in the *Clay and Clay Minerals* journal:

Thomas Underwood, Valentina Erastova & H. Chris Greenwell.

Ion Adsorption at Clay Mineral Surfaces:

The Hofmeister Series for Hydrated Smectite Minerals.

Clays & Clay Min., 2016, 64 (4), pages: 472-487, DOI:10.1346/CCMN.2016.0640310

The main aim of this chapter is to quantify the strength of adsorption of charge-balancing cations to the mineral surface montmorillonite, previously introduced in Chapter 3. This is achieved by calculating the free-energy of adsorption of the ion to the surface using the well-tempered metadynamics algorithm. Primarily, the aim is to discern whether divalent or monovalent ions will be preferentially adsorbed to the mineral surface, and therefore whether the low-salinity effect can be explained by cation exchange (whereby it is energetically favourable for a monovalent sodium ion to replace a divalent calcium ion that is initially charge balancing the clay). The results show that the ions exhibit a wide variety of behaviours, readily forming several metastable states above the clay surface depending upon the ions hydration properties and the hydration properties of the clay. In this instance, sodium ions will energetically replace calcium ions on the surface of montmorillonite, driving the low-salinity effect through mechanisms presented in Chapter 3.

Chapter 5: Kaolinite-Organic Interactions.

This chapter has previously been published in its presented form in the Journal of Physical Chemistry C:

Thomas Underwood, Valentina Erastova& H. Chris Greenwell.

Wetting Effects and Molecular Adsorption at Hydrated Kaolinite Clay Mineral Surfaces.

J. Phys. Chem. C, 2016, 120 (21), pp 1143311449, DOI: 10.1021/acs.jpcc.6b00187

This chapter introduces kaolinite, an uncharged clay, and models its interactions with various organic molecules representative of the basic molecular building blocks of oil. The interactions of decane, decanoic acid and primary decanamine with kaolinite are studied. Kaolinite presents two different basal surfaces to the pore spaces within the reservoir, and both surfaces are considered. The primary result is that the relative affinity of the organic molecules to the kaolinite surface may be readily switched between the hydroxylated aluminol surface and the silicate surface according to the pH and the nature of the organic head functional group.

Chapter 6: Kaolinite Wettability at Varying Brine Concentration.

This chapter builds upon the work presented in Chapter 5 by introducing electrolyte solutions at various NaCl concentrations to the surface of kaolinite. The chapter attempts to elucidate the phenomenon of low-salinity EOR by decoupling the three-phase clay-oil-brine system into simpler two-phase systems: clay-oil, clay-brine and oil-brine. Immersion energies (work of adhesions) of NaCl brines to kaolinite surfaces are calculated and compared to experimental values. Furthermore, contact angles are measured for brine-clay interfaces, and are compared to experiment. A molecular mechanism for the *salinity* component of the low-salinity enhanced oil recovery phenomenon is discerned. Overall, this chapter attempts to introduce a more quantitative and insightful approach to interpreting the phenomenon of low-salinity EOR via atomistic MD simulations. This chapter is currently being finalised for submission.

Chapter 7: Conclusions and Future Outlook

This chapter draws together the results of all other chapters and highlights the key conclusions of the thesis. It presents the overall successes of the work and discusses where there is future potential for examining the phenomenon of low-salinity enhanced oil recovery using atomistic simulations.

Also presented in this chapter is a set of ideas (additional alleyways examined throughout the period of research) that may lead to fruitful insights related to surface chemistry/low-salinity enhanced oil recovery.

Bibliography

[1] Energy Information Administration (U.S.) and Government Publications Office. *International Energy Outlook: 2016 with Projections to 2040*. International Energy Outlook. U.S. Government Printing Office, 2016.

[2] TP Castor, WH Somerton, and JF Kelly. Recovery mechanisms of alkaline flooding. In *Surface phenomena in enhanced oil recovery*, pages 249–291. Springer, 1981.

[3] S Kokal and A Al-Kaabi. Enhanced oil recovery: challenges & opportunities. *World Petroleum Council: Official Publication*, 12(1):64–68, 2010.

[4] T Ahmed and P McKinney. *Advanced Reservoir Engineering*. Gulf Professional Publishing, 2011.

[5] A Muggeridge, A Cockin, K Webb, H Frampton, I Collins, T Moulds, and P Salino. Recovery rates, enhanced oil recovery and technological limits. *Philosophical Transactions of the Royal Society A*, 372(2006):20120320, 2014.

[6] PL McGuire, JR Chatham, FK Paskvan, DM Sommer, and FH Carini. Low salinity oil recovery: An exciting new eor opportunity for Alaska's North Slope. In *SPE Western Regional Meeting*. Society of Petroleum Engineers, 2005.

[7] GE Power: Water and Process Technologies. Low salinity water flooding injection. `https://www.gewater.com/products/enhanced-oil-recovery`, 2017. [Online; accessed 01-04-2017].

[8] BG Thomas, A Iliyas, TE Johansen, K Hawboldt, and F Khan. Towards sustainable and environmentally friendly enhanced oil recovery in offshore Newfoundland, Canada. In *Offshore Technology Conference*. Offshore Technology Conference, 2010.

[9] JJ Sheng. Critical review of low-salinity waterflooding. *Journal of Petroleum Science and Engineering*, 120:216–224, 2014.

[10] JC Martin. The effects of clay on the displacement of heavy oil by water. In *Venezuelan Annual Meeting*. Society of Petroleum Engineers, 1959.

[11] GG Bernard. Effect of floodwater salinity on recovery of oil from cores containing clays. In *SPE California Regional Meeting*. Society of Petroleum Engineers, 1967.

[12] KJ Webb, CJJ Black, and H Al-Ajeel. Low salinity oil recovery-log-inject-log. In *Middle East Oil Show*. Society of Petroleum Engineers, 2003.

[13] GR Jerauld, KJ Webb, C-Y Lin, and J Seccombe. Modeling low-salinity waterflooding. In *SPE Annual Technical Conference and Exhibition*. Society of Petroleum Engineers, 2006.

[14] NR Morrow, G-Q Tang, M Valat, and X Xie. Prospects of improved oil recovery related to wettability and brine composition. *Journal of Petroleum Science and Engineering*, 20(3):267–276, 1998.

[15] HO Yildiz, M Valat, and NR Morrow. Effect of brine composition on wettability and oil recovery of a prudhoe bay crude oil. *Journal of Canadian Petroleum Technology*, 38(01), 1999.

[16] G-Q Tang and NR Morrow. Influence of brine composition and fines migration on crude oil/brine/rock interactions and oil recovery. *Journal of Petroleum Science and Engineering*, 24(2):99–111, 1999.

[17] O Fassi-Fihri, M Robin, and E Rosenberg. Wettability studies at the pore level: a new approach by the use of cryo-scanning electron microscopy. *SPE Formation Evaluation*, 10(01):11–19, 1995.

[18] F Civan. *Reservoir Formation Damage*. Gulf Professional Publishing, Burlington, 2011.

[19] P Zhang, MT Tweheyo, and Tor Austad. Wettability alteration and improved oil recovery by spontaneous imbibition of seawater into chalk: Impact of the potential determining ions Ca^{2+}, Mg^{2+}, and SO_4^{2-}. *Colloids and Surfaces A: Physicochemical and Engineering Aspects*, 301(1):199–208, 2007.

[20] G-Q Tang. *Brine Composition and Waterflood Recovery for Selected Crude Oil/brine/rock Systems*. University of Wyoming, 1998.

[21] D Tiab and EC Donaldson. *Petrophysics: theory and practice of measuring reservoir rock and fluid transport properties*. Gulf professional publishing, 2015.

[22] A RezaeiDoust, T Puntervold, and T Austad. Chemical verification of the eor mechanism by using low saline/smart water in sandstone. *Energy & Fuels*, 25(5):2151–2162, 2011.

[23] N Morrow and J Buckley. Improved oil recovery by low-salinity waterflooding.

Journal of Petroleum Technology, 63(05):106–112, 2011.

[24] A Lager, KJ Webb, CJJ Black, M Singleton, and KS Sorbie. Low salinity oil recovery-an experimental investigation1. *Petrophysics*, 49(01), 2008.

[25] DJ Ligthelm, J Gronsveld, J Hofman, N Brussee, F Marcelis, and H van der Linde. Novel waterflooding strategy by manipulation of injection brine composition. In *EUROPEC/EAGE Conference and Exhibition*. Society of Petroleum Engineers, 2009.

[26] A RezaeiDoust, T Puntervold, S Strand, and T Austad. Smart water as wettability modifier in carbonate and sandstone: A discussion of similarities/differences in the chemical mechanisms. *Energy & fuels*, 23(9):4479–4485, 2009.

[27] R Kareem. *Nano Geochemistry of Low Salinity Enhanced Oil Recovery*. PhD thesis, Durham University, 2016.

[28] T Hassenkam, MP Andersson, E Hilner, J Matthiesen, S Dobberschütz, KN Dalby, N Bovet, SLS Stipp, P Salino, C Reddick, and IR Collins. Could atomic-force microscopy force mapping be a fast alternative to core-plug tests for optimizing injection-water salinity for enhanced oil recovery in sandstone? *SPE Journal*, 21(03):720–729, 2016.

[29] Dawn L Geatches, A Jacquet, SJ Clark, and HC Greenwell. Monomer adsorption on kaolinite: modeling the essential ingredients. *Journal of Physical Chemistry C*, 116(42):22365–22374, 2012.

[30] J Zhong, X Wang, D Du, L Wang, Y Yan, and J Zhang. Combined molecular dynamics and quantum mechanics study of oil droplet adsorption on different self-assembly monolayers in aqueous solution. *Journal of Physical Chemistry C*, 117(24):12510–12519, 2013.

[31] ACT Van Duin, S Dasgupta, F Lorant, and WA Goddard. Reaxff: a reactive force field for hydrocarbons. *Journal of Physical Chemistry A*, 105(41):9396–9409, 2001.

[32] Christopher J Cramer. *Essentials of computational chemistry: theories and models*. John Wiley & Sons, 2013.

[33] D Frenkel and B Smit. *Understanding molecular simulation: from algorithms*

to applications, volume 1. Academic press, 2001.

[34] HC Greenwell, W Jones, PV Coveney, and S Stackhouse. On the application of computer simulation techniques to anionic and cationic clays: a materials chemistry perspective. *Journal of Materials Chemistry*, 16(8):708–723, 2006.

[35] JL Suter, RL Anderson, HC Greenwell, and PV Coveney. Recent advances in large-scale atomistic and coarse-grained molecular dynamics simulation of clay minerals. *Journal of Materials Chemistry*, 19(17):2482–2493, 2009.

[36] JA Greathouse, KL Johnson, and HC Greenwell. Interaction of natural organic matter with layered minerals: recent developments in computational methods at the nanoscale. *Minerals*, 4(2):519–540, 2014.

Chapter 2

Understanding Oil-Brine Interfaces: Validation of Force Fields and the Role of NaCl Concentration

This chapter introduces the concept of using atomistic simulations to model the interfacial properties of different liquid phases. The presented work focusses solely on the liquid-vapour & liquid-liquid interfaces of alkanes and NaCl electrolytes. This chapter trials various force fields in an attempt to interpret their applicability to model more complex (three-phase) systems. The primary aim of this chapter is to validate the choice of oil and water models used in later chapters. Whilst the article is written in the plural form (*i.e. we* rather than *I*) the entirety of the article (simulations, analysis and writing) has been completed by thesis author.

Abstract

In this study, classical molecular dynamic simulations have been used to calculate the surface tension of water and decane in their liquid-vapour phases. Six different force fields for water, and three further force fields for alkane are compared to experimental data. CGenFF, OPLS-AA and TraPPE-UA all accurately reproduce the interfacial properties of decane. The TIP4P2005 (four-point) water model is shown to be the most accurate water model for predicting the interfacial properties of water. The SPC/E water model is the best three-point parameterisation of water for this purpose. The salinity dependence on surface/interfacial tension is accurately captured using the Smith & Dang parameterisation of NaCl. We observe that the Smith & Dang model slightly overestimates the surface/interfacial tensions at higher salinities. This is ascribed to an overestimation of the ion exclusion at the interface.

2.1 Introduction

The liquid-liquid interface plays an important role in many physical, chemical and biological processes. From phase transfer catalysis to liquid chromatography; liquid-liquid extraction to pharmaceutical drug delivery[1].

One compelling process dictated by the liquid-liquid interface is low-salinity enhanced oil recovery (EOR). A procedure where oil extraction rates are improved upon decreasing the salt concentration of a water-flood[2]. The low-salinity EOR effect is thought to be due to wettability alterations at the oil-brine-mineral interface over a wide range of scales, from the macroscopic to nanoscopic[2]. Yet, despite extensive scientific efforts, the underlying mechanisms driving this wettability change are yet to be fully discerned, especially at the molecular level[3]. Consequently, it is becoming increasingly important to understand the properties of the brine-oil interface with atomic resolution, and how these properties change upon introduction (or reduction) of inorganic salts. A true molecular understanding of the brine-oil interface may provide the key needed to unlock the mystery of low-salinity EOR.

Experimental studies of the atomic structuring of fluid-fluid interfaces have historically been hindered by the lack of appropriate techniques capable of probing the interface with sufficient resolution. More recently, however, surface sensitive experimental techniques, such as sum frequency generation (SFG) spectroscopy, second harmonic generation (SHG) spectroscopy, and x-ray reflectivity measurements, have been able to probe the properties of fluid-vapour and fluid-fluid interfaces[4]. For example, Braslau *et al.* measured the surface width of the water-vapour interface (the distance between bulk-like liquid region of water and bulk-like vapour region) as 3.2 Å using x-ray reflectivity and capillary wave theory[5], whilst similar experiments by Sanyal *et al.* discerned the ethanol-vapour interfacial width as 6.9 Å[6]. The interface between water and alkane has also been experimentally measured using x-ray reflectivity, as in the study of Mitrinovic *et al.*, who measured the width of the water-hexane interface as 3.5 Å[7]; and Tikhonov *et al.*, who measured the interfacial width of water-docosane ($C_{22}H_{46}$) as 5.7 Å[8].

Such advancements in experimental techniques have been mirrored in the computational realm. Recently, classical molecular dynamics (MD) simulations have been used to help interpret the phenomena present at the interfaces of water-vapour[9], electrolyte-vapour[10] and water-alkane[11,12]. In turn, MD simulations, are becoming increasing utilised to understand the phenomenon of low-salinity enhanced oil recovery. Such simulations frequently examine the interface between rock, oil and brine at the molecular level[13,14,15,16]. Many of these studies, however, fundamentally fail to validate the accuracy of the underlying interactions at the liquid-surface and liquid-liquid interface; *viz.* the studies fail to validate the mutual compatibility of the force fields (the set of interaction parameters) describing the clay, the oil, the water, and the inorganic solvated ions.

2.1.1 Water and Oil Models in Literature

No single force field is truly universal, and most MD studies of low-salinity enhanced oil recovery combine at least three separate force fields without prior validation of their respective interfacial properties.

Many different water models exist in the literature, and most excel at capturing certain aspects of water's unusual physical properties. For example, the TIP4P2005 model excels at modelling the phase behaviour of water over a variety of temperatures and pressures, especially when compared to other models such as SPC/E[17,18]. However, the SPC/E model of water more accurately reproduces the experimental dielectric constant of water[17,18]. As no one water model is truly universal, it is not uncommon to observe various models being used in three-phase MD simulations. Commonly used water models applied to low-salinity EOR include the SPC[19], SPC/E[20], TIP3P[21] and TIP4P[21] parameterisations.

Similar arguments also apply to the various parameterisation of oil molecules. Typical oil models used in previous work include CGenFF[22], TraPPE[23] and OPLS[24]. Both TraPPE and OPLS were parameterised to model organic solvents (with TraPPE specifically parameterised to model alkanes)[23,24]. OPLS, however, is frequently combined with ClayFF[13,25] (a force field frequently used to model mineral surfaces), despite the fact that both force fields are parameterised with different Lennard-Jones

mixing rules, and are therefore not inherently compatible. In contrast to TraPPE and OPLS, CGenFF is more general. CGenFF offers fully automated atom typing, and therefore offers large potential throughput.

The InterfaceFF[26] force field has seen increasing use in recent years[27,28]. It has been parameterised empirically to accurately reproduce the interfacial properties of mineral surfaces, however its potential to model three-phase simulations is limited by the compatibility between organic and water models.

With the increasing quantity of MD simulations related to enhanced oil recovery being presented in literature, it is becoming more apparent that the two-phase interfacial behaviour between oil and water must be examined in thorough detail. In particular, it is becoming important to understand the role that salt concentration plays upon the interfacial behaviour between oil and water.

In the present work, we investigate the utility of various force fields to accurately reproduce the interfacial behaviour between water and decane at different NaCl concentrations. The aim of the article is to interpret the phenomena of the liquid-liquid interface at the molecular level, and to trial various organic force fields for future use in more complex three-phase simulations.

The rest of the article is organised as follows. Section 2.2 describes the computational methodology used throughout the paper. Section 2.3 presents the results of this study. The results section is further broken down into an examination of the alkane force fields at various temperatures (section 2.3.1), the properties of the water-vapour interface without salts (section 2.3.2) and with salts (section 2.3.3), and finally the properties of the water-alkane interface at various NaCl concentrations (section 2.3.4).

2.2 Computational Methods

2.2.1 System Setup

Three different systems are presented in this study. In the first, a 5×5×5 nm^3 box of 392 decane molecules is inserted into 5×5×20 nm^3 simulation box. In the second, a 5×5×5 nm^3 box of 4139 water molecules is inserted into 5×5×20 nm^3 simulation box. The number of decane and water molecules in each film is calculated to match the bulk density of each solvent at 293.15 K and 1.01325 bar, 0.727 g/cm^3 for decane and 0.9982 g/cm^3 for water respectively[29]. In the third system, the decane and water films are combined in a 5×5×10 nm^3 simulation box. Each system was generated using the Packmol software package[30]. A post-equilibration snapshot of each system is presented in Figure 2.1.

Systems involving water were further examined at various NaCl concentrations. Systems were setup in terms of NaCl molal concentration, up to a maximum of 3.00 mol/kg, in increments of 0.50 mol/kg. This was achieved by replacing water molecules with the relevant amount of sodium and chloride ions. The number of water molecules and ions present in each simulation is presented in Table 2.1. Additionally, 0.20 mol/kg NaCl solution was examined. Whilst simulation results are presented in molal concentration (mol/kg), experimental results are often presented in terms of molar concentration (mol/L). The conversion from molar concentration to molal concentration is presented in Table 2.1, using data extrapolated from the CRC Handbook of Chemistry & Physics[31].

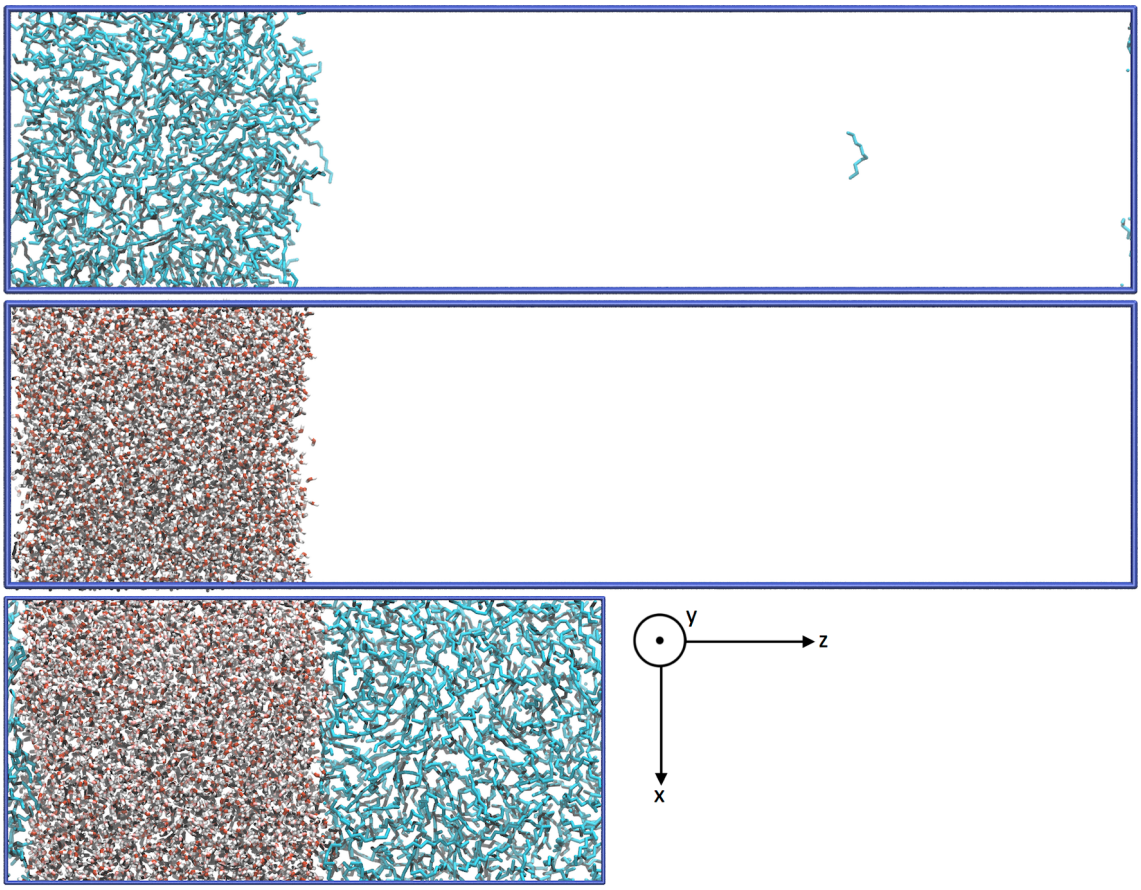

Figure 2.1: The alkane-vapour, water-vapour and water-alkane interface examined in this study (top to bottom). Each simulations is 5 × 5 nm in the xy-plane. Liquid-vapour simulations are extended to 20 nm in the z-axis, whilst water-alkane simulations are extended to 10 nm in the z-axis.

Table 2.1: The amount of water molecules, aqueous sodium ions and aqueous chloride ions present in each simulation. Conversions between molal and molar concentrations have been calculated using the density of NaCl electrolyte at various concentrations[31].

m (mol/kg)	N_{water}	N_{Na}	N_{Cl}	$Mass_{NaCl}$ (%)	ρ (g/cm^3)	M (mol/L)
0.00	4139	0	0	0.0	0.998	0.00
0.20	4109	15	15	1.1	1.005	0.20
0.50	4063	38	38	2.9	1.018	0.51
1.00	3989	75	75	5.7	1.040	1.02
1.50	3913	113	113	8.6	1.061	1.56
2.00	3837	151	151	11.3	1.082	2.10
2.50	3763	188	118	13.9	1.102	2.63
3.00	3687	226	226	16.6	1.122	3.17

2.2.2 Force Fields

Three different force field parameterisations for decane have been tested in this study: TraPPE-UA[23], OPLS-AA[32,24] and CGenFF[22,33,34]. TraPPE-UA is a united atom force field, where CH_3- and -CH_2- groups are modelled as soft spheres. OPLS-AA and CGenFF are both all atom models, where carbon and hydrogen atoms are modelled explicitly.

Six different water models were examined in the water-vapour interface: SPC[19], SPC/E[20], TIP3P[21], TIP3Pc[22], TIP4P[21] and TIP4P2005[35]. TIP3Pc refers to the CHARMM variant of the original TIP3P parameterisation, whereby hydrogen atoms contain Lennard-Jones sites.

The Smith and Dang parameterisation has been used to model aqueous sodium and chloride ions[36].

In all simulations, non-bonded interactions between two atoms in different molecules, or between atoms separated by three or more bonds within the same molecule, have been calculated using a combination of Coulomb's law and a 12-6 Lennard-Jones potential:

$$U(r_{ij}) = \frac{1}{4\pi\epsilon_0}\frac{q_i q_j}{r_{ij}} + 4\epsilon_{ij}\left[\left(\frac{\sigma_{ij}}{r_{ij}}\right)^{12} - \left(\frac{\sigma_{ij}}{r_{ij}}\right)^{6}\right] \tag{2.2.1}$$

where ϵ_{ij} represents the strength of the non-bonded dispersion interaction, σ_{ij} represents the equilibrium separation, and r_{ij} is the current separation distance between atoms i and j. A complete list of the non-bonded parameters is presented in Table 2.2 and Table 2.3 for decane and water respectively. Interaction parameters for sodium and chloride ions are also presented in Table 2.3.

Table 2.2: The nonbonded input parameters of CGenFF, OPLS-AA & TraPPE-UA. CH2* corresponds to the carbon atom bonded to CH3, *i.e.* CH2(-CH3).

	CGenFF			OPLS-AA			TraPPE-UA	
	σ (nm)	ϵ (kJ/mol)	q (e)	σ (nm)	ϵ (kJ/mol)	q (e)	σ (nm)	ϵ (kJ/mol)
CH3	0.365	0.326	−0.271	0.350	0.276	−0.180	0.375	0.815
CH2*	0.358	0.234	−0.179	0.350	0.276	−0.120	0.395	0.815
CH2	0.358	0.234	−0.180	0.350	0.276	−0.120	0.395	0.815
H3	0.239	0.100	+0.090	0.250	0.126	+0.060	N/A	
H2	0.239	0.146	+0.090	0.250	0.126	+0.060	N/A	

Table 2.3: The nonbonded input parameters of the examined water models. Also presented are the input parameters for aqueous NaCl. Empty entries correspond to null inputs. The Mw atom type corresponds to the charge-carrying dummy atom in the 4-point water models.

Force Field	Atom	σ (nm)	ϵ (kJ/mol)	q (e)
SPC	O	0.316557	0.650194	−0.82
	H			+0.41
SPC/E	O	0.316557	0.650194	−0.8476
	H			+0.4238
TIP3P	O	0.315057422683	0.63639	−0.834
	H			+0.417
TIP3Pc	O	0.315057422683	0.63639	−0.834
	H	0.0400013524445	0.192464	+0.417
TIP4P	O	0.315365	0.648520	
	H			+0.52
	Mw			−1.04
TIP4P2005	O	0.315890	0.774908	
	H			+0.5564
	Mw			−1.1128
Smith-Dang	Na	0.23500	0.54392	+1
	Cl	0.44000	0.41840	−1

All simulations (except those involving OPLS) utilised Lorentz-Berthelot mixing rules to calculate the non-bonded Lennard-Jones interactions between unlike species:

$$\sigma_{ij} = \frac{\sigma_{ii} + \sigma_{jj}}{2} \qquad \epsilon_{ij} = \sqrt{\epsilon_{ii}\epsilon_{jj}} \tag{2.2.2}$$

Simulations involving OPLS have used geometric mixing rules to calculate cross-term Lennard-Jones interactions:

$$\sigma_{ij} = \sqrt{\sigma_{ii}\sigma_{jj}} \qquad \epsilon_{ij} = \sqrt{\epsilon_{ii}\epsilon_{jj}} \tag{2.2.3}$$

The non-bonded (Lennard-Jones and electrostatic) interactions between atoms separated by exactly three bonds (1-4 pair interactions) are excluded in simulations using the TraPPE-UA force field and are scaled by half in simulations using OPLS-AA. For CGenFF, the Lennard-Jones 1-4 pair interactions are calculated using custom mixing terms as presented in Table 2.4, whilst 1-4 Coulomb interactions are fully evaluated.

Table 2.4: The 1-4 pair interactions between carbon and hydrogen used in CGenFF.

i	j	σ_{ij} (nm)	ϵ_{ij} (kJ/mol)
C*	C*	0.338541512893	0.041840000000
C*	H*	0.288651184677	0.078275472531

Covalent bonds between atoms have been modelled in terms of harmonic potentials:

$$U(r_{ij}) = \frac{k_r}{2}(r_{ij} - r_0)^2 \tag{2.2.4}$$

where r_{ij} is the bond distance. The TraPPE-UA parameterisation maintains fixed bond lengths for all C-C bonds in a simulation.

Bond bending interactions are modelled in terms of harmonic potentials for OPLS-AA, TraPPE-UA and all water models:

$$U(\theta) = \frac{k_\theta}{2}(\theta - \theta_0)^2 \tag{2.2.5}$$

where θ is the angle formed between three atoms.

CGenFF used a Urey-Bradley potential to define bond bending interactions:

$$U(\theta) = \frac{k_\theta}{2}(\theta - \theta_0)^2 + \frac{k^{UB}}{2}(r_{ik} - r_0)^2 \tag{2.2.6}$$

where r_{ik} is the distance between atom i and k in the angle formed by the triplet ijk.

The torsion (dihedral) potential describes the interaction between the planes formed by the first three, and last three atoms, of four consecutively bonded atoms. The torsion about a carbon-carbon bond is defined using the Ryckaert and Bellemans model for both OPLS-AA and TraPPE-UA:

$$U(\phi) = \sum_{i=0}^{5} C_i(\cos(\psi))^i \tag{2.2.7}$$

where $\psi = \phi - 180^\circ$ and ϕ is the angle between the planes. CGenFF uses a dihedral potential of the form:

$$U(\phi) = k_\phi(1 + \cos(n\phi - \phi_s)) \tag{2.2.8}$$

where ϕ_s sets the angle of minimum energy and n determines the number of minima in the dihedral potential.

Covalent (harmonic) bonds involving hydrogen atoms were constrained in all simulations using the LINCS algorithm with a series expansion accurate to fourth order.

A complete list of bonded parameters used in this study are presented in Tables 2.5, 2.6 and 2.7.

Table 2.5: The angle and bonded terms for OPLS-AA and TraPPE-UA. r_0 is given in nm and k_r is in kJ/(mol·nm^2). θ_0 is given in degrees and k_θ is in kJ/(mol·rad^2).

	OPLS-AA		TraPPE-UA	
Bond	r_0	k_r	r_0	k_r
C-C	0.1529	224262.4	0.154	Fixed
C-H	0.109	284512	N/A	N/A
Angle	θ_0	k_θ	θ_0	k_θ
C-C-C	112.7	488.273	114	519.65389
C-C-H	110.7	313.8	N/A	N/A
H-C-H	107.8	276.144	N/A	N/A

Table 2.6: The torsion terms for OPLS-AA and TraPPE-UA. All torsion coefficients are in units of kJ/mol.

Force Field	Torsion	C_0	C_1	C_2	C_3	C_4	C_5
TraPPE-UA	C-C-C-C	8.39736	16.78632	1.13393	-26.3176	0	0
CGenFF	C-C-C-C	2.9288	-1.4644	0.2092	-1.6736	0	0
	C-C-C-H	0.6276	1.8828	0	-2.5104	0	0
	H-C-C-H	0.6276	1.8828	0	-2.5104	0	0

Table 2.7: The angle, bonded and torsion terms for CGenFF. r_0 is given in nm; k_r, k^{UB} and k_ϕ are in kJ/(mol·nm^2); θ_0 and ϕ_s are in degrees; and k_θ is in kJ/(mol·rad^2).

Bond	r_0	k_r		
CH3-CH2	0.1528	186188		
CH2-CH2	0.153	186188		
CH3-H3	0.1111	269449.6		
CH2-H2	0.1111	258571.2		
Angle	θ_0	k_θ	r_0	k^{UB}
CH2-CH2-CH2	113.6	488.2728	0.2561	9338.69
CH3-CH2-CH2	115	485.344	0.2561	6694.4
CH3-CH2-H2	110.1	289.5328	0.2179	18853.1
CH2-CH2-H2	110.1	221.752	0.2179	18853.1
CH2-CH3-H3	110.1	289.5328	0.2179	18853.1
H3-CH3-H3	108.4	297.064	0.1802	4518.72
H2-CH2-H2	109	297.064	0.1802	4518.72
Torsion	ϕ_s	k_ϕ	n	
CH2-CH2-CH2-CH2	0	0.269868	2	
	180	0.626554	3	
	0	0.395723	4	
	0	0.470742	5	
CH3-CH2-CH2-CH2	0	0.629734	2	
	180	0.340285	3	
	0	0.452876	4	
	0	0.853159	5	
CH2-CH2-CH2-H2	0	0.81588	3	
CH3-CH2-CH2-H2	0	0.75312	3	
H2-CH2-CH2-H2	0	0.92048	3	
H3-CH3-CH2-CH2	0	0.66944	3	
H3-CH3-CH2=H2	0	0.66944	3	

2.2.3 Molecular Dynamics Simulations

All simulations were calculated using GROMACS 5.1.4[37] with an electrostatic and van der Waals cutoff radii of 2.0 nm. Long range electrostatics were calculated using a Particle-Mesh-Ewald (PME) summation with grid spacings of 0.1 nm. The PME summation used a spline interpolation order of 4, and long-range electrostatic interactions were accurate to within 99.999%.

All simulations were initialised with an energy minimisation calculation to minimise any unphysical atomic overlaps. This was achieved using a steepest descents algorithm, which was terminated once the maximum force on any one atom was less than 100 kJ/(mol·nm).

All simulations were subsequently equilibrated for 1 ns. Simulations of liquid-vapour phase surface tensions were calculated in the canonical ensemble (constant particle number - N, constant volume - V and constant temperature T) at 293.15K, using a V-rescale thermostat set to rescale system temperatures every 0.5 ps. Liquid-liquid interfacial tension simulations were calculated in the isothermal-isobaric ensemble (constant particle number - N, constant volume - V and constant pressure - P) at 293.15 K and 1.01325 bar. NPT simulations were equilibrated using a V-rescale thermostat with a temperature coupling constant of 0.5 ps. Pressure coupling was achieved using a Berendsen barostat, with a pressure coupling constant of 1 ps.

Following equilibration, all simulations were run for a production period of 10 ns. During the production period, all simulations used a Nosé-Hoover thermostat with a temperature coupling constant of 0.5 ps and a Nosé-Hoover chain length of 1. NPT simulations used an isotropic Parrinello-Rahman barostat during the production period, with a pressure coupling constant of 1 ps. Unless otherwise stated, all production simulations have been calculated at 293.15 K and 1.01325 bar.

2.2.4 Analyses

Thermodynamic data from each simulation were output every 1 ps. Final values for thermodynamic quantities were averaged over all 10 ns, and errors were calculated using a block-averaging method, with each block averaging over a 1 ns timeframe. In all figures, error bars are presented to ±2 standard errors of the mean (a confidence interval of 95%).

The surface tension across an interface has been calculated using the diagonal components of the local pressure tensor:

$$\gamma = \frac{1}{2}\int_0^{L_z} [p_{\mathrm{N}}(z) - p_{\mathrm{T}}(z)]dz \tag{2.2.9}$$

where L_z is the length of the simulation in z (the direction normal to the interface) and $p_{\mathrm{N}}(z)$ & $p_{\mathrm{T}}(z)$ represent the normal and tangential components of the pressure tensor with respect to the interface:

$$p_{\mathrm{N}}(z) = \frac{p_{\mathrm{xx}}(z) + p_{\mathrm{yy}}(z)}{2} \tag{2.2.10}$$

$$p_{\mathrm{T}}(z) = p_{\mathrm{zz}}(z) \tag{2.2.11}$$

The diagonal components of the local pressure tensor (p_{xx}, p_{yy} & p_{zz}) have been calculated using the Irving-Kirkwood formalism[38].

Density profiles across the interface have been calculated following a two-stage process. Firstly, the simulation trajectory is centred about the centre of mass of the primary solvent phase in each simulation (typically water). This reduces artefacts caused by the collective drift of the interface throughout the simulation. The primary phase is calculated by clustering all molecules in the system. The largest cluster is then selected as the primary (liquid) phase. Any molecule further than 0.35 nm from the primary phase is excluded from the centre of mass calculation, and therefore does not affect the centering of the system. A cutoff of 0.35 nm was selected as this corresponds to the first minimum in the radial distribution function (RDF) of water[39,40]. Consequently, water molecules in the vapour phase are excluded in the centre of mass calculation for the bulk liquid water phase, and therefore do

not artificially shift the resulting density profiles normal to the interface. After the system has been centred, the density profile is calculated across the interface using a bin size of 0.01 nm. Where applicable, the density profile has been fit to the equation:

$$\rho(z) = \frac{\rho_l + \rho_v}{2} + \frac{\rho_l - \rho_v}{2} \operatorname{erf}\left(\frac{z - z_0}{\sqrt{2}\Delta}\right) \tag{2.2.12}$$

where ρ_l is the liquid density of the primary phase, ρ_v is the vapour density of the primary phase, z_0 is the location of the interface, and Δ is the interfacial width. The error function has been shown to optimally map to fluid-vapour and fluid-fluid interfaces under capillary wave (thermal) fluctuations[41]. Note that the tanh function is frequently used to map to equilibrium fluid-vapour and fluid-fluid interfaces. A comparison between the tanh and error functions for the density profiles of fluid-vapour interfaces has been performed by Bu *et al.* They note that, when the interface is subject to capillary wave fluctuations, the error function more accurately reproduces the experimental density profiles (calculated by XRF) of liquid-vapour interfaces compared to the tanh function[41].

The density profiles calculated using the above methodology are subject to capillary waves due to thermal fluctuations. Recently, computation techniques have been able to resolve the *intrinsic* density profile of the liquid-vapour and liquid-liquid interface[42]. That is, the interface between two phases excluding the contribution of thermal fluctuations (capillary waves), which act as to smear the density profiles across the interface. The amplitude of these capillary waves scales as:

$$\left\langle \xi^2(q) \right\rangle \propto \frac{kT}{q} \tag{2.2.13}$$

where the maximum wave vector, q, depends upon the size of the simulated interface.

The calculation of the intrinsic density profile has been evaluated by offsetting the amplitude of the thermal fluctuations (ξ) from the interface:

$$\rho_i(z) = \frac{1}{A} \left\langle \sum_i \delta(z - z_i + \xi(x_i, y_i)) \right\rangle \tag{2.2.14}$$

where index i sums over all atoms of phase i, and z is the position of the local non-intrinsic interface. The intrinsic density profiles have been calculated using the ITIM method[42] as presented by Sega *et al.*[43], using a probe sphere radius of 0.2 Å. Within the ITIM method a probe sphere is moved along test lines perpendicular to the plane of the fluid-vapour or fluid-fluid interface. Once the probe sphere touches the first atom within of the phase of interest, this molecule is marked as being interfacial. This process is repeated over the entire interfacial area in the simulation. The intrinsic density profile is then calculated using the offset (ξ) of the marked interfacial atoms.

2.3 Results

2.3.1 The Alkane-Vapour Interface

Figure 2.2 presents the calculated surface tension values of decane over a range of temperatures. The results show that the three tested force fields accurately reproduce the overall trend of surface tension at various temperatures. Whilst we have examined decane solely, the considered force fields are widely transferable. Both OPLS-AA and TraPPE-UA have previously been shown to accurately predict the surface tension values of ethane through to hexadecane[44,45]. To the author's knowledge, there have been no surface tension calculations of alkanes using the CGenFF force field.

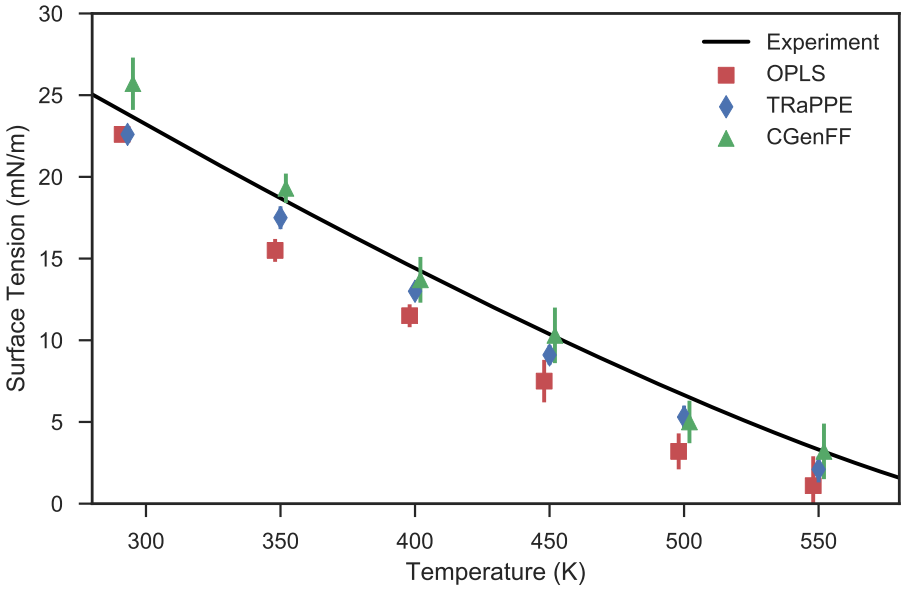

Figure 2.2: Surface tension of decane as a function of temperature. Data points have been offset for clarity. Experimental curve has been reproduced from the NIST standard reference database[29] and from Jesper & Kring[46].

Both OPLS-AA and TraPPE-UA systematically underestimate the surface tension of decane at all temperatures, OPLS more-so than TraPPE-UA. CGenFF overestimates surface tension at lower temperatures, and underestimates surface tension at higher temperatures. Our results concord with the work of Ismail *et al.*, who show that OPLS-AA consistently underestimates the surface tension of various saturated

n-alkanes[44]; and with Mendoza *et al.*, who present that TraPPE-UA is generally in good agreement with experimental data[45]. Our results are also consistent with the study of Caleman *et al.*, who show that OPLS-AA often underestimates the surface tension values of a wide variety of organic liquids[47].

Previous work by Nicolas & Smit has shown that the accurate calculation of surface tension for saturated alkanes is linearly proportional to the liquid density predicted in the simulations[48]. Values for the liquid and vapour density of decane have been calculated by fitting the interfacial density profile to equation 2.2.12. The liquid density (ρ_l), vapour density (ρ_v) and interfacial width (Δ) of decane at 293.15 K is presented in Table 2.8.

Table 2.8: The surface tension, density and interfacial width of decane at 293.15K.

Oil Model	γ (mN/m)	ρ_l (kg/m^3)	ρ_v (kg/m^3)	Δ (Å)
TraPPE-UA	22.6 (0.4)	729.8	0.039	2.6
CGenFF	25.7 (1.6)	741.5	0.060	2.4
OPLS-AA	22.6 (0.4)	730.3	0.036	2.5
Experimental[29]	23.823	730.33	0.007	

Our results show that both TraPPE-UA and OPLS-AA marginally underestimate the liquid density of decane at 293.15 K, and consequently both underestimate the surface tension. Conversely, CGenFF overestimates the liquid density, and therefore the surface tension of decane. The accurate reproduction of liquid-vapour densities depends on the treatment of long-range dispersion forces[49]. Ismail *et al.* show that Lennard-Jones cutoffs greater than 16 Å are required to yield results in agreement with explicit long range methods (evaluated in reciprocal space)[44], whilst the simulations of Mendoza *et al.* and Lopez *et al.* also show the utility of using Ewald-summations to treat these long range dispersion forces[45,50].

Figure 2.3 presents the interfacial density profiles (both intrinsic and non-intrinsic) of the decane-vapour interface at 293.15K. The density profiles show that all three force fields act remarkably similarly, even though CGenFF and OPLS-AA are all-atom representations of decane, and TraPPE-UA is a united-atom representation. The intrinsic density profiles present four discrete peaks of decane before the density becomes bulk-like.

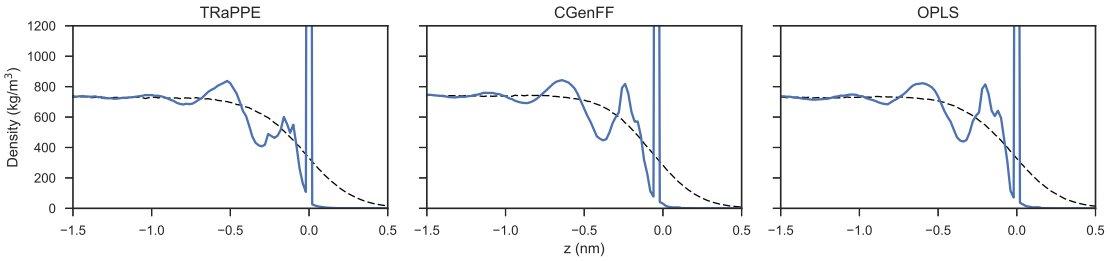

Figure 2.3: The intrinsic (bold line) and non-intrinsic (dashed line) interfacial density profiles of decane using various force fields.

Overall, our simulations of alkane-vapour interfaces agree with experimental observables and with various previous computational results. Our novel result is to show that CGenFF is equally adaptable to model *n*-alkane interfaces as the more frequently used TraPPE-UA and OPLS-AA.

2.3.2 The Water-Vapour Interface

The calculated surface tension values of pure water are presented in Table 2.9. It can be seen that almost all water models underestimate the experimentally observed surface tension of water by at least 15%. The only exception to this is TIP4P2005, which underestimates the surface tension of water by 7%. Our results compare favourably to the study of Vega & De Miguel[17]. Like their work, we find that the accurate reproduction of surface tension follows the trend:

$$\text{TIP4P2005} > \text{SPC/E} > \text{TIP4P} > \text{SPC} > \text{TIP3P}$$

Table 2.9: The surface tensions, liquid densities and interfacial widths of water-vapour interfaces using various force fields. Two standard errors of the mean are presented in parentheses.

Water Model	γ (mN/m)	δ_{exp}^{sim} (%)	ρ_l (g/cm^3)	Δ (Å)
SPC	54.1 (0.8)	-26	979.2	3.7
SPC/E	61.8 (0.7)	-15	1000.4	3.3
TIP3P	50.8 (0.6)	-30	987.8	3.9
TIP3Pc	55.8 (0.5)	-23	1016.9	3.7
TIP4P	56.3 (0.5)	-23	995.2	3.6
TIP4P2005	67.9 (0.7)	-7	997.2	3.2
Experiment[31]	72.8		998.2	3.2[5]

The TIP3Pc model, which introduces LJ sites on hydrogen atoms, performs better than the original TIP3P parameterisation, but still underestimates the surface tension of water by 23%. We observe that, generally, the four-point water models perform better than the three-point models, in keeping with the observations of Vega & De Miguel[17]. Of all the three-point water models, SPC/E most accurately reproduces the experimental surface tension of water, whilst of the four-point water models, the TIP4P2005 parameterisation performs the best.

The density profiles of TIP4P2005 and SPC/E water are presented in Figure 2.4. Analysing the intrinsic density profiles, it can be seen that water forms three separate density peaks at the water-vapour interface. This information is lost due to the capillary wave fluctuations present in the simulation when examining the non-intrinsic density profile solely. Also notable, is that most water models appear to overestimate the interfacial width of water compared to the results of Braslau *et al.*[5], see Table 2.9. The TIP4P2005 and SPC/E water model most accurately predict the experimentally observed interfacial width of water. Overall, the TIP4P2005 is best placed to model water-vapour interfaces. Of the three-point water models, SPC/E is the most favourable.

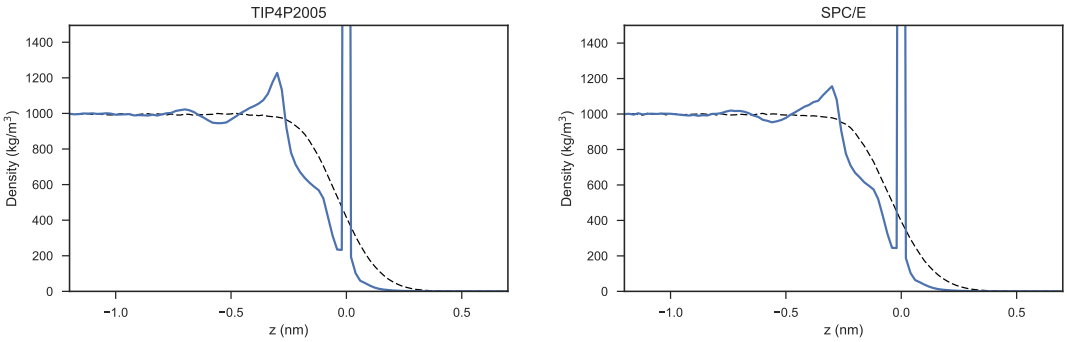

Figure 2.4: The intrinsic (bold line) and non-intrinsic (dotted line) density profile of TIP4P2005 and SPC/E water models.

2.3.3 The Water-Vapour Interface at Various NaCl Concentrations

Upon introducing inorganic salts to a solvent, the surface tension of the solution increases. Typically, this behaviour is explained due to an exclusion of ions from the liquid-vapour interface[3]. This directly alters the surface tension between the two phases as described by Gibbs adsorption isotherm:

$$d\gamma = -\Gamma_{\mathrm{Na}} d\mu_{\mathrm{Na}} - \Gamma_{\mathrm{Cl}} d\mu_{\mathrm{Cl}} \tag{2.3.15}$$

where Γ_i is the surface excess and μ_i is the chemical potential of species $i \in \{\mathrm{Na}, \mathrm{Cl}\}$.

Proceeding, we have chosen three water models to examine the trends in surface tension as a function of salinity. The TIP4P2005 and SPC/E water models were examined as they represent the best four-point and three-point water models respectively. The TIP3Pc water model was also examined, as it is frequently simulated in conjunction with secondary organic phases[15,16]. The variation of surface tension with NaCl concentration is presented in Figure 2.5.

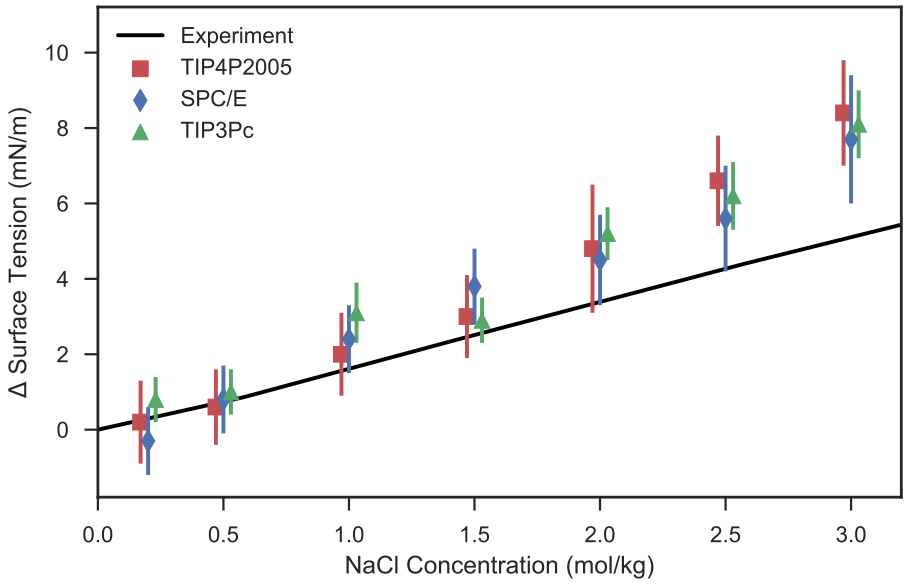

Figure 2.5: The variation of surface tension with additional NaCl salts. The experimental curve is extrapolated using data from Vargaftik *et al.*[51], Ali *et al.*[52], and Aveyard & Saleem[53].

Firstly, we note that the overall trend of surface tension variation with NaCl concentration is well captured by the classical MD simulations. The simulations are able to accurately predict the experimental surface tensions of NaCl solutions up to 1.5 mol/kg, however, the simulations slightly overestimate the surface tension of NaCl electrolyte at higher concentrations, deviating more drastically as concentrations increase beyond 2.0 mol/kg. Similar behaviour was noted by D'Auria & Tobias, who observed that the surface tension of the TIP3P water model was overestimated when used in conjunction with the Smith & Dang parameterisation at NaCl concentrations of 1.2 mol/kg and 6.17 mol/kg[54]. With respect to low-salinity enhanced oil recovery, it appears that the MD simulations (at their current scale) are not directly be able to capture the *low-salinity* effect, whereby optimal salt concentrations function below 5 mM (mol/L)[2]. The error bars associated with the computations are far larger than the resolution required to resolve interfacial properties at the mM scale. However, the overall trend of interfacial wettability alteration with salt concentration can be discerned from the classical MD simulations.

Secondly, we observe that the simulated surface tensions of all three water models agree with each other at each concentration. This implies that the accurate modelling of interfaces containing electrolytes depends more so on the parameterisation of the ion, rather than the water model. This conclusion concords with the work of Neyt *et al.* , who presented that the salinity dependence of the electrolyte-vapour interface varied primarily with ion parameterisation, rather than the water model, whilst the utilised water model sets the accuracy of the surface tension calculation without additional NaCl[55]. Notably, Neyt *et al.* presented that the TIP4P2005 water model used in conjunction with the OPLS parameterisation of NaCl, typically returned surface tensions within 0.2% of the experimental trend[55].

As presented in equation 2.3.15, the change in surface tension is linked to the surface excess (or reduction) of ions at the liquid-vapour interface. In this study, the surface excess of Na^+ and Cl^- ions across the electrolyte-water interface has been calculated as:

$$\Gamma_i = \int_{-\infty}^{z_{\text{Gibbs}}} [\rho_i(z) - \rho_i^{\text{liq}}]dz + \int_{z_{\text{Gibbs}}}^{\infty} [\rho_i(z) - \rho_i^{\text{vap}}]dz \tag{2.3.16}$$

where $\rho_i(z)$ is the non-intrinsic density profile of phase i across the interface, ρ_i^{liq} is the bulk liquid density of phase i, and ρ_i^{vap} is the bulk vapour density of phase i (typically $\rho_i^{\text{vap}} = 0$ for ions in liquid-vapour simulations). z_{Gibbs} is the location of the Gibbs dividing plane, which is priorly calculated by minimising Γ_{water}, such that:

$$\Gamma_{\text{water}} = \int_{-\infty}^{z_{\text{Gibbs}}} [\rho_{\text{water}}(z) - \rho_{\text{water}}^{\text{liq}}]dz + \int_{z_{\text{Gibbs}}}^{\infty} [\rho_{\text{water}}(z) - \rho_{\text{water}}^{\text{vap}}]dz = 0 \qquad (2.3.17)$$

Figure 2.6 presents the negative total surface excess of ions ($\Gamma_{\text{NaCl}} = \Gamma_{\text{Na}} + \Gamma_{\text{Cl}}$) at the water-vapour interface calculated from all simulations as a function of NaCl concentration. We observe that, compared to the experimental data of Ali *et al.*, the simulations marginally overestimate the negative total surface excess of NaCl, $-\Gamma_{\text{NaCl}}$, especially at higher concentrations[56]. In turn, this elucidates why the surface tension values are overestimated in the simulations at higher salt concentrations. The surface tension values are overestimated due to the overestimation of ionic exclusion at the liquid-vapour interface.

Overall, the MD simulations appear capable of capturing the key mechanisms dictating the water-vapour interface at various NaCl concentrations.

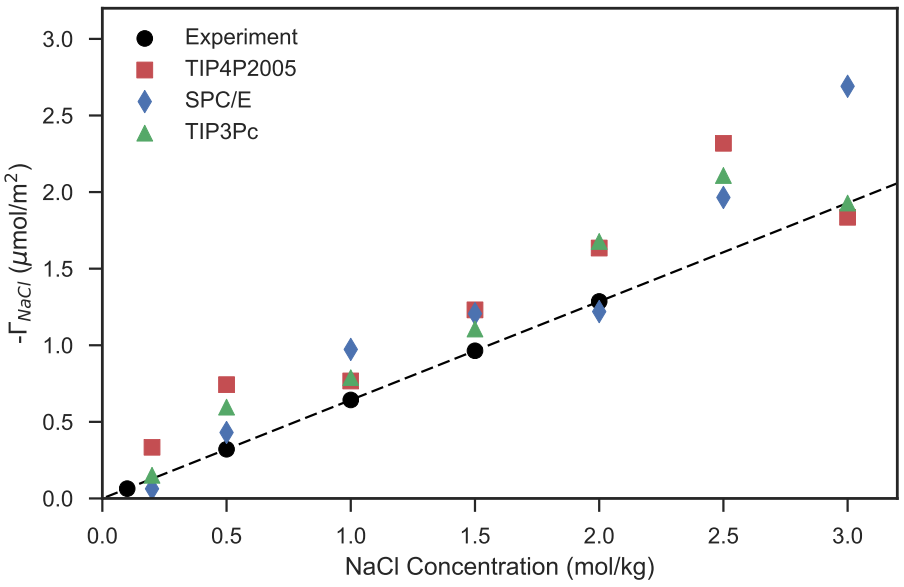

Figure 2.6: The surface excess of NaCl at the water-vapour interface as a function of NaCl concentration. Experimental data is taken from Ali *et al.*[56]

2.3.4 The Water-Alkane Interface at Various NaCl Concentrations

Table 2.10 presents the interfacial tension values of the decane-water interface, without salts, for various force field combinations as predicted by the MD simulations. We have chiefly examined TraPPE-UA and CGenFF due to their compatibility (*i.e.* consistent use of Lennard-Jones mixing rules) with ClayFF; which makes these force fields more suitable for use in complex three-phase simulations. Priority has also been placed on testing the TIP4P2005 and SPC/E water models, as these most accurately model the interfacial properties of pure water. TIP3Pc has also been examined as it is the default three-point water model used in conjunction with CGenFF[22].

Table 2.10: The decane-water interfacial tensions calculated using a combination of various force fields. Two standard errors of the mean are presented in parentheses. Experimental results are from Zeppieri *et al.*[57], Goebel & Lunkenheimer[58] and Aveyard & Haydon[59].

Oil Model	Water Model	γ (mN/m)	$\delta_{\text{exp}}^{\text{sim}}$ (%)
TraPPE-UA	TIP4P2005	56.7 (1.7)	+8
TraPPE-UA	TIP4P2005*	54.2 (1.0)	+3
CGenFF	SPC/E	55.3 (1.2)	+5
CGenFF	TIP3Pc	48.2 (1.2)	−8
CGenFF	TIP4P	51.9 (1.8)	−1
Experiment		52.5 (0.6)	

In addition to the usual TIP4P2005 water model interacting with TraPPE-UA, we have examined the parameters as described by Ashbaugh *et al.*[60], presented in Table 2.11, denoted TIP4P2005*. The TIP4P2005* water model uses custom Lennard-Jones interactions between the oxygen atoms of water and the TraPPE-UA beads. These custom interactions have been finely tuned to accurately reproduce the hydration free energy of alkanes[60]. All other parameters of the TIP4P2005* water model are identical to the original TIP4P2005 parameterisation.

Table 2.11: The custom Lennard-Jones interaction parameters used in TIP4P2005*, as described by Ashbaugh *et al.*[60].

i	j	σ_{ij} (nm)	ϵ_{ij} (kJ/mol)
CH3	OW	1.155913149	0.036137328
CH2	OW	1.080777512	0.055639523

We note that the MD simulations are able to predict the interfacial tension of the water-decane interface within 10% of the empirically observed values. The simulations of this interface are notably more accurate than the simulations of the water-vapour interface. The combination of different force fields appears more robust for the water-decane interface, compared to the water-vapour interface. This is likely due to the absence of a vapour phase in the simulations, which when inaccurately modelled (in particular, the vapour density), can lead to deviations in the predicted surface tension, as noted by Nicolas & Smit[48].

Figure 2.7 presents the deviation of decane-water interfacial tension with increasing NaCl concentration for various combinations of force fields. The computed interfacial tensions accurately follow the experimental trend observed by Aveyard & Saleem[53] up to 1.0 mol/L.

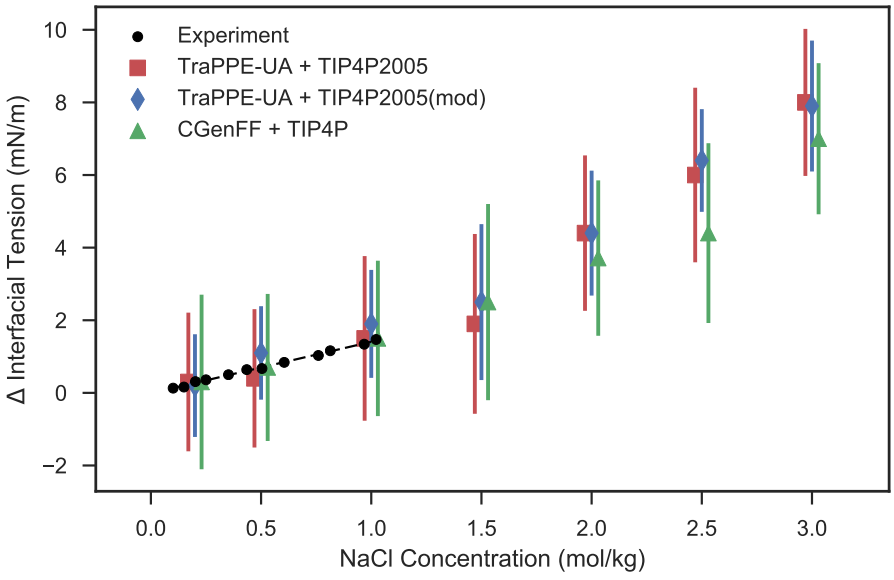

Figure 2.7: The variation of decane-water interfacial tension with additional NaCl salts. Experimental data are taken from Aveyard & Saleem[53].

Much like the water-vapour interface, the different parameter sets agree with each other at each NaCl concentration. This again highlights that the ion parameterisation may be more important for the accurate modelling of the water-vapour/water-decane interface.

The variation in interfacial tension predicted at the interface between water and decane is remarkably similar to that at the water-vapour interface. This is apparent in Figure 2.8, which compares the change in surface tension at the water-vapour interface against the change in interfacial tension at the water-alkane interface. This implies that the overall change in interfacial tension is therefore due to the properties primarily within the water phase.

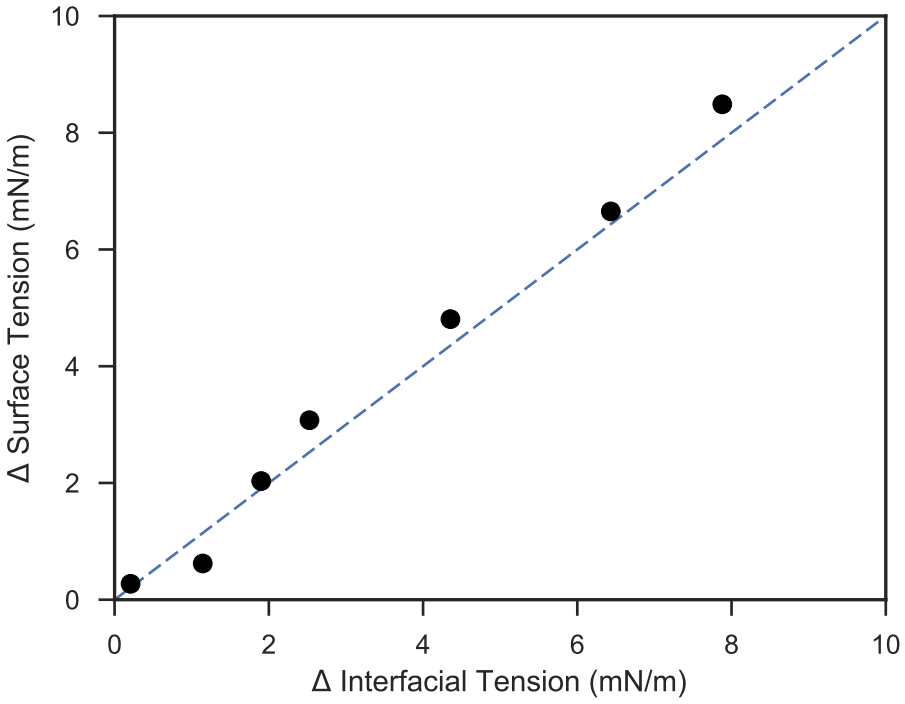

Figure 2.8: The change in surface tension at the water-vapour interface (y-axis) against the change in interfacial tension at the water-alkane interface (x-axis). The diagonal line represents when the two properties are linearly proportional.

2.4 Conclusions

In this study the interfacial properties of water and decane have been examined at various NaCl concentrations using classical molecular dynamics. By choosing an appropriate set of interaction parameters (force fields), one can obtain remarkable agreement between model and experimental observation. In particular, the TIP4P2005 water model is best placed to examine the interfacial properties of water. The SPC/E parameterisation is the best three-point water model to interpret the interfacial behaviour of water. CGenFF, OPLS-AA and TraPPE-UA all accurately reproduce the interfacial properties of decane. In combination, CGenFF and TraPPE-UA are compatible with various water models, and are able to accurately predict the interfacial tension of the water-decane interface. The salinity dependence on surface/interfacial tension is well captured using the Smith & Dang parameterisation of NaCl. We observe that the model slightly overestimates the surface/interfacial tensions at higher salinities. This is due to an overestimation of the ion exclusion at the interface. The simulations further suggest that the salinity dependence on surface/interfacial tension is dictated by the parameterisation of the salt ions. Future work will examine this hypothesis, and will model different ion parameterisations. Future work will also examine the role of divalent cations at the water-vapour/water-alkane interface, whereby, charge inversion may play a determining role on the behaviour of the liquid-liquid interface. Furthermore, different monovalent and divalent ions will be examined, as many are important to the phenomenon of low-salinity enhanced oil recovery.

Bibliography

[1] I Benjamin. Molecular structure and dynamics at liquid-liquid interfaces. *Annual Review of Physical Chemistry*, 48(1):407–451, 1997.

[2] JJ Sheng. Critical review of low-salinity waterflooding. *Journal of Petroleum Science and Engineering*, 120:216–224, 2014.

[3] ML Schlossman. Liquid–liquid interfaces: studied by x-ray and neutron scattering. *Current Opinion in Colloid & Interface Science*, 7(3):235–243, 2002.

[4] KB Eisenthal. Liquid interfaces probed by second-harmonic and sum-frequency spectroscopy. *Chemical Reviews*, 96(4):1343–1360, 1996.

[5] A Braslau, M Deutsch, PS Pershan, AH Weiss, J Als-Nielsen, and J Bohr. Surface roughness of water measured by x-ray reflectivity. *Physical Review Letters*, 54(2):114, 1985.

[6] MK Sanyal, SK Sinha, KG Huang, and BM Ocko. X-ray-scattering study of capillary-wave fluctuations at a liquid surface. *Physical Review Letters*, 66(5):628, 1991.

[7] DM Mitrinovic, Z Zhang, SM Williams, Z Huang, and ML Schlossman. X-ray reflectivity study of the water- hexane interface. *Journal of Physical Chemistry B*, 103(11):1779–1782, 1999.

[8] AM Tikhonov, DM Mitrinovic, M Li, Z Huang, and ML Schlossman. An x-ray reflectivity study of the water-docosane interface. *Journal of Physical Chemistry B*, 104(27):6336–6339, 2000.

[9] M Matsumoto and Y Kataoka. Study on liquid–vapor interface of water. i. simulational results of thermodynamic properties and orientational structure. *Journal of Chemical Physics*, 88(5):3233–3245, 1988.

[10] P Jungwirth and DJ Tobias. Specific ion effects at the air/water interface. *Chemical Reviews*, 106(4):1259–1281, 2006.

[11] AR van Buuren, SJ Marrink, and HJC Berendsen. A molecular dynamics study of the decane/water interface. *Journal of Physical Chemistry*, 97(36):9206–9212, 1993.

[12] JL Rivera, C McCabe, and PT Cummings. Molecular simulations of liquid-liquid interfacial properties: Water-n-alkane and water-methanol-n-alkane sys-

tems. *Physical Review E*, 67(1):011603, 2003.

[13] L Zhang, X Lu, X Liu, K Yang, and H Zhou. Surface wettability of basal surfaces of clay minerals: insights from molecular dynamics simulation. *Energy & Fuels*, 30(1):149–160, 2016.

[14] K Kobayashi, Y Liang, S Murata, T Matsuoka, S Takahashi, K-I Amano, N Nishi, and T Sakka. Stability evaluation of cation bridging on muscovite surface for improved description of ion-specific wettability alteration. *Journal of Physical Chemistry C*, 2017.

[15] T Underwood, V Erastova, P Cubillas, and HC Greenwell. Molecular dynamic simulations of montmorillonite-organic interactions under varying salinity: an insight into enhanced oil recovery. *Journal of Physical Chemistry C*, 119(13):7282–7294, 2015.

[16] T Underwood, V Erastova, and HC Greenwell. Wetting effects and molecular adsorption at hydrated kaolinite clay mineral surfaces. *Journal of Physical Chemistry C*, 120(21):11433–11449, 2016.

[17] C Vega and E De Miguel. Surface tension of the most popular models of water by using the test-area simulation method. *Journal of Chemical Physics*, 126(15):154707, 2007.

[18] PG Kusalik and IM Svishchev. The spatial structure in liquid water. *Science*, 265(5176):1219–1221, 1994.

[19] HJC Berendsen, PPM Postma, WF van Gunsteren, and J Hermans. Interaction models for water in relation to protein hydration. In *Intermolecular Forces*, pages 331–342. Springer, 1981.

[20] HJC Berendsen, JR Grigera, and TP Straatsma. The missing term in effective pair potentials. *Journal of Physical Chemistry*, 91(24):6269–6271, 1987.

[21] WL Jorgensen, J Chandrasekhar, JD Madura, RW Impey, and ML Klein. Comparison of simple potential functions for simulating liquid water. *Journal of Chemical Physics*, 79(2):926–935, 1983.

[22] K Vanommeslaeghe, E Hatcher, C Acharya, S Kundu, S Zhong, J Shim, E Darian, O Guvench, P Lopes, and I Vorobyov. CHARMM general force field: A force field for drug-like molecules compatible with the CHARMM all-atom addi-

tive biological force fields. *Journal of Computational Chemistry*, 31(4):671–690, 2010.

[23] MG Martin and IJ Siepmann. Transferable potentials for phase equilibria. 1. united-atom description of n-alkanes. *Journal of Physical Chemistry B*, 102(14):2569–2577, 1998.

[24] WL Jorgensen, DS Maxwell, and J Tirado-Rives. Development and testing of the opls all-atom force field on conformational energetics and properties of organic liquids. *Journal of the American Chemical Society*, 118(45):11225–11236, 1996.

[25] JA Greathouse, DQ Pike, HC Greenwell, CT Johnston, J Wilcox, and RT Cygan. Methylene blue adsorption on the basal surfaces of kaolinite: Structure and thermodynamics from quantum and classical molecular simulation. *Clays and Clay Minerals*, 63(3):185–198, 2015.

[26] H Heinz, T-J Lin, R Kishore Mishra, and F S Emami. Thermodynamically consistent force fields for the assembly of inorganic, organic, and biological nanostructures: the interface force field. *Langmuir*, 29(6):1754–1765, 2013.

[27] H Heinz, H Koerner, KL Anderson, RA Vaia, and BL Farmer. Force field for mica-type silicates and dynamics of octadecylammonium chains grafted to montmorillonite. *Chemistry of Materials*, 17(23):5658–5669, 2005.

[28] JL Bradley-Shaw, PJ Camp, PJ Dowding, and K Lewtas. Molecular dynamics simulations of glycerol monooleate confined between mica surfaces. *Langmuir*, 32(31):7707–7718, 2016.

[29] EW Lemmon, MO McLinden, DG Friend, PJ Linstrom, and WG Mallard. NIST chemistry webbook, NIST standard reference database number 69. *National Institute of Standards and Technology, Gaithersburg*, 2011.

[30] L Martínez, R Andrade, EG Birgin, and JM Martínez. Packmol: a package for building initial configurations for molecular dynamics simulations. *Journal of Computational Chemistry*, 30(13):2157–2164, 2009.

[31] WM Haynes. *CRC Handbook of Chemistry and Physics, 92nd Edition*. 100 Key Points. CRC Press, 2011.

[32] WL Jorgensen and J Tirado-Rives. The OPLS [optimized potentials for liquid

simulations] potential functions for proteins, energy minimizations for crystals of cyclic peptides and crambin. *Journal of the American Chemical Society*, 110(6):1657–1666, 1988.

[33] K Vanommeslaeghe and AD MacKerell Jr. Automation of the CHARMM general force field (CGenFF) i: bond perception and atom typing. *Journal of Chemical Information and Modeling*, 52(12):3144, 2012.

[34] K Vanommeslaeghe, EP Raman, and AD MacKerell Jr. Automation of the CHARMM general force field (CGenFF) ii: assignment of bonded parameters and partial atomic charges. *Journal of Chemical Information and Modeling*, 52(12):3155, 2012.

[35] JLF Abascal and C Vega. A general purpose model for the condensed phases of water: TIP4P/2005. *Journal of Chemical Physics*, 123(23):234505, 2005.

[36] DE Smith and LX Dang. Computer simulations of NaCl association in polarizable water. *Journal of Chemical Physics*, 100(5):3757–3766, 1994.

[37] MJ Abraham, T Murtola, R Schulz, S Páll, JC Smith, B Hess, and E Lindahl. Gromacs: High performance molecular simulations through multi-level parallelism from laptops to supercomputers. *SoftwareX*, 1:19–25, 2015.

[38] JH Irving and JG Kirkwood. The statistical mechanical theory of transport processes. iv. the equations of hydrodynamics. *The Journal of Chemical Physics*, 18(6):817–829, 1950.

[39] P Mark and L Nilsson. Structure and dynamics of the TIP3P, SPC, and SPC/E water models at 298 K. *Journal of Physical Chemistry A*, 105(43):9954–9960, 2001.

[40] AK Soper and MG Phillips. A new determination of the structure of water at 25 C. *Chemical Physics*, 107(1):47–60, 1986.

[41] W Bu, D Kim, and D Vaknin. Density profiles of liquid/vapor interfaces away from their critical points. *Journal of Physical Chemistry C*, 118(23):12405–12409, 2014.

[42] LB Pártay, G Hantal, P Jedlovszky, Á Vincze, and G Horvai. A new method for determining the interfacial molecules and characterizing the surface roughness in computer simulations. application to the liquid–vapor interface of water.

Journal of Computational Chemistry, 29(6):945–956, 2008.

[43] M Sega, SS Kantorovich, P Jedlovszky, and M Jorge. The generalized identification of truly interfacial molecules (itim) algorithm for nonplanar interfaces. *Journal of Chemical Physics*, 138(4):044110, 2013.

[44] AE Ismail, M Tsige, PJ In't Veld, and GS Grest. Surface tension of normal and branched alkanes. *Molecular Physics*, 105(23-24):3155–3163, 2007.

[45] FN Mendoza, R Lopez-Rendon, J Lopez-Lemus, J Cruz, and J Alejandre. Surface tension of hydrocarbon chains at the liquid–vapour interface. *Molecular Physics*, 106(8):1055–1059, 2008.

[46] JJ Jasper and EV Kring. The isobaric surface tensions and thermodynamic properties of the surfaces of a series of n-alkanes, C5 to C18, 1-Alkenes, C6 to C16, and of n-Decylcyclopentane, n-Decylcyclohexane and n-Dcylbenzene. *Journal of Physical Chemistry*, 59(10):1019–1021, 1955.

[47] C Caleman, PJ van Maaren, M Hong, JS Hub, LT Costa, and D van der Spoel. Force field benchmark of organic liquids: density, enthalpy of vaporization, heat capacities, surface tension, isothermal compressibility, volumetric expansion coefficient, and dielectric constant. *Journal of Chemical Theory and Computation*, 8(1):61–74, 2011.

[48] JP Nicolas and B Smit. Molecular dynamics simulations of the surface tension of n-hexane, n-decane and n-hexadecane. *Molecular Physics*, 100(15):2471–2475, 2002.

[49] M Sega and C Dellago. Long-range dispersion effects on the water/vapor interface simulated using the most common models. *Journal of Physical Chemistry B*, 121(15):3798–3803, 2017.

[50] J López-Lemus, Mauricio Romero-Bastida, TA Darden, and J Alejandre. Liquid–vapour equilibrium of n-alkanes using interface simulations. *Molecular Physics*, 104(15):2413–2421, 2006.

[51] NB Vargaftik, BN Volkov, and LD Voljak. International tables of the surface tension of water. *Journal of Physical and Chemical Reference Data*, 12(3):817–820, 1983.

[52] K Ali, S Bilal, and S Siddiqi. Concentration and temperature dependence of

surface parameters of some aqueous salt solutions. *Colloids and Surfaces A: Physicochemical and Engineering Aspects*, 272(1):105–110, 2006.

[53] R Aveyard and SM Saleem. Interfacial tensions at alkane-aqueous electrolyte interfaces. *Journal of the Chemical Society, Faraday Transactions 1: Physical Chemistry in Condensed Phases*, 72:1609–1617, 1976.

[54] R DAuria and DJ Tobias. Relation between surface tension and ion adsorption at the air- water interface: A molecular dynamics simulation study. *Journal of Physical Chemistry A*, 113(26):7286–7293, 2009.

[55] JC Neyt, A Wender, V Lachet, A Ghoufi, and P Malfreyt. Prediction of the concentration dependence of the surface tension and density of salt solutions: atomistic simulations using drude oscillator polarizable and nonpolarizable models. *Physical Chemistry Chemical Physics*, 15(28):11679–11690, 2013.

[56] K Ali and S Bilal. Surface tension, surface excess concentration, enthalpy and entropy of surface formation of aqueous salt solutions. *Colloids and Surfaces A: Physicochemical and Engineering Aspects*, 417:183–190, 2013.

[57] S Zeppieri, J Rodríguez, and AL López de Ramos. Interfacial tension of alkane+water systems. *Journal of Chemical & Engineering Data*, 46(5):1086–1088, 2001.

[58] A Goebel and K Lunkenheimer. Interfacial tension of the water/n-alkane interface. *Langmuir*, 13(2):369–372, 1997.

[59] R Aveyard and DA Haydon. Thermodynamic properties of aliphatic hydrocarbon/water interfaces. *Transactions of the Faraday Society*, 61:2255–2261, 1965.

[60] HS Ashbaugh, L Liu, and LN Surampudi. Optimization of linear and branched alkane interactions with water to simulate hydrophobic hydration. *Journal of Chemical Physics*, 135(5):054510, 2011.

Chapter 3

Montmorillonite-Organic Interactions under Varying Salinity

The main aim of this chapter is to interpret the phenomenon of low-salinity EOR at the surface of montmorillonite, a highly-charged clay. The chapter has an in-depth breakdown of the potential mechanisms driving wettability alteration at clay surfaces. The MD simulations examine a mixture of decane and decanoic acid at various NaCl concentrations with Na^{+}- and Ca^{2+}- charge-balanced montmorillonite.

This chapter has previously been published in its presented form in the Journal of Physical Chemistry C:

Thomas Underwood, Valentina Erastova, Pablo Cubillas & H. Chris Greenwell.

Molecular Dynamic Simulations of Montmorillonite-Organic Interactions under Varying Salinity: An Insight into Enhanced Oil Recovery.

J. Phys. Chem. C, 2015, 119 (13), pages: 7282-7294, DOI: 10.1021/acs.jpcc.5b0055

Thomas Underwood was responsible for running all simulations and writing the published article. Valentina Erastova helped with initial setup of simulations, and with proofreading the article. Pablo Cubillas and H. Chris Greenwell helped proof-read the final article.

Abstract

Enhanced oil recovery is becoming commonplace in order to maximise recovery from oilfields. One of these methods, low-salinity enhanced oil recovery (EOR) has shown promise, however the fundamental underlying chemistry requires elucidating. Here, three mechanisms proposed to account for low-salinity enhanced oil recovery in sandstone reservoirs are investigated using molecular dynamic simulations. The mechanisms probed are electric double layer expansion, multicomponent ionic exchange and pH effects arising at clay mineral surfaces. Simulations of smectite basal planes interacting with uncharged non-polar decane, uncharged polar decanoic acid and charged Na-decanoate model compounds are used to this end. Various salt concentrations of NaCl are modelled: 0‰, 1‰, 5‰ and 35‰ to determine the role of salinity upon the three separate mechanisms. Furthermore, the initial oil/water-wetness of the clay surface is modelled. Results show that electric double layer expansion is not able to fully explain the effects of low-salinity enhanced oil recovery. The pH surrounding a clay's basal plane, and hence the protonation and charge of acid molecules is determined to be one of the dominant effects driving low-salinity EOR. Further, results present that the presence of calcium cations can drastically alter the oil wettability of a clay mineral surface. Replacing all divalent cations with monovalent cations through multicomponent cation exchange dramatically increases the water wettability of a clay surface, and will increase EOR.

3.1 Introduction

In an age of increasing energy demand global oil resources must be utilised as efficiently as possible. Current primary and secondary oil recovery methods may leave up to 65% of the original oil in place (OOIP) within a reservoir[1]. Growth in oil demand, oil price and ageing reservoirs are but a few reasons why companies have been looking at different methods to optimise oil recovery rates within existing assets over the past few decades. Such techniques are referred to as enhanced oil recovery; these include a wide variety of processes such as steam injection, CO_2 injection, in situ combustion and chemical flooding. Since the 1990s an additional EOR method, injection of low-salinity water, has been tested in both the lab and the field, with promising results[2]. Low-salinity EOR could offer many economical benefits compared to other EOR methods as low-salinity water can be produced on-site and does not require the addition of specialty chemicals.

It has been established that the salinity and saturation of formation water[3,4,5], the reservoir's initial wettability[3] along with the presence of clay minerals[6,7] and polar oil components[4] all play an important role on the degree to which the injection of low-salinity water increases oil production. Moreover, the presence of clay minerals is seen to be a key requirement for low-salinity EOR to operate[4,6,7,8]. This is due to the role that clays play in determining the wettability state of a rock. Clay minerals and quartz grains are widely present in the pores of sandstone reservoirs, where they form surface coatings. As such, clay surfaces are thought to interact heavily with the polar components of oil[4,9]. Different types of clay are present in sandstone reservoirs, with the dominant clay minerals being kaolinite, illite, smectite, illite-smectite mixed layer clays and chlorite[10]. Kaolinite is considered as oil wetting while smectite/chlorite surfaces are water wetting[11].

To date, studies have proposed more than 17 separate mechanisms by which low-salinity flooding can enhance oil recovery. These are explained in some detail in the recent review by Sheng (2014)[12]. Nevertheless, a definitive conclusion as to which mechanism truly underpins low-salinity enhanced oil recovery has yet to be fully determined. In the present paper three of the frequently cited mechanisms are tested at the molecular level. They are: electric double layer (EDL) expansion,

multi-component ionic exchange and pH level reactions.

The electric double layer is a description of the electric field surrounding a charged colloid particle, in this instance, a negatively charged clay particle within a reservoir. A widely accepted model of a colloidal EDL is the Gouy-Chapman-Stern double layer[13], whereby a portion of the charge-balancing interlayer cations are adsorbed to the clay, in what is known as a Stern Layer, whilst the remaining cations and anions create the traditional diffuse double layer, see Figure 3.1.

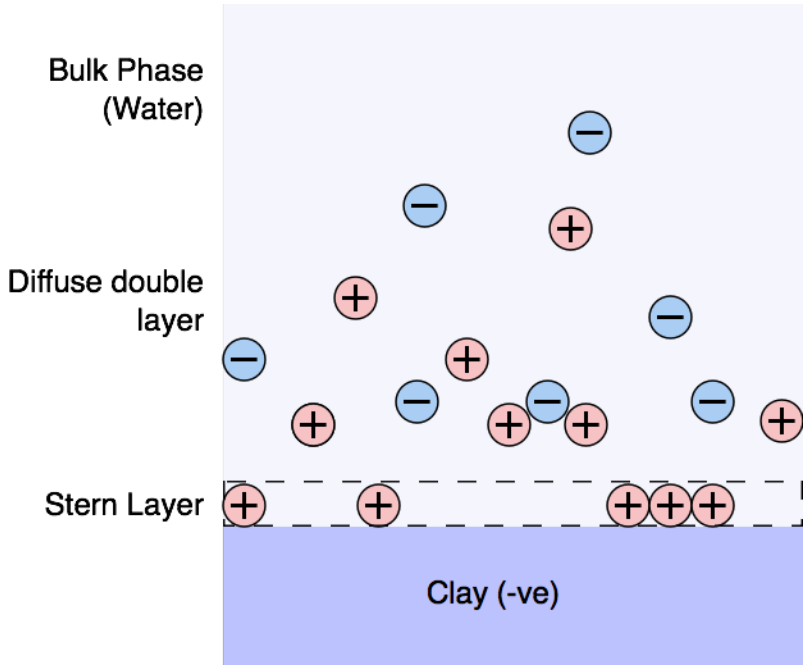

Figure 3.1: The Gouy-Chapman-Stern model of a clay's electric double layer.

The important relationship that dictates the depth of the EDL, and hence the electric field strength at a fixed point, can be predicted by DLVO theory[13]. According to DLVO theory, a clay's EDL expands as salinity decreases, hence any positively charged molecule bound to the clay surface will become more strongly attracted to the clay surface, whilst negatively charged molecules will become increasingly repelled by the charged clay's surface[13]. Furthermore, as the EDL of a clay expands, it becomes more likely to interact with surrounding clay particles, and bulk clay swelling can occur. It is exactly this process that is proposed to cause the release of fine clay particles, along with associated oil, in the fines migration theory of low-salinity EOR[4,14].

Multicomponent ionic exchange is another theory proposed to explain the effects of low-salinity EOR[14]. It is thought that there are eight separate mechanisms through which oil molecules can be bound to a clay surface[15], though only 4 of these mechanisms are believed to be of importance to low-salinity EOR[14]. These mechanisms are presented in Table 3.1 and Figure 3.2.

Table 3.1: The mechanisms of multicomponent ionic exchange[15]. Key mechanisms relevant to low-salinity EOR have been highlighted[14].

Mechanism	**Organic functional group**
Cation exchange	Amino, ring NH, heterocyclic N (aromatic ring)
Cation bridging	Carboxylate, amines, carbonyl, alcoholic OH
Ligand exchange	Carboxylate
Water bridging	Amino, Carboxylate, carbonyl, alcoholic OH
Anion exchange	Carboxylate
Hydrogen bonding	Amino, carbonyl, carboxyl, phenolic OH
Protonation	Amino, heterocyclic N, carbonyl, carboxylate
Van der Waals interaction	Uncharged organic units

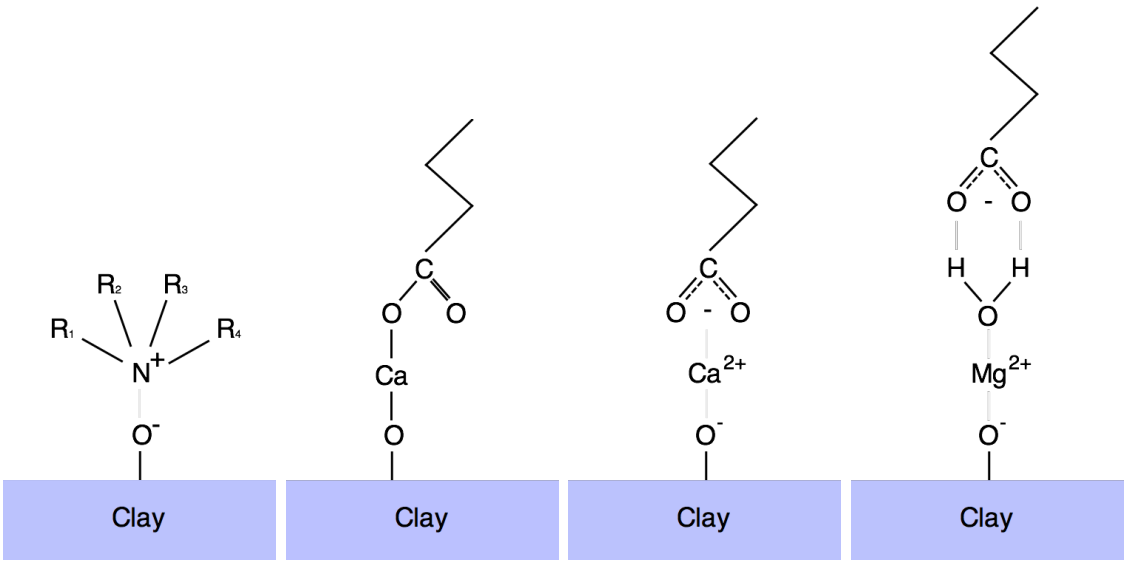

(a) Cation exchange (b) Ligand exchange (c) Cation bridging (d) Water bridging

Figure 3.2: A schematic of the important bridging mechanisms influencing low-salinity EOR.

Cation exchange is a mechanism whereby positively charged organic ions, such as amine/ammonium groups or heterocyclic rings containing nitrogens, are able to replace the inorganic cations that usually charge balance a clay surface (Figure 3.2a). Ligand bridging is a phenomenon where multivalent cations, for example Ca^{2+} or Mg^{2+}, form covalent bonds between tetrahedral clay oxygen and, for example, an oxygen atom on a charged organic molecule present in oil (Figure 3.2b). Cation bridging is an adsorption mechanism between an organic molecule ionically bonded to a divalent cation, which in turn, is charge balancing the surface of the clay (Figure 3.2c). It is a weaker bonding mechanism compared to ligand bridging. Finally, water bridging can occur if a strongly solvated cation, for example Mg^{2+}, is charge balancing the clay. In this instance, the solvation shell surrounding the Mg^{2+} ion, can order such as to attract organics through a dipole-dipole interaction (Figure 3.2d). It is hypothesised that low-salinity EOR occurs because the divalent cations that bridge the organic oil molecule to the clay can be readily exchanged by monovalent cations due to the expanded electric double layer[14], thereby releasing the oil molecules by disrupting ligand bridging, cation bridging or water bridging.

To be more explicit, the mechanism leading to oil-cation-clay bridging between divalent calcium and uncharged polar organic molecule is referred to as *cation-polar bridging* in this work. The bridging mechanism via calcium ion and charged deprotonated acid is referred to as *cation-charged bridging*.

Mechanisms leading to low-salinity EOR owing to pH effects encompass a large range of effects that depend on the pH level of the system surrounding the clay surface. It has been proposed that the generation of surfactants from crude oil components at elevated (*i.e.* alkaline) pH levels alter the overall wettability of the reservoir matrix[16]. The concept has been further developed, with the suggestion that the injection of low-salinity water can produce hydroxyl ions from a clay-calcium site, following the equilibrium reaction[14]:

$$\text{Clay}{-}\text{Ca}^{2+} + \text{H}_2\text{O} \rightleftharpoons \text{Clay}{-}\text{H}^{+} + \text{Ca}^{2+} + \text{HO}^{-}$$

Such a pH change would cause a low-salinity flood to act like an alkaline flood, which has been theorised to improve oil recovery rates[16]. However, more recent

studies dispel the hypothesis of a low-salinity flood acting akin to an alkaline flood[14]. To date, the best low-salinity water flooding results have been on crude oil that possessed an acid number less than 0.05 mg/g, whilst an alkaline flood requires an acid number greater than 0.2 mg/g[14]. Furthermore, it has been argued that the CO_2 found inherently within most reservoirs can act as a pH buffer in the connate water, reducing the potential of large pH fluctuations[14].

A further pH dependent mechanism has been proposed whereby the hydroxyl ion released from a clay-calcium-water interaction is able to interact with a polar oil compound. The free hydroxyl ion interacts with a polar organic, for example a carboxylic acid, and depending on the pH level, deprotonates the organic, removing the hydrogen bonding mechanism tethering the organic to the clay[8].

$$\text{Clay}-\text{RCOOH} + \text{OH}^- \rightleftharpoons \text{Clay} + \text{RCOO}^- + \text{H}_2\text{O}$$

A key challenge arises owing to the problems associated with probing all these postulated processes directly with molecular level insight. This is a wider challenge, occurring in related areas of clay science and to address this, computational chemistry simulations have become an essential adjunct to laboratory experimental methods for studying clay surfaces and interlayers.

In recent times, quantum mechanical (QM) simulations have become a useful tool to model the interaction of simple organic molecules on clays, for example the adsorption of monomers on kaolinite surfaces[17] amongst others[18,19]. Such methods explicitly include electron interactions, and are able to model reaction mechanisms between clay, brine, organic and water. However, the complexity of composition and structure of most clay minerals and the sheer number of interactions involved in low-salinity EOR rule out the use of QM methods with their restricted time- and length-scales in this instance.

Atomistic molecular dynamics (MD) treat atoms as spheres, intramolecularly bonded to one another via a set of springs. This simpler approach dramatically increases both the length scale and time scale that can be simulated. Indeed, classical MD is one of the key techniques used to model clay systems in the literature[20,21]. The main disadvantage of classical MD simulations is the lack of bond breaking and

bond formation, hence chemical reactions are impossible to model using classical MD without specialist forcefields[22].

The aim of the present study is to model the effects of double layer expansion, multicomponent ionic exchange, and pH levels on the absorption of organic oil molecules on smectite clay basal surfaces as a function of salt concentration using atomistic MD. This present study only considers clay basal surfaces, owing to the challenge in modelling highly dynamic and pH responsive clay edges using classical MD. Clay minerals representative in terms of structure, composition and charge density, of smectite (montmorillonite) clay basal surfaces in sandstone oil reservoirs were modelled. The effect of changing from monovalent to divalent cation type, using Na^+ and Ca^{2+}, and varying salinities from freshwater (0‰, 0 parts NaCl per 1000 H_2O by weight) to seawater (35‰) on the adhesion of model oil molecules (including non polar, polar neutral and polar charged functional groups) to clay surfaces was studied. Both initially water-wet and initially oil-wet systems have been modelled.

3.2 Methodology

3.2.1 Model Construction

The clay unit cell used in this study was a Wyoming-like montmorillonite (MMT) with stoichiometry $[Al_3Mg_1]$ $[Si_8O_{20}]$ $(OH)_4 \cdot nH_2O$. The octahedral layer of the clay contained one Mg atom for every three Al atoms, whilst both tetrahedral layers contained no isomorphic substitutions. The resulting unit cell, shown in Figure 3.3, possessed a single net negative charge, which was subsequently balanced with Na^+ or Ca^{2+} cations in the simulations of Na-montmorillonite and Ca-montmorillonite respectively.

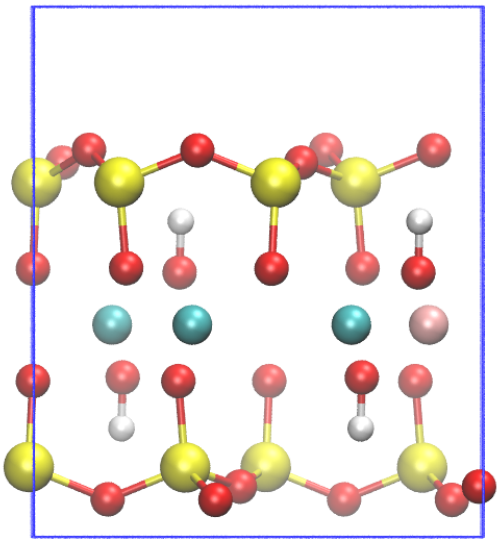

Figure 3.3: The montmorillonite unit cell used in this study. Colours as defined in Section 3.2.5.

Montmorillonite was deemed the most suitable 2:1 clay for this study due to its high cation exchange capacity and its proposed role in low-salinity enhanced oil recovery[10]. In contrast, other clays commonly found in reservoirs, such as illites and kaolinites, possess a lower cation exchange capacity (CEC) or are 1:1 non-swelling clays respectively, and do not exemplify properties such as cation exchange or double layer expansion. The montmorillonite clay was constructed using data readily available on the American mineralogist crystal structure database[23].

The organic molecules considered in this study were neutral non-polar decane ($C_{10}H_{22}$), protonated polar neutral decanoic acid ($CH_3(CH_2)_8COOH$) and charged sodium decanoate $Na^+(CH_3(CH_2)_8COO)^-$. This set of organics was ideal to highlight the effects of ionic exchange in low-salinity EOR. Additionally, pH level effects were modelled by altering the protonation state of the decanoic acid. Basal {001} surfaces of montmorillonite (the periodic models have no edge sites) are relatively pH stable and unlikely to vary within the pH range encountered within a typical oil reservoir[24,25]. All organic molecules used in this study were created using the Avogadro molecular editing suite[26].

Periodically replicated supercells contained one layer of montmorillonite composed of 84 unit cells (12×7×1), dimensions of approximately 6×6×6 nm^3, and a d-spacing of approximately 5 nm. Montmorillonite structures initially occupied the region $0 < z < 0.7$ nm in all models, and the clay position varied little over all timescales modelled. Subsequently, 80 organic molecules of either decane, decanoic acid or (Na)decanoate were inserted above the single clay layer. The simulations of protonated decanoic acid represented a pH level below the pKa of decanoic acid (4.9)[27] and were ideal to probe cation-polar bridging effects. Simulations of deprotonated decanoate represented pH levels greater than the pKa of decanoic acid and were ideal to simulate the cation-charged bridging mechanism.

Initially water-wet simulations were generated by randomly dispersing the organic molecules and ions within the interlayer and subsequently solvating the system. To create initially oil-wet conditions, the clay mineral was fixed in place. The interlayer was randomly dispersed with organics and ions, and a subsequent MD simulation was run to allow the organic molecules to equilibrate at the clay surface. The system was subsequently solvated, and the position restraints on the clay layers relaxed. This process created ideal starting configurations for both water-wet and oil-wet clay surfaces, see Figures 3.4a and 3.4b respectively.

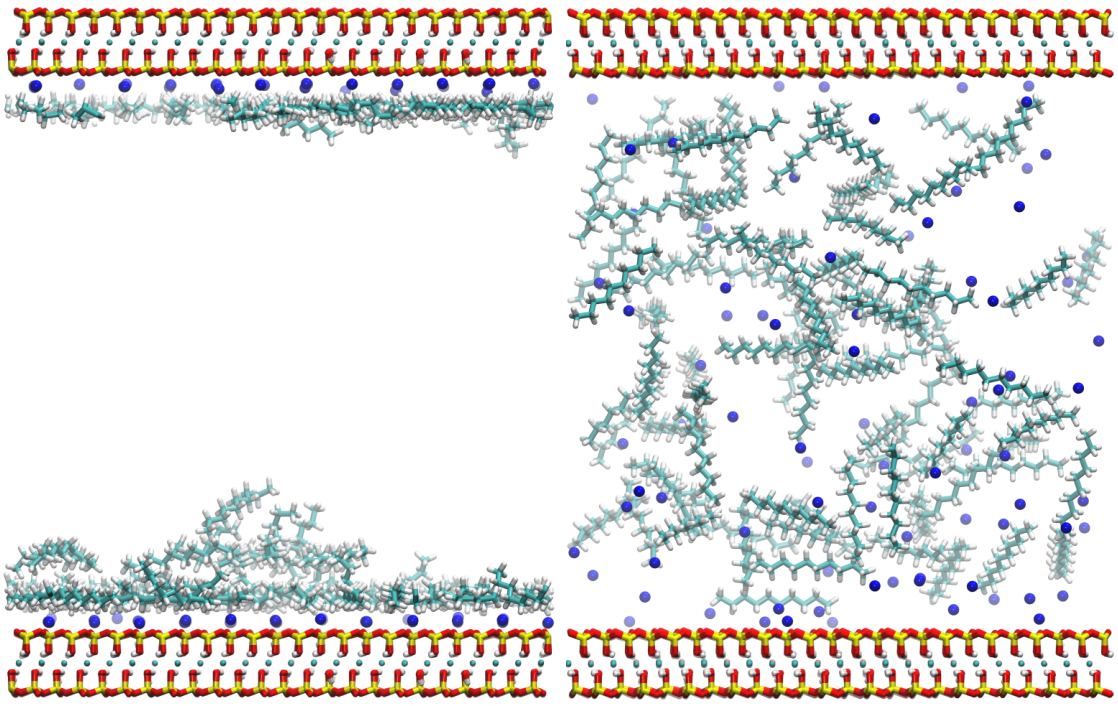

(a) Initially oil-wet NaMMT. (b) Initially water-wet NaMMT.

Figure 3.4: Snapshot of an initially oil-wet (left) and initially water-wet (right) NaMMT intercalated with decane molecules, pre-production, water molecules not represented. Colours as defined in Section 3.2.5.

The variations of initial configurations are presented in Table 3.2. In total, 56 separate configurations were set up and simulated.

Table 3.2: The permutations of the initial conditions modelled within this study.

Variable	Permutation			
Clay Mineral	NaMMT	CaMMT		
Intercalated Organic	Decane	Decanoic Acid	Na-Decanoate	None
Starting configuration	Oil-wet	Water-wet		
Salt concentration (NaCl)	0‰	1‰	5‰	35‰

3.2.2 Parameters

The ClayFF forcefield, specifically parameterised to model clays and clay-like minerals, was used to model the montmorillonite clay within this study[28]. The ClayFF force field is designed such that the entire interactions within, and structure of, the clay is described wholly by the non-bonded Lennard-Jones and Coulomb potentials (with the exception of hydroxyl groups within the clay layer, however all bonds involving hydrogens were constrained in this study).

The CGenFF forcefield was utilised to model the organic molecules interacting with clay layers. This forcefield has been parameterized for organic systems, has proven to reproduce physically accurate representations of hydrocarbons and similar organics[29,30], and is compatible with ClayFF[31].

The TIP3P water model was used to simulate the water between clay layers. It has been shown that this water model is consistent with both ClayFF and CGenFF force fields[31].

Lorentz-Berthelot mixing rules for van der Waals interactions are utilised in both CGenFF and ClayFF force fields, and have been used here to model organic-brine-clay interactions.

3.2.3 Simulation Details

All MD simulations were performed using GROMACS version 4.6.5[32] with electrostatic and the van der Waals cutoff distances set to 1.2 nm.

Every simulation was initialised with an energy minimisation run to reduce excessive forces on any one atom. This was accomplished using a steepest descents algorithm, with convergence achieved once the maximum force on any one atom was less than 100 kJ/(mol·nm).

Subsequently, simulations were run for a 50 ps equilibration period in the constant number of particles, pressure and temperature (NPT) ensemble with a velocity-rescale Berendsen thermostat, temperature coupling constant set to 0.1 ps, and a semi-isotropic Berendsen barostat (in which the pressure fluctuations x and y are coupled, but the pressure fluctuations in z are independent of those in xy), with pressure-coupling constant 1 ps. The Berensden thermostat and barostat offered swift equilibration of the system, and convergence was validated as the d-spacing (the separation between the clay layers through the periodic boundaries) and potential energy converged.

Unless otherwise stated, equilibration was followed by a 10 ns production run in the NPT ensemble using a velocity-rescale thermostat, with a temperature coupling constant of 1 ps, and a semi-isotropic Parrinello-Rahman barostat, with a pressure coupling constant of 1 ps. All simulations were run at approximately ambient conditions, a pressure of 1 bar and a temperature of 300 K. It was necessary to run simulations at ambient, rather than reservoir temperatures, as the ClayFF force field has been parameterised to model systems at room temperature, and considerable validation would be needed against, for example neutron scattering data, to ensure it holds at high T and P, work presently ongoing for future studies.

3.2.4 Analysis Techniques

Analysis of densities and electric potentials across the interlayer of the clay were carried out using the analysis tools within GROMACS 4.6.5. Cluster analysis was carried out using VMD 1.9.1, with a cluster defined when two organic molecules are within 3 Å of one other, or when an organic molecule is within 3 Å of previously defined cluster. The cutoff distance was set to 3 Å to exclude water molecules being between two organics within any cluster[33].

Divalent cation bridges were defined as any divalent cation, i.e. Ca^{2+}, within 5 Å of the clay basal plane and within 3 Å of an organic molecule. The 5 Å cutoff between clay and cation was determined using radial distribution functions (RDFs) to include the cations contained within the both the Stern layer and first hydration layer of the clay surface. Again, the 3 Å cutoff was determined to be the correct

length to exclude water molecules existing between organic and divalent cation.

3.2.5 Visualization

All snapshots were taken using VMD 1.9.1[34]. All simulations contain a single clay layer, which has been reproduced twice in all snapshots at the bottom and top of the figures. The clay layers are identical and are periodic images of one another. The colour scheme of all snapshots are defined as follows. The clay structure contains silicon (yellow), oxygen (red), aluminium (blue), magnesium (pink) and hydrogen (white) atoms. Organic molecules contain carbon (light blue), hydrogen (white) and oxygen (red). Ions are represented as large spheres and consist of sodium (blue), chloride (red) and calcium (green) atoms. Unless specified this colour scheme is kept consistent.

Density profiles between clay layers contain organics (black), sodium (blue), calcium (green) and chloride (red).

Colour schemes are presented in legends for all figures for both dynamic cluster analysis and cation bridging plots.

3.3 Results and Discussion

Unless otherwise stated, all data presented in the following sections were averaged from the last 5 ns of the 10 ns production simulation.

Section 3.3.1 discusses the potential role of double layer expansion in low-salinity EOR via MD simulations of charged smectite clays. Sections 3.3.2, 3.3.3 and 3.3.4 introduce organic oil molecules and examine their interactions with water-wet clay surfaces. Section 3.3.2 discusses non-polar uncharged decane, section 3.3.3 regards polar uncharged decanoic acid and section 3.3.4 regards the interactions of charged Na-decanoate with water-wet Na/CaMMT.

Section 3.3.5 discusses the key differences between initially oil-wet and water-wet simulations of Na/CaMMT interacting with the complete set of oil organic molecules. Section 3.3.6 investigates the properties of organic desorption from CaMMT over extended production runs up to 100 ns. Sections 3.3.7 and 3.3.8 regard the dynamic properties of all simulations. Section 3.3.7 presents the rate of organic clustering and Section 3.3.8 presents the rate of change of divalent cation bridges in the system as a function of time and salt concentration.

3.3.1 Electric Double Layer Effects

To examine the effects of salinity on double layer expansion simulations were run on NaMMT and CaMMT without organic molecules at various brine strengths.

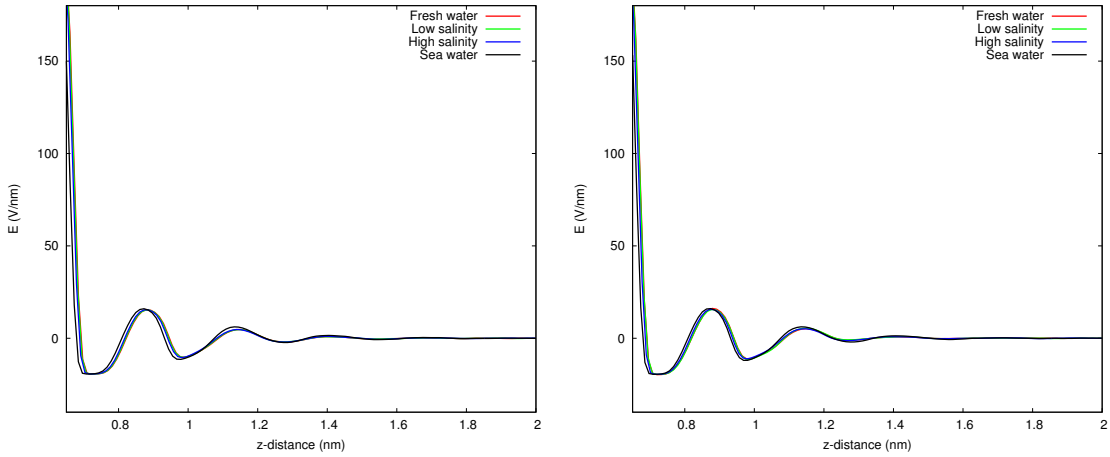

(a) The electric field strength of Na-MMT. (b) The electric field strength of Ca-MMT.

Figure 3.5: The variation in electric field strength, and hence electric double layers, generated by NaMMT (left) and CaMMT (right) basal planes at various salinities. Colours as defined in legend.

Figure 3.5a presents the electric field between the surface of the clay and $z = 2$ nm averaged over the last 5 ns of a 10 ns production run as a function of salt concentration. Figure 3.5b presents the electric field between the surface of the clay and $z = 2$ nm for CaMMT as a function of salt concentration. Note that the electric field strength presents identical trends for both NaMMT and CaMMT in Figure 3.5. This suggests that EDL expansion is not the key mechanism driving divalent cation exchange, as double layers should differ between NaMMT and CaMMT for ionic exchange to occur. Furthermore, both figures highlight several other important features.

Firstly, it can be noted that the electric field generated by the clay is entirely screened by the charge of the ions in the double layer within 1.5 nm from the clay basal plane for both NaMMT and CaMMT at all tested salt concentrations. Henceforth, the results presented in subsequent sections are to be considered as simulations of organic oil molecules interacting with two independent clay basal planes, rather that organics *intercalated* between two clay sheets.

Secondly, and more pertinently, there is no correlation between double layer expansion and salt concentration present in these simulations. The results show no expansion of the EDL. The results agree with several recent findings, whereby a Stern layer of fixed cations charge balance the clay, and the simulations refute the double layer expansion hypothesis of low-salinity EOR in this instance[35,36].

DLVO theory states that for a sufficiently highly charged clay-like surface, a Stern layer of immobile cations will be adsorbed to the clay, and act as a buffer to cancel the charge of the clay. The oscillatory nature of the electric field presented in Figure 3.5 can be described in this manner, whereby an exchangeable layer of cations charge balanced the clay, followed sequentially by a more mobile layer of anions and cations.

3.3.2 Effects of Salinity on Decane

The non-polar decane models in this study include partial charges on all carbon and hydrogen atoms and are expected to scarcely interact with the clay. Previous work has shown that decane molecules form organic aggregates in brines of various strength.[37]

The Interactions of Decane with Initially Water-Wet NaMMT

Figure 3.6a presents the final snapshot of a NaMMT simulation interacting with 80 decane molecules at a salt concentration of 5‰ NaCl.

The formation of organic aggregates is clear in Figure 3.6a. The decane molecules coalesce together and act independently of the charged clay surface. This behaviour is not surprising. It is energetically favourable for the hydrophobic hydrocarbons to aggregate and minimise their surface interactions with the polar solvent molecules.

Figure 3.7a presents the density profile of decane molecules and salt ions across the clay interlayer at varying salt concentrations. Note the symmetry across the interlayer and the discrete separation between the organic molecules and the fully-solvated ions shielding the clay. The organic molecules always form aggregates between the clay layers independent of salinity. The results show that non-polar uncharged molecules do not interact with the silicate surfaces of the water-wet clay, in concordance with previous experimental work, where the majority of hydrocarbon-clay interactions occur on hydroxyl clay surfaces.[11]

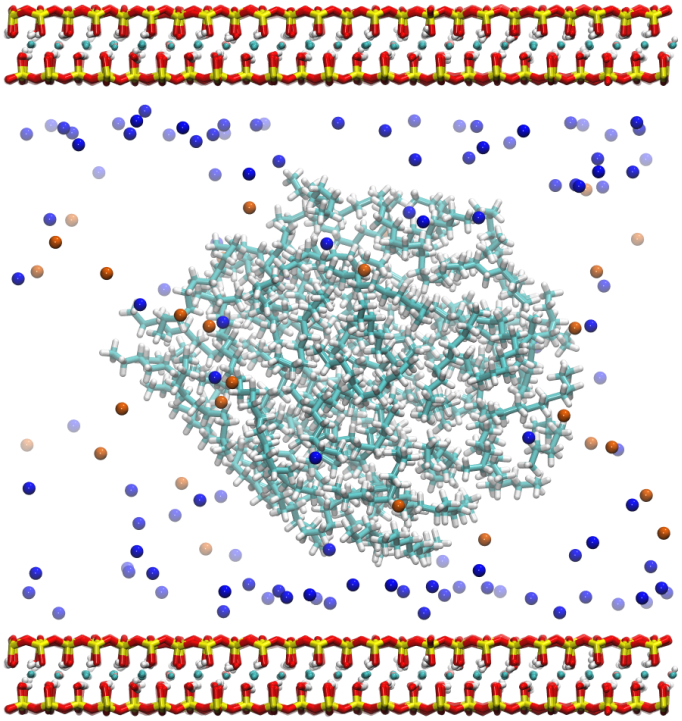

(a) A snapshot of NaMMT interacting with decane molecules.

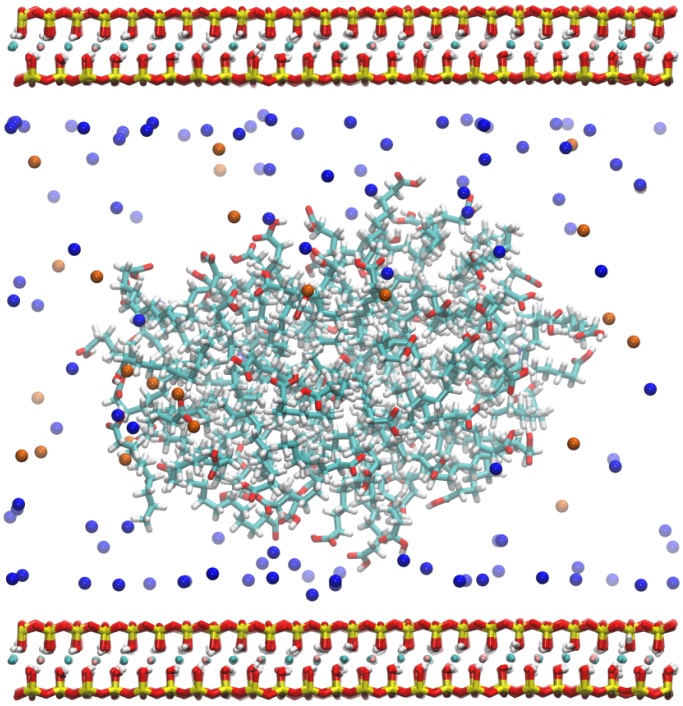

(b) A snapshot of NaMMT interacting with decanoic acid molecules.

Figure 3.6: Post-production snapshots of decane (left) and decanoic acid (right) interacting with NaMMT modelled with 5‰ NaCl after 10 ns. Both snapshots present to formation of organic aggregates. Colours as defined in Section 3.2.5.

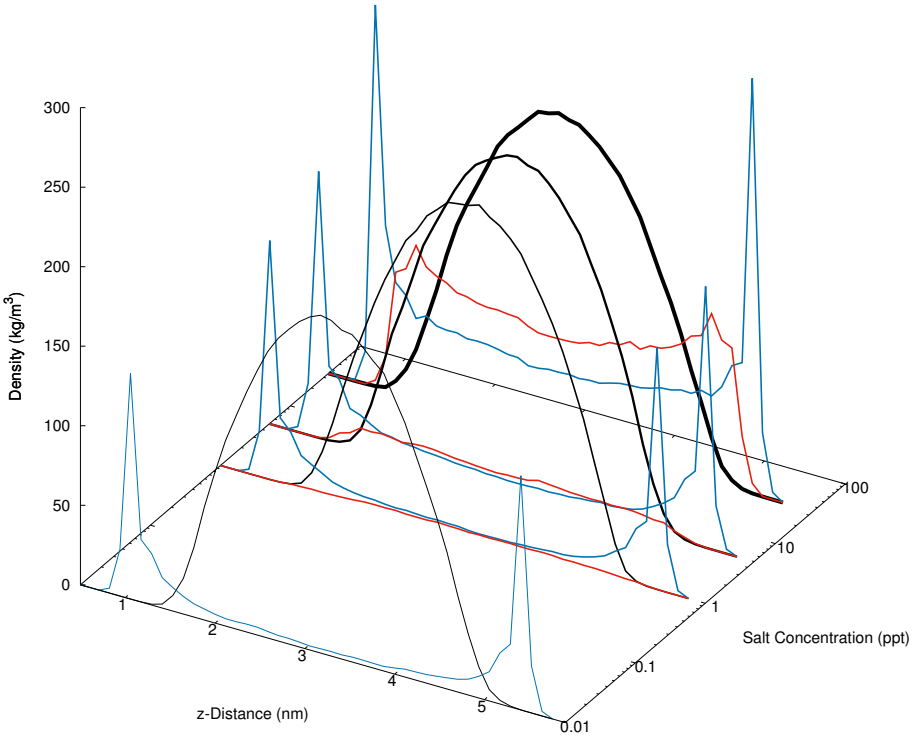

(a) The density profile of NaMMT interacting with decane.

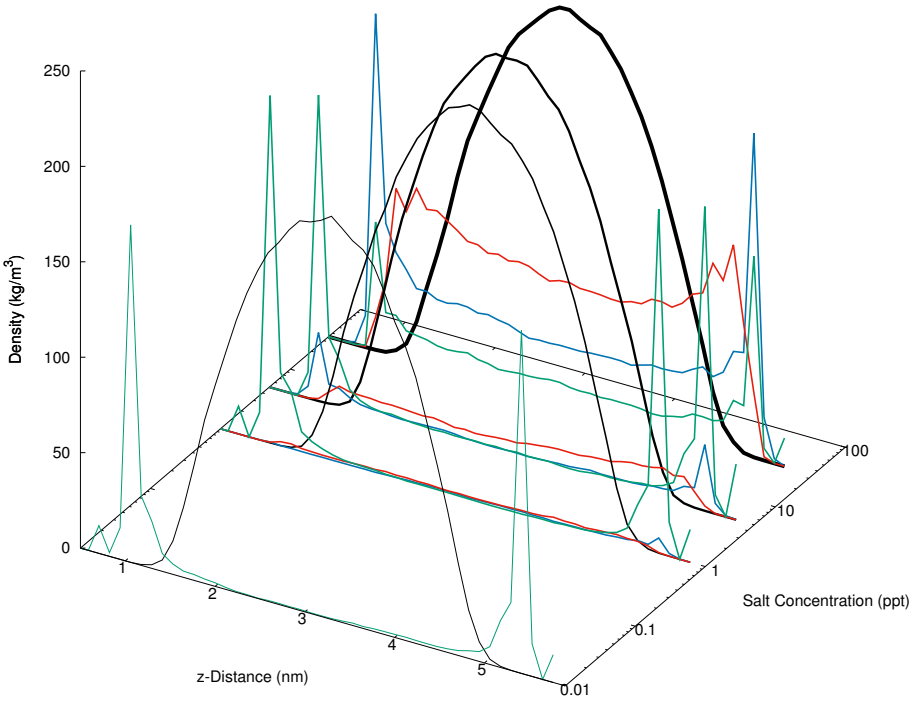

(b) The density profile of CaMMT interacting with decane.

Figure 3.7: Density profiles of NaMMT (left) and CaMMT (right) interacting with decane at various salinities averaged over the last 5 ns of a 10 ns production simulation. Colours as defined in Section 3.2.5.

The Interactions of Decane with Initially Water-Wet CaMMT

The introduction of calcium as the charge balancing cation of the clay does not affect the observed behaviour of intercalated decane, as shown in the density profile of CaMMT with decane, Figure 3.7b. The formation of organic aggregates can be seen across all simulations of decane, under all variations of brine strength and clay composition.

It is notable however, that the divalent calcium cations are able to form a Stern layer at the clay surface, whilst the sodium cations are always fully hydrated, as can be seen from the small peak of calcium ions adjacent to the clay in Figure 3.7b. A Stern layer of calcium ions was observed to form at all salt concentrations, and suggests that the divalent cation bridging mechanisms may act, at least partially, independent of the salt concentration. The results agree with the conclusions of Bourg *et al.*, that Stern layer adsorption is independent of salinity, however, the cited study found a preference for sodium ions over calcium ions within the Stern layer[35]. The chief difference between the presented study and the work of Bourg *et al.* is the utilisation of different water models. Here, we have used the TIP3P water model, whilst the work of Bourg *et al.* uses the SPC/E water model[35].

3.3.3 Effects of Salinity on Decanoic Acid

The introduction of polar carboxylic functional groups in the form of decanoic acid molecules is expected to alter the behaviour of the clay-organic interactions. Bulk decanoic acid in brine forms micelles[37], however cation-polar bridging events are expected to be seen in the simulations of decanoic acid interacting with smectite clays.

The Interactions of Decanoic Acid with Initially Water-Wet NaMMT

Figure 3.6b presents the final snapshot of polar uncharged decanoic acid in NaMMT with a brine concentration of 5‰ NaCl. The Figure shows that the polar uncharged organic molecules form micelles between the clay layers, with the hydrophilic carboxylic functional groups orientated on the external surface of the micelle and the hydrophobic hydrocarbon tails minimising their contact with the polar water molecules on the inside of the micelle. Once again, the results show that the organic aggregates, in this case micelles, do not interact with the clay.

The Interactions of Decanoic Acid with Initially Water-Wet CaMMT

The introduction of calcium as the charge balancing cation of the clay does not affect the observed behaviour of decanoic acid interacting with water-wet montmorillonite. The formation of micelles is observed in all simulations of decanoic acid, under all variations of brine strength and clay composition.

To summarise, the results present the formation of micelles in the simulations of polar decanoic acid interacting with both water-wet NaMMT and water-wet CaMMT at all salinities. Furthermore, simulations show a tendency for divalent calcium cations to balance the charge of the clay and form a Stern layer. This behaviour was observed in all simulations of decane and decanoic acid interacting with water-wet CaMMT, and the behaviour is independent of salinity. The results show that cation bridging between clay and polar organic is not present in water-wet clays. The importance of initially oil-wet clays is paramount for the low-salinity EOR effect, as has been observed previously in experiments.[3]

3.3.4 Effects of Salinity on Na-decanoate

The introduction of charged organic decanoate molecules was expected to produce the most relevant results to describe cation-charged bridging in low-salinity EOR. Interplay between clays and the organic molecules were expected to increase, as direct Coulomb forces are much stronger than the dipole interactions between polar organics.

The Interactions of Na-Decanoate with Initially Water-Wet NaMMT

Figure 3.8a is an end-snapshot of a simulation of NaMMT with 80 Na-decanoates at a salt concentration of 5‰ NaCl.

Again, the aggregation of organic molecules can be noted. The conglomerates are smaller in comparison to the uncharged polar decanoic acid molecules.

Furthermore, the distance between clay basal plane and organic cluster is larger than that in the previous examples of decane and decanoic acid. This is due to the overwhelming interaction between clay and organic being Coulomb repulsive and the absence of mediating divalent cations.

The Interactions of Na-Decanoate with Initially Water-Wet CaMMT

The presence of divalent calcium cations introduced several interesting features to the simulations. Figure 3.8b is an end-snapshot of a simulation of CaMMT interacting with 80 Na-decanoate molecules at a salt concentration of 5‰ NaCl. It can be observed that the majority of sodium and calcium cations appear to screen the charge of the clay from the organic molecules.

Despite this shielding, there are features indicative of cation-charged bridging present in Figure 3.8b. First, note the bridging between the clay and organic molecules. See Figure 3.9a for magnified view.

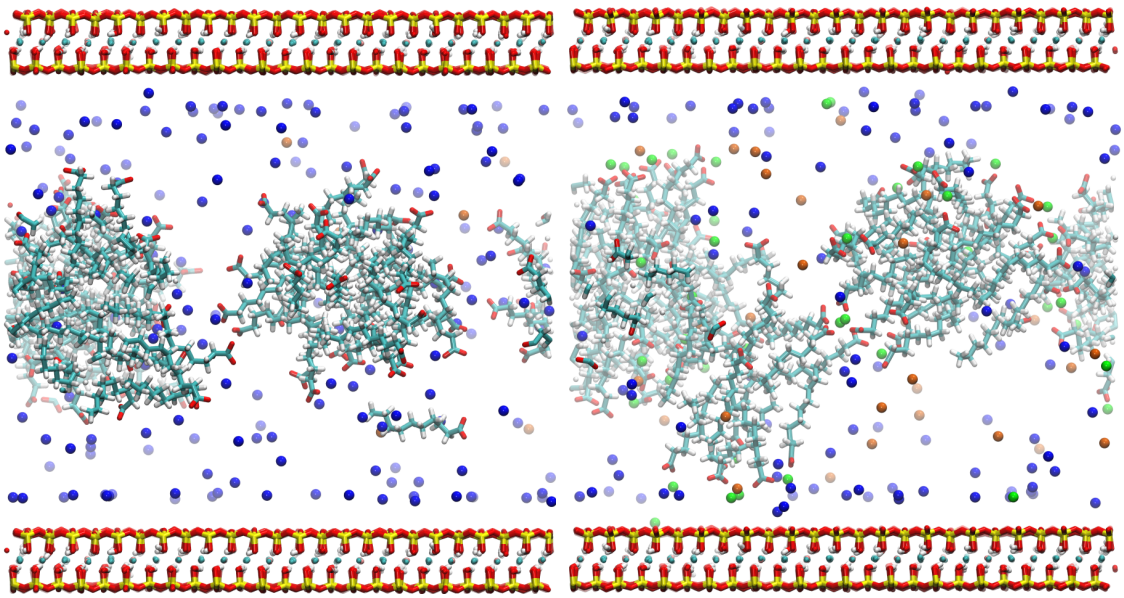

(a) A snapshot of NaMMT with 80 Na-decanoate molecules.

(b) A snapshot of CaMMT with 80 Na-decanoate molecules.

Figure 3.8: Post-production snapshots of Na-decanoate interacting with NaMMT (left) and CaMMT (right) modelled with 5‰ NaCl after 10 ns. Colours as defined in Section 3.2.5.

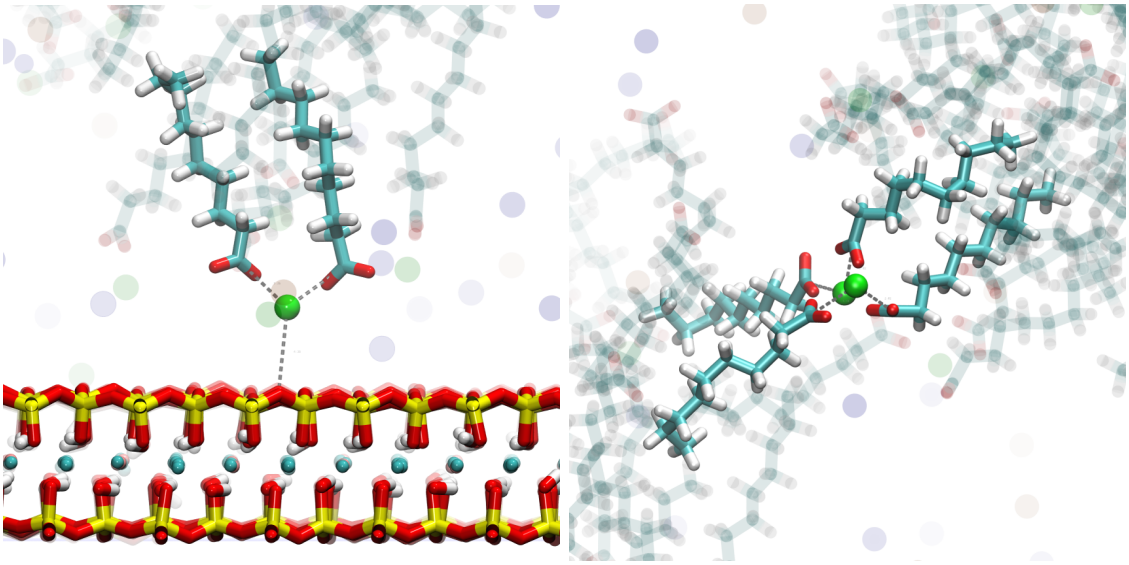

(a) Cation-charged bridging between clay and charged Na-decanoate molecules.

(b) Cation-charged bridging between identical organic molecules.

Figure 3.9: Enhanced snapshots of Na-decanoate interacting with CaMMT, Figure 8b. Colours as defined in Section 3.2.5.

The results show the capability for divalent cations to bridge between like-charged clay layers and organic molecules. This is evidence that cation-charged bridging can play a role in oil recovery. However, the distribution of calcium cations between clay layers does not fluctuate as a function of salinity, see Figure 3.10. Salinity does not affect the amount of divalent cations between water-wet clays and charged organics. Hence, the cation-charged exchange mechanism is independent of salinity for water-wet clays.

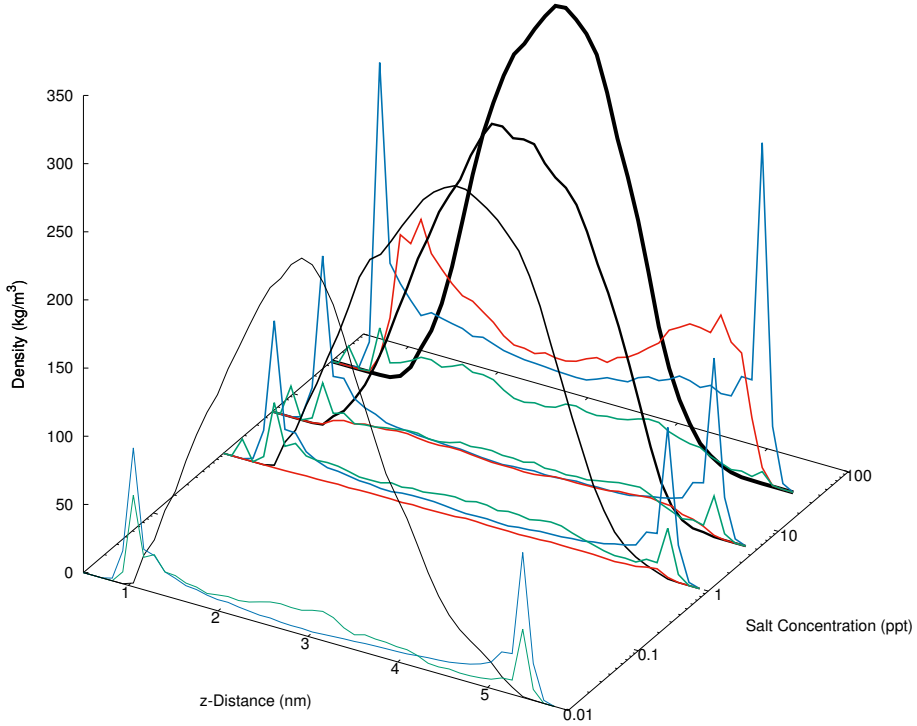

Figure 3.10: The density profile of CaMMT interacting with 80 Na-decanoate molecules at various salinities. Colours as defined in Section 3.2.5.

Figure 3.8b also presents divalent cation-charged bridging between organic molecules (see Figure 3.9b for an enhanced snapshot). This indicates that divalent cations within the interlayer can link separate aggregates or micelles to one another.

The density profiles present that the cation-charged bridging mechanism for charged organics is independent of salinity for water-wet clays. The snapshots show that cation-charged bridging mechanism events can occur in the simulations, however scarcely.

3.3.5 Oil-Wet vs. Water-Wet Clays

To examine the difference between initially water-wet and initially oil-wet clay basal surfaces, the corresponding oil-wet systems were created as described in Section 3.2.1. The following results are taken from the last 5 ns of a 10 ns production run.

Initially oil-wet simulations of organics interacting with NaMMT resulted in the formation of organic aggregates between clay layers at all salinities. Initially oil-wet clays behaved identically to water-wet clays in the absence of divalent cations.

Initially oil-wet simulations of decane interacting with CaMMT resulted in the formation of organic aggregates between the clay layers at all salinities, showing that non-polar uncharged organic molecules do not contribute to the wettability of a clay surface.

Figure 3.11a and Figure 3.11b presents the density profiles of decanoic acid and Na-decanoate between CaMMT clay layers at various salinity levels.

Figure 3.11a presents the density profiles of decanoic acid molecules and ions between initially oil-wet CaMMT layers. Note the widely varying density profiles of organic molecules as a function brine concentration. The fresh water system creates an almost homogenous distribution of organics, whilst the calcium ions shield the charge of the clay. As the brine strength is increased to 1‰ and 5‰ NaCl respectively, the formation of organic aggregates on the clay surface is seen.

Figure 3.11b presents the density profile of Na-decanoate interacting with CaMMT at various salt concentrations. The presence of charged organics and divalent cations maintain the oil-wet state of the system regardless of the salt concentration. This highlights that the protonation of the acids in the oil, and hence the pH level surrounding the clay, plays a vital role in low-salinity EOR.

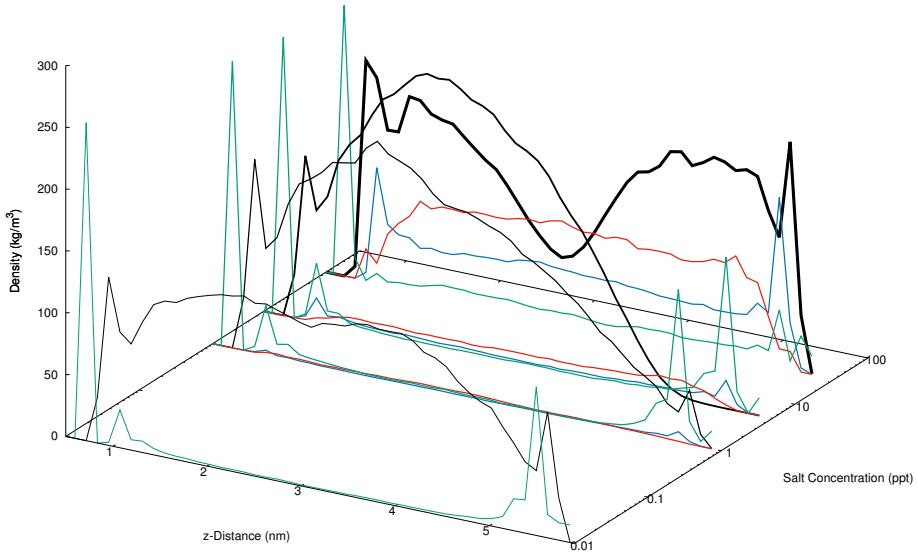

(a) CaMMT interacting with decanoic acid. Averaged between 5 ns and 10 ns.

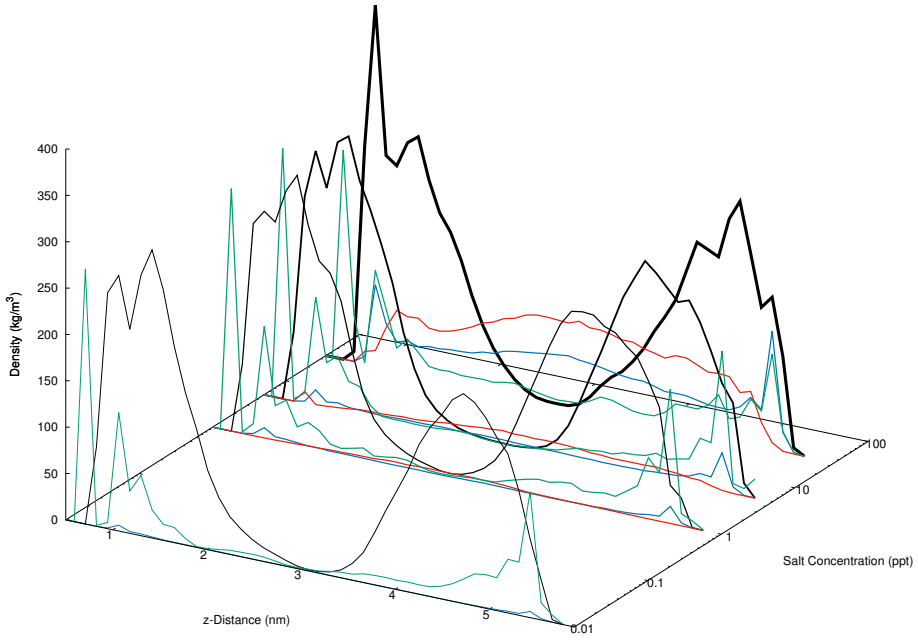

(b) CaMMT interacting with Na-decanoate. Averaged between 5 ns and 10 ns.

Figure 3.11: Density profiles of initially oil-wet CaMMT interacting with decanoic acid (top) and Na-decanoate (bottom) at various salinities averaged over various times of the same production run. Colours as defined in Section 3.2.5.

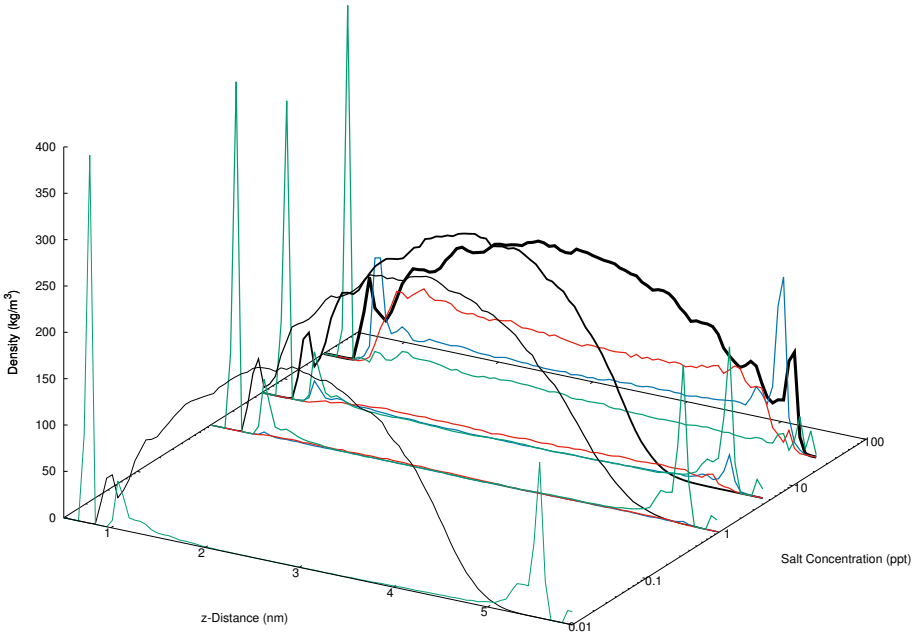

(c) CaMMT interacting with decanoic acid. Averaged between 15 ns and 20 ns.

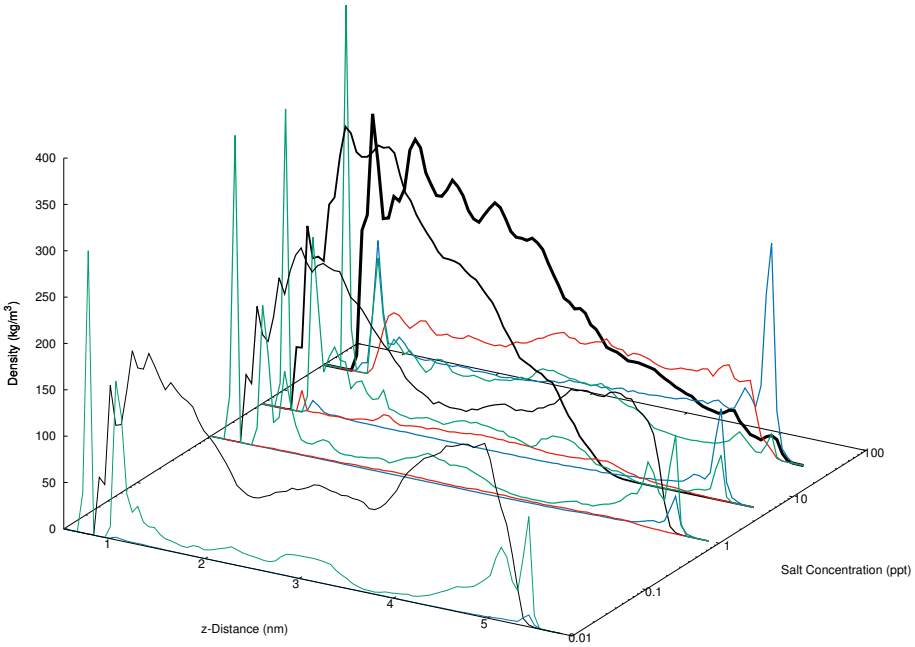

(d) CaMMT interacting with Na-decanoate. Averaged between 45 ns and 50 ns.

Figure 3.11: Density profiles of initially oil-wet CaMMT interacting with decanoic acid (top) and Na-decanoate (bottom) at various salinities averaged over various times of the same production run *(cont.)*. Colours as defined in Section 3.2.5.

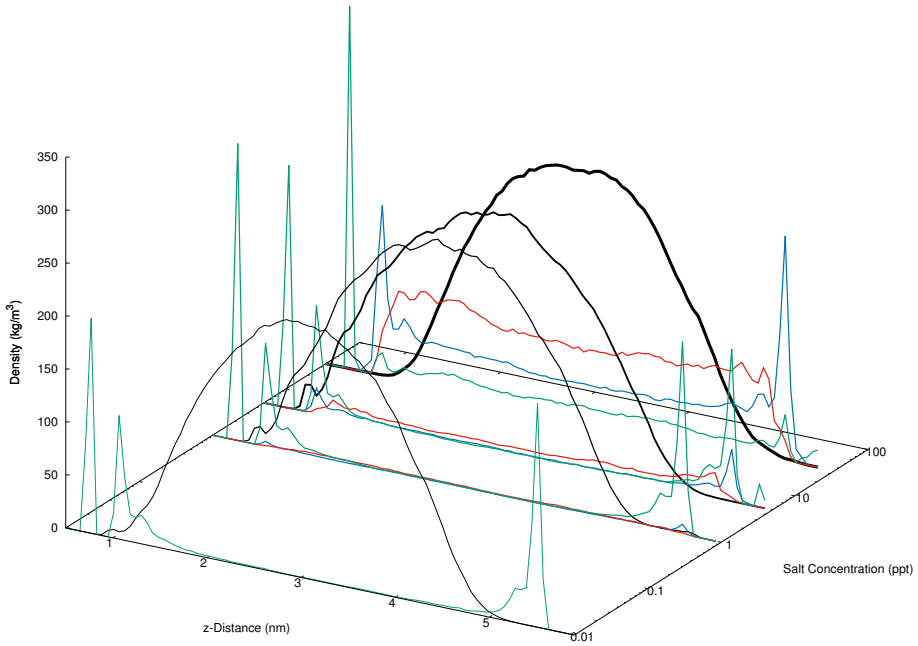

(e) CaMMT interacting with decanoic acid. Averaged between 45 ns and 50 ns.

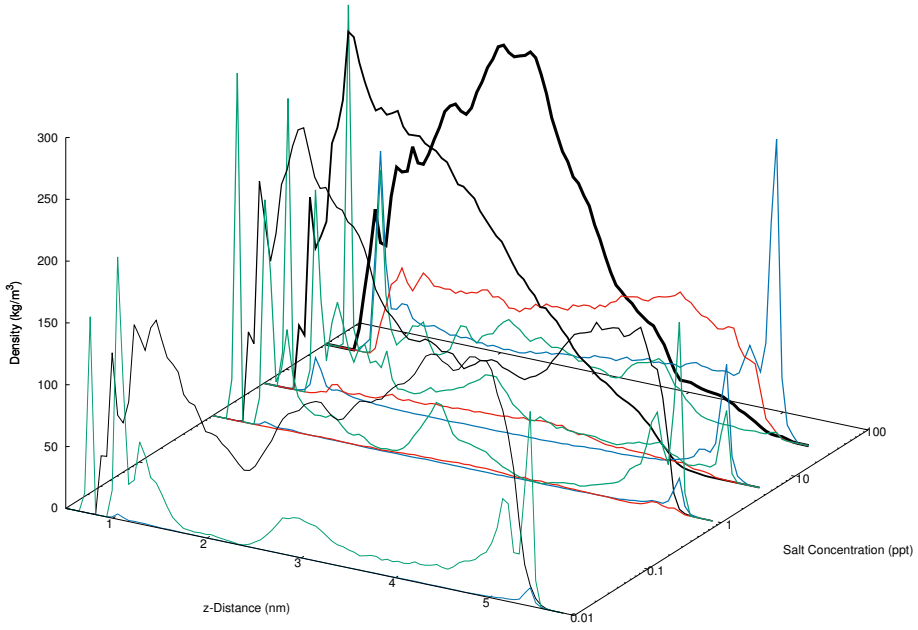

(f) CaMMT interacting with Na-decanoate. Averaged between 95 ns and 100 ns.

Figure 3.11: Density profiles of initially oil-wet CaMMT interacting with decanoic acid (top) and Na-decanoate (bottom) at various salinities averaged over various times of the same production run *(cont.)*. Colours as defined in Section 3.2.5.

3.3.6 Extended Simulations of Initially Oil-Wet CaMMT

The large discrepancy in density profiles of oil-wet and water-wet charged organics interacting with CaMMT suggested extended simulations were warranted.

Figures 3.11c and 3.11e present the density profiles of polar decanoic acid averaged between 15 ns and 20 ns, and 45 ns and 50 ns of the same production run respectively. The results show that extending the simulation of decanoic acid interacting with initially oil-wet CaMMT to 50 ns reproduced organic aggregates between clay layers. The final state of polar decanoic acid interacting with CaMMT is independent of salinity, however the dynamics of polar organic desorption appear to be salt dependent (see the following Sections 3.3.7 and 3.3.8).

Figures 3.11d and 3.11f present the density profiles of charged decanoate averaged between 45 ns and 50 ns, and 95 ns and 100 ns of the same production run. Both figures show desorption of organics from one basal plane as divalent cations are replaced by monovalent cations. Again, it is concluded that the replacement of divalent for monovalent cations and hence the ionic content of a flood is more important than its salinity.

To summarise, all initially oil-wet simulations of NaMMT show desorption of organic matter from the clay surface. Hence, replacing all the divalent cations in the system with monovalent cations will increase EOR effects.

Negatively charged decanoate molecules will remain adsorbed to a clay surface when a bridging cation is present via the cation-charged bridging mechanism. This effect is independent of salt concentration.

The results concord with the hypothesis that the initial wetness of the reservoir matrix is of importance to EOR[3], but also propose that that the wettability of a reservoir is directly affected by its ionic content. Initially oil-wet NaMMT becomes water-wet independent of the organic molecule and salt concentration, whilst initially oil-wet CaMMT may remain oil-wet depending upon the organics constituting the oil. Further, the results suggest that the ionic content of a water-flood may be more important that its salinity, flooding a field with monovalent ions will increase the wettability of the reservoir matrix.

3.3.7 Dynamic Clustering Analysis

Clustering of organic molecules is observed in all simulations to some extent. Clustering analysis over a simulation's trajectory probes the dynamic effects of this process.

Figure 3.12a shows the number of clusters in the simulation of decanoic acid interacting with initially water-wet NaMMT as a function of time and salt concentration. It can be seen that the formation of micelles occurs on the nanoscale independently of salinity. The noise at approximately 6 and 8 ns corresponds to a single molecule breaking off of the dominant cluster and instantaneously being reabsorbed into the micelle.

The behaviour presented in Figure 3.12a is typical amongst all the initially water-wet simulations of both NaMMT and CaMMT with all three forms of organics.

Figure 3.12b presents the number of organic clusters for initially water-wet NaMMT interacting with Na-decanoate. In this system, the organics form several separate clusters, rather than one large aggregate, as is also the case of Na-decanoate interacting with CaMMT. This is because the charged decanoate molecules repel each other, whilst in the water-wet CaMMT system, the divalent cations can bridge the like-charged organics to one another.

Figure 3.12c presents the number of clusters of polar decanoic acid interacting with initially oil-wet NaMMT as a function of time and salt concentration. The initial number of clusters in this simulation is two, i.e. one cluster on each of the modelled clay surfaces. As the simulations progress, several organic molecules break away from the oil-wet surface to create a new separate cluster. This process continues, and within 1 ns the maximum number of separate clusters can be seen. After a nanosecond, the separate clusters begin to coalesce, and any further organics desorbed from the clay surface are rapidly encompassed in one of the previously existing clusters.

The only scenario where this behaviour is not observed is for originally oil-wet simulations of CaMMT interacting with charged decanoate, Figure 3.12d. These systems remain oil-wet as previously discussed, and the number of clusters does not vary over the timescale modelled.

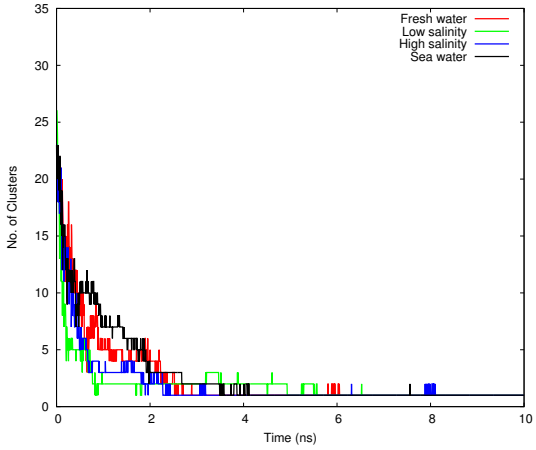

(a) Initially water-wet NaMMT with decanoic acid.

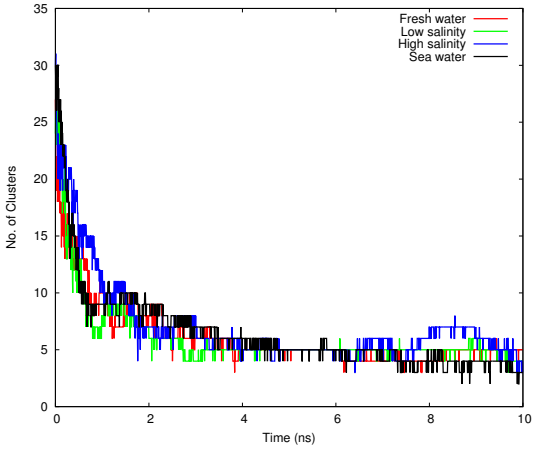

(b) Initially water-wet NaMMT with Na-decanoate.

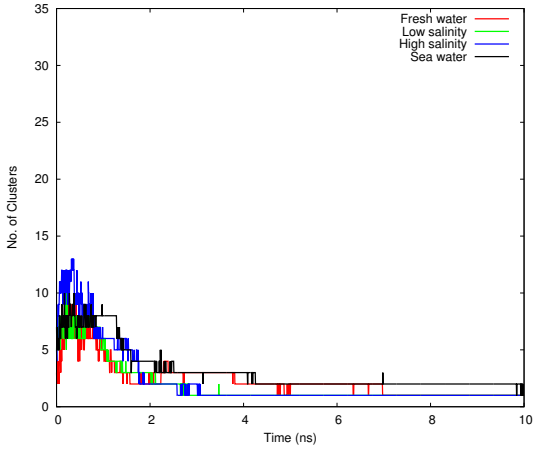

(c) Initially oil-wet NaMMT with decanoic acid.

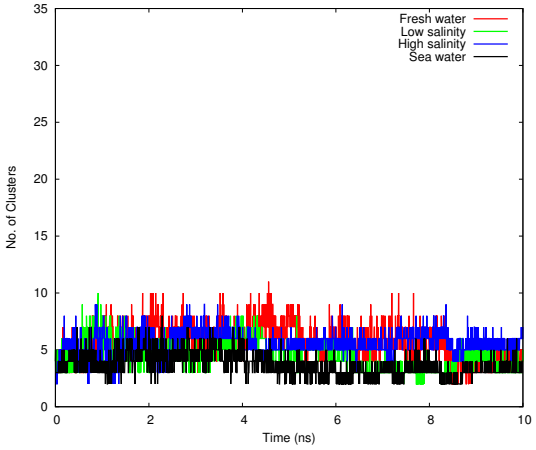

(d) Initially oil-wet CaMMT with Na-decanoate.

Figure 3.12: The number of clusters in a simulation as a function of time and salt concentration. See legends for colour scheme.

3.3.8 Dynamic Divalent Cation Bridge Analysis

A divalent cation bridge is determined to be any divalent cation that is within 5 Å of the clay surface and within 3 Å of an organic oil molecule, as discussed in the analysis techniques, Section 3.2.4. This measure is a useful quantity in determining the rate of organic desorption from a clay surface, and is useful to determine both the occurrence of divalent cation bridging as well as its dependence on salt concentration.

Figure 3.13a presents the number of divalent cation-polar bridges for the initially oil-wet simulation of CaMMT interacting with polar decanoic acid. Here, the number of cation bridges decreases as the simulation progresses, and that the difference between salinity levels is minimal. At the end of all simulations the number of potentially cation bridging cations has reduced to near zero.

Figure 3.13b presents the number of divalent cation-charged bridges for initially oil-wet simulations of CaMMT interacting with charged Na-decanoates at various salt concentrations. Note, the increased amount of bridges in this system compared to the polar decanoic acid. This is due to the charge of the organic. There is a slight decrease in the total number of bridges with time, however the number of cation-charged bridges appears to converge to a non-zero number during the simulation. Also note the independence of salinity in cation-charged bridging.

In general, all systems of CaMMT present a decrease of divalent cation bridges with time, and all are independent of interlayer salinity. The amount of cation bridges in simulations of oil wet CaMMT with decane decreases to zero after 1 ns, decreases to zero after 10 ns for decanoic acid, and converges to a finite number with decanoate.

Figure 3.13c shows the number of divalent cation bridges for initially water-wet CaMMT interacting with Na-decanoate. It can be seen that there are intermittent cation-charged bridging events occurring throughout the simulation, however these events flitter in and out of existence. The initial wettability of a clay appears to be an important factor for the cation-charged bridging mechanism, as previously discussed.

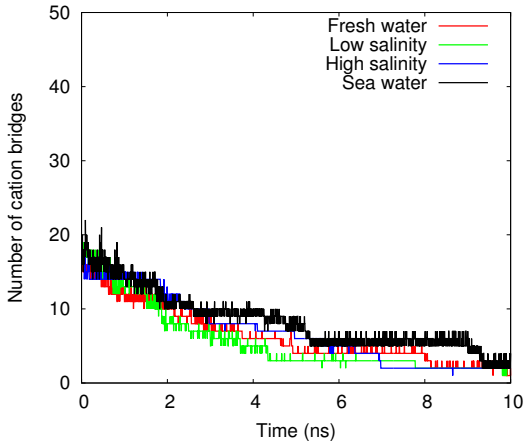

(a) Initially oil-wet CaMMT with decanoic acid.

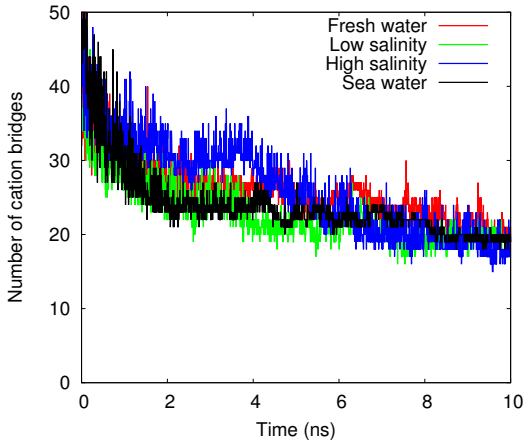

(b) Initially oil-wet CaMMT with Na-Decanoate.

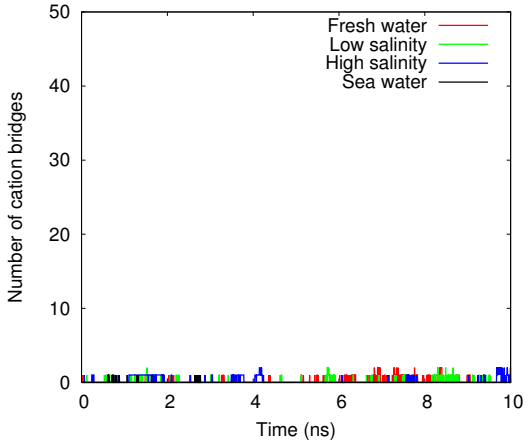

(c) Initially water-wet CaMMT with Na-Decanoate.

Figure 3.13: The amount of potentially bridging divalent cations as a function of time and salt concentration. See legends for colour scheme.

3.4 Conclusions

The use of molecular dynamics simulations has helped elucidate some of the key mechanisms underpinning low-salinity enhanced oil recovery. The following are the key conclusions discerned from the simulations of smectite clays with oil organics as a function of salinity and initial clay wetness.

Electric double layer expansion does not vary with salinity, and is not a driving factor for low-salinity EOR. Further work is required to interpret the importance of pH on the effective charge of the clay basal plane.

All multicomponent ionic exchange mechanisms proposed to affect low-salinity EOR are *independent of salt concentration* and hence cannot explain the effects of low-salinity EOR. Non-polar, uncharged organic molecules do not interact with charged hydrated smectite clay minerals to any extent. Polar, uncharged molecules form micelles, and do not interact with charged smectite clay surfaces profusely. Depending upon a clay's initial wettability, charged organic molecules can interact heavily with clay basal planes. For an initially oil-wet clay, the cation bridging mechanism is prevalent, whilst for an initially water-wet clay, the cation bridging mechanism is absent. Water bridging has not been observed in any simulation, however more densely charged divalent cations, i.e. Mg^{2+}, may be required to observe such effects. A Stern layer of unhydrated calcium cations is observed in both oil-wet and water-wet simulations of CaMMT. The amount of unhydrated cations in the Stern layer is independent of the salt concentration of the system, and hence divalent cation bridging and ligand bridging may occur independently of salt concentration.

The simulations present that, in the systems studied, the key drivers of low-salinity EOR are twofold.

One, the pH level surrounding the clay, and hence the protonation and charge of organic oil molecules. Cation-charged bridging is present between oil-wet clay and organic, however divalent cation-polar bridging is not. A key question arises in how the salt concentration surrounding the clay surface might affect the protonation of the polar acids within oil. Investigation of this mechanism would require QM modelling.

Two, that the wettability of a clay is dependent upon the charge balancing cation. The simulations show that replacing divalent calcium ions with monovalent sodium cations will increase clay water wetness, and subsequently improve oil recovery rates. The ionic content of a flood is more important that the concentration.

The molecular level insight into clay organic interactions occurring during EOR offer hitherto unaccessed resolution. Future work shall investigate the role of $CaCl_2$ as well as NaCl brine to further elucidate the effect of monovalent vs divalent cations on the wetness of clays. Highly hydrating cations, such as Mg^{2+} may also be modelled to examine the full potential of water bridging in EOR. The cation exchange mechanism shall be investigated by modelling positively charged organics (containing nitrogen in the functional group) and organics containing aromatic rings. This shall determine whether cation-π interactions play any role in low-salinity EOR. Further clay minerals found at a higher abundance within reservoirs, such as kaolinite and illite, shall also be modelled.

Supplementary Information

Radial distribution functions have been used to determine cut-offs for cation bridging events, these can be viewed in the appendices. Additional density profiles, dynamic clustering and dynamic cation bridging figures are also available in the appendices.

Bibliography

[1] International Energy Agency. *World energy outlook 2013.* International Energy Agency, Paris, 2013.

[2] JJ Sheng. *Modern Chemical Enhanced Oil Recovery: Theory and Practice.* Gulf Professional Publishing, Burlington, 2010.

[3] MM Sharma and PR Filoco. Effect of brine salinity and crude-oil properties on oil recovery and residual saturations. *SPE J. (Soc. Pet. Eng.)*, 5(03):293–300, 2000.

[4] G-Q Tang and NR Morrow. Influence of brine composition and fines migration on crude oil/brine/rock interactions and oil recovery. *J. Pet. Sci. Eng.*, 24(2):99–111, 1999.

[5] Y Zhang and NR Morrow. Comparison of secondary and tertiary recovery with change in injection brine composition for crude-oil/sandstone combinations. In *SPE/DOE Symposium on Improved Oil Recovery*, Tulsa, 2006. Society of Petroleum Engineers.

[6] KK Mohan, RN Vaidya, MG Reed, and HS Fogler. Water sensitivity of sandstones containing swelling and non-swelling clays. *Colloids Surf., A*, 73:237–254, 1993.

[7] K Skrettingland, T Holt, MT Tweheyo, and I Skjevrak. Snorre low-salinity-water injection - core flooding experiments and single-well field pilot. *SPE Reservoir Eval. Eng.*, 14(02):182–192, 2011.

[8] T Austad, A RezaeiDoust, and T Puntervold. Chemical mechanism of low salinity water flooding in sandstone reservoirs. In *SPE Improved Oil Recovery Symposium*, Tulsa, 2010.

[9] O Fassi-Fihri, M Robin, and E Rosenberg. Wettability studies at the pore level: a new approach by the use of cryo-scanning electron microscopy. *SPE Form. Eval.*, 10(01):11–19, 1995.

[10] F Civan. *Reservoir Formation Damage.* Gulf Professional Publishing, Burlington, 2011.

[11] JL Bantignies, CCD Moulin, and H Dexpert. Wettability contrasts in kaolinite and illite clays: characterization by infrared and x-ray absorption spectro-

scopies. *J. Phys. IV*, 7(C2):C2–867, 1997.

[12] JJ Sheng. Critical review of low-salinity waterflooding. *J. Pet. Sci. Eng.*, 120:216–224, 2014.

[13] EJW Verwey and JTG Overbeek. *Theory of the Stability of Lyophobic Colloids*. Courier Dover Publications, New York, 1999.

[14] A Lager, KJ Webb, CJJ Black, M Singleton, and KS Sorbie. Low salinity oil recovery - an experimental investigation. *Petrophysics*, 49(1):28, 2008.

[15] G Sposito. *The Chemistry of Soils*. Oxford University Press, New York, 2008.

[16] PL McGuire, JR Chatham, FK Paskvan, DM Sommer, and FH Carini. Low salinity oil recovery: an exciting new eor opportunity for alaska's north slope. In *SPE Western Regional Meeting*, Irvine, 2005. Society of Petroleum Engineers.

[17] DL Geatches, A Jacquet, SJ Clark, and HC Greenwell. Monomer adsorption on kaolinite: modeling the essential ingredients. *J. Phys. Chem. C*, 116(42):22365–22374, 2012.

[18] J Zhong, X Wang, J Du, L Wang, Y Yan, and J Zhang. Combined molecular dynamics and quantum mechanics study of oil droplet adsorption on different self-assembly monolayers in aqueous solution. *J. Phys. Chem. C*, 117(24):12510–12519, 2013.

[19] VM Sánchez and CR Miranda. Modeling acid oil component interactions with carbonate reservoirs: a first-principles view on low salinity recovery mechanisms. *J. Phys. Chem. C*, 118(33):19180–19187, 2014.

[20] JL Suter, RL Anderson, HC Greenwell, and PV Coveney. Recent advances in large-scale atomistic and coarse-grained molecular dynamics simulation of clay minerals. *J. Mater. Chem.*, 19(17):2482–2493, 2009.

[21] HC Greenwell, W Jones, PV Coveney, and S Stackhouse. On the application of computer simulation techniques to anionic and cationic clays: a materials chemistry perspective. *J. Mater. Chem.*, 16(8):708–723, 2006.

[22] ACT Van Duin, S Dasgupta, F Lorant, and WA Goddard. Reaxff: a reactive force field for hydrocarbons. *J. Phys. Chem. A*, 105(41):9396–9409, 2001.

[23] RT Downs and M Hall-Wallace. The american mineralogist crystal structure database. *Am. Mineral.*, 88(1):247–250, 2003.

[24] X Liu, X Lu, M Sprik, J Cheng, EJ Meijer, and R Wang. Acidity of edge surface sites of montmorillonite and kaolinite. *Geochim. Cosmochim. Acta*, 117:180–190, 2013.

[25] S Tazi, B Rotenberg, M Salanne, M Sprik, and M Sulpizi. Absolute acidity of clay edge sites from ab-initio simulations. *Geochim. Cosmochim. Acta*, 94:1–11, 2012.

[26] MD Hanwell, DE Curtis, DC Lonie, T Vandermeersch, E Zurek, and GR Hutchison. Avogadro: An advanced semantic chemical editor, visualization, and analysis platform. *J. Cheminf.*, 4:17, 2012.

[27] MD Barratt. Quantitative structure-activity relationships (QSARs) for skin corrosivity of organic acids, bases and phenols: principal components and neural network analysis of extended datasets. *Toxicol. In Vitro*, 10(1):85–94, 1996.

[28] RT Cygan, J-J Liang, and AG Kalinichev. Molecular models of hydroxide, oxyhydroxide, and clay phases and the development of a general force field. *J. Phys. Chem. B*, 108(4):1255–1266, 2004.

[29] K Vanommeslaeghe, E Hatcher, C Acharya, S Kundu, S Zhong, J Shim, E Darian, O Guvench, P Lopes, I Vorobyov, and AD Mackerell. CHARMM general force field: A force field for drug-like molecules compatible with the CHARMM all-atom additive biological force fields. *J. Comput. Chem.*, 31(4):671–690, March 2010.

[30] P Bjelkmar, P Larsson, MA Cuendet, B Hess, and R Lindahl. Implementation of the CHARMM force field in GROMACS: analysis of protein stability effects from correction maps, virtual interaction sites, and water models. *J. Chem. Theory Comput.*, 6(2):459–466, January 2010.

[31] LB Wright and TR Walsh. First-principles molecular dynamics simulations of NH_4^+ and CH_3COO^- adsorption at the aqueous quartz interface. *J. Chem. Phys.*, 137(22):224702, 2012.

[32] B Hess, C Kutzner, D van der Spoel, and E Lindahl. GROMACS 4: Algorithms for highly efficient, load-balanced, and scalable molecular simulation. *J. Chem. Theory Comput.*, 4(3):435–447, February 2008.

[33] F Franks. *Water : a matrix of life*. Royal Society of Chemistry, London, 2nd

ed. edition, 2000.

[34] W Humphrey, A Dalke, and K Schulten. VMD: Visual molecular dynamics. *J. Mol. Graphics*, 14(1):33–38, February 1996.

[35] IC Bourg and G Sposito. Molecular dynamics simulations of the electrical double layer on smectite surfaces contacting concentrated mixed electrolyte (NaCl-$CaCl_2$) solutions. *J. Colloid Interface Sci.*, 360(2):701–715, 2011.

[36] C Tournassat, Y Chapron, P Leroy, M Bizi, and F Boulahya. Comparison of molecular dynamics simulations with triple layer and modified Gouy-Chapman models in a 0.1 m NaCl-montmorillonite system. *J. Colloid Interface Sci.*, 339(2):533–541, 2009.

[37] A Khelifa, P Stoffyn-Egli, PS Hill, and K Lee. Effects of salinity and clay type on oil-mineral aggregation. *Mar. Environ. Res.*, 59(3):235–254, 2005.

Chapter 4

The Hofmeister Series for Montmorillonite

The aim of this chapter is to quantify the strength of adsorption of charge-balancing cations to the mineral surface montmorillonite, previously introduced in Chapter 3. This is achieved by calculating the free-energy of adsorption of the ion to the surface using the well-tempered metadynamics algorithm. Primarily, the aim is to discern whether divalent or monovalent ions will be preferentially adsorbed to the mineral surface, and therefore whether the low-salinity effect can be explained by cation exchange (whereby it is energetically favourable for a monovalent sodium ion to replace a divalent calcium ion that is initially charge balancing the clay).

This chapter was invited for publication and has previously published in its presented form in the *Clay and Clay Minerals* journal:
Thomas Underwood, Valentina Erastova & H. Chris Greenwell.
Ion Adsorption at Clay Mineral Surfaces:
The Hofmeister Series for Hydrated Smectite Minerals.
Clays & Clay Min., 2016, 64 (4), pages: 472-487, DOI:10.1346/CCMN.2016.0640310
Thomas Underwood was responsible for running all simulations and writing the published article. Valentina Erastova and H. Chris Greenwell helped proofread the final article.

Abstract

Many important properties of clay minerals are defined by the species of charge-balancing cation. Phenomena such as clay swelling and cation exchange depend upon the cation species present and it is therefore important to understand how the cations bind with the mineral surface at a fundamental level. In the present study, the binding affinities of several different charge-balancing cations with the basal surface of the smectite clay montmorillonite have been calculated using molecular dynamics in conjunction with the well-tempered metadynamics algorithm. The results follow a Hofmeister series of preferred ion adsorption to the smectite basal surfaces of the form:

$$K^+ > Na^+ > Ca^{2+} > Cs^+ > Ba^{2+}$$

The results also reveal the energetically favourable position of the ions above the clay basal surfaces. Key features of the free energy profiles are illustrated by Boltzmann population inversions and analyses of the water structures surrounding the ion and clay surface. The results show that weakly hydrated cations (K^+ and Cs^+) preferentially form inner-sphere surface complexes (ISSC) above the ditrigonal siloxane cavities of the clay. The strongly hydrated cations (Na^+, Ca^{2+} and Ba^{2+}) preferentially form outer-sphere surface complexes. The results provide insight into the adsorption mechanisms of several ionic species upon smectite clay minerals, and are relevant to many phenomena thought to be affected by cation-exchange, such as nuclear waste disposal, herbicide/pesticide-soil interactions and enhanced oil recovery.

4.1 Introduction

Clays are naturally occurring layered phyllosilicate minerals which are known to play an important role in many geochemical processes, whether within marine systems, terrestrial soils or within the subsurface in aquifers and oil reservoirs[1]. Owing to their high surface area, permanent negative charge and cation exchange properties, smectite clay minerals have found an increasing multitude of practical applications and have been extensively studied using analytical laboratory based techniques. In recent years, computational techniques, such as molecular dynamics (MD) and ab-initio calculations (including density functional theory - DFT), have become increasingly beneficial in helping improve our understanding of clay mineral properties at the atomistic level[2,3].

Three types of clay mineral surfaces are apparent: (i) the external basal surfaces, (ii) the external clay edges; (iii) the interlayer basal surfaces. The adsorption and exchange of cations at the different clay minerals surfaces can comprehensively alter the physical and chemical properties of the clay mineral. Interlayer bound potassium, for example, acts as a swelling inhibitor, preventing hydration and expansion of the interlayer region, whilst sodium promotes swelling when present in smectite-like clay minerals[4]. Furthermore, owing to their use as a barrier material in underground nuclear waste repositories it is becoming increasingly important to understand how radioactive cations, such as barium and caesium, adsorb to clay mineral surfaces, with potentially significant ramifications for nuclear waste repository design and operation[5]. Since the behaviour of clay minerals depend upon the species of charge-balancing cation, it is important to understand how the cation binds with the mineral surface, and how the cations affinity to the surface differs from ion to ion; however, studying the behaviour of cations at clay mineral surfaces and within interlayers is particularly challenging. Nuclear magnetic resonance (NMR) studies have been undertaken on non-paramagnetic synthetic clays offering insight on ion dynamics and distribution[6], while the use of quasi-elastic neutron scattering (QENS) on well-ordered vermiculite clay gels, as well as smectites, has allowed the study of cation/water structure in interlayers[7,8]. Additional insight into swelling energetics and structure has been obtained from computer simulation of

hydrated clay minerals[4,9,10].

A key property of many clay minerals is cation-exchange, where a more labile cation is substituted by a less labile one to modify the clay mineral activity. The traditional view of alkaline metal ion selectivity for cation-exchange follows a Hofmeister-like series[11]:

$$K^+ \approx Cs^+ > Na^+ > Ba^{2+} \approx Ca^{2+}$$

The reasoning for this sequence have been postulated through (at least) two arguments:

1. The ratio of hydrated cation size to interlayer spacing, whether the hydrated ion can fit within the steric cavities of the interlayer spacing[12,13];

2. The cation's ability to partially dehydrate at the mineral surface and thus form strong inner-sphere surface complexes[14].

Whilst many historical studies of the Hofmeister series have examined the hydration properties of the ions, in recent years it has become increasingly apparent that ion-macromolecule interactions also play a dominant role[15]. Previous computational work has been able to elucidate some of the properties of cation-exchange clay systems. It has previously been shown that whilst the binding energy between potassium and montmorillonite is greater than that between caesium and montmorillonite, the caesium-montmorillonite system is overall more stable due to the decreased enthalpy of hydration of the potassium over the caesium in the solvent phase[16]. The result shows it is important to consider not only the effect of the ion interacting with the mineral surface, but also with the bulk solvent phase. Previously, this has been achieved using an explicit solvent bath or through the use of thermodynamic cycles[17,18].

In this present study, classical molecular dynamic simulations have been used in conjunction with well-tempered metadynamics to determine the free energy of adsorption of, as well as the competition between, cations at the hydrated basal surfaces of the smectite clay mineral montmorillonite. The following simulations are particularly pertinent for understanding of the phenomenon of multicomponent

cation-exchange during low salinity enhanced oil recover, whereby organic matter, bridged to the surface through divalent cations, becomes desorbed from the basal surface of a clay mineral[19].

4.2 Methods

4.2.1 Model Setup

The clay unit cell used in this study was a Wyoming-like montmorillonite with atomic coordinates taken from the American Mineralogist Crystal Structure Database and with stoichiometry[20,21]:

$$M^{+}\ [Al_3Mg_1][Si_8O_{20}](OH)_4.nH_2O$$

In this model the octahedral sheets of the clay contained one Mg atom for every three Al atoms, whilst both tetrahedral sheets contained no isomorphic substitutions. The resulting unit cell possessed a single net negative charge, corresponding to a surface charge density of approximately 0.35 C m^{-2}. Periodically replicated super-cells were generated containing one layer of montmorillonite, composed of 18 unit cells (6×3×1), with dimensions of approximately 30×30×100 Å, and a pore-spacing of approximately 90 Å (Figure 4.1).

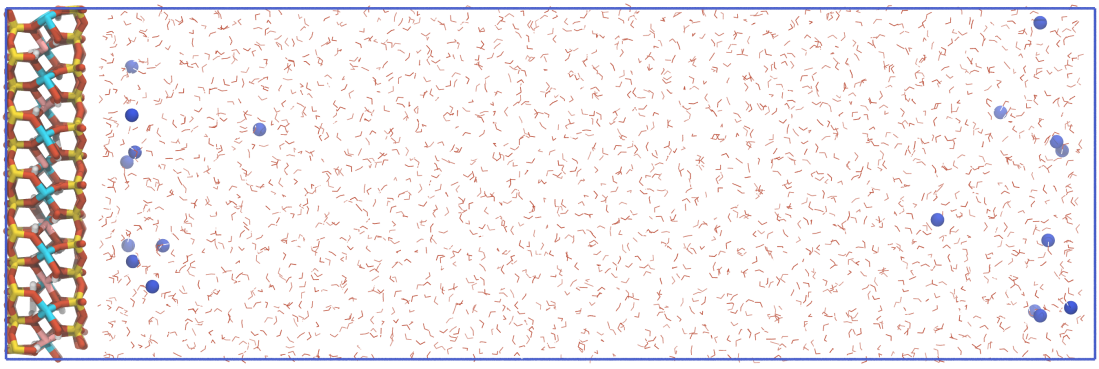

Figure 4.1: An example supercell used in the simulations. This example is of sodium cations (dark blue) interacting with montmorillonite. The colour scheme of the clay is as follows: Silicons are yellow; oxygens are red; aluminums are blue; magnesiums are pink and hydrogens are white. Also presented in stick form are the water molecules within the nano-pore spacing.

Montmorillonite structures initially occupied the region $0 < z < 7$ Å in all the following simulations, and the clay position varied little over all timescales modelled. The simulation super-cells were subsequently hydrated (with approximately 2500 water molecules) and the requisite number of cations added to the system to charge balance the montmorillonite surface. In total, five independent systems were set up differing according to the type of charge-balancing cation. The cations considered in this study were: sodium (Na^+), potassium (K^+), caesium (Cs^+), calcium (Ca^{2+}) and barium (Ba^{2+}).

The clay mineral has been modelled using the ClayFF force field, which is specifically parameterised to model layered minerals[22]. The ClayFF force field is designed such that the entire interactions within, and structure of, the clay is described wholly by the non-bonded Lennard-Jones and Coulomb potentials (hydroxyl groups are bonded as an exception). The standard SPC water model has been used to parameterise the solvent[23]. Ion parameters are taken from a variety of sources and are consistent with the ClayFF and SPC force fields[24,25,26,27,22].

4.2.2 Equilibration Details

All simulations have been initialized with an energy minimization run to reduce any excessive force on any one atom. This was accomplished using a steepest descents algorithm, with convergence achieved once the maximum force on any one atom was less than 10 kJ mol^{-1} $Å^{-1}$. Subsequently, equilibration simulations were run for a 10 ns period in the constant number of particles, pressure and temperature (NPT) ensemble at 300 K and 1 bar using a velocity-rescale Berendsen thermostat, temperature coupling constant set to 0.1 ps, and a semi-isotropic Berendsen barostat (in which the pressure fluctuations x and y are coupled, but the pressure fluctuations in z are independent of those in xy), with pressure-coupling constant 1 ps. The Berensden thermostat and barostat offered swift equilibration of the system, and convergence was adjudged to have been attained once both the d-spacing (the separation between the clay layers through the periodic boundaries) and potential energy had converged.

4.2.3 Metadynamic Details

Subsequent to equilibration, the super-cell was translated along the z-axis such that the apical oxygen atoms of the silicate sheet of the lowest clay basal surface lay upon the z = 0 Å plane. Before any free energy calculations were carried out, the clay model was fixed in place as a rigid structure. Subsequently, a single cation was chosen at random to be the test ion, upon which the free energy calculations have been performed. All other ions in the system were free to move according to the force fields used in the simulations.

The well-tempered metadynamics algorithm was used to explore the free energy curve of the clay-ion-water system as a function of the clay-ion separation (i.e. the reaction coordinate). During the metadynamics simulation the forces calculated with conventional molecular dynamics are modulated by adding Gaussian functions to the Hamiltonian at points along the reaction coordinate[28]. Here, twenty-five separate well-tempered metadynamic simulations were run, five for each cation type. It is important to run multiple ensemble simulations when calculating equilibrium thermodynamic properties, such as binding energies, since any one simulation is unlikely to sufficiently sample all of the phase-space required to satisfy the ergodic hypothesis[29]. Five separate ensemble simulations were deemed sufficient to reduce the total uncertainty in the free energy profiles generated using the metadynamic algorithm in this work. Each metadynamic simulation was run for a duration of 200 ns at 300 K in the constant number of particles, volume and temperature (NVT) ensemble. Gaussian functions with an initial height of 1.20 kJ mol^{-1}, a width of 0.10 Å, and a bias factor of 10 were applied to the Hamiltonian every 0.5 ps. Convergence of the well-tempered metadynamics algorithm was ensured by observing that the Gaussian height tended to zero throughout all well-tempered metadynamic simulations. Checks were also made to ensure that the test ion sampled all of the available planar xy-space, in conjunction with clay-ion separation space.

Due to the translational symmetry of the clay mineral, additional bias potentials were added to the test ion. This constrained the ion within a single unit cell of the montmorillonite surface. Any additional sampling would simply increase computational time, yet yield no additional information. This constraint was achieved using

a spring-like bias of the form:

$$V_{wall}(x) = k(x - x_{min})^4 \in x > x_{max} \tag{4.2.1}$$

where k is the elastic spring constant of the wall, set to 500 kJ mol^{-1}, and x_{max} is the lower limit of the wall. Similar boundaries were setup to constrain the lower bounds of the test ion in the x-direction, to constrain the ion in the y-direction, as well as to keep the test ion within 10 Å of the mineral surface.

4.2.4 Simulation Details

All MD simulations were performed using GROMACS version 4.6.7[30] with the Particle-Mesh-Ewald summation method for determining the electrostatic contribution, with a real-space electrostatic cut-off of 12 Å, a reciprocal space precision of 99.999%, in addition to a van der Waals cut-off distance of 1.2 Å. The well-tempered metadynamic algorithm has been implemented using PLUMED 2.1.2[31,32], which works in conjunction with GROMACS, whilst all images of the simulated structures have been produced using VMD 1.9.2[33].

4.2.5 Analysis Details

All free energy analyses have been carried out using the internal tools for GROMACS 4.6.7 and PLUMED 2.1.2[31,32]. The Python module MDAnalysis 0.13[34] and Matplotlib 1.5.1[35] were used to further analyse simulation trajectories and generate figures of water densities and radial distribution functions (RDFs). The plotted free energy profiles present the average free energy at each point along the reaction coordinate as a bold line and the relative error (plus-minus) is presented in the shaded area. The values of individual binding energies are given with the corresponding standard error as plus-minus. All ion density profiles (dotted lines in the free energy profiles) have been calculated using the last 5 ns of the 10 ns equilibration period, i.e. from an unbiased simulation.

4.3 Results

It is initially worth highlighting the general shape of the free energy curves (Figure 4.2). After a short range repulsion between ion and mineral surface, and beyond (often several) minima, the free energy profiles plateau. In the long clay-ion separation limit, this plateau can be decomposed as a combination of clay (F^{clay}_{self}), ion (F^{ion}_{self}) and solvent (F^{water}_{self}) self-energies; clay-water ($F^{clay}_{hydration}$) and ion-water ($F^{ion}_{hydration}$) hydration energies; as well as long-range interaction terms ($F^{clay-ion}_{electrostatic}$). Namely the binding free energy (F), can be expressed as:

$$\lim_{z\to\infty} F(z) = F^{clay}_{self} + F^{ion}_{self} + F^{water}_{self} + F^{clay}_{hydration} + F^{ion}_{hydration} + F^{clay-ion}_{electrostatic} \quad (4.3.2)$$

This means that the overall binding energy ($\Delta F_{binding}$) of the ion to the surface can be calculated as:

$$\Delta F_{binding} = F(z_{min}) - \lim_{z\to\infty} F(z) \quad (4.3.3)$$

where z_{min} is the location of the global energy minimum with respect to clay-ion separation. Note that at sufficiently large z, the individual self-energies of the unbound system and hydration terms in equation 4.3.2 are independent of z, since the hydration shells of the ion and clay no longer overlap. Thus, at large z, when comparing binding energies between different ion species, one needs only to consider the difference between the long-range clay-ion electrostatic term. Since all simulations have been run at the same temperature (300 K) and ionic strengths the long-range electrostatic term, which can be described through Poisson-Boltzmann theory, is postulated to be equal for all different ions at any arbitrary z. It is therefore justified to normalise the free energy profiles subject to the boundary condition that for large clay-ion separation:

$$\lim_{z\to\infty} F(z) = 0 \quad (4.3.4)$$

Following this argument, a direct comparison of the binding free energies differences between dissimilar species of monovalent and divalent cations have been calculated (Table 4.1).

Table 4.1: Binding energies and stable clay-ion separations of cations to the basal surface of montmorillonite. The global energy minimum for each ion is bolded. Clay-ion separation values are given in Angstrom and Binding Energies are in kJ mol^{-1}. The Primary ISSC is defined as the inner-sphere complex located above the hexagonal siloxane cavity of the clay, whilst the secondary ISSC is the complex above a basal surface oxygen.

	VdW	Primary ISSC		Secondary ISSC		OSSC		SHSSC	
Ion	Radii	Separation	Energy	Separation	Energy	Separation	Energy	Separation	Energy
Na^+	2.35		-	2.3	-2.76 (0.43)	**3.8**	**-9.00 (0.35)**	6.0	-3.68 (0.37)
K^+	3.33	**1.3**	**-10.56 (1.29)**	2.6	-2.46 (0.70)	4.7	-3.83 (0.37)		-
Cs^+	3.87	**2.0**	**-8.34 (0.40)**	2.7	-7.51 (0.38)	4.6	-4.64 (0.26)		-
Ca^{2+}	2.87		-		-	**3.8**	**-16.76 (0.41)**		-
Ba^{2+}	3.81	1.9	+18.26 (3.55)	2.6	-0.54 (1.82)	**4.2**	**-16.66 (1.46)**	5.8	-8.38 (1.25)

4.3.1 Free Energy Profiles

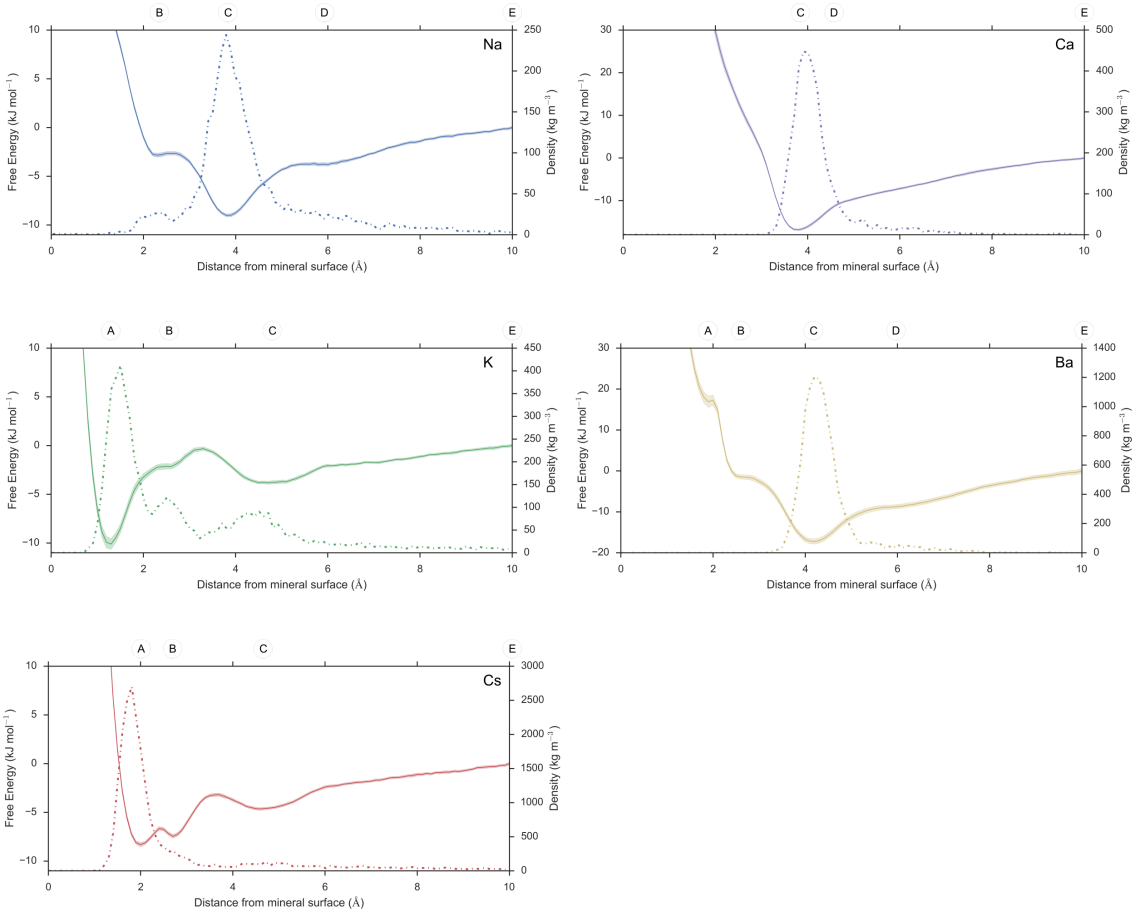

Figure 4.2: The free energy profile of all cations as a function of clay-ion separation. The shaded region indicates the standard error in the metadynamic calculation at each point along the free-energy diagram. Also presented is the ion density as a function of distance from clay basal surface (dotted line). The points (A), (B), (C) and (D) are noted as points of interest within the free-energy diagram.

The free energy profile for all the systems considered (Figure 4.2), highlight several points of interest along the reaction-coordinate. These are highlighted by the points (A), (B), (C), (D) and (E) across the top of the figure. To be consistent, the points correspond to the coordination states of the ion. In brief, (A) corresponds to a primary inner-sphere surface complex (ISSC); (B) corresponds to a secondary ISSC; (C) corresponds to outer-sphere surface complex (OSSC) and (D) corresponds to a secondary hydration shell surface complex (SHSSC). These terms shall be explained in the following sections. The point (E) corresponds to a clay-ion separation of 10 Å, the maximal distance of the reaction-coordinate in the metadynamic simulations.

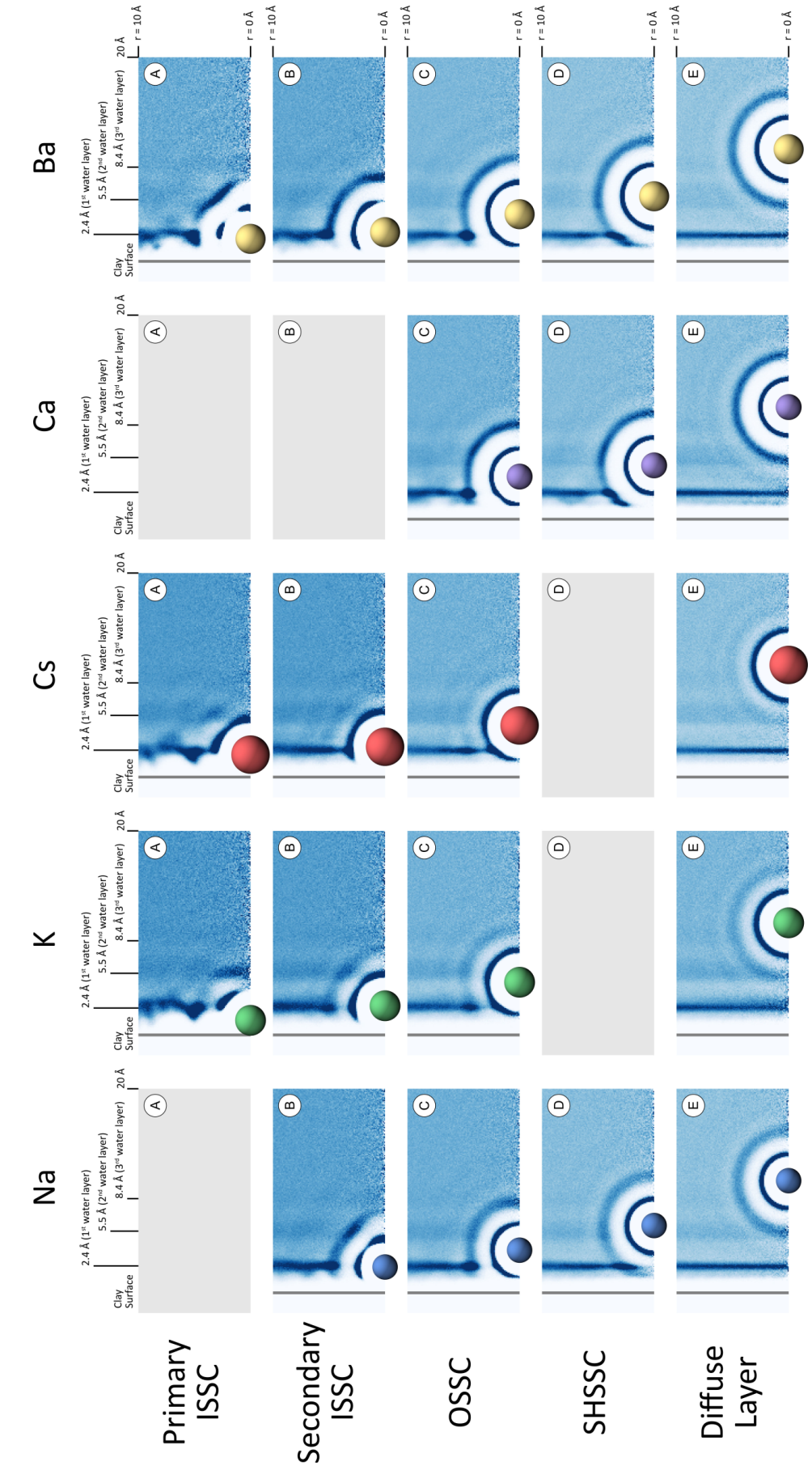

Figure 4.3: The water oxygen density surrounding the clay and ion at point of interest along the free-energy curve.

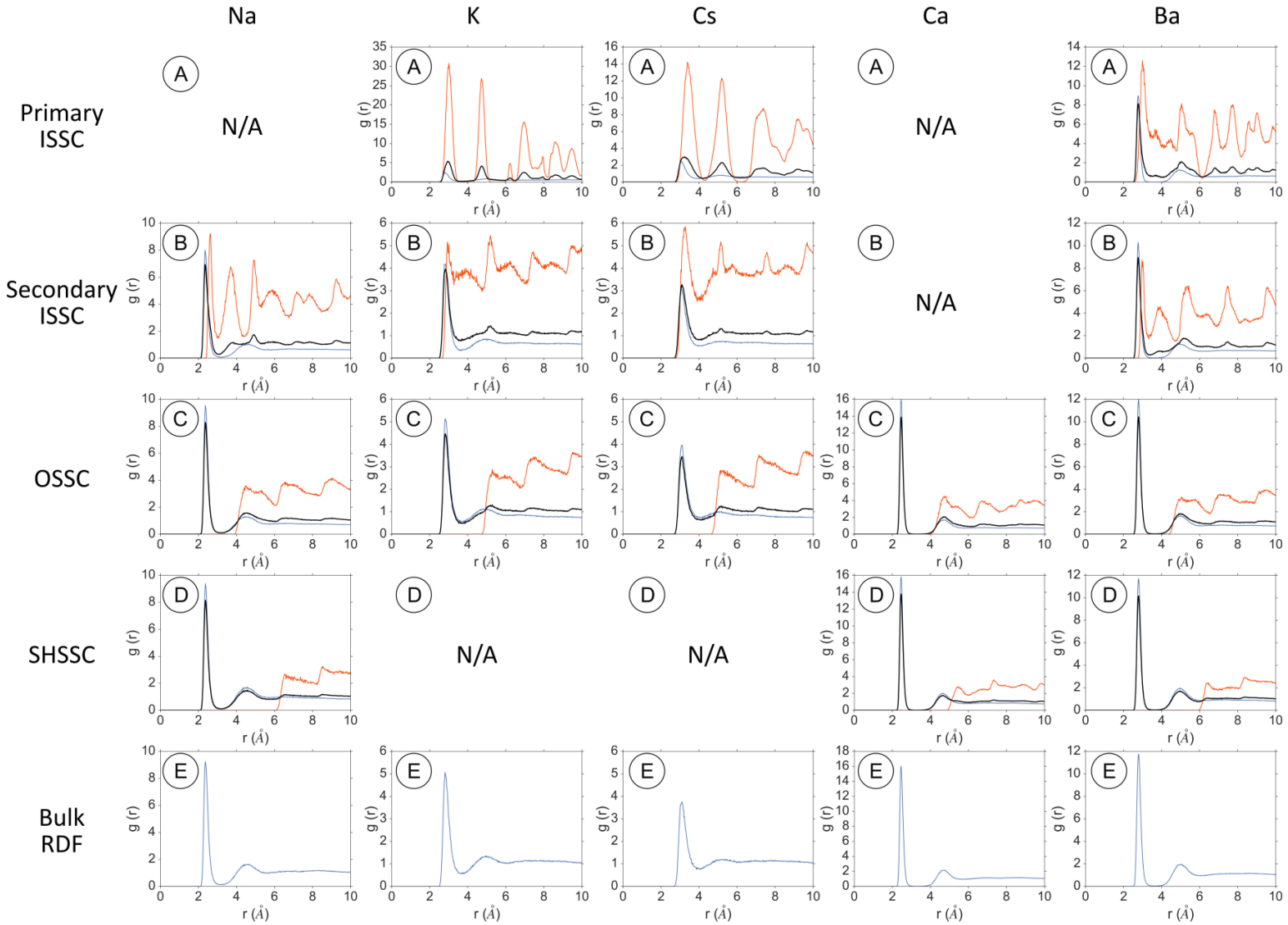

Figure 4.4: The RDF's between each cation and oxygen atoms at each point of interest along the free-energy diagram. Blue is the RDF between cation and water oxygen, orange is between cation and clay oxygen, and black is between cation and all oxygen atoms.

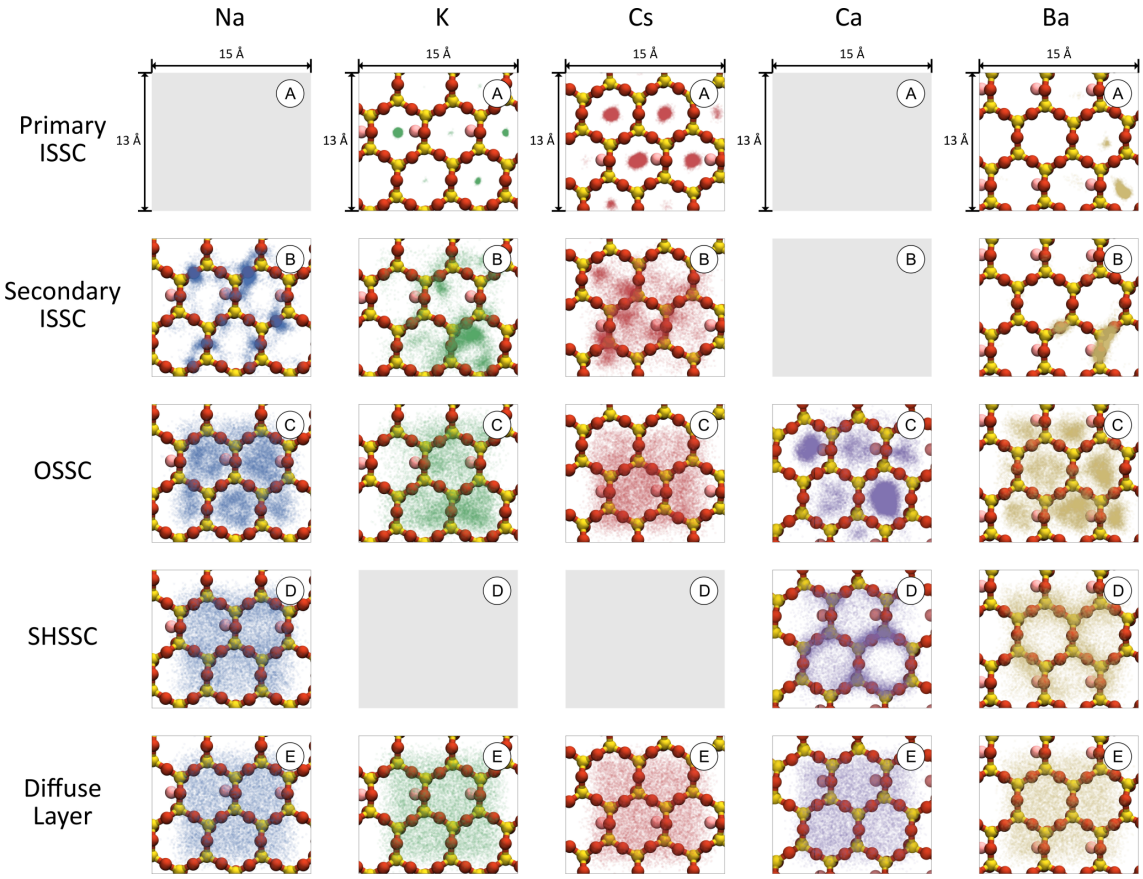

Figure 4.5: The xy-planar density of the examined cations at each point of interest along the free energy curve.

4.3.2 Na-Montmorillonite

The free energy profile for the sodium-montmorillonite system (Figure 4.2 - Na) shows that at close separation distances (less than 2 Å) the montmorillonite-ion interaction is entirely repulsive. This represents the close-range repulsion between clay and ion due to electron wave-function overlap. Beyond this, the ion experiences three individual clay-ion separations of (meta-)stable equilibria. The global minimum, and thus the most energetically favorable montmorillonite-sodium separation is at 3.8 Å, with a binding energy of -9.00±0.35 kJ mol^{-1} (Figure 4.2 - Na(C)). A secondary, metastable minimum, is located nearer to the clay surface, at a clay-sodium distance of 2.3 Å, with a binding energy of -2.76±0.43 kJ mol^{-1} (Figure 4.2 - Na(B)). A third, metastable minimum, is located further from the clay surface, at a separation value of 6 Å and with a binding energy of -3.68±0.37 kJ mol^{-1} (Figure 4.2 - Na(D)).

The global minimum corresponds to a system where the sodium cation is fully hydrated, and the ions solvation shell is associated to the mineral surface via hydrogen bonding. This can be observed in the overlapping water structures of the first hydration shell of the ion with the first hydration layer of the clay (Figure 4.3 - Na(C)). This phenomenon is well known, and referred to as an outer-sphere solvation complex (OSSC). In contrast, the metastable minimum nearer the clay surface corresponds to an inner-sphere solvation complex (ISSC), whereby the cation is only partially hydrated, and is directly adsorbed to the mineral surface via electrostatic interactions (Figure 4.3 - Na(B)). The metastable minimum farthest away from the clay surface corresponds to where the second hydration shell of the sodium ion overlaps with the first hydration layer of the clay (Figure 4.3 - Na(D)). This situation is observed for several cations and shall be hereafter denoted as a secondary hydration shell surface complex (SHSSC). Also presented is the water structure surrounding the ion and clay at a clay-ion separation of 10 Å (Figure 4.3 - Na(E)). It can be noted that at such distance, the hydration layers of the clay and ion no longer overlap.

The radial distribution functions (RDFs) between sodium ion and water/basal clay oxygen further reiterate that the minima correspond to ISSC and OSSC. It can be seen that for the ISSC (Figure 4.4 - Na(B)), the basal clay oxygen atoms are shared with water oxygen atoms in the first coordination shell of the ion. In contrast,

for the OSSC (Figure 4.4 - Na(C)), the basal clay oxygen atoms are contained within the second coordination shell of the ion. For the SHSSC (Figure 4.4 - Na(D)), the clay basal oxygen atoms contribute to the third coordination shell of the sodium ion. Also presented is the RDF for the system at a clay-ion separation of 10 Å (Figure 4.4 - Na(E)). In this case the hydration layers of the ion and clay no longer interact and the resulting RDF is that of the sodium ion with bulk water.

The planar density of the ion above the mineral surface shows that, for the ISSC, the sodium ion is extremely localised above a single basal clay oxygen (Figure 4.5 - Na(B)). In contrast, the OSSC is less localised above the clay basal surface (Figure 4.5 - Na(C)), with a preference to be located above one of the hexagonal siloxane cavities of the mineral surface. For the SHSSC and beyond, the ion's position above the basal clay surface is no longer localised, and is homogeneously dispersed across the unit cell (Figure 4.5 - Na(C) and Na(D)).

4.3.3 K-Montmorillonite

The free energy profile for potassium (Figure 4.2 - K) presents several features similar to that of sodium. Again, it can be seen that beyond the typical close distance repulsion, three separate (meta)stable minima are observed. The global minimum, in this instance, is located near the surface of the mineral, at a montmorillonite-potassium separation of 1.3 Å, with a binding energy of -10.56±1.29 kJ mol^{-1} (Figure 4.2 - K(A)). The next most stable minimum is located at 4.7 Å, with a binding energy of -3.83±0.37 kJ mol^{-1} (Figure 4.2 - K(C)). There is also a metastable minimum between these two points at a clay-potassium separation of 2.6 Å with a binding energy of -2.46±0.70 kJ mol^{-1} (Figure 4.2 - Na(B)).

Focusing on the global energy minimum (point A), both the water structure (Figure 4.3 - K(A)) and the RDF (Figure 4.4 - K(A)) reveal that the ion forms an ISSC in its most energetically favourable state. In particular, the RDF shows that the first coordination shell of the potassium ion is largely composed of clay oxygen atoms. The xy-planar density of the potassium ion in its ISSC state (Figure 4.5 - K(A)) shows that the ion is extremely localised above the hexagonal cavities of the clay surface. This behaviour is in contrast to the ISSC observed for sodium.

The terms primary ISSC and secondary ISSC are here introduced to denote the difference between these two different forms of ISSC. A primary ISSC denotes an ion that sits above one of the hexagonal cavities of the clay surface, whilst the term secondary ISSC denotes that the ion sits above one of the basal oxygen atoms of the clay.

The least energetically favourable metastable minimum is located at point (B) in the free energy profile (Figure 4.2 - K(B)). The water structure (Figure 4.3 - K(B)) and RDF (Figure 4.4 - K(B)) indicate that this minimum is also an ISSC. The xy-planar density of the ion above the surface (Figure 4.5 - K(B)) indicates that this is a secondary ISSC. The results show that potassium can stably form both primary, and secondary, inner-sphere surface complexes.

The most energetically favourable metastable minimum is located at point (C) in the free energy profile (Figure 2 K(C)). Here the potassium ion forms an OSSC, as the first hydration shell of the ion overlaps with the first hydration layer of the clay (Figure 4.3 - K(C)). The RDF (Figure 4.4 - K(C)) also highlights that the basal clay oxygen atoms coordinate within the second hydration shell of the potassium cation. Like the sodium ion, the OSSC of potassium is loosely localised above the hexagonal siloxane cavities of the basal surface, as evidenced by the xy-planar density distribution (Figure 4.5 - K(C)). Beyond this point, the potassium ion is not observed to form a SHSSC and moves freely across the xy-plane (Figure 4.5 - K(E)).

4.3.4 Cs-Montmorillonite

The free energy diagram for the caesium-montmorillonite system (Figure 4.2 - Cs) is very similar to that of potassium. Again, three separate minima are observed. The global energy minimum is at a montmorillonite-caesium separation of 2.0 Å with a binding energy of -8.34±0.40 kJ mol^{-1} (Figure 4.2 - Cs(A)). The secondary minimum is at a clay-ion distance of 2.7 Å with a binding energy of -7.51±0.38 kJ mol^{-1} (Figure 4.2 - Cs(B)) and the tertiary minimum is located at a clay-ion distance of 4.6 Å with a binding energy of -4.64±0.26 kJ mol^{-1} (Figure 4.2 - Cs(C)).

The global minimum of caesium forms an ISSC as can be observed through the water structure (Figure 4.3 - Cs(A)) and caesium-oxygen RDF results (Figure 4.4 - Cs(A)). Like potassium, the global energy minimum of caesium is localised above the hexagonal siloxane cavities of the clay surface (Figure 4.5 - Cs(A)) and is therefore observed to form primary ISSCs.

The second and third minima of caesium correspond to a secondary ISSC and OSSC respectively. This is evidenced by the overlapping of the water structures surrounding the ion and clay (Figure 4.3 - Cs (B) and Cs(C)), the overlapping oxygen atoms in the RDFs (Figure 4.4 - Cs(B) and Cs(C)), as well as the ion localisations above the xy-plane (Figure 4.5 - Cs(B) and Cs(C)). Much like potassium therefore, caesium readily forms both secondary ISSCs and OSSCs. Unlike potassium however, the secondary ISSC is more energetically stable than the OSSC.

4.3.5 Ca-Montmorillonite

In contrast with the results for other ions presented so far, the free energy profile for calcium shows only one stable minimum (Figure 4.2 - Ca). This minimum is at a clay-ion distance of 3.8 Å and has a binding energy of -16.76±0.41 kJ mol^{-1} (Figure 4.2 - Ca(C)). The water structures surrounding the calcium and clay in conjunction with the RDFs between ion and oxygen atoms show that this global energy minimum is an OSSC. The water structure (Figure 4.3 - Ca(C)) shows that the first hydration shell of the calcium overlaps with the first hydration layer of the clay basal surface. Furthermore, the RDF (Figure 4.4 - Ca(C)) indicates that the basal oxygen atoms of the clay contribute to the second hydration shell of the calcium. The planar density of the calcium ion in its global OSSC state (Figure 4.5 - Ca(C)) presents that the calcium ion sits above the hexagonal siloxane cavities of the basal surface of the clay, in agreement with the trends observed for the monovalent ions. Nonetheless, the OSSC for the calcium ion is more localised compared to the OSSCs for monovalent ions.

Point (D) in the calcium system refers to the sudden change in gradient of the free energy curve. This change in gradient is due to the completion of the second hydration shell of the calcium ion as is shown in the water density profile (Figure 4.3 - Ca(D)). At this point the clay no longer contributes to the hydration shells of the calcium ion, as is confirmed by comparing the RDF between calcium and basal clay oxygen atoms with the RDF between calcium and all oxygen atoms (Figure 4.4 - Ca(D)). The planar density profile for point (D) (Figure 4.5 - Ca(D)) shows that calcium ion sits above the either the basal oxygen of silicon atoms of the clay. Therefore, the aforementioned completion of the second coordination shell of the calcium ion is achieved with water oxygen atoms.

4.3.6 Ba-Montmorillonite

The free energy profile of the montmorillonite-barium system (Figure 4.2 - Ba) presents several interesting features not observed in the free energy profile for calcium. The global energy minimum (point C) corresponds to a clay-ion separation of 4.2 Å with a binding energy of -16.66±1.46 kJ mol^{-1} (Figure 4.2 - Ba(C)). There is also a second, energetically expensive, metastable minima in the free energy curve (point A). This metastable minimum is located at a clay-ion separation value of 1.9 Å and has a binding energy of +18.26±3.55 kJ mol^{-1} (Figure 4.2 - Ba(A)), i.e. energy is required to place the ion into this metastable minimum. Two plateaus can also be seen in the free energy profile of barium. Point (B) is at a clay-ion separation of 2.6 Å and has a binding energy of -0.54±1.82 kJ mol^{-1} (Figure 4.2 - Ba(B)), whilst point (D) is at a clay-ion separation of 5.8 Å and has a binding energy of -8.38±1.25 kJ mol^{-1} (Figure 4.2 - Ba(D)).

The water density profiles and RDFs of the barium-montmorillonite system explain how the ion binds with the mineral surface. At points (A) and (B), the ion is directly coordinated by basal oxygen atoms, forming primary and secondary ISSCs respectively (Figures 4.3 and 4.4 - Ba(A) and Ba(B)). The water structure shows that the global energy minimum occurs when the barium ion is an OSSC (Figure 4.3 - Ba (C). In such an occurrence, the basal oxygen atoms of the clay contribute to the second hydration shell of the cation, as can be seen in the corresponding RDF (Figure 4.4 - Ba(C)). The plateau at point (D) of the free energy curve occurs when the second hydration layer of the barium ion begins to completely coordinate with water oxygen atoms (Figure 4.3 - Ba(D)).

Analysis of the planar density of barium above the xy-plane of the clay shows that the two ISSCs are extremely localised above a cavity of the clay siloxane (Figure 4.5 - Ba (A)) or directly above basal oxygen atoms (Figure 4.5 - Ba (B)) for the metastable minimum (point A) and plateau (point B) respectively. Similar to all other OSSCs, the OSSC of barium is localized above one of the hexagonal siloxane cavities of the clay (Figure 4.5 - Ba (C)), whilst at all clay-ion separations greater than this distance, the cation freely traverses across the xy-plane of the clay mineral (Figure 4.5 - Ba (D)).

4.4 Discussion

The results show that the charge-balancing cations of montmorillonite can form four different stable surface complexes: a primary ISSC located above the siloxane cavity of the basal clay surface; a secondary ISSC located above a basal oxygen atom; an OSSC loosely located above siloxane cavity; and a SHSSC, which is due to the overlap of the ions second hydration sphere with the clay minerals first hydration layer. No further surface complexes were observed in the simulations.

The formation of two separate ISSCs has been noted in the literature previously. In particular, it has been shown that weakly hydrated interlayer cations (K^+, Cs^+) form ISSCs above the siloxane cavity of the clay interlayer[36,37,38], whilst strongly hydrated cations (Na^+) form ISSCs on tetrahedral charge sites[4,39,38]. The results presented here supplement this previous work, and further suggest that the formation of ISSCs for strongly hydrating cation can occur in the absence of tetrahedral charge substitutions. Moreover, they implicate that the formation of different surface complexes is related to the hydration properties of the cation. The stable surface complexation of a cation is related to the hydrated radii of the atom, which is, in turn, inversely proportional to the charge/size ratio of the ion (see Table 4.2).

Table 4.2: The atomic radii and therefore charge to size ratio for each ion. The hydrated radii are calculated as the first minima in the RDF of each respective ion. The stable surface complex of each ion is linked to the size of the ions hydration radii and thus charge to size ratio.

Ion	Atomic Radii	Charge/Size Ratio	Hydrated Radii	Stable Complex
Na^+	1.90	0.53	3.23	OSSC
K^+	2.43	0.41	3.83	ISSC
Cs^+	2.98	0.34	3.87	ISSC
Ca^{2+}	1.94	1.03	3.13	OSSC
Ba^{2+}	2.53	0.79	3.49	OSSC

The weakly hydrated cations, K^+ and Cs^+, have very similar hydration radii (Table 4.2), and therefore exhibit similar behavior. In both cases, the primary ISSC is the most energetically favourable state of the ion, and the secondary ISSC and OSSC are metastable. The strongly hydrated monovalent cation, Na^+, forms secondary ISSCs, OSSCs and SHSSCs, and is energetically most stable in its OSSC. Similarly,

divalent cations form globally stable OSSCs, in concordance with the relevant literature ((Brown and Kevan, 1988)[40], (Papelis and Hayes, 1996)[41], (Chen and Hayes, 1999)[42], (Strawn and Sparks, 1999)[43], (Greathouse et al., 2000)[44]). Barium exhibits interesting behaviour; it is an ion that can form stable primary ISSCs and OSSCs, with plateaus in the free energy profile associated with the formation of a secondary ISSC and a SHSSC[45]. This is due to the larger atomic radius of barium compared to calcium, whereby the charge/size ratio of barium lies somewhere between that of calcium and sodium.

Overall, the results are well converged. The largest errors encountered are for the free energy profiles of potassium and barium. Since the free energy profile for barium contains several plateaus and minima, the metadynamic algorithm requires more simulation time to sample all clay-ion separation phase space compared to other ions. The potassium ion contains a large error due to the lack of convergence in the global energy minimum. This is due to the complex coordination of oxygen atoms to the potassium ion, and shall be elaborated upon further in the following sections.

4.4.1 Accuracy of Results

To further analyse the accuracy of the free energy profiles, a comparison is made between the equilibrium density profile of the unbiased equilibration simulation with the density profile derived from the free energy. The cation density surrounding the montmorillonite surface is derived from the free energy profile as:

$$n(d) \propto \exp\left(\frac{-\Delta F(d)}{kT}\right) \tag{4.4.5}$$

where $n(d)$ is the density profile of the ion surrounding the clay, $\Delta F(d)$ is the corresponding free energy at the point d and kT is the thermal energy at temperature T.

The analysis shows that the free energy profiles capture the overall trends observed in the unbiased density profile (Figure 4.6). In particular, the strongly hydrating cations (Na^+, Ca^{2+} and Ba^{2+}) density profiles match extremely well. The

free energy profiles generated for Na^+, Ca^{2+} and Ba^{2+} capture the essential details of the equilibrium density profile and agrees with previous results of cationic distribution surrounding montmorillonite basal surfaces[46,47]. The ion densities calculated from the free energy profiles for the weakly hydrating cations (K^+ and Cs^+) vary considerably compared to the equilibrium density. In the case of potassium, the metadynamic density underestimates the the proportion of secondary ISSCs and OSSCs, suggesting that the free energy calculation overestimates the global binding energy of potassium to montmorillonite. In contrast, the metadynamic density overestimates the proportion of secondary ISSCs and OSSCs for caesium. This suggests that the free energy profile underestimates the global binding energy of caesium. Clearly, there is a phenomenon occurring for the weakly hydrated cations, causing their binding energies to be less accurate compared to their more strongly hydrated counterparts.

The chief difference between the unbiased and the metadynamic simulations is that the coordinates of the clay are kept constant within the metadynamic simulations. This may alter the overall accuracy of the free energy results by undermining the dynamic properties of the clay. This noted, however, the metadynamic simulations were simulated for two hundred times longer than the unbiased potential simulations. One would therefore expect the free energy profiles of the metadynamic simulation to be more converged in comparison to the overall unbiased density profiles.

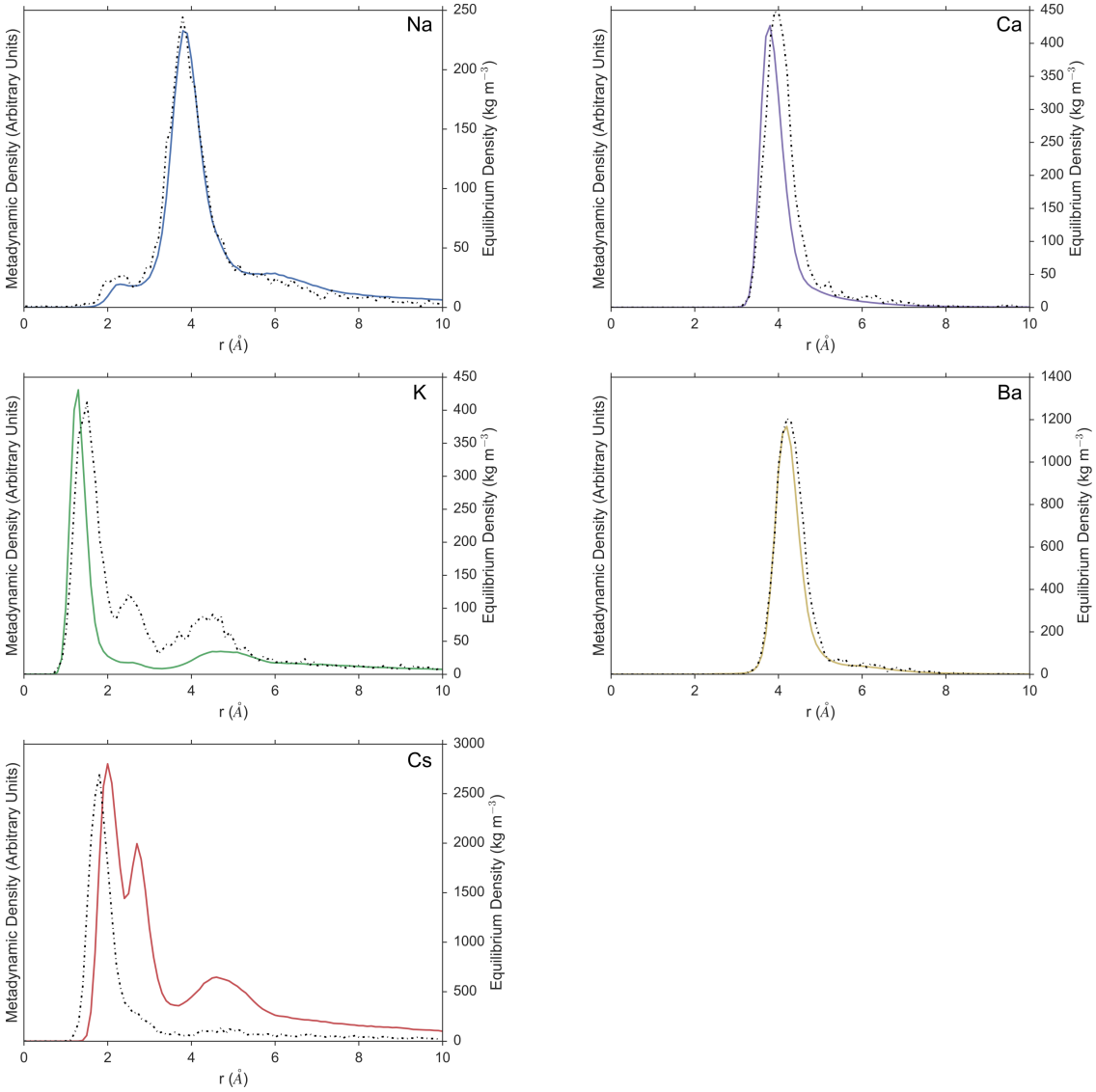

Figure 4.6: A comparison of ionic densities surrounding the clay surface. Bold coloured line is the density calculated from the free energy profile, and the dotted line is the density calculated from an unbiased simulation.

4.4.2 Coordination Analysis

The lower accuracy in the binding energies for potassium and caesium can be explained by examining the coordination number of the ion in its most energetically stable state. This is calculated by integrating under the first peak of the radial distribution function (RDF) for each ion (Table 4.3). Note that in bulk, the coordination of ions ranges between 6 to 8 oxygen atoms, systematically 1 to 2 counts over the expected literature values[48]. In the SHSSC and OSSC states, the ion remains completely coordinated with water oxygen atoms. In the secondary ISSC the strongly hydrated sodium ion is coordinated by five water oxygen atoms and one clay oxygen atom. This, along with the xy-planar density for sodium in its ISSC, proves that the strongly hydrated monovalent cation coordinates directly above a single basal clay oxygen atom. The coordination of the secondary ISSCs for the weakly hydrating cations, potassium and caesium, show that 2 to 3 clay oxygen atoms are contained within the ions first coordination shell. The secondary ISSCs for potassium and caesium complex with a triad of basal oxygen atoms, in keeping with previous literature[36].

Profoundly, for the primary ISSC of potassium and caesium, the ion is coordinated with six oxygen clay atoms, as well as four/six water oxygen atoms. This drastic change in the total coordination number of potassium and caesium is the reason that the binding energy calculations are less precise for these ions. It is believed that the structure of the basal siloxane surface is formed of ditrigonal cavities, rather than the hexagonal cavities observed in these simulations[49]. This suggests a limitation in the force field used within these calculations. The recently developed polarizable force field is parameterised to accurately reproduce the ditrigonal structure of a clay mineral surface, and may be a more suitable choice going onwards with further binding energy calculations[49]. Also, the Interface force field, which includes explicit bonding between surface atoms and dissimilar atom types for basal oxygen atoms, may be more suited to this task[50].

Table 4.3: The coordination number of each ion in each surface complexation state. Expected coordination numbers are taken from Varma etal[48].

Species	Expected CN	Observed CN	Clay CN	Water CN	Clay (%)	Water (%)
Primary ISSC						
Na^+	5	-	-	-	-	-
K^+	6	9.3	5.9	3.4	64	36
Cs^+	7	11.8	5.9	5.9	50	50
Ca^{2+}	5-7	-	-	-	-	-
Ba^{2+}	5-7	8.5	1.1	7.4	13	87
Secondary ISSC						
Na^+	5	5.9	1.1	4.8	19	81
K^+	6	7.6	1.9	5.7	25	75
Cs^+	7	9.4	2.7	6.7	29	71
Ca^{2+}	5-7	-	-	-	-	-
Ba^{2+}	5-7	8.5	1.1	7.4	13	87
OSSC						
Na^+	5	5.9	0	5.9	0	100
K^+	6	7.6	0	7.6	0	100
Cs^+	7	9.3	0	9.3	0	100
Ca^{2+}	5-7	8	0	8	0	100
Ba^{2+}	5-7	9	0	9	0	100
SHSSC						
Na^+	5	5.8	0	5.8	0	100
K^+	6	-	-	-	-	-
Cs^+	7	-	-	-	-	-
Ca^{2+}	5-7	8	0	8	0	100
Ba^{2+}	5-7	9	0	9	0	100
Bulk						
Na^+	5	5.9	0	5.9	0	100
K^+	6	7.8	0	7.8	0	100
Cs^+	7	8.2	0	8.2	0	100
Ca^{2+}	5-7	8	0	8	0	100
Ba^{2+}	5-7	9	0	9	0	100

4.4.3 Equilibrium Constants and the Hofmeister Series for Montmorillonite

To compare binding energies between divalent and monovalent cations at basal surfaces it is required to divide the divalent binding affinity by two (or double the monovalent value) since it takes two monovalent ions to replace a single divalent ion in identical clay systems. This is valid assuming that the chemical environments of the two monovalent ions do not overly interact with one another. Following this procedure, the results present a Hofmeister-like series for ion adsorption to smectite mineral surfaces of the form:

$$K^+ > Na^+ > Ca^{2+} > Cs^+ > Ba^{2+}$$

Furthermore, the binding energy difference between ion A and B ($\Delta\Delta G_{AB}$)can be tabulated by considering the difference in global binding energies between the respective atoms (Table 4.4). These values are related to the exchange equilibrium constant (K_A^B) as[51]:

$$\Delta\Delta G_{AB} = -RT \ln(K_A^B) \tag{4.4.6}$$

where K_A^B relates to the equilibrium reaction between clay, cation A and cation B[51]:

$$\text{A}-\text{Clay} + \text{B}^+ \rightleftharpoons \text{B}-\text{Clay} + \text{A}^+ \tag{4.4.7}$$

The calculated equilibrium constants generally agree with the literature values (Table 4.5). The $\Delta\Delta G_{AB}$ binding energy differences are of the order of the thermal energy at 300K (2.476kJ) or smaller in all instances. Overall, the values of K_A^B and $\Delta\Delta G_{AB}$ show that the basal surface of montmorillonite is weakly selective, in agreement with literature results[51].

Table 4.4: The binding energy difference ($\Delta\Delta G_{AB}$) between ion species.

$\Delta\Delta G_{AB}$	Na^+	K^+	Cs^+	Ca^{2+}	Ba^{2+}
Na^+		-1.56	0.66	0.62	0.67
K^+	1.56		2.22	2.18	2.23
Cs^+	-0.66	-2.22		-0.04	0.01
Ca^{2+}	-0.62	-2.18	0.04		0.05
Ba^{2+}	-0.67	-2.23	-0.01	-0.05	

Table 4.5: The exchange equilibrium constants (K_A^B) for each ion exchange reaction. Literature values of Bourg & Sposito and Benson are presented in bold[51,52].

K_A^B	Na^+	K^+	Cs^+	Ca^{2+}	Ba^{2+}
Na^+	-	1.87	0.77	0.78	0.76
K^+	0.54 **0.58**	-	0.41	0.42	0.41
Cs^+	1.30 **1.23**	2.44	-	1.02	1.00
Ca^{2+}	1.28 **1.21**	2.40 **1.04**	0.98 **0.26**	-	0.98
Ba^{2+}	1.31 **1.44**	2.45	1.00	1.02	-

4.5 Conclusions

In this study multiple ensembles of molecular dynamic simulations used in conjunction with well-tempered metadynamics, have been used to form the basis for deriving the adsorption energies and mechanisms of simple ions to hydrated mineral surfaces. The methodology is robust and can be transferred to a wide variety of applications to measure the affinity between mineral surfaces and a marked assortment of organic material. The results immediately suggest further ways to improve the accuracy of the calculation of binding energies to clay mineral surfaces. When calculating the binding energy of poorly hydrating molecules to clay surfaces, such as potassium and caesium, it is critically important to accurately portray the ditrigonal coordination of basal surface oxygens on the siloxane surface.

Detailed analysis of the water structure and planar xy density of cations in their energetically favourable states has revealed four separate surface-ion complexations. Both primary and secondary ISSCs are observed for the weakly and strongly hydrated cations respectively. A second hydration shell surface complex, whereby the second hydration shell of the cation overlaps with the first hydration layer of the mineral surface, is observed for sodium. Outer-shell surface complexes are observed to form for the strongly hydrated ions, sodium, barium and calcium. Using the metadynamic algorithm, the results have confirmed the idea of a Hofmeister series for smectite-like minerals. For basal surfaces, the series follows the form:

$$K^+ > Na^+ > Ca^{2+} > Cs^+ > Ba^{2+}$$

and this insight impacts upon a wide range of industrial applications of clay minerals.

Finally, the preference for monovalent ions to be adsorbed to the surface over the naturally occurring divalent ions is important for many industrial applications using the cation-exchange mechanism, whereby an inherently present divalent calcium ion is replaced with monovalent cation which can improve, for example, water-wettability, and thus increase oil extraction rates in enhanced oil recovery. Future work entails studying the adsorption of ions as a function of salt concentration, the energetics of intercalated ions as well as the calculating the energy barriers at clay edge sites. Furthermore, the role of tetrahedral substitutions may play a large role in the stability of such ionic systems.

Bibliography

[1] F Bergaya and G Lagaly. General introduction: clays, clay minerals, and clay science. *Developments in Clay Science*, 1:1–18, 2006.

[2] HC Greenwell, W Jones, PV Coveney, and S Stackhouse. On the application of computer simulation techniques to anionic and cationic clays: A materials chemistry perspective. *Journal of Materials Chemistry*, 16(8):708–723, 2006.

[3] JL Suter, RL Anderson, HC Greenwell, and PV Coveney. Recent advances in large-scale atomistic and coarse-grained molecular dynamics simulation of clay minerals. *Journal of Materials Chemistry*, 19(17):2482–2493, 2009.

[4] ES Boek, PV Coveney, and NT Skipper. Monte carlo molecular modeling studies of hydrated Li-, Na-, and K-smectites: Understanding the role of potassium as a clay swelling inhibitor. *Journal of the American Chemical Society*, 117(50):12608–12617, 1995.

[5] BF Ngouana and AG Kalinichev. Structural arrangements of isomorphic substitutions in smectites: Molecular simulation of the swelling properties, interlayer structure, and dynamics of hydrated Cs-montmorillonite revisited with new clay models. *Journal of Physical Chemistry C*, 118(24):12758–12773, 2014.

[6] GM Bowers, DL Bish, and RJ Kirkpatrick. H_2O and cation structure and dynamics in expandable clays: 2h and 39k nmr investigations of hectorite. *Journal of Physical Chemistry C*, 112(16):6430–6438, 2008.

[7] J Swenson, R Bergman, and WS Howells. Quasielastic neutron scattering of two-dimensional water in a vermiculite clay. *Journal of Chemical Physics*, 113(7):2873–2879, 2000.

[8] V Marry, E Dubois, N Malikova, J Breu, and W Haussler. Anisotropy of water dynamics in clays: insights from molecular simulations for experimental QENS analysis. *Journal of Physical Chemistry C*, 117(29):15106–15115, 2013.

[9] ES Boek and M Sprik. Ab initio molecular dynamics study of the hydration of a sodium smectite clay. *Journal of Physical Chemistry B*, 107(14):3251–3256, 2003.

[10] RM Shroll and DE Smith. Molecular dynamics simulations in the grand canonical ensemble: Application to clay mineral swelling. *Journal of chemical physics*,

111(19):9025–9033, 1999.

[11] BB Hanshaw. Cation-exchange constants for clays from electrochemical measurements. In *12th Annual Meeting of the Clay Minerals Society*. Citeseer, 1964.

[12] RG Gast. Standard free energies of exchange for alkali metal cations on wyoming bentonite. *Soil Science Society of America Journal*, 33(1):37–41, 1969.

[13] RG Gast. Alkali metal cation exchange on chambers montmorillonite. *Soil Science Society of America Journal*, 36(1):14–19, 1972.

[14] G Eisenman. Cation selective glass electrodes and their mode of operation. *Biophysical journal*, 2(2):259–323, 1962.

[15] Y Zhang and PS Cremer. Interactions between macromolecules and ions: the hofmeister series. *Current opinion in chemical biology*, 10(6):658–663, 2006.

[16] BJ Teppen and DM Miller. Hydration energy determines isovalent cation exchange selectivity by clay minerals. *Soil Science Society of America Journal*, 70(1):31–40, 2006.

[17] B Rotenberg, V Marry, R Vuilleumier, N Malikova, C Simon, and P Turq. Water and ions in clays: Unraveling the interlayer/micropore exchange using molecular dynamics. *Geochimica et Cosmochimica Acta*, 71(21):5089–5101, 2007.

[18] B Rotenberg, J-P Morel, V Marry, P Turq, and N Morel-Desrosiers. On the driving force of cation exchange in clays: Insights from combined microcalorimetry experiments and molecular simulation. *Geochimica et Cosmochimica Acta*, 73(14):4034–4044, 2009.

[19] T Underwood, V Erastova, P Cubillas, and HC Greenwell. Molecular dynamic simulations of montmorillonite–organic interactions under varying salinity: An insight into enhanced oil recovery. *Journal of Physical Chemistry C*, 119(13):7282–7294, 2015.

[20] RT Downs and M Hall-Wallace. The american mineralogist crystal structure database. *American Mineralogist*, 88(1):247–250, 2003.

[21] A Viani, AF Gualtieri, and G Artioli. The nature of disorder in montmorillonite by simulation of x-ray powder patterns. *American Mineralogist*, 87(7):966–975, 2002.

[22] RT Cygan, J-J Liang, and AG Kalinichev. Molecular models of hydroxide, oxyhydroxide, and clay phases and the development of a general force field. *Journal of Physical Chemistry B*, 108(4):1255–1266, 2004.

[23] HJC Berendsen, JR Grigera, and TP Straatsma. The missing term in effective pair potentials. *Journal of Physical Chemistry*, 91(24):6269–6271, 1987.

[24] DE Smith and LX Dang. Computer simulations of nacl association in polarizable water. *Journal of Chemical Physics*, 100(5):3757–3766, 1994.

[25] DE Smith and KX Dang. Computer simulations of cesium-water clusters: Do ion-water clusters form gas-phase clathrates? *Journal of chemical physics*, 101(9):7873–7881, 1994.

[26] S Koneshan, RM Lynden-Bell, and Jayendran C Rasaiah. Friction coefficients of ions in aqueous solution at 25 c. *Journal of the American Chemical Society*, 120(46):12041–12050, 1998.

[27] J Aqvist. Ion-water interaction potentials derived from free energy perturbation simulations. *Journal of Physical Chemistry*, 94(21):8021–8024, 1990.

[28] A Barducci, G Bussi, and M Parrinello. Well-tempered metadynamics: a smoothly converging and tunable free-energy method. *Physical Review Letters*, 100(2):020603, 2008.

[29] PV Coveney and S Wan. On the calculation of equilibrium thermodynamic properties from molecular dynamics. *Physical Chemistry Chemical Physics*, 18(44):30236–30240, 2016.

[30] S Pronk, S Páll, R Schulz, P Larsson, P Bjelkmar, R Apostolov, MR Shirts, JC Smith, PM Kasson, and D van der Spoel. Gromacs 4.5: a high-throughput and highly parallel open source molecular simulation toolkit. *Bioinformatics*, page btt055, 2013.

[31] M Bonomi, D Branduardi, G Bussi, C Camilloni, D Provasi, P Raiteri, D Donadio, F Marinelli, F Pietrucci, and RA Broglia. PLUMED: A portable plugin for free-energy calculations with molecular dynamics. *Computer Physics Communications*, 180(10):1961–1972, 2009.

[32] GA Tribello, M Bonomi, D Branduardi, C Camilloni, and G Bussi. Plumed 2: New feathers for an old bird. *Computer Physics Communications*, 185(2):604–

613, 2014.

[33] W Humphrey, A Dalke, and K Schulten. Vmd: visual molecular dynamics. *Journal of molecular graphics*, 14(1):33–38, 1996.

[34] N Michaud-Agrawal, EJ Denning, TB Woolf, and O Beckstein. MDAnalysis: a toolkit for the analysis of molecular dynamics simulations. *Journal of computational chemistry*, 32(10):2319–2327, 2011.

[35] John D Hunter. Matplotlib: A 2d graphics environment. *Computing In Science & Engineering*, 9(3):90–95, 2007.

[36] S-H Park and G Sposito. Structure of water adsorbed on a mica surface. *Physical Review Letters*, 89(8):085501, 2002.

[37] M Nakano, K Kawamura, and Y Ichikawa. Local structural information of Cs in smectite hydrates by means of an EXAFS study and molecular dynamics simulations. *Applied Clay Science*, 23(1):15–23, 2003.

[38] V Marry and P Turq. Microscopic simulations of interlayer structure and dynamics in bihydrated heteroionic montmorillonites. *Journal of Physical Chemistry B*, 107(8):1832–1839, 2003.

[39] F-R C Chang, NT Skipper, and G Sposito. Computer simulation of interlayer molecular structure in sodium montmorillonite hydrates. *Langmuir*, 11(7):2734–2741, 1995.

[40] DR Brown and L Kevan. Aqueous coordination and location of exchangeable copper (2+) cations in montmorillonite clay studied by electron spin resonance and electron spin echo modulation. *Journal of the American Chemical Society*, 110(9):2743–2748, 1988.

[41] C Papelis and KF Hayes. Distinguishing between interlayer and external sorption sites of clay minerals using x-ray absorption spectroscopy. *Colloids and Surfaces A: Physicochemical and Engineering Aspects*, 107:89–96, 1996.

[42] C-C Chen and KF Hayes. X-ray absorption spectroscopy investigation of aqueous co (ii) and sr (ii) sorption at clay-water interfaces. *Geochimica et Cosmochimica Acta*, 63(19):3205–3215, 1999.

[43] DG Strawn and DL Sparks. The use of XAFS to distinguish between inner-and outer-sphere lead adsorption complexes on montmorillonite. *Journal of Colloid*

and Interface Science, 216(2):257–269, 1999.

[44] JA Greathouse, K Refson, and G Sposito. Molecular dynamics simulation of water mobility in magnesium-smectite hydrates. *Journal of the American Chemical Society*, 122(46):11459–11464, 2000.

[45] P-C Zhang, PV Brady, SE Arthur, W-Q Zhou, D Sawyer, and DA Hesterberg. Adsorption of barium (II) on montmorillonite: an EXAFS study. *Colloids and Surfaces A: Physicochemical and Engineering Aspects*, 190(3):239–249, 2001.

[46] B Rotenberg, V Marry, N Malikova, and P Turq. Molecular simulation of aqueous solutions at clay surfaces. *Journal of Physics: Condensed Matter*, 22(28):284114, 2010.

[47] JA Greathouse, DB Hart, GM Bowers, RJ Kirkpatrick, and RT Cygan. Molecular simulation of structure and diffusion at smectite–water interfaces: Using expanded clay interlayers as model nanopores. *Journal of Physical Chemistry C*, 119(30):17126–17136, 2015.

[48] S Varma and SB Rempe. Coordination numbers of alkali metal ions in aqueous solutions. *Biophysical chemistry*, 124(3):192–199, 2006.

[49] S Tesson, M Salanne, B Rotenberg, S Tazi, and V Marry. Classical polarizable force field for clays: Pyrophyllite and talc. *Journal of Physical Chemistry C*, 120(7):3749–3758, 2016.

[50] H Heinz, T-J Lin, R Kishore Mishra, and FS Emami. Thermodynamically consistent force fields for the assembly of inorganic, organic, and biological nanostructures: the interface force field. *Langmuir*, 29(6):1754–1765, 2013.

[51] IC Bourg and G Sposito. Ion exchange phenomena. In PM Huang, Y Li, and ME Sumner, editors, *Handbook of Soil Sciences: Properties and Processes, Second Edition*, Handbook of Soil Science. CRC Press, 2011.

[52] LV Benson. A tabulation and evaluation of ion exchange data on smectites. *Environmental Geology*, 4(1):23–29, 1982.

Chapter 5

Kaolinite-Organic Interactions

This chapter introduces kaolinite, an uncharged clay, and models its interactions with various organic molecules representative of the basic molecular building blocks of oil. In this chapter, the interactions of decane, decanoic acid and primary decanamine with kaolinite are studied. Kaolinite is a mineral presenting two different surfaces to pore spaces within the reservoir, and both surfaces are considered in this chapter.

This chapter has previously been published in its presented form in the Journal of Physical Chemistry C:

Thomas Underwood, Valentina Erastova& H. Chris Greenwell.

Wetting Effects and Molecular Adsorption at Hydrated Kaolinite Clay Mineral Surfaces.

J. Phys. Chem. C, 2016, 120 (21), pp 1143311449, DOI: 10.1021/acs.jpcc.6b00187

Thomas Underwood was responsible for running all simulations and writing the published article. Valentina Erastova and H. Chris Greenwell helped proofread the final article.

Abstract

In this study, classical molecular dynamics simulations have been used to understand the key interactions and surface structure of a set of organic molecules at the hydrated surfaces of the 1:1 clay mineral kaolinite. Decane, decanoic acid and decanamine have been modelled at both the hydroxylated and silicate surfaces of kaolinite. Additionally, the effect of pH is observed *via* looking at the protonated decanamine and decanoate anion forms. The key results show that relative affinity of the organic molecules to the kaolinite surface may be readily switched between the hydroxylated and silicate surfaces according to the pH and the nature of the organic head functional group. Decane molecules readily form droplets atop the silicate surface and do not adsorb to the hydroxyl surface, as do protonated decanoic acids. In stark contrast, decanoate anions do not adsorb to the silicate surface, yet adsorb to the hydroxyl surface through an anion exchange mechanism. Decanamine readily adsorbs to both silicate and hydroxyl surfaces, though the hydroxyl-amine interactions are mediated through water bridges. Once charged, the decanamine remains adsorbed to both surfaces, however, both interactions are ionically mediated, rather than through van der Waals and hydrogen bonds. Furthermore, protonated decanamine is observed to adsorb to the hydroxyl surface *via* anion bridges, a phenomenon that is typically associated with positively charged layered double hydroxides rather than negatively charged clay minerals.

5.1 Introduction

Hydrated mineral surfaces play an important role in many geochemical processes, whether within lacustrine/marine systems, terrestrial soils, aeolian dusts or within the subsurface in aquifers and oil reservoirs[1]. Under hydrous conditions, stable mineral surfaces include the silicates, carbonates, (oxy)hydroxides, *inter alia*[2,3]. Furthermore, a wide spectrum of low molecular weight organic molecules can exist within the natural environment, either as a result of natural processes or through anthropogenic inputs. Such organics encompass, amongst others, herbicides and pesticides, nutrients/fertilisers and detrital materials, weathered organic matter from peats and soils (typically humic and fulvic acids), crude oil derived hydrocarbons, fats/oils, explosives, pharmaceuticals, endocrine disrupting chemicals, etc. Owing to the moderate abundance of aqueous or humid environments, coupled with a relatively high hydration energy of many minerals, the interactions between minerals and organic molecules rarely involve ideal dry surfaces, but are far more likely to occur at hydrated surfaces with consequently very different physi- and chemisorption properties.[4]

Owing to the abundance of silica within the Earth's crust, weathering processes and hydrothermal alteration results in the formation of finegrained silicate minerals. When aluminium becomes incorporated in the structure, aluminosilicate minerals form, including the cation exchange mineral families: zeolites and clay minerals[5]. As a result of their high surface area and cation exchange properties, these minerals, whether from natural deposits or synthetic analogues, have found multiple practical applications and have been extensively studied using both analytical laboratory based techniques as well as molecular simulations[6,7,8]. The surfaces of both zeolite and clay minerals present an interesting contrast to silicate minerals as surface bound exposed cations possess a large enthalpy of hydration and (depending on the cation) present water wetting domains, where as the silicate domains behave more akin to quartz, with hydrophobic properties[9].

Though the clay minerals with large cation exchange capacity are of significant interest, they constitute a far smaller fraction of total soil mineral content relative to the aluminosilicate kaolinite minerals[10]. Kaolinite minerals make up a significant volume fraction of soil, aeolian and riverine/lacustrine minerals, and also a significant proportion of available surfaces in sandstone oil reservoirs[11]. Kaolinite is noted for its industrial applications, particularly in the production of porcelain and other ceramics, as a coating agent in, for example, paper production and also as an adsorbent and binder. These applications arise owing to the properties of kaolinite as a result of its structure.

5.1.1 Kaolinite Structure and Properties

Clay minerals, along with quartz, often form surface coatings in the pores of sandstone reservoirs[5], as can be seen from scanning electron and atomic force microscopy for example, Figure 5.1. Illites, smectites, illite-smectites mixed layers and kaolinites are amongst the most abundant types of clay mineral found within sandstone reservoirs[5], and whilst illites and smectites are generally considered as water-wetting, kaolinite is considered to be oil-wetting[4].

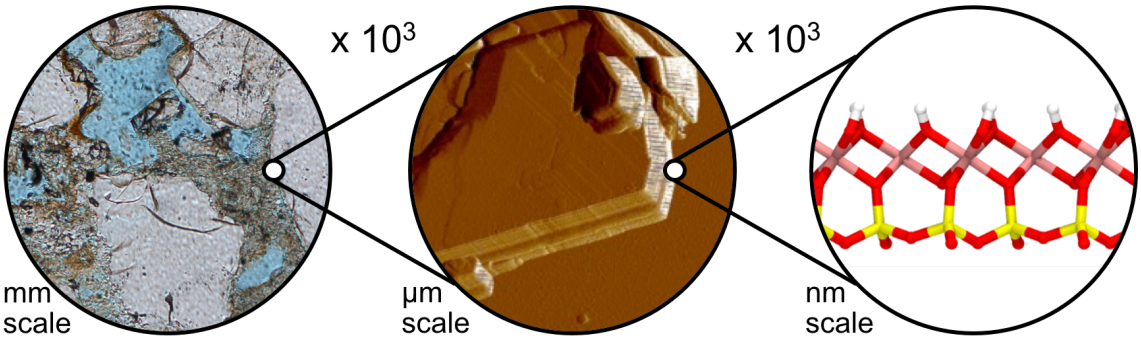

Figure 5.1: Optical microscope image (left) of a sandstone core presenting a composition of large quartz grains (silver), pore water (blue) and clay minerals between quartz grains (grey and brown). Atomic force microscope image of kaolinite grains stacked upon each other (center), and the atomic structure of a single kaolinite layer (right).[12]

Structurally, kaolinite is a member of the 1:1 non-swelling group of clay minerals, where the structure of each layer is composed of one tetrahedral (T) SiO_4 sheet

bonded to a gibbsite-like octahedral (O) AlO_6 sheet, giving rise to an OT structure (Figure 5.1, right). The cation exchange clay minerals mainly belong to the 2:1 clay minerals, where the octahedral layer is sandwiched between two tetrahedral sheets (TOT repeat unit). As such, while the 2:1 clay minerals present a similar basal surface either side of the layer mid-plane, in kaolinite the upper and lower surfaces of one sheet are very different, where the gibbsite-like oxygens are often terminated by hydrogen atoms, creating a layer of hydroxyl groups. Henceforth, the gibbsite-like layer shall be referred to as the *hydroxyl surface*, whilst the SiO_4 layer shall be referred to as the *siloxane surface*.

Due to the low amount of isomorphic substitutions in kaolinite, kaolinite group clay minerals (including dickite and nacrite) do not have a permanent charge and do not swell, and the majority of clay-organic interactions occur either at particle basal planes or at at clay edge sites. In contrast, swelling 2:1 clays interact with organic matter at basal planes, edge sites and within the intercalated region between adjacent clay sheets[1]. The surface charge of kaolinite is pH dependent, as deprotonation of the hydroxyl groups can induce a net negative charge, however, in most instances, the major charge sites of kaolinite occur along the edges, rather than on the basal planes, of the clay particle[13,14,15].

5.1.2 Kaolinite-Organic Adsorption Mechanisms

The possible adsorption mechanisms of small organic molecules on clay basal surfaces have been previously studied in the literature[16]. Table 5.1 presents the important reported adsorption mechanisms between clay and organic molecules, and the relevant functional groups associated with each adsorption mechanism.

Table 5.1: The adsorption mechanisms of organic-clay interactions.[16]

Mechanism	**Organic functional group**
Cation exchange	Amino, ring NH, heterocyclic N (aromatic ring)
Anion exchange	Carboxylate
Water bridging	Amino, carboxylate, carbonyl, alcoholic OH
Cation bridging	Carboxylate, amines, carbonyl, alcoholic OH
Hydrogen bonding	Amino, carbonyl, carboxyl, phenolic OH
Van der Waals interaction	Uncharged organic units

The exchange mechanisms in Table 5.1 (cation and anion exchange) describe the dynamic replacement of a small metal ion M initially adsorbed to a clay surface by a larger organic molecule, functional group B. The cation exchange mechanism, see Figure 5.2 (left), can be represented by the formula:

$$\text{Clay}-\text{M}^{+} + \text{B}^{+}_{(\text{aq})} \longrightarrow \text{Clay}-\text{B}^{+} + \text{M}^{+}_{(\text{aq})} \tag{5.1.1}$$

In this instance, B usually refers to a organic molecule with a quaternary nitrogen atom (in this study -NH_3^+) and M is typically a monovalent cation (for example, Na^+).

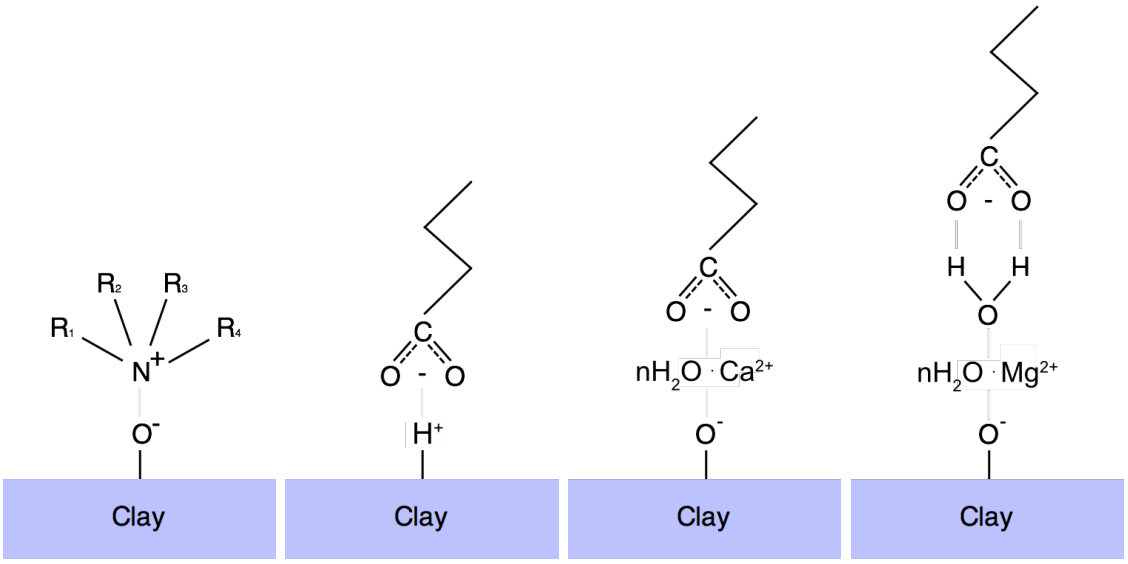

Figure 5.2: A schematic of four proposed organic-clay adsorption mechanisms. Left presents an example of cation exchange, where an organic molecule is directly bound to the clay. Center left presents the analogous mechanism, anion exchange. Center right presents cation bridging, whereby a hydrated divalent ion bridges a charged organic molecule to a like-charged clay surface. Right is an example of water bridging, whereby an organic molecule is adsorbed to the clay through several separate molecules including water.

Anion exchange is the analogous mechanism to cation exchange. In this case, the organic molecule contains a negatively charged functional group, for example a carboxyl, and M is a univalent exchangeable anion bound to a protonated surface hydroxyl group or clay edge site. The mechanisms is thought to be more prominent in metal hydroxides (the positively charged clay counterpart) compared to negatively charged clay minerals.[16]

Cation and water bridging mechanisms, see Figure 5.2 (center right and right respectively), are both weak bonding mechanisms between clay and organic molecules. Water bridging can be represented by the formula:

$$\text{Clay}-\text{M}(\text{H}_2\text{O}) + \text{B}_{(\text{aq})} \longrightarrow \text{Clay}-\text{M}(\text{H}_2\text{O})\text{B} \tag{5.1.2}$$

where B is an anionic or polar functional group and M is a hydrated exchangeable cation. Water bridging is thought to be more prevalent in the presence of strongly solvated cations (for example Mg^{2+}), since B is less likely to displace the bridging water molecule in such instances. When a direct bond is formed between B and M, the bonding mechanism is known as cation bridging.

Hydrogen bonding between organics and clay sites typically occur between -OH functional groups of an organic and mineral surface oxygens. The hydrogen bonding mechanism is proposed to be scarce and is weakly bonding as the clay surface oxygens are not excessively electronegative[16]. The van der Waals interaction mechanism, in contrast, occurs between all organics and a clay surface, and is ever-present.

5.1.3 Previous Simulation Studies of Kaolinite

Computational simulations offer great potential to examine the properties of clay mineral interfaces at an atomistic level. Previous simulation studies of clay mineral surfaces are widespread, and have broached a vast array of topics, from clay disordering, to dynamics and hydration. In particular, the use of computational simulations to study the properties of organic molecules at or on mineral surfaces has provided fertile ground for research (see the article by Greenwell et al.[8] for a recent review on the uses of molecular simulations for clay minerals). Whilst mineral-organic interfaces have been heavily studied in the past, previous simulation studies of kaolinite minerals in particular, have primarily focused on the adsorption mechanisms of either a single molecule, or a relatively small number, of organic molecules to the clay surface.

Ab-initio quantum mechanical density functional theory (DFT) calculations have been used to model the adsorption of simple monomers[17], sugars[18] and saturated hydrocarbons[19] on both the hydroxyl and the siloxane surfaces of kaolinite. Such studies frequently minimise the ground state structure of an organic molecule on the surfaces of kaolinite (sometimes including water) without including any dynamic properties. Most studies observe a preference for organic adsorption to the hydrophilic hydroxyl surface, compared to the hydrophobic siloxane surface, due to the formation of short lived hydrogen bonds between the surface, the organic, and mediating water molecules[17,18,19]. With the inclusion of charged species and salts, ionic interactions become more favourable than the hydrogen bonds and become the primary cause of organic adsorption to the hydroxyl surface[17]. Furthermore, it has also been shown that whilst polar molecules tend to form a complex hydrogen bonding network with the hydroxyl surface, the polar functional group does not affect the interaction between the organic and the siloxane surface, thus the polar molecules interact similarly with the siloxane surface as that of their non-polar counterpart[19].

In contrast to quantum mechanical methods, classical molecular dynamic and Monte Carlo simulations can sample a larger range of phase space, and have been able to model the effects of a multitude of organics on solvated kaolinite surfaces. Recent results have concluded that, for example, certain organic molecules (cationic

dyes) have a preference to adsorb to the siloxane, rather than the hydroxyl surface[20], in disagreement with most DFT studies based on energy analyses[18,19]. The study noticed the formation of organic aggregates on the siloxane surface after 10 ns, a timescale untenable to *ab-initio* calculations at this point in time.

In the previous work by the current authors, the interactions of organic matter with smectite clay surfaces at various salinities had been investigated[21]. The work presented that it was the ionic composition of the brine, rather than the salinity itself, that played an important role upon the adsorption of organic matter to mineral surfaces.

The aim of the present study is to model the interactions of small organic molecules with hydrated kaolinite basal surfaces, to ascertain under what conditions small organic materials adsorb to the siloxane and hydroxyl surface. Organic molecules possessing a shared 10 carbon alkyl backbone, but with varying functional groups, have been simulated on kaolinite clay basal surfaces using classical molecular dynamics. The results are pertinent to a range of phenomena dominated by clay-organic interactions. The aim is to gain a fundamental understanding of the effect of the functional group and charge upon the adsorption of the organic molecules to both the siloxane and hydroxyl basal surfaces of kaolinite. In Section 2 the computational model and input parameters are described. The results for decane interacting with the basal surfaces of kaolinite are presented in Section 5.3.1. The results for decanoic acid and decanoate anions are presented in Sections 5.3.2 and 5.3.3 respectively, whilst the results for decanamine and protonated decanamine are presented in 5.3.4 and 5.3.5.

5.2 Computational Details

5.2.1 Model Setup

The kaolinite unit cell used in this study had the stoichiometry $Al_2Si_2O_5(OH)_4$ (see Figure 5.3), with initial atomic positions taken from the American Mineralogist Crystal Structure Database[22,23], and whilst the unit cell possessed zero net charge, the siloxane and hydroxyl surfaces possess a slight net negative and positive surface charge respectively due to electron polarization (whereby this polarization is implicitly captured by the partial charges on each atom as defined by the utilized force field).

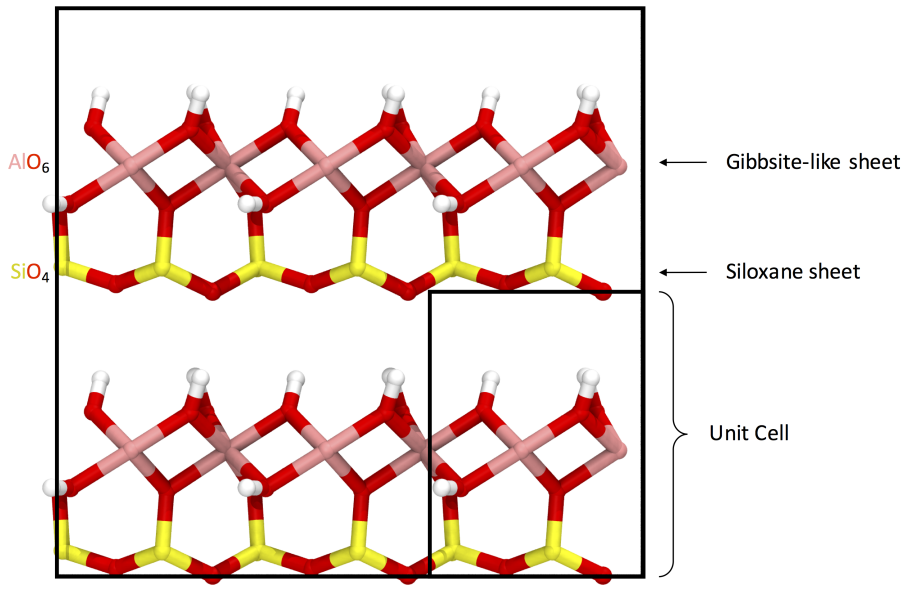

Figure 5.3: The unit cell of Kaolinite used in this study. The clay structure contains silicon (yellow), oxygen (red), aluminum (pink), and hydrogen (white) atoms.

Periodically replicated supercells contained two adjacent sheets of kaolinite composed of 168 unit cells (12 × 7 × 2), with dimensions of approximately 6 × 6 × 10 nm, with each pair of layers separated by a nanopore spacing of approximately 9 nm. The kaolinite structures initially occupied the region $0 < z < 1.2$ nm in all models, and the clay position varied little over all timescales modelled. Two hundred organic molecules were subsequently positioned near the hydroxyl and siloxane surfaces, one hundred within 1 nm of the hydroxyl surface, and the other hundred within 1 nm of the siloxane surface, as to increase clay-organic interactions and reduce phase-

space sampling time[21]. This was achieved using the program PackMol[24], resulting in a system similar to that presented in Figure 5.4. The system was subsequently solvated with (approximately 9000) water molecules to recreate hydrous conditions. It has previously been shown that the organic molecules considered in this study adsorb to the mineral surface when simulated in vacuum[21].

Figure 5.4: A snapshot showing the initial model of decane interacting with kaolinite before water is added. The PackMol software package[24] has been used to create the densely packed organic phase adjacent to the siloxane and hydroxyl surfaces. All simulations start with similar configurations. The clay structure contains the same color scheme as in Figure 5.3, whilst the oil molecules contain carbon (blue) and hydrogen (white).

The organic molecules considered in this study were neutral non-polar decane ($C_{10}H_{22}$), polar decanoic acid ($CH_3(CH_2)_8COOH$) and decanamine ($CH_3(CH_2)_8NH_2$). Additionally, pH effects were considered by altering the protonation state of the decanoic acid and decanamine. Decanoic acid has a pK_a of approximately 4.9[25], and is likely to be found in both neutral and anionic forms in the majority of natural settings. In contrast, the pK_a of decanamine is approximately 10.6[26], meaning that the decanamine will most likely be found in its protonated cationic form in the majority of natural environments, with the notable exception for cementitious materials or drilling fluids where alkaline conditions exist. The following simulations

where all decanamine molecules are neutral are unlikely to be encountered in most environmental conditions but a portion of the population of decanamine molecules will be neutral and thus the simulations provide a useful proxy for comparison. Both decanoate ($CH_3(CH_2)_8COO^-$) and protonated decanamine ($(CH_3(CH_2)_8NH_3^+$) have been simulated. In such simulations the system has been charge-balanced by the addition of sodium and chloride ions respectively. All organic molecules used in this study were created using the Avogadro molecular editing suite[27].

In this study it has been assumed that the charge of the clay basal surface remains neutral, though the protonation state of the organic species varies. The pH at which a mineral surface is neutral is termed the point of zero charge (pzc). At the pzc the mineral surface is net neutral, and though the majority of surface sites will be neutral (e.g. AlOH) there will also be a contribution from a balance of negative (e.g. AlO^-) and positively charged ($AlOH_2^+$) sites. From a simulation perspective, for a surface containing approximately 1000 hydroxyl groups, the simulations are too small to accurately describe the bulk properties of the required charged sites (1 in approximately 333)[28]. In recent work by Gupta and Miller[29] it has been shown through the use of atomic force microscopy that the pzc for the aluminol surfaces of kaolinite is between pH 6 and pH 7. It has also been shown that the siloxane surface of kaolinite is SiO_2 coordinated at pH > 4, and that major silica pH variations arise from edge sites rather than relatively inert basal surfaces[13]. The surface charge of the aluminol hydroxyl surface is strongly pH dependent, with $AlOH_2^+$ groups starting to become AlOH groups at approximately pH 6 and AlOH groups beginning to deprotonate to AlO^- groups at approximately pH 8. As can be seen in work by Jiang, Hirasaki and Miller[28], the AlOH coordination of the aluminol surface exists between pH ranges of approximately 6 and 12, with peak AlOH coordination at approximately pH 9. This then limits the feasibility of the hydroxyl surface model used in the simulations to a range of pH values between approximately pH 6 and pH 12 as can be seen in Figure 5.5, with the most representative pH of the surface model at approximately pH 9. Also presented on Figure 5.5 is the relative concentration of R-COOH to R-COO^- and R-NH_2 to R-NH_3^+ as a function of pH. Note that the siloxane surface model is representative of pHs above approximately 4, and is thus

likely to accurately represent the interactions of the siloxane surface of kaolinite with all organics tested. In contrast, the hydroxyl surface model is most representative of a system at approximately pH 9, and is thus better suited at emulating the properties of R-COO^- and R-NH_3^+ with the aluminol surfaces of kaolinite. The simulations of R-COOH and R-NH_2 interacting with the aluminol surface of kaolinite are presented for comparative purposes, but as shall be shown, the organic-siloxane interactions dominate in both these scenarios. Overall, the force fields utilised in this study have not been parameterised to model pH imbalances on mineral surfaces, however this topic is currently being considered and is subject to future work. The authors note in particular the recent work by Heinz that has been shown to correctly model pH variations on mineral faces[30,31].

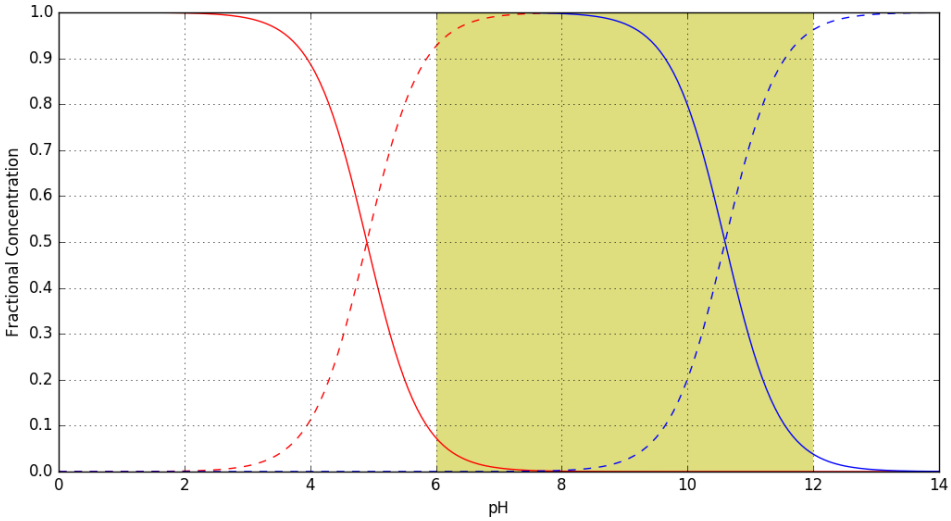

Figure 5.5: The pH range of the AlOH aluminol surface modelled within the simulations.[28]. The silicate surface is assumed to be SiO_2 coordinated at pH's above approximately 4[13,32]. Also presented are the fractional portions of R-COOH (red) to R-COO^- (dotted red) and R-NH_3^+ (blue) to R-NH_2 (dotted blue) as a function of pH.

The ClayFF force field[33] has been used to model the kaolinite clay mineral within the simulations. The force field has been specifically parameterized to model clay-like minerals, and is described wholly through non-bonded Lennard-Jones and Coulomb potentials (with the exception of bonded hydroxyl groups within the clay structure). The CHARMM36 force field[34,35] was utilized to model the organic oil

molecules within the clay nanopore. The force field was designed to describe organic systems, and has been proven to reproduce physically accurate representations of hydrocarbons, lipids and similar organics[36]. The CHARMM36 TIP3P water model (which is derived from the TIP3P parameterization by Jorgensen[37] but includes LJ sites on hydrogens and flexible geometry) was used to simulate the water molecules between clay mineral layers. Although ClayFF has been parameterized consistently with the SPC water model, it has since been shown that the force field equally produces qualitatively accurate results when used in conjunction with the CHARMM36 TIP3P water model[38]. Both ClayFF and CHARMM36 force fields have recently been tested in conjunction, and have been shown to accurately reproduce the equilibrium properties of organic molecules interacting with hydrated mineral surfaces[38]. Previous simulations have been able to show that the adsorption of, for example, acetate and ammonium molecules parameterized with CHARMM, to quartz surfaces parameterized with ClayFF, are not only consistent with *ab-initio* molecular dynamics, but also with experimental X-ray reflectivity (XRF) data[39]. Both the quantity and length of hydrogen bonds between the organic molecules and mineral surface agreed within error to both DFT and XRF data. Lorentz-Berthelot mixing rules for van der Waals interactions are utilized in both CHARMM36 and ClayFF force fields, and have been used here to model the intermolecular organic-clay interactions.

5.2.2 Simulation Details

All simulations were performed using the molecular dynamics suite, GROMACS 4.6.7[40,41]. All simulations were run using real-space particle-mesh-Ewald (PME) electrostatics and a van der Waals cutoff of 1.2 nm. Each simulation was initialized with an energy minimization using a steepest descents algorithm, with convergence achieved once the maximum force on any one atom was less than 100 kJ mol^{-1} nm^{-1}. Subsequently, simulations were run for a 50 ps equilibration period in the constant number of particles, pressure and temperature (NPT) ensemble with a velocity-rescale Berendsen thermostat, temperature coupling constant set to 0.1 ps, and a semi-isotropic Berendsen barostat, with pressure-coupling constant 1 ps. The Berensden thermostat and barostat offered swift equilibration of the system, and

convergence was validated as the d-spacing and potential energy converged. The use of a semi-isotropic barostat allowed computationally efficient decoupling of volume fluctuations in the z direction and xy plane. This equilibration simulation was followed by a 50 ns production run in the NPT ensemble using a velocity-rescale thermostat, with a temperature coupling constant of 1 ps, and a semi-isotropic Parrinello-Rahman barostat, with a pressure coupling constant of 1 ps. All simulations were run at approximately ambient conditions, a pressure of 1 bar and a temperature of 300 K. It was necessary to run simulations at ambient, as the ClayFF force field has been parameterized to model systems at room temperature, and considerable validation would be needed to ensure it accurately reproduces structures and properties at various other temperatures and pressures.

5.2.3 Analysis Techniques and Visualization

All subsequent snapshots of simulation trajectories have been produced using VMD 1.9.2[42]. All simulations contain two adjacent kaolinite layers, which have been reproduced twice in all snapshots at the left and right of the figures. The clay layers are identical and are periodic images of one another. The color scheme of all snapshots are defined as follows. The clay structure contains silicon (yellow), oxygen (red), aluminum (pink), and hydrogen (white) atoms. Organic molecules contain carbon (light blue), hydrogen (white), oxygen (red) and nitrogen (dark blue). Ions are represented as van der Waals spheres and consist of sodium (blue) and chloride (red) ions. Unless otherwise specified this color scheme is kept consistent. Water molecules are present in all simulations, but are not rendered in the snapshots for clarity.

Atomic partial densities across the nanopore were calculated using the built-in analysis tools within GROMACS 4.6.7, and subsequently plotted using Python and MatPlotLib. All density profiles have been averaged over the final 5 ns of the 50 ns production run, and have been subsequently integrated and re-scaled such that the maximum peak in partial density is set to one, in an attempt to increase clarity. The zero in the z-distance of the density plots correspond to the siloxane surface of the kaolinite clay mineral.

The average end-to-end molecular angle has been calculated using the MDAnalysis[43] Python library. The angle of an organic molecule is defined *via* the vector generated between CH_3 carbon and the final carbon (or nitrogen for decanamine) on the opposing molecular functional group. For decane, the choice between head and tail end of the vector is arbitrary. Each organic molecule generates one vector, and the orientation of this organic is measured in spherical coordinates over the final 5 ns of the 50 ns production simulation. The convention used in the present work is such that the clay mineral sheet lies upon the xy plane, and the azimuthal angle is defined as the angle around the z axis upon the clay plane, originating from the x axis, see Figure 5.6 (left) for a schematic. The elevation angle is thus defined as the orientation above or below the xy plane and therefore above or below the clay mineral. A positive elevation angle means that the functional group of an organic points away from the hydroxyl surface and toward the siloxane surface, whilst a negative elevation angle represents the opposite molecular orientation. See Figure 5.6 (center) and Figure 5.6 (right) for a schematic representation of a vector with positive and negative elevation angles respectively.

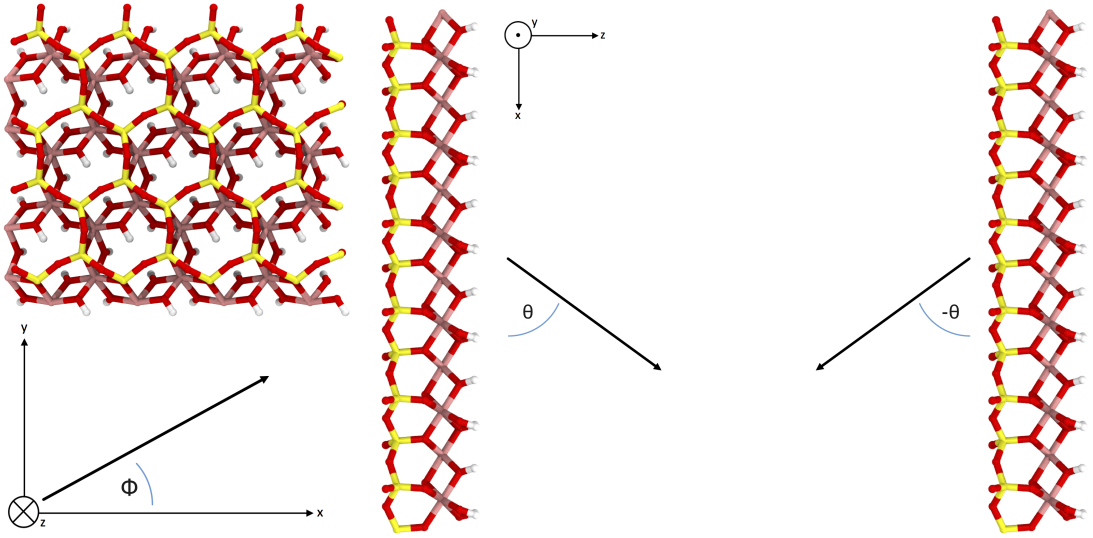

Figure 5.6: A schematic of angles definitions. The azimuthal angle (left) is defined as the angle on the xy plane, about the z axis. The elevation angle (right) is defined as the angle above or below the xy plane, and thus above or below the basal surface of the clay.

5.3 Results & Discussion

5.3.1 Interactions of Decane with Kaolinite

Decane forms the backbone of all the subsequent organic molecules tested, and the behaviour observed for decane is expected to play a role in the mechanics of the other simulations. The simulation results show complete organic molecule withdrawal from the hydrophilic hydroxyl surface, with organic adsorption to the hydrophobic siloxane surface, as is clear from the final snapshot of the simulation in Figure 5.7. This process occurs very rapidly. After a 50 ps equilibration period both oil aggregates have formed clear droplet structures, with the hydroxyl droplet already withdrawn from the surface, see Figure 5.8 (top). After a few nanoseconds, the two oil droplets coalesce and form a single droplet, Figure 5.8 (bottom).

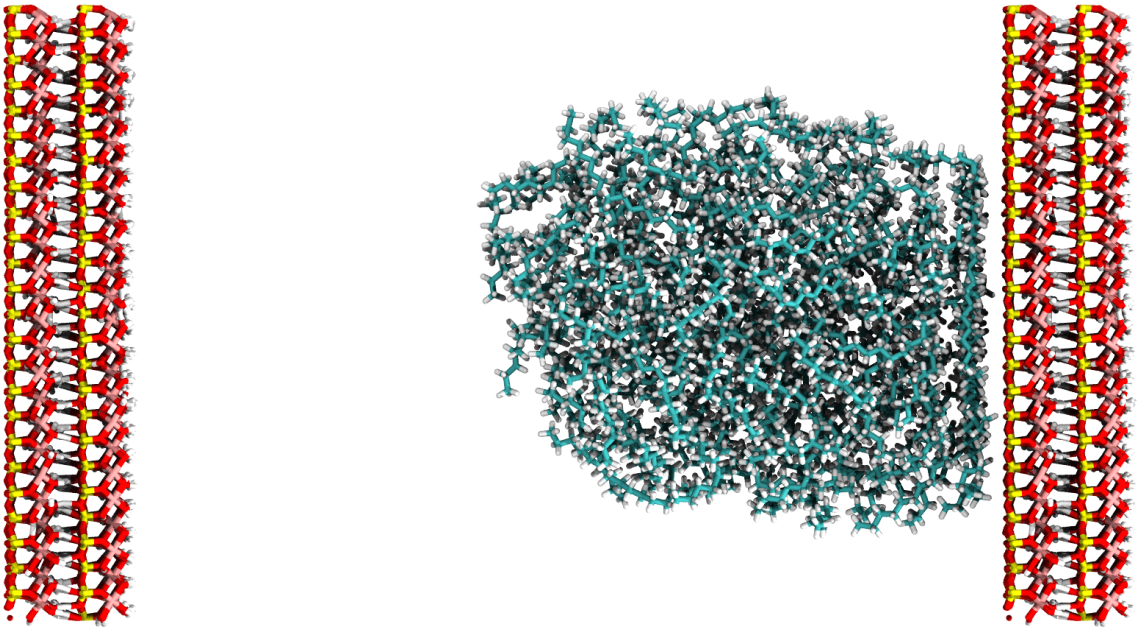

Figure 5.7: The post-production snapshot of decane interacting with kaolinite. Note the complete withdrawal of decane from hydroxyl surface and adsorption to siloxane surface.

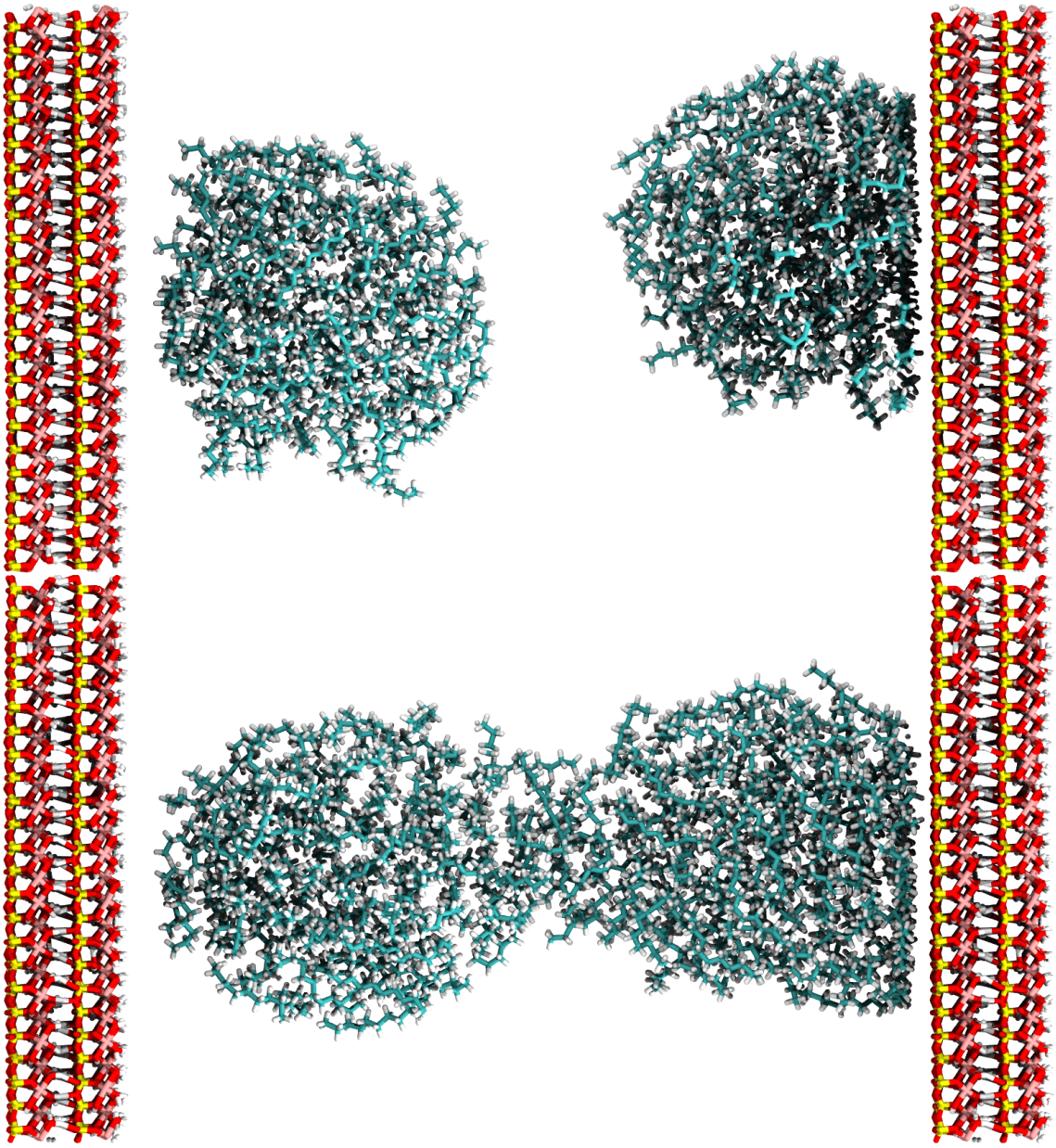

Figure 5.8: Simulation snapshots of decane interacting with kaolinite at various times throughout the simulation. The upper snapshot presents the rapid formation of two separate oil droplets after the 50 ps equilibration period, whilst the lower snapshot presents the two oil droplets coalescing after 2 ns. Following this process, the oil droplet remains adsorbed to the siloxane surface.

Figure 5.9 (top) presents the partial density profile of decane molecules across the pore spacing. It can be seen that the organics nearest the siloxane surface of the kaolinite form discrete layers parallel to the plane of the surface. The results suggest that the organics near the surface lie horizontally and stack upon one other. This effect can also be observed slightly in Figure 5.7. Future work shall examine how the phenomenon originates, comparing the average oxygen-oxygen distance of the siloxane surface and determining whether this correlates to the carbon-carbon or hydrogen-hydrogen separation of the oil. In previous work, Swadling *et al.*[44,45] and Thyveetil *et al.*[46,47] have observed coupling between molecular alignment and the thermal undulations within layered minerals, though these are less likely in kaolinite owing to the thickness of the double repeat used in these simulations.

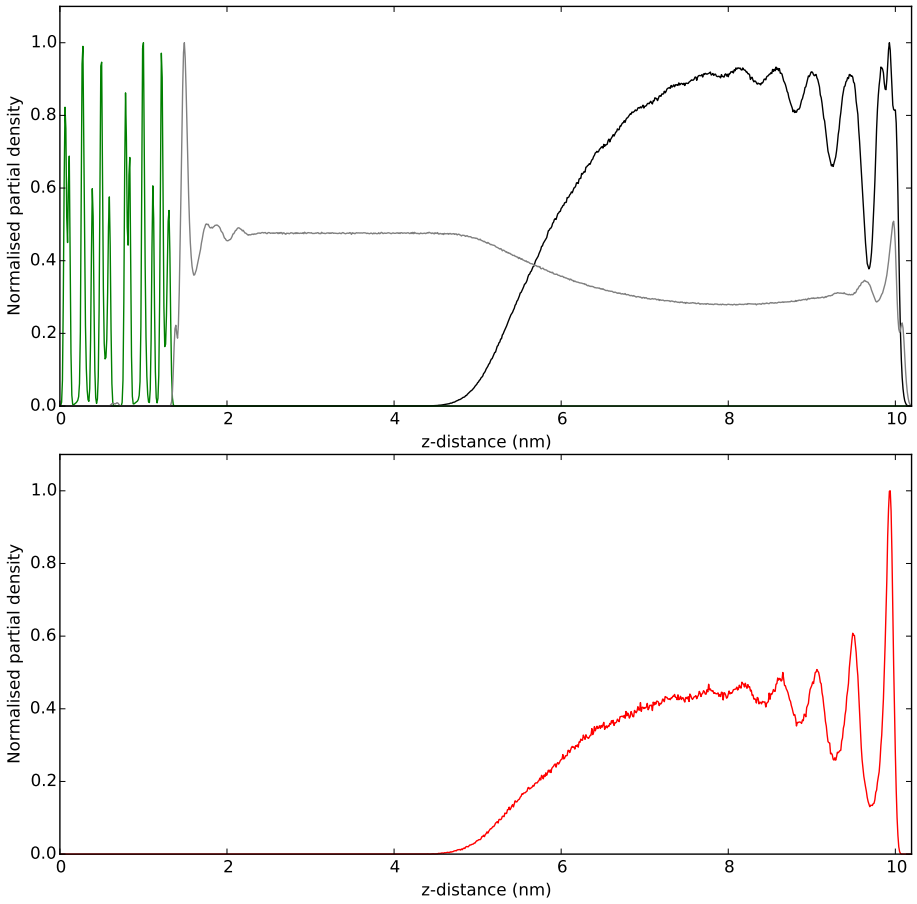

Figure 5.9: The re-scaled density profiles of decane across the pore spacing. The top subfigure presents all components in the system, kaolinite (green), water (grey) and decane (black). The lower subfigure presents the density profile of CH_3 carbons within the functional groups of decane.

Figure 5.9 (bottom) presents the partial density of CH_3 carbons within the pore spacing. Again it is clear that the CH_3 groups form well ordered layers adjacent to the clay. Due to the symmetry of decane, neither end of the molecule has a larger binding affinity to the clay surface, nor possess differing hydration enthalpies, and it is not surprising that the saturated alkanes lie parallel to the plane in this instance.

The first prominent peak in the decane partial density profile is approximately 3.1 Å from the siloxane surface, with subsequent peaks approximately 4.4 Å apart from each other. These peaks correspond to the interactions of the clay with the backbone carbons, and the interactions between intermolecular carbons respectively. The simulations present that van der Waals interactions are the primary adsorption mechanism for decane on the siloxane surface, as the electrostatic partial charges of decane are minimal. It is favourable for water, rather than decane, to hydrate the surface of the clay mineral, establishing extensive hydrogen bonding with the hydroxylated surface. Overall, van der Waals interactions between decane and the clay surface are responsible for organic adsorption to the siloxane surface, whilst the preferential hydrogen bonding between water and the clay surface is responsible for the withdrawal of decane from the hydroxyl surface.

Figure 5.10 (left) presents the angle distribution for decane molecules within the kaolinite nanopore. Note the fairly large spread of organic molecule orientation, however, also note that some organic molecules possess a favourable orientation at an elevation angle of 0 rad, i.e. parallel to the kaolinite surface, and an azimuthal angle of $+\pi/3$ rad and $-2\pi/3$ rad.

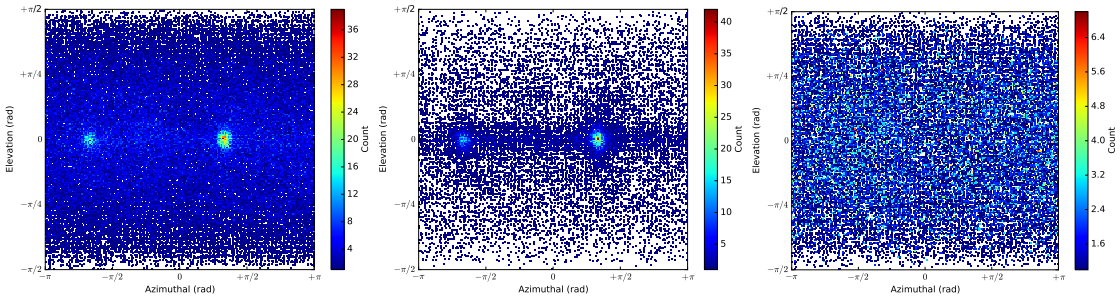

Figure 5.10: The angle distribution of all decane molecules in the pore spacing (left), decane molecules within 0.5 nm of the siloxane surface (center) and decane furthest from the clay surface, at least 3 nm from surface (right).

Figure 5.10 (center) presents the orientation of the organic subset closest to the siloxane surface, i.e. all organics within the first density peak in the density profile of Figure 5.9 (z $>$ 9.5 nm). There is a strong relationship between the elevation angle of an organic and its proximity to the basal surface. The azimuthal angle is heavily biased toward $+\pi/3$ rad and $-2\pi/3$ rad. These angles correspond to opposing directions, hence the organics lie along the same axis of symmetry. This axis of symmetry happens to be one of the hexagonal axes of symmetry of the siloxane surface, and to be specific, it pertains to one of the axes of symmetry of basal oxygens. The results present that the organics closest to the surface not only lie horizontally, but also tend to lie along one of the siloxane axes of hexagonal symmetry. Future work shall examine the origin of this ordering phenomenon, comparing the average oxygen-oxygen distance of the siloxane surface and determining whether this correlates to the carbon-carbon or hydrogen-hydrogen separation of the oil.

Figure 5.10 (right) presents the angle profile of decane molecules furthest from the siloxane surface (z $<$ 7 nm in Figure 5.9). This subset of adsorbed organics possesses no prejudice to azimuthal angle. The orientation of organics is distributed evenly, and the organics are oriented as though the clay minerals were not present.

5.3.2 Interactions of Decanoic Acid with Kaolinite

Decanoic acid is still dominated by the alkane chain and thus might be expected to behave similarly to decane, however, the role of the hydrophilic COOH group is considered to alter the behaviour of organic-clay and organic-water interactions. Figure 5.11 (top) presents a post-production snapshot of decanoic acid interacting with kaolinite. Again, when compared to the starting configuration in Figure 5.4, it is clear that organics readily withdraw from the hydroxyl surface and adsorb on the siloxane surface. Note that the decanoic acid forms a less broad droplet compared to decane, indicating that the polar functional groups act as to increase the contact angle, and thus interfacial tension, of the oil phase. Upon rotating the system, the simulations present that the droplet additionally acts as a film across the clay surface, see Figure 5.11 (bottom).

Figure 5.12 (top) presents the density profiles of the clay, organic molecules and water across the pore space. As with decane, the decanoic acid molecules form horizontal layers close the siloxane surface, and the effect of the COOH functional group appears to be minimal to the overall adsorption behaviour of decanoic acid. Figure 5.12 (bottom) shows the partial densities of CH_3 and COOH functional groups across the pore space. It can be seen that in close proximity to the clay surface, the behaviour of CH_3 and COOH is very similar. The density of COOH appears to reach further into the pore spacing compared to CH_3 however. This is due to the hydrophilic nature of the COOH functional groups; it is favourable for the organic cluster to create a micelle-like structure on the clay surface, minimising hydrophilic-hydrophobic interactions between CH_3/CH_2 groups in the decanoic acid with water.

The first peak distance between the clay surface and the CH_3 functional group is again 3.1 Å, whilst the distance between surface and the COOH functional group is 3.4 Å. Further peaks are separated by approximately 4.4 Å for both CH_3 and COOH. Again, the primary adsorption mechanism seen here is van der Waals interactions between organic and siloxane surface.

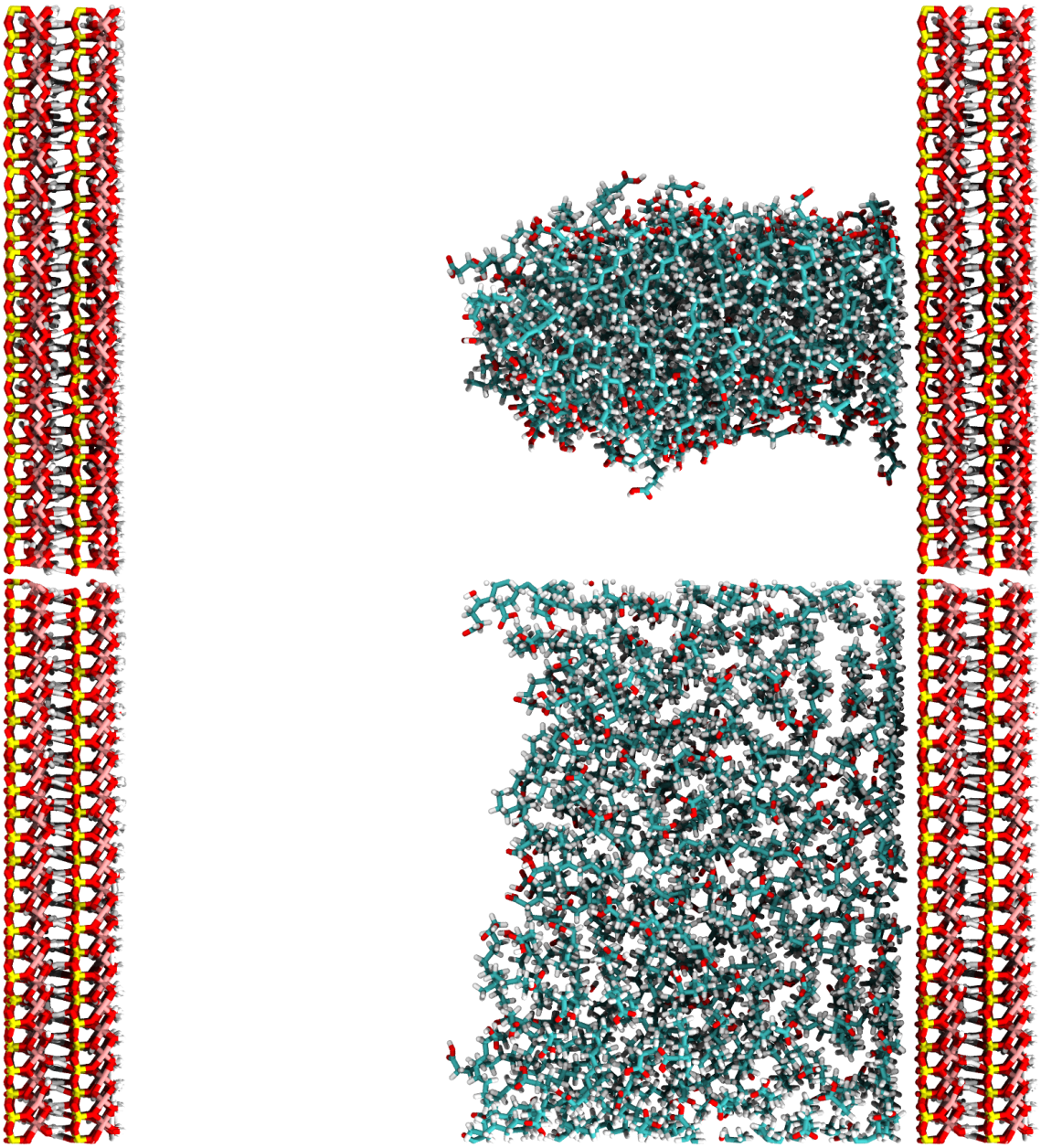

Figure 5.11: Post-production snapshots of decanoic acid interacting with kaolinite (top and bottom rotated through 90°). Note the complete withdrawal of the organic from hydroxyl surface, with adsorption to siloxane surface, much like decane, Figure 5.7.

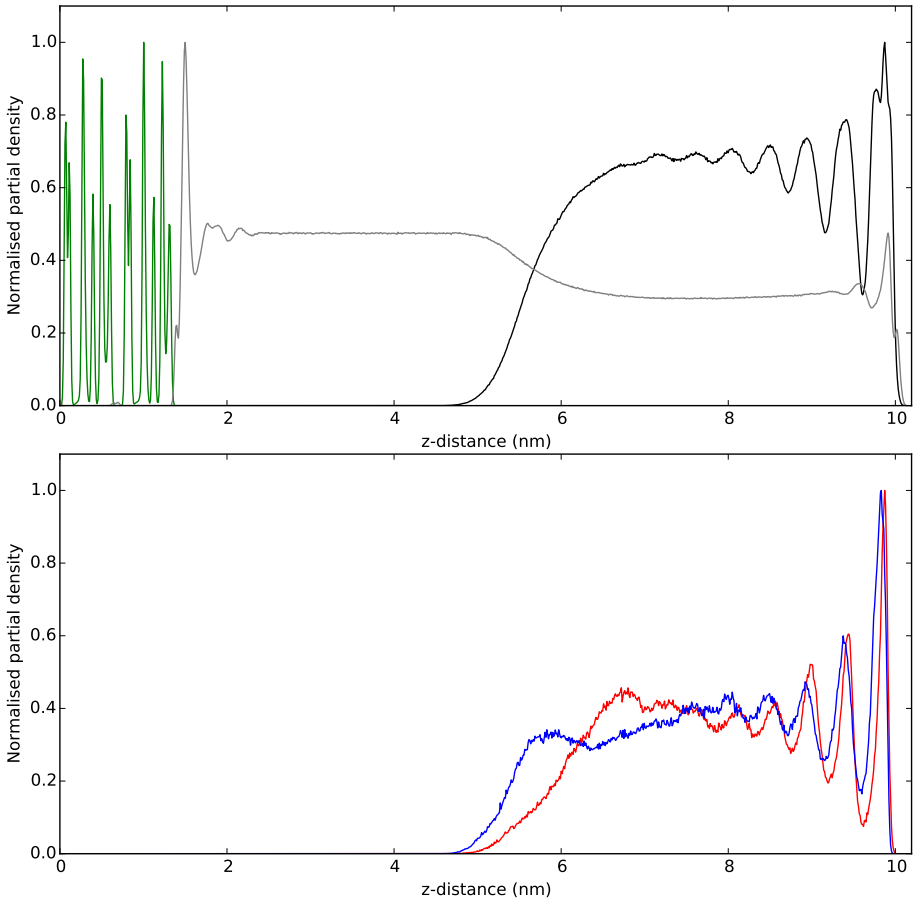

Figure 5.12: The re-scaled density profiles of decanoic acid across the pore spacing. The top subfigure presents all components in the system, kaolinite (green), water (grey) and decanoic acid (black). The lower subfigure presents the density profile of CH_3 carbons (red) and COOH carbons (blue) of the decanoic acid molecules within the nanopore.

As with the decane simulations, no interactions between hydroxyl surface and organic molecules are observed. The results confirm that the binding affinity of the water phase is greater than that of the polar COOH group, and that the hydroxyl surface is readily hydrated by water in preference to decanoic acid. In contrast, the binding affinity of the hydrocarbons on the siloxane surface is greater than the hydration energy of water on the same siloxane surface.

Figure 5.13 (left) presents the angle analysis for all decanoic acid molecules within the kaolinite pore. The organic molecules generate a very distinctive concentric elliptical distribution of angles, very dissimilar to that observed for decane, Figure 5.10. Figure 5.13 (center) again presents the orientation of the organics closest to the clay, i.e. all organics within the first peak in the density profile of Figure 5.12 (z $>$ 9.5 nm). Note that the organics lie azimuthally along one of the hexagonal axis of symmetry of the siloxane surface (once again, in line with basal oxygen atoms), at an angle of $+\pi/3$ rad and $-2\pi/3$ rad. The two primary nodes (the areas of highest angle concentration) are centred upon the xy plane, *i.e.* where the elevation angle is zero, and thus the majority of the organics lie horizontal to the siloxane surface. Figure 5.13 (right) presents the angle profile of decanoic acid molecules furthest from the siloxane surface (z $<$ 7 nm in Figure 5.11). It can be seen that the organics maintain a preferential orientation, with the carboxylic acid heads pointing into the pore spacing (negative elevation), thus increasing polar-polar interactions between organic and solvent. The preference in azimuthal angles is due to the cylindrical droplet formation of the organics at the surface. The polar functional groups have a marked effect on the orientation of the organics far into the pore spacing, a phenomenon that is not observed in the decane simulations.

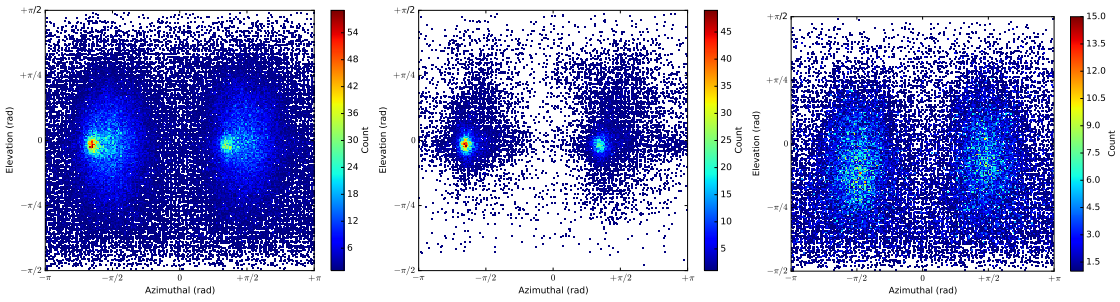

Figure 5.13: The angle distribution of all decanoic acid molecules in the pore spacing (left), organic molecules within 0.5 nm of the siloxane surface (center) and decanoic acid molecules furthest from the clay surface, at least 3 nm from surface (right).

5.3.3 Interactions of Decanoate Anions with Kaolinite

The deprotonation of decanoic acid is expected to dramatically alter organic-clay behaviour as ionic interactions are far stronger than the hydrogen bonds observed for decane and protonated decanoic acid[17]. Figure 5.14 presents the final snapshot of the production run of Na-decanoate interacting with kaolinite. The behaviour is comprehensively different to that of decane and decanoic acid. The results show complete organic withdrawal from the siloxane surface, and adsorption to the hydroxyl surface.

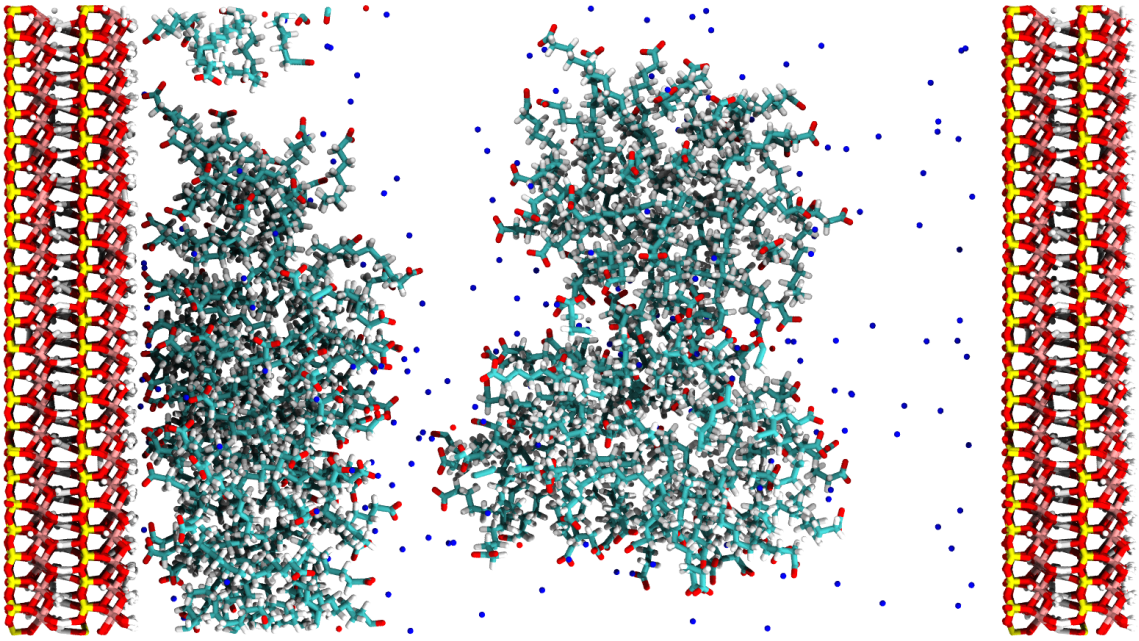

Figure 5.14: The post-production snapshot of Na-decanoate interacting with kaolinite. Note the stark difference in behaviour compared to protonated decanoic acid (Figure 5.11), *viz* complete withdrawal from the siloxane surface yet adsorption to hydroxyl surface.

It is also worth highlighting, in particular, the distribution and behaviour of the charge-balancing sodium cations. Figure 5.15 (top) clearly presents the affinity of sodium to adsorb to both the electronegative siloxane and electropositive hydroxyl surfaces of kaolinite. The simulations show that the sodium cations form inner-sphere surface complexes (ISSCs) on the hydroxyl surface and outer-sphere surface complexes (OSSCs) on the siloxane surface. ISSCs are defined as ions directly adsorbed to the surface of a mineral, whilst OSSCs are hydrated ions indirectly

adsorbed to the surface *via* a mediating water molecule. One may think that ISSCs are inherently more strongly bound to a clay surface, whilst OSSCs in comparison are less strongly bound to a mineral surface, however this has recently been shown to not necessarily be true, and any conclusions drawn from the behaviour ISSC versus OSSC must be considered on a case-by-case basis[48]. The result is surprising however, not only are sodium ions able to adsorb to the electronegative siloxane surface, but also the electropositive hydroxyl surface. The sodium adsorption to the hydroxyl surface may be ascribed to ionic interactions between cations and atoms further within the clay mineral, for example the gibbsite oxygens or aluminums, whilst the phenomenon may also be described by the presence of the negatively charged organic matter.

Figure 5.15 (top) also presents the density profile of the decanoate molecules in the pore spacing. The profile shows two distinct regions of organic aggregation, one set of organics adsorbed to the hydroxyl surface of the clay and a separate cluster within the pore spacing. The partial densities show that the charged organics withdraw readily from the siloxane surface, and do not interact with the clay surface thereafter. No occurrence of cation bridging between siloxane and decanoate is observed here, a result that is consistent with previous observations of the siloxane surfaces in 2:1 smectite clays[21]. The decanoates initially adjacent to the hydroxyl surface remain adsorbed throughout the 50 ns production run *via* an anion exchange mechanism.

Figure 5.15 (bottom) presents the distribution of the decanoate CH_3 and COO^- groups within the nanopore spacing. It is clear from the Figure that the COO^- functional groups mediate the organic adsorption to the hydroxyl surface, whilst the CH_3 groups play a minimal role.

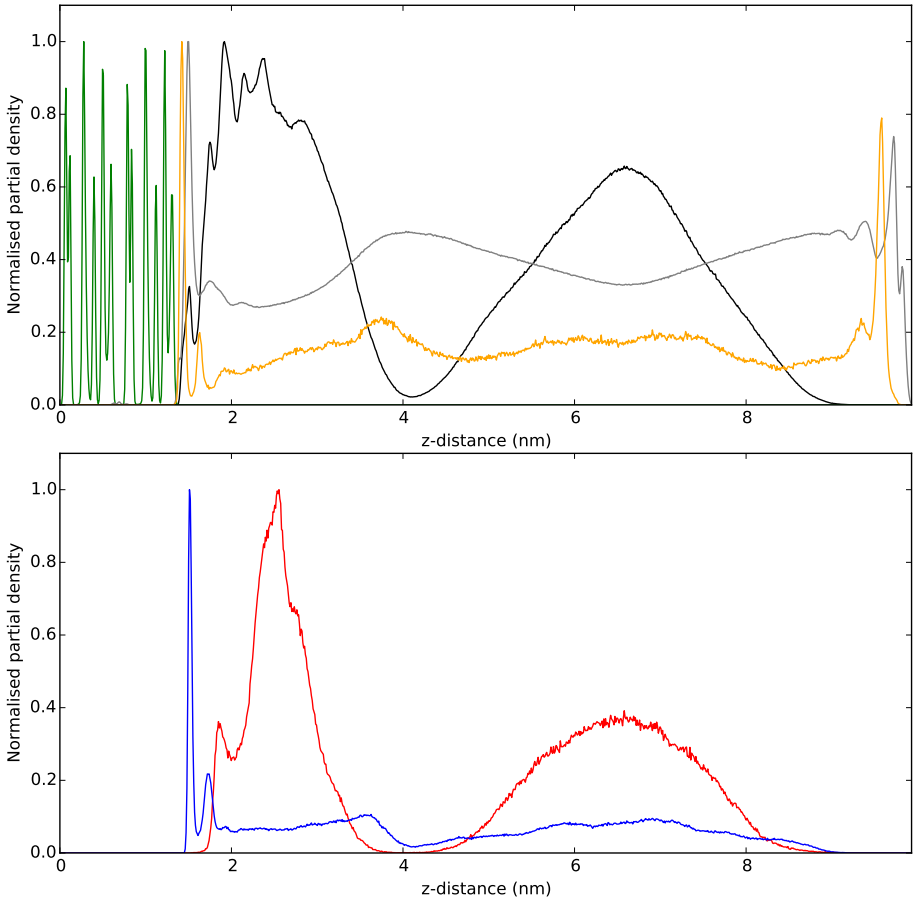

Figure 5.15: The re-scaled density profiles of Na-decanoate across the pore spacing. The top subfigure presents all components in the system, kaolinite (green), water (grey), decanoic acid (black) and charge balancing sodium ions (orange). The lower subfigure presents the density profile of CH_3 carbons (red) and COO^- carbons (blue) of the decanoate anions within the nanopore.

Figure 5.16 (left) presents the angle profile of decanoate organics adsorbed to the hydroxyl surface (z $<$ 4 nm). There appears to be little trend in the angle distribution, which suggests that organics point in all directions. A slight preference for the elevation angle to be aimed toward $-\pi/2$ rad relates to the attraction between charged functional groups and the sodium ions adsorbed to the hydroxyl surface. Figure 5.16 (right) presents the angle distribution of organic molecules floating within the pore spacing. It can be seen that the organics orientate randomly, as expected of a spherical aggregate.

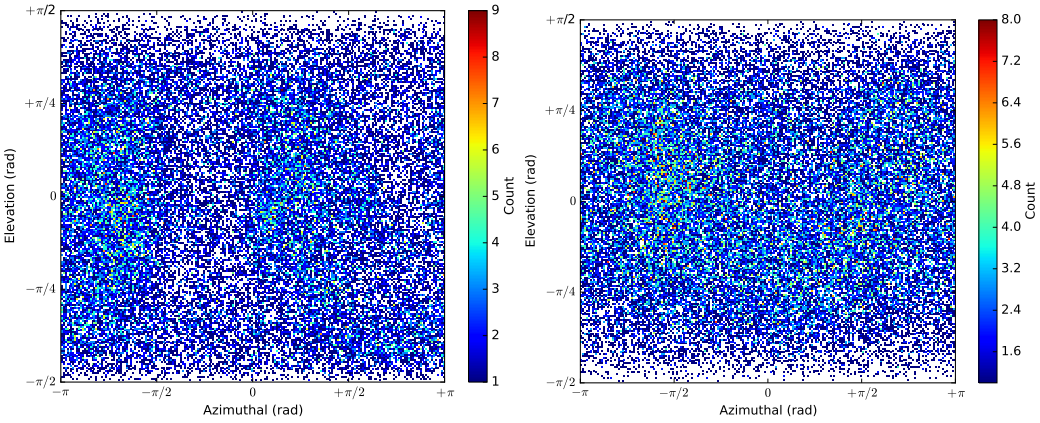

Figure 5.16: The angle distribution of all Na-decanoate molecules adsorbed to the hydroxyl surface spacing (left), and those floating within the nanopore region (right).

5.3.4 Interactions of Decanamine with Kaolinite

The effect of introducing NH_2 functional groups can be seen in Figure 5.17 (top), the post-production snapshot of decanamine on kaolinite. Two separate organic aggregates can be observed in the snapshot, one tightly packed cluster adsorbed to the siloxane surface, and another in close proximity of the hydroxyl surface. Upon rotating the system, Figure 5.17 (bottom), it can be observed that both aggregates create cylindrical films, one adsorbed directly to the siloxane surface, and one floating above the hydroxyl surface.

The film adsorbed upon the siloxane surface forms clear horizontal layers, similar to the results of uncharged and polar organics previously presented. The film within the pore spacing appears to have withdrawn from the hydroxyl surface, however, the aggregate drifts very little throughout the simulation, as can be seen from the density profiles, Figure 5.18 (top). The implication is that the NH_2 functional groups can form strong hydrogen bonds and subsequently form water-bridging networks with the hydroxyl surface.

The partial density profile of CH_3 and NH_2 functional groups are presented in Figure 5.18 (bottom). The distance between siloxane surface and the first peak of CH_3 and NH_2 is 3.3 Å and 2.8 Å respectively. The increased affinity between surface and NH_2 group is due to the larger degree of polarity in the primary amine compared to CH_3 groups. The large electronegative nitrogen and slightly electropositive hydrogens are thought to create strong $N-H\cdots O$ hydrogen bonds with the surface in comparison to the van der Waals interactions formed by the CH_3 termini. The average distance between density peaks on the siloxane surface is again 4.4 Å, which suggests that the intermolecular interactions between organic molecules is similar for decane, decanoic acids and decanamine. Also note the density profile of NH_2 groups in the cluster near the hydroxyl surface. Here, the NH_2 groups form small density maxima near the hydroxyl surface. In comparison to the water density in Figure 5.15 (top) it can be seen that the NH_2 maxima lie within the hydration peaks of the clay surface. That is, the NH_2 groups lie between the first and second hydration layer/shell of the hydroxyl surface. The results present the formation of water bridges between clay and organic molecule, however, unlike tra-

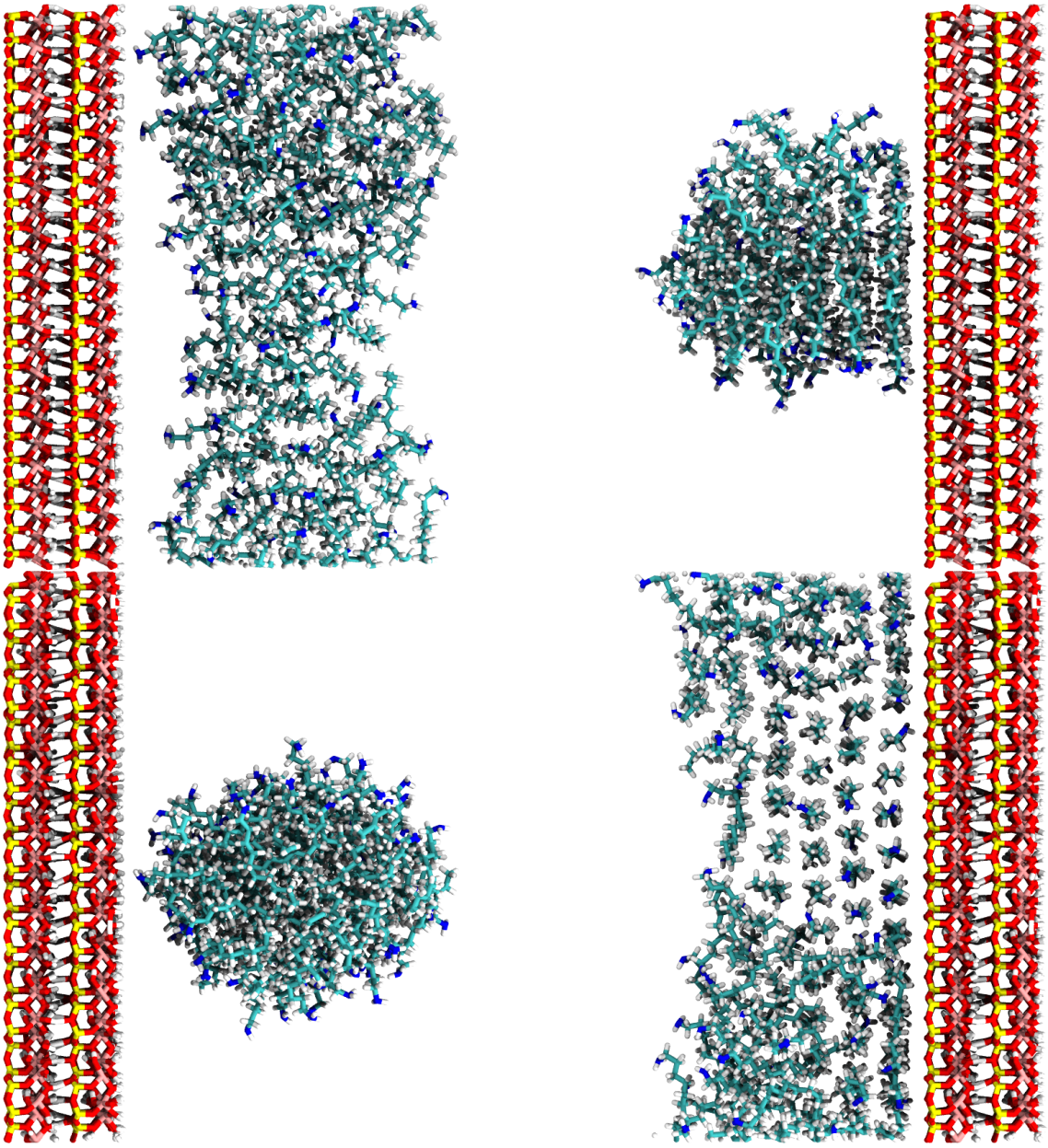

Figure 5.17: Post-production snapshots of decanamine interacting with kaolinite. Observe the adsorption of organic molecules to both hydroxyl and siloxane surfaces.

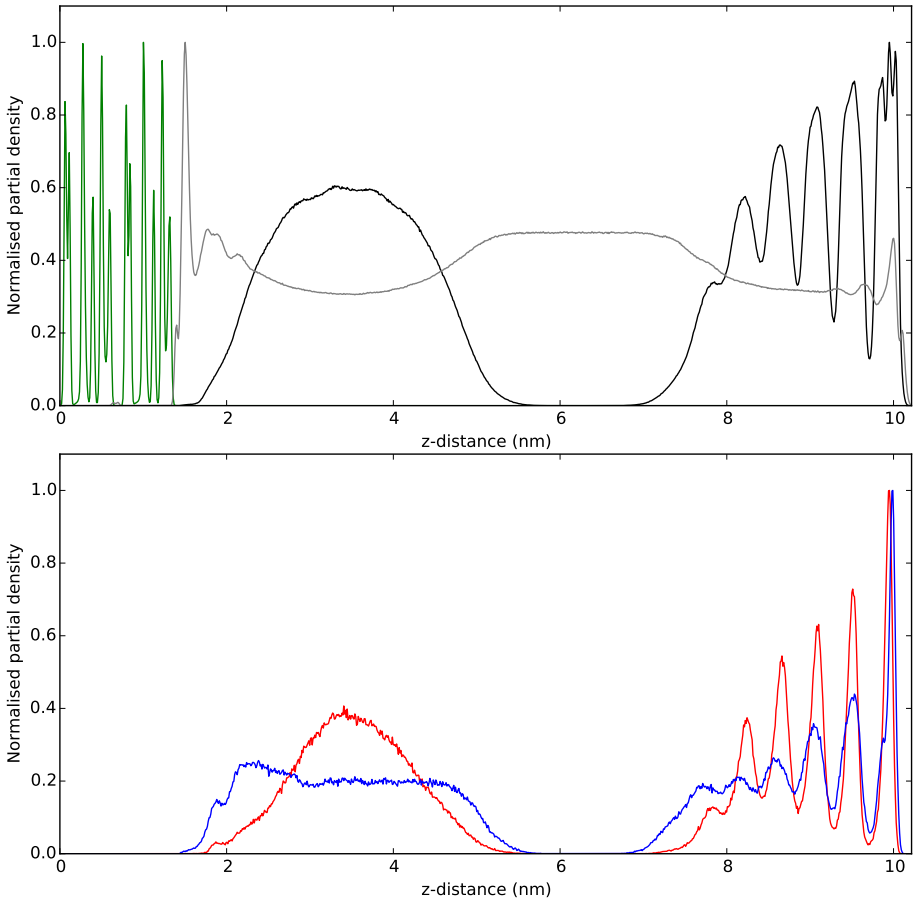

Figure 5.18: The re-scaled density profiles of decanamine across the pore spacing. The top subfigure presents all components in the system, kaolinite (green), water (grey) and decanamine (black). The lower subfigure presents the density profile of CH_3 carbons (red) and NH_2 nitrogens (blue) of the decanamine molecules within the nanopore.

ditional water-bridging where the interaction is mediated by a strongly solvated ion, here the bridging occurs without salt. The NH_2 functional group is able to form water bridges with the hydroxyl surface through a layer of water molecules. It has previously been observed that the first hydration layer of the hydroxyl surface can be frozen in place[49,50], and this may explain why such an effect is observed here. The simulations present that NH_2 functional groups can adsorb to both surfaces of the kaolinite clay.

Figure 5.19 (left) shows the angle distribution amongst the molecules contained within the cluster in close proximity to the hydroxyl surface. The figure presents a slight preference for the polar groups to be pointing toward the hydroxyl surface, inferring that clay-organic interactions exist. There is also a preference for the organics to be orientated at $\pm\pi/2$ rad in the azimuthal plane. This effect is due to the cylindrical structure of the organic droplet in this simulation after 50 ns. Figure 5.19 (center) presents the angle distribution of decanamine in the organic cluster adsorbed to the siloxane surface. A clear preference for the NH_2 group to point into the pore spacing can be seen. This infers that the NH_2 group is liable to interact with the surrounding solvent, whilst the CH_3 chain ends interact with the hydrophobic siloxane surface. Figure 5.19 (right) is the angle distribution of organics closest to the siloxane surface, contained within the peak closest to the clay in Figure 5.18 ($z > 9.5$ nm). It is clear that the majority of organics lie parallel to the basal surface here, with an elevation angle of 0 rad. The distinct azimuthal pattern observed in Figure 5.19 (center) can also be seen here, with the majority of organics lying along an azimuthal angle of 0 and $\pm\pi$ rad, and a small portion lying along the azimuthal angle of $-3\pi/2$ rad. All of these axes correspond to one of the hexagonal axis of symmetry of the siloxane surface, as previously discussed.

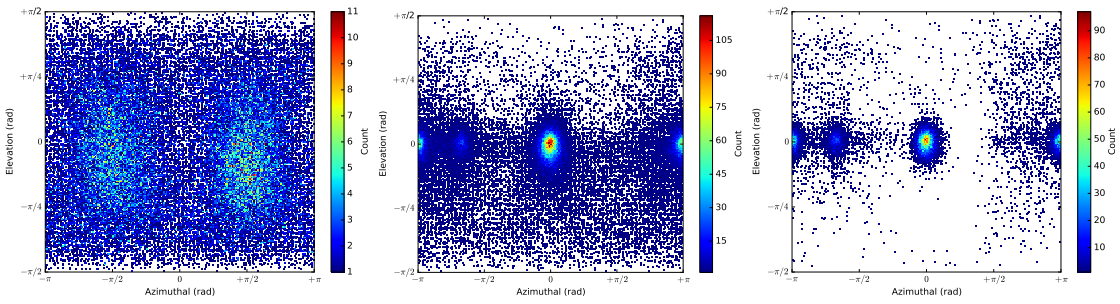

Figure 5.19: The angle distribution of the decanamine cluster adjacent to the hydroxyl surface (left), decanamine molecules adsorbed to the siloxane surface (center) and decanamine molecules closest to the siloxane surface, at least 0.5 nm from surface (right).

5.3.5 Interactions of Protonated Decanamine with Kaolinite

Figure 5.20 is the post-production snapshot of protonated decanamine interacting with kaolinite. Again, two separate organic aggregates can be observed in Figure 5.20, one adsorbed to the siloxane surface, and another adsorbed to the hydroxyl surface.

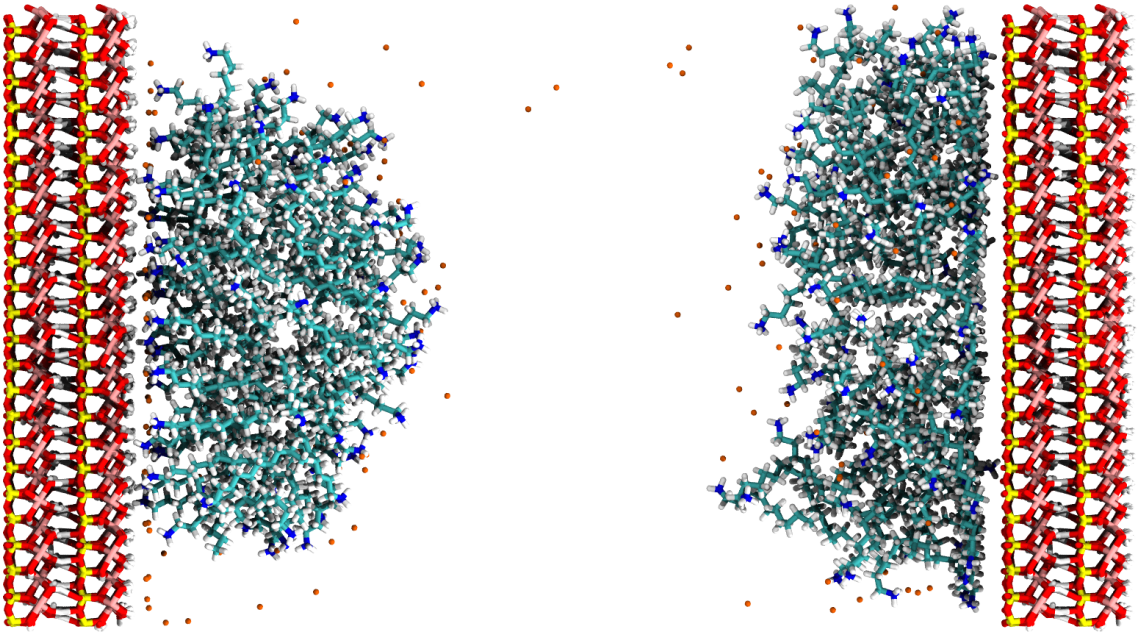

Figure 5.20: The post-production snapshot of protonated decanamine interacting with kaolinite. Note the difference in behaviour compared to deprotonated decanamine (Figure 5.17), *viz* adsorption to both siloxane surface and hydroxyl surfaces.

Figure 5.21 (top) is the density profile of protonated decanamine and chloride ions across the pore spacing. Unlike the organic anions in the decanoate simulations, the charge balancing chloride ions only adsorb to the positive hydroxyl layer of the kaolinite surface. The result suggests that the hydroxyl surface will readily adsorb both anions and cations, whilst the siloxane surface will selectively adsorb cations.

The organic molecules adsorbed to the siloxane surface are less ordered compared to the layered structuring observed in the previous simulations. This is due to the ionic repulsion between NH_3^+ functional groups overwhelming the van der Waals and hydrogen bonding networks previously stacking the organic molecules upon

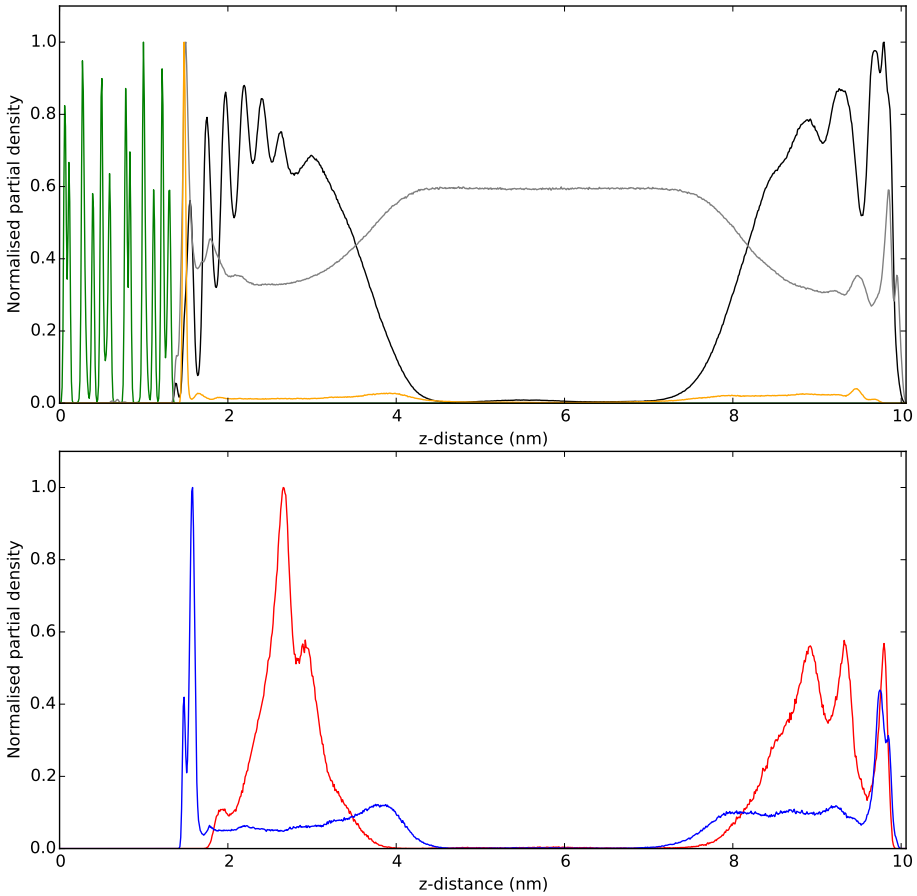

Figure 5.21: The re-scaled density profiles of protonated decanamine across the pore spacing. The top subfigure presents all components in the system, kaolinite (green), water (grey), decanamine (black) and charge balancing chloride ions (orange). The lower subfigure presents the density profile of CH_3 carbons (red) and NH_3^+ nitrogens (blue) of the protonated decanamine molecules within the nanopore.

the siloxane layer. Despite this, the layer of organic molecules closest to the clay surface appear to be positioned parallel to the siloxane layer. This orientation then maximizes both the ionic interactions between NH_3^+ and the surface as well as the van der Waals interactions between the backbone of the organic and the surface. It can also be seen from the partial density profile of NH_3^+ and CH_3 functional groups, Figure 5.21 (bottom), that the first layer of organics on the siloxane surface lie parallel to the surface. Beyond this, the organics are less strictly structured, as NH_3^+ functional groups repel one another. The primary adsorption mechanism observed here is cation exchange for NH_3^+ groups, and van der Waals interactions for CH_3/CH_2 backbones.

The adsorption of the organic molecules to the hydroxyl surface is mediated by the small anions within the pore spacing. Note that the chloride ions appear to form slight inner-sphere surface complexes, suggesting that the primary adsorption mechanism is anion bridging in this instance. This is a mechanism that is not well described in literature, as it is thought to be too weak and short lived to play a significant role in the structure of kaolinite surfaces. As previously noted, it is thought that anion bridging occurs primarily on positively charged hydroxide minerals (layered double hydroxides), and is short-lived as the anions are readily replaced by water molecules[16]. The presented results here show that anion bridging is not only possible, but also occurs in 1:1 clays, in addition to layered hydroxide minerals.

Figure 5.22 (left) presents the angle distribution of organics adsorbed to the hydroxyl surface of the kaolinite clay (z $<$ 5 nm). The figure presents no clear preference for azimuthal direction of organics, however a clear trend in elevation can be seen. The organics tend to face either directly toward or away from the clay surface, at an angle of $-\pi/2$ or $+\pi/2$ respectively. The result suggests that the NH_3^+ functional groups are directly causing the adsorption of decanaminium to the hydroxyl surface. Figure 5.22 (center) shows the angle distribution for the organics adsorbed to the siloxane surface. It can be seen that there is a preference for the organics to lie horizontal to the basal plane, and a slight preference for the NH_3^+ functional groups to point into the pore spacing. Figure 5.22 (right) presents the angles of organics nearest the siloxane surface (z $>$ 9.5 nm) and also shows an indistinct azimuthal preference. However, it is clear from the figure that the NH_3^+ groups point directly toward the clay. Figure 5.22 (right) presents that the protonated decanamine molecules are ionically attracted to the siloxane clay surface, forming cation exchange adsorption sites.

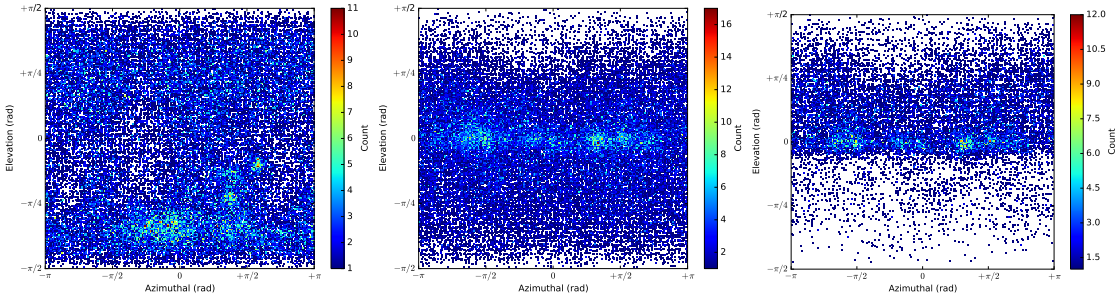

Figure 5.22: The angle distribution of protonated decanamine molecules adsorbed to the hydroxyl surface (left), protonated decanamine molecules adsorbed to the siloxane surface (center) and protonated decanamine molecules closest to the siloxane surface, at least 0.5 nm from surface (right).

5.4 Conclusions

In this article, the authors have been able to describe the interaction between a range of organic molecules; including non-polar, polar, and ionic molecules, with the hydrated siloxane and hydroxyl mineral surfaces of kaolinite using molecular dynamic simulations. To the author's knowledge, this is the first time that such a systematic study has been carried out with a large amount of organic molecules on kaolinite.

The results present, in the first instance, the formation of clusters and micelle-like films upon the siloxane surface for decane, decanoic acid and decanamine. Upon altering the pH of the system, and thus the charge of the organic molecules, drastic changes occur between the clay-organic interactions. As ionic interactions for charged organics overwhelm the weaker hydrogen bonding network between water and clay[17], the affinity between organic molecules and hydroxyl surfaces can be drastically altered. The current work suggests that the charge of the organic molecule, and thus the pH of the system, has a particular relevance to alter the behaviour of the clay-organic interactions, with large implications for a wide range of applications, from surfactant treatments to enhanced oil recovery.

Additionally, the work presents how charge balancing ions play an important role in the interactions between organic matter and clay minerals. The simulation results present that both siloxane and hydroxyl surfaces will adsorb sodium ions, whilst chloride ions are selectively adsorbed to the hydroxyl surface. This unusual property warrants further examination, and is currently under investigation from the current authors. Anion bridging has also been observed between kaolinite and positively charged organics, a phenomenon not typically associated with clay minerals.

The work presents the important role that molecular dynamic simulations can play in elucidating the fundamental interactions between molecules at an atomic resolution. It shows the marked variety of properties that clay minerals possess, and that kaolinite exhibits a far richer range of chemistry compared to the typically examined 2:1 clay minerals. Further work on this topic will address the role of salt composition and concentration within the nanopore, and the function this plays upon the clay-organic interactions.

July 13, 2017

Supplementary Information

Further details on the computational models and parameterisations thereof can be found in the Appendices.

Bibliography

[1] PV Brady. *The Physics and Chemistry of Mineral Surfaces*. CRC Press, Boca Raton, FL, 1996.

[2] DJ Vaughan, RAD Pattrick, and Mineralogical Society (Great Britain). *Mineral Surfaces (The Mineralogical Society Series)*, volume 5. Chapman & Hall, New York, 1995.

[3] GE Brown Jr. How minerals react with water. *Science*, 294(5540):67–69, 2001.

[4] J-L Bantignies, CCD Moulin, and H Dexpert. Wettability contrasts in kaolinite and illite clays: Characterization by infrared and x-ray absorption spectroscopies. *Clays & Clay Minerals*, 45(2):184–193, 1997.

[5] MJ Wilson, L Wilson, and I Patey. The influence of individual clay minerals on formation damage of reservoir sandstones: A critical review with some new insights. *Clay Minerals*, 49(2):147–164, 2014.

[6] JA Greathouse, KL Johnson, and HC Greenwell. Interaction of natural organic matter with layered minerals: Recent developments in computational methods at the nanoscale. *Minerals*, 4(2):519–540, 2014.

[7] JL Suter, RL Anderson, HC Greenwell, and PV Coveney. Recent advances in large-scale atomistic and coarse-grained molecular dynamics simulation of clay minerals. *Journal of Materials Chemistry*, 19(17):2482–2493, 2009.

[8] HC Greenwell, W Jones, PV Coveney, and S Stackhouse. On the application of computer simulation techniques to anionic and cationic clays: A materials chemistry perspective. *Journal of Materials Chemistry*, 16:708–723, 2006.

[9] G Sposito, NT Skipper, R Sutton, S-H Park, AK Soper, and JA Greathouse. Surface geochemistry of the clay minerals. *Proceedings of the National Academy of Sciences of the U.S.A*, 96(7):3358–3364, 1999.

[10] M J Wilson. The origin and formation of clay minerals in soils: Past, present and future perspectives. *Clay Minerals*, 34(1):7–25, 1999.

[11] RH Worden and S Morad. *Clay Mineral Cements in Sandstones (Special Publication 34 of the IAS)*. Wiley-Blackwell, Malden, MA, 2003.

[12] Pablo Cubillas and Rikan Kareem. SEM and AFM Images of Kaolinite Clay Minerals. Unpublished Work.

[13] PV Brady, RT Cygan, and KL Nagy. Molecular controls on kaolinite surface charge. *Journal of Colloid & Interface Science*, 183(2):356–364, 1996.

[14] BK Schroth and G Sposito. Surface charge properties of kaolinite. *Clays & Clay Minerals*, 45(1):85–91, 1997.

[15] E Tombácz and M Szekeres. Surface charge heterogeneity of kaolinite in aqueous suspension in comparison with montmorillonite. *Applied Clay Science*, 34(1):105–124, 2006.

[16] G Sposito. *The Chemistry of Soils*. Oxford University Press, New York, 2008.

[17] DL Geatches, A Jacquet, SJ Clark, and HC Greenwell. Monomer adsorption on kaolinite: Modeling the essential ingredients. *J. Phys. Chem. C*, 116(42):22365–22374, 10 2012.

[18] JI Lee, SG andChoi, W Koh, and SS Jang. Adsorption of β-d-Glucose and Cellobiose on Kaolinite Surfaces: Density Functional Theory (DFT) Approach. *Applied Clay Science*, 71:73–81, 2013.

[19] ER Johnson and A Otero-de-la Roza. Adsorption of organic molecules on kaolinite from the exchange-hole dipole moment dispersion model. *J. Chem. Theory Comput.*, 8(12):5124–5131, 12 2012.

[20] JA Greathouse, DL Geatches, DQ Pike, HC Greenwell, CT Johnston, J Wilcox, and RT Cygan. Methylene blue adsorption on the basal surfaces of kaolinite: Structure and thermodynamics from quantum and classical molecular simulation. *Clays & Clay Minerals*, 63(3):185–198, 2015.

[21] T Underwood, V Erastova, P Cubillas, and HC Greenwell. Molecular dynamic simulations of montmorillonite-organic interactions under varying salinity: An insight into enhanced oil recovery. *Journal of Physical Chemistry C*, 119(13):7282–7294, 2015.

[22] RT Downs and M Hall-Wallace. The american mineralogist crystal structure database. *American Mineralogist*, 88(1):247–250, 2003.

[23] DL Bish. Rietveld refinement of the kaolinite structure at 1.5 k. *Clays & Clay Minerals*, 41(6):738–744, 1993.

[24] L Martínez, R Andrade, EG Birgin, and JM Martínez. Packmol: a package for building initial configurations for molecular dynamics simulations. *Journal of Computational Chemistry*, 30(13):2157–2164, 2009.

[25] MD Barratt. Quantitative structure-activity relationships (qsars) for skin corrosivity of organic acids, bases and phenols: Principal components and neural network analysis of extended datasets. *Toxicology In Vitro*, 10(1):85–94, 1996.

[26] DD Perrin. *Ionisation Constants of Inorganic Acids and Bases in Aqueous Solution*. Pergamon Press, Exeter, UK, 1984.

[27] MD Hanwell, DE Curtis, DC Lonie, T Vandermeersch, E Zurek, and GR Hutchison. Avogadro: An advanced semantic chemical editor, visualization, and analysis platform. *Journal of Cheminformatics*, 4:17, 2012.

[28] T Jiang, GJ Hirasaki, and CA Miller. Characterization of kaolinite ζ potential for interpretation of wettability alteration in diluted bitumen emulsion separation. *Energy & Fuels*, 24(4):2350–2360, 2010.

[29] V Gupta and JD Miller. Surface force measurements at the basal planes of ordered kaolinite particles. *Journal of Colloid Interface Science*, 344(2):362–371, 2010.

[30] FS Emami, V Puddu, RJ Berry, V Varshney, SV Patwardhan, CC Perry, and H Heinz. Prediction of specific biomolecule adsorption on silica surfaces as a function of ph and particle size. *Chemistry of Materials*, 26(19):5725–5734, 2014.

[31] H Heinz, T-J Lin, RK Mishra, and FS Emami. Thermodynamically consistent force fields for the assembly of inorganic, organic, and biological nanostructures: The interface force field. *Langmuir*, 29(6):1754–1765, 2013.

[32] Xihui Yin, Vishal Gupta, Hao Du, Xuming Wang, and Jan D Miller. Surface charge and wetting characteristics of layered silicate minerals. *Advances in Colloid & Interface Science*, 179:43–50, 2012.

[33] RT Cygan, J-J Liang, and AG Kalinichev. Molecular models of hydroxide, oxyhydroxide, and clay phases and the development of a general force field. *Journal of Physical Chemistry B*, 108(4):1255–1266, 2004.

[34] K Vanommeslaeghe, E Hatcher, C Acharya, S Kundu, S Zhong, J Shim, E Darian, O Guvench, P Lopes, I Vorobyov, and A D Mackerell. CHARMM General Force Field: A Force Field for Drug-like Molecules Compatible with the CHARMM All-Atom Additive Biological Force Fields. *Journal of Computational Chemistry*, 31(4):671–690, March 2010.

[35] P Bjelkmar, P Larsson, MA Cuendet, B Hess, and E Lindahl. Implementation of the CHARMM Force Field in GROMACS: Analysis of Protein Stability Effects from Correction Maps, Virtual Interaction Sites, and Water Models. *Journal of Chemical Theory & Computation*, 6(2):459–466, January 2010.

[36] RW Pastor and AD MacKerell Jr. Development of the CHARMM Force Field for Lipids. *Journal of Physical Chemistry Letters*, 2(13):1526–1532, 2011.

[37] WL Jorgensen, J Chandrasekhar, JD Madura, RW Impey, and ML Klein. Comparison of simple potential functions for simulating liquid water. *Journal of the American Chemical Society*, 79(2):926–935, 1983.

[38] LB Wright and TR Walsh. First-Principles Molecular Dynamics Simulations of NH_4^+ and CH_3COO^- Adsorption at the Aqueous Quartz Interface. *Journal of Chemical Physics*, 137(22):224702, 2012.

[39] AA Skelton, P Fenter, JD Kubicki, DJ Wesolowski, and PT Cummings. Simulations of the quartz(1011)/water interface: A comparison of classical force fields, ab initio molecular dynamics, and x-ray reflectivity experiments. *Journal of Physical Chemistry C*, 115(5):2076–2088, 2011.

[40] B Hess, C Kutzner, D van der Spoel, and E Lindahl. Gromacs 4: Algorithms for highly efficient, load-balanced, and scalable molecular simulation. *Journal of Chemical Theory & Computation*, 4(3):435–447, February 2008.

[41] S Pronk, S Páll, R Schulz, P Larsson, P Bjelkmar, R Apostolov, MR Shirts, JC Smith, PM Kasson, D van der Spoel, B Hess, and E Lindahl. GROMACS 4.5: a High-Throughput and Highly Parallel Open Source Molecular Simulation Toolkit. *Bioinformatics*, 29(7):845–854, 2013.

[42] W Humphrey, A Dalke, and K Schulten. Vmd: Visual molecular dynamics. *Journal of Molecular Graphics*, 14(1):33–38, February 1996.

[43] N Michaud-Agrawal, EJ Denning, TB Woolf, and O Beckstein. MDAnalysis: A Toolkit for the Analysis of Molecular Dynamics Simulations. *Journal of Computational Chemistry*, 32(10):2319–2327, 2011.

[44] JB Swadling, PV Coveney, and HC Greenwell. Clay minerals mediate folding and regioselective interactions of rna: A large-scale atomistic simulation study. *Journal of the American Chemical Society*, 132(39):13750–13764, 2010. PMID: 20843023.

[45] JB Swadling, JL Suter, HC Greenwell, and PV Coveney. Influence of surface chemistry and charge on mineral-rna interactions. *Langmuir*, 29(5):1573–1583, 2013.

[46] M-A Thyveetil, PV Coveney, JL Suter, and HC Greenwell. Emergence of undulations and determination of materials properties in large-scale molecular dynamics simulation of layered double hydroxides. *Chemistry of Materials*, 19(23):5510–5523, 2007.

[47] M-A Thyveetil, PV Coveney, HC Greenwell, and JL Suter. Role of host layer flexibility in dna guest intercalation revealed by computer simulation of layered nanomaterials. *J. Am. Chem. Soc.*, 130(37):12485–12495, 2008.

[48] T Underwood, V Erastova, and H C Greenwell. Ion adsorption at smectite clay mineral surfaces: A hofmeister series for hydrated smectite mineral. *Clays & Clay Minerals*, 2016. Submitted.

[49] X-L Hu and A Michaelides. Water on the hydroxylated (001) surface of kaolinite: From monomer adsorption to a flat 2d wetting layer. *Surface Science*, 602(4):960–974, 2008.

[50] X-L Hu and A Michaelides. Ice formation on kaolinite: Lattice match or amphoterism? *Surface Science*, 601(23):5378–5381, 2007.

Chapter 6

Kaolinite Wettability at Varying Brine Concentrations

This chapter builds upon the work presented in Chapter 5 by introducing electrolyte solutions of various NaCl concentrations to the surface of kaolinite. The chapter attempts to elucidate the phenomenon of low-salinity EOR by decoupling the three-phase clay-oil-brine system into simpler two-phase systems. The primary aim of this chapter is to determine the wettability dependence of kaolinite on NaCl brine concentration. Whilst the article is written in the plural form (*i.e. we* rather than *I*) the entirety of the article (simulations, analysis and writing) has been completed by thesis author.

Abstract

This research aims to clarify the fundamental mechanisms of clay-oil-brine interfaces that underpin low-salinity enhanced oil recovery (EOR), a technique whereby sea water, partially desalinated, is used to yield increasing amounts of crude oil from reservoirs. In this study we have used classical molecular dynamic simulations to examine salinity induced wettability changes at the basal surfaces of kaolinite. We have measured both the contact angle, and the energy of adhesion, of water to the siloxane and aluminol surface of kaolinite as a function of NaCl concentration. We observe kaolinite to become increasingly water-wet at lower salinities, and therefore less oil-wet at lower salt concentrations. We determine that this wettability alteration is due to the entropically driven alterations at the oil-brine interface. The results describe a direct mechanism that can explain the salinity dependence of low-salinity enhanced oil recovery.

6.1 Introduction

Low-salinity enhanced oil recovery (EOR) is a technique used to optimise extraction rates from sandstone reservoirs. The technique, whereby sea water, partially desalinated, is used to push increasing amounts of crude oil from reservoirs, boosts both reservoir lifetime and overall production rates of oil[1]. Unfortunately, the underlying mechanisms driving the process remain a mystery. Formation of a complete and coherent picture of the physics driving the low-salinity phenomenon can help unlock previously untapped resources, and help alleviate the impending global energy crisis[2].

The processes dictating low-salinity EOR are currently thought to be due to molecular-level interactions located at the three-phase clay-oil-brine interface. This is due to the complex surface chemistry frequently exhibited amongst clay minerals[1]. These minerals often form surface coatings in the pores of sandstone reservoirs[3]. Illites, smectites, illite-smectites mixed layers and kaolinites are amongst the most abundant types of clay mineral found within sandstone reservoirs[3], and whilst illites and smectites are generally considered as water-wetting, kaolinite is considered to be oil-wetting[4]. Subsequently, the presence of kaolinite material is deemed one of the major potential contributors to the low-salinity effect[5].

Recently, molecular dynamics (MD) simulations have seen increasing use in interpreting the phenomenon of surface wettability at the molecular level. Kaolinite, in particular, has been examined several times in literature. Ŝolc *et al.* examined various different water models on the two separate basal surfaces of kaolinite using classical MD simulations[6]. They observed that all tested water models completely wetted the hydroxylated aluminol surface of kaolinite, however, their simulations contained a limited amount of water molecules (not enough to completely saturate the surface), and therefore this conclusion can be questioned. They also observed that all water models formed droplets on the silicate surface of kaolinite, with a resulting contact angle of $105° \pm 1°$. Tenney & Cygan examined the contact angle formed between supercritical CO_2, brine and kaolinite[7]. They measured the resulting contact angle of CO_2 and observed discrete differences between neat water, water containing 0.78 mol/kg NaCl, and water containing 0.26 mol/kg $CaCl_2$. They ob-

served the surfaces of kaolinite to become increasingly water-wet upon introducing inorganic salts. Their results clearly show that the salinity and ionic composition of a brine can alter the wettability of a third phase at a mineral surface.

In the present work, we attempt to understand the wettability alteration at the basal surfaces of kaolinite owing to changes in salt concentration within the bulk water phase. The aim is to understand how salinity can cause the effects observed in low-salinity enhanced oil recovery. The article is broken down into the following sections. Section 6.1.1 introduces a conceptual model which decouples the complex three-phase (clay-oil-brine) system into three separate two-phase systems. Consequently, we argue that the clay-oil-brine system can be examined by proxy by modelling the simpler two-phase clay-brine system. Section 6.2 describes the computational models and simulation input parameters used within the study, and section 6.3 presents the key results of the study.

6.1.1 Conceptual Model

Consider the system presented in Figure 6.1, an oil droplet adsorbed to a clay mineral surrounded by an electrolyte solution (brine).

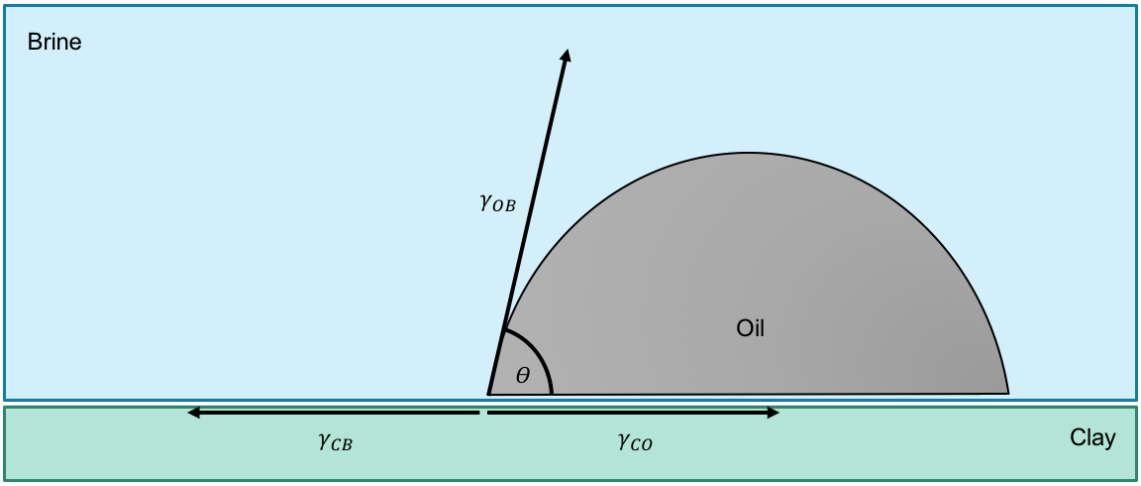

Figure 6.1: A schematic oil droplet within a reservoir. The angle formed between the oil and the clay can be described by Young's equation.

The behaviour of this three-phase system can be described by Young's equation:

$$\cos(\theta) = \frac{\gamma_{\mathrm{CB}} - \gamma_{\mathrm{CO}}}{\gamma_{\mathrm{OB}}} \tag{6.1.1}$$

where γ_{CB} is the interfacial tension between clay and brine, γ_{CO} is the interfacial tension between clay and oil, and γ_{OB} is the interfacial tension between oil and brine. We note that this equation assumes an ideal droplet, *i.e.* there are no additional terms in equation 6.1.1 due to, for example, line tension. Using this expression, we are able to describe the complex three-phase clay-oil-brine system by examining the properties of the three separate interfacial tensions in equation 6.1.1. The primary question now becomes, how does Young's equation/interfacial tensions vary with salt concentration?

Let us propose that γ_{CO} is independent of the salt *concentration* in the system. This is valid assuming that the ions are immiscible in the oil. Note, γ_{CO} may depend on salt composition, *i.e.* divalent cation bridges may increase γ_{CO} compared to monovalent ions, but we shall assume that it is independent of the salt *concentration*.

The oil-brine interfacial tension, γ_{OB}, will vary with salt concentration. That is:

$$\gamma_{\mathrm{OB}} = \gamma_{\mathrm{OB}}(c) \tag{6.1.2}$$

Let us also propose that $\gamma_{\mathrm{OB}}(c)$ scales as $\gamma_{\mathrm{BV}}(c)$, where γ_{BV} is surface tension between brine and its vapour. This statement has been proven in previous MD simulation results (see Chapter 2), and is apparent in Figure 6.2. The physical reasoning behind this is that the dielectric properties of the alkane phase are much closer to a vacuum, than they are to a phase of water.

Finally, we shall assume that γ_{CV}, the interfacial tension between water vapour and clay, is independent of salt concentration. Consequently, the complex three-phase clay-oil-brine system represented in Figure 6.1 can be approximated by systems excluding the oil phase. For example, the salinity dependence in low-salinity enhanced oil recovery can be examined by modelling the two-phase water-clay sys-

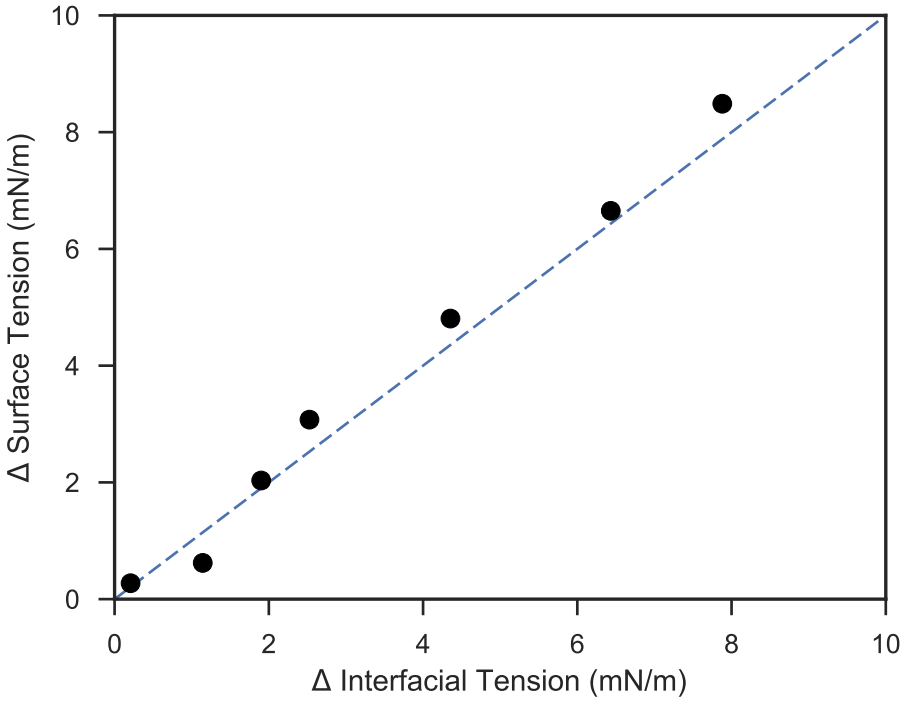

Figure 6.2: The change in surface tension at the water-vapour interface (y-axis) against the change in interfacial tension at the water-alkane interface (x-axis). The diagonal line represents when the two properties are linearly proportional.

tem presented in Figure 6.3, and by the Young's equation:

$$\cos(\theta) = \frac{\gamma_{\mathrm{CV}} - \gamma_{\mathrm{CB}}}{\gamma_{\mathrm{BV}}} \tag{6.1.3}$$

In the following study, we have calculated MD simulations of water droplets at different salinities on the basal surfaces of kaolinite. We have also examined the energy of adhesion of water to each surface at different salinities. The results attempt to resolve the salinity dependence of low-salinity EOR.

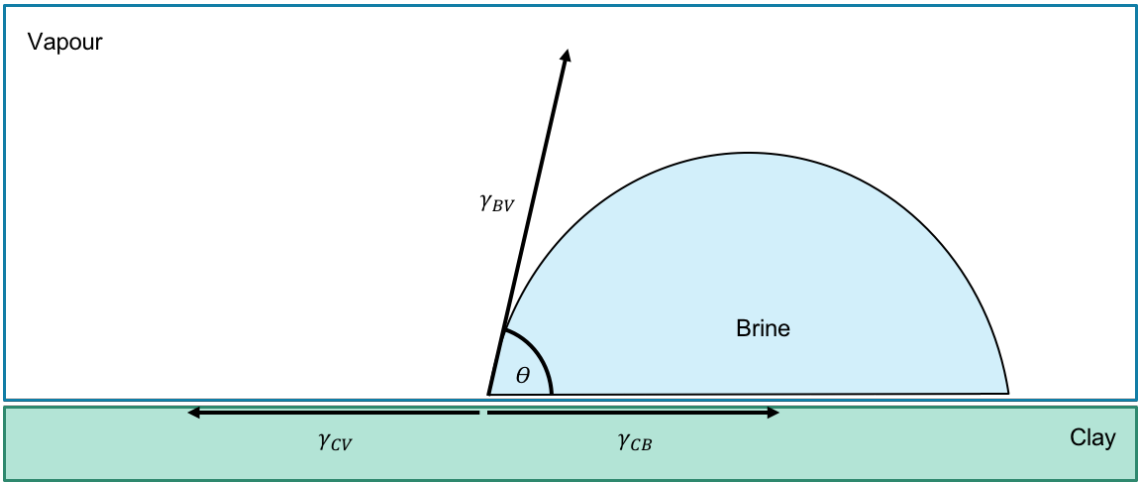

Figure 6.3: A schematic water droplet on a clay mineral. The salinity dependence of this system scales much like the three-phase clay-oil-brine system.

6.2 Computational Methods

6.2.1 System Setup

The kaolinite unit cell used in this study had the stoichiometry $Al_2Si_2O_5(OH)_4$ with initial atomic positions taken from the American Mineralogist Crystal Structure Database[8,9]. Contact angle simulations used a supercell of 32×5×3 kaolinite unit cells. The simulation was extended in the direction normal to the basal plane of the clay (the z direction) to 30 nm. The resulting simulation had dimension of approximately 17×5×30 nm^3. Subsequently, 2000 water molecules were placed in a cylindrical geometry directly adjacent to the clay. This was achieved using the program Packmol[10]. The cylindrical geometry of the droplet reduced undesirable effects due to line tension altering the final contact angle[7,11]. A set amount of water molecules were replaced with sodium and chloride ions to generate droplets of various salinities. The concentrations examined were 0, 0.2, 0.5, 1.0, 1.5 and 2.0 mol/kg. The precise amount of water molecules, sodium ions and chloride ions in each simulation is presented in Table 6.1.

Table 6.1: The amount of water molecules and aqueous sodium and chloride ions in each contact angle simulation.

m (mol/kg)	N_{water}	N_{Na}	N_{Cl}
0.00	2000	0	0
0.20	1986	7	7
0.50	1964	18	18
1.00	1928	36	36
1.50	1892	54	54
2.00	1856	72	72

Additional simulations have been set up to examine the energy of adhesion of water to each surface of kaolinite. In such simulations, the unit cell of kaolinite was replicated 8 x 5 x 4 times. The system was, once again, extended in the z direction to 30 nm, and a film of water was placed adjacent to the interface of interest. The water film contained 4000 water molecules. Consequently, the amount of ions at each salt concentration is double that presented in Table 6.1. The final simulation dimensions measured approximately 4 x 4 x 30 nm^3, see Figure 6.4.

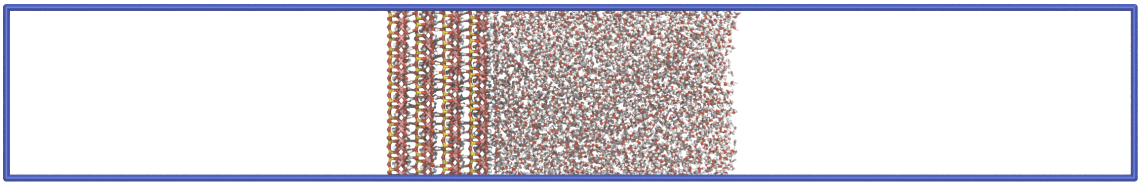

Figure 6.4: An example simulation used to examine the energy of adhesion of water to the aluminol surface of kaolinite.

6.2.2 Force Fields

In all simulations, non-bonded interactions between two atoms have been calculated using a combination of Coulomb's law and a 12-6 Lennard-Jones potential:

$$U(r_{ij}) = U_{\text{elec}}(r_{ij}) + U_{\text{disp}}(r_{ij}) = \frac{1}{4\pi\epsilon_0}\frac{q_i q_j}{r_{ij}} + 4\epsilon_{ij}\left[\left(\frac{\sigma_{ij}}{r_{ij}}\right)^{12} - \left(\frac{\sigma_{ij}}{r_{ij}}\right)^{6}\right] \tag{6.2.4}$$

where ϵ_{ij} represents the strength of the non-bonded dispersion interaction, σ_{ij} represents the equilibrium separation, and r_{ij} is the current separation distance between atoms i and j.

All simulations have utilised Lorentz-Berthelot mixing rules to calculate the non-bonded Lennard-Jones interactions between unlike species:

$$\sigma_{ij} = \frac{\sigma_{ii} + \sigma_{jj}}{2} \qquad \epsilon_{ij} = \sqrt{\epsilon_{ii}\epsilon_{jj}} \tag{6.2.5}$$

The ClayFF forcefield, specifically parameterized to model clays and clay-like minerals, was used to model the kaolinite clay within this study[12]. The ClayFF force field is designed such that the entire interactions within, and structure of, the clay is described wholly by the non-bonded Lennard-Jones and Coulomb potentials (with the exception of hydroxyl groups within the clay layer).

The TIP4P2005 water model was used to simulate the water, as it has been shown to most accurately reproduce the interfacial properties of water compared to other available models, see Chapter 2 and Vega *et al.*[13].

The Smith and Dang parameterisation has been used to model aqueous sodium and chloride ions[14]. It has also been shown to accurately model the interfacial properties of water at various NaCl concentrations (see Chapter 2).

A complete list of non-bonded interaction parameters for clay, water, and ions is presented in table 6.2.

Table 6.2: The nonbonded parameters used in this study for clay, water, and ions.

Description	Atom-type	σ_{ii} (nm)	ϵ_{ii} (kJ/mol)	q_i (e)
Clay Tetrahedral Silicon	ST	0.33020	7.701E-06	2.1
Clay Octohedral Aluminium	AO	0.42712	5.564E-06	1.575
Clay Bridging Oxygen	OB	0.31655	0.6502	-1.05
Clay Hydroxyl Oxygen	OH	0.31655	0.6502	-0.95
Clay Hydroxyl Hydrogen	HO			0.425
Water Oxygen	OW	0.315890	0.774908	
Water Hydrogen	HW			0.5564
Water Charged Site	MW			-1.1128
Aqueous Sodium Ion	NA	0.235	0.54392	+1
Aqueous Chloride Ion	CL	0.44	0.4184	-1

Covalent bonds between atoms have been modelled in terms of harmonic potentials:

$$U(r_{ij}) = \frac{k_r}{2}(r_{ij} - r_0)^2 \tag{6.2.6}$$

where r_{ij} is the bond distance. The equilibrium bond separation for TIP4P2005 was set to $r_{OH} = 0.9572$ Å and $r_{OM} = 0.1546$ Å. The equilibrium bond separation for hydroxyl atoms in the clay was set to $r_{OH} = 1.0$ Å. All bonds were constrained in all simulations using the LINCS algorithm with a series expansion accurate to fourth order.

Bond bending interactions are modelled in terms of a harmonic potential for the TIP4P2005 water model:

$$U(\theta) = \frac{k_\theta}{2}(\theta - \theta_0)^2 \tag{6.2.7}$$

where θ is the angle formed between hydrogen-oxygen-hydrogen atoms. The equilibrium HOH angle for this water model was set to $\theta_0 = 104.52°$ with a harmonic spring constant of $k_\theta = 628.02$ kJ/(mol·rad^2).

6.2.3 Molecular Dynamics Simulations

All simulations were calculated using GROMACS 5.1.4[15] with an electrostatic and van der Waals cutoff radius of 1.4 nm. Long range electrostatics were calculated using a Particle-Mesh-Ewald (PME) summation with grid spacings of 0.1 nm. The PME summation used a spline interpolation order of 4, and long-range electrostatic interactions were accurate to within 99.999%.

All simulations were initialised with an energy minimisation calculation to minimise any unphysical atomic overlaps. This was achieved using a steepest descents algorithm, which was terminated once the maximum force on any one atom was less than 100 kJ/(mol·nm).

All simulations were subsequently equilibrated for 1 ns in the canonical (NVT) ensemble at 293.15 K. Temperature coupling was achieved using a velocity-rescale thermostat set to rescale system temperatures every 0.5 ps.

Following equilibration, all simulations were run for a production period of 10 ns. During the production period, all simulations used a Nosé-Hoover thermostat with a temperature coupling constant of 0.5 ps and a Nosé-Hoover chain length of 1.

6.2.4 Analyses

Thermodynamic data from each simulation was output every 1 ps. Final values for thermodynamic quantities (energy of adhesions) were averaged over all 10 ns, and errors were calculated using a block-averaging method, with each block averaging over a 1 ns timeframe. In all figures, error bars are presented to ± 2 standard errors of the mean (a confidence interval of 95%).

Contact angles have been extracted from the simulations using the following protocol:

1. At each time-step, the system is centred about the center of mass of the clay.
2. The trajectory is split up into 200 ps intervals. This generates 50 separate trajectories for each simulation.
3. The 1D density of the clay in the z direction is output to a file.

4. The clay density is analysed to extract the location of outermost atomic layer of clay.

5. The 2D density of water (along to the axis of the cylidrical droplet) is output to a file.

6. The water density is normalised by the bulk density of water. Contours are extracted corresponding to half the bulk density of water. We use this contour profile to define the edge of our water droplet. An example of this is presented in Figure 6.5 (middle).

7. A circular Hough transform is applied to the contour data calculated in the previous step. The circular Hough algorithm is able to find imperfect instances of circles within the density data using a voting algorithm. The five circles of best fit are output and used in the analysis of contact angles.

8. The contact angle between clay surface and water droplet is calculated using: (a) the location of the clay basal surface, (b) the location of the circle of best fit (the circle's origin in $\{x, y\}$), (c) the radius of the circle of best fit.

An example of this protocol is presented in Figure 6.5. In this image, the contact angle formed by water on the aluminol surface of kaolinite is presented. The top image presents a snapshot from the trajectory. The water density is averaged over 200 ps chunks, and the edge of droplet is defined by the contour of half bulk water density, as shown in the middle image. The bottom image presents the overall density profile of water. Also presented is the circle of best fit, and a horizontal line corresponding to the outermost atomic layer of the clay. Note that the circular Hough transform is robust enough to ignore the formation of a water droplet on the lower (siloxane) surface of the clay, as well as the formation of a monolayer of water on the aluminol surface.

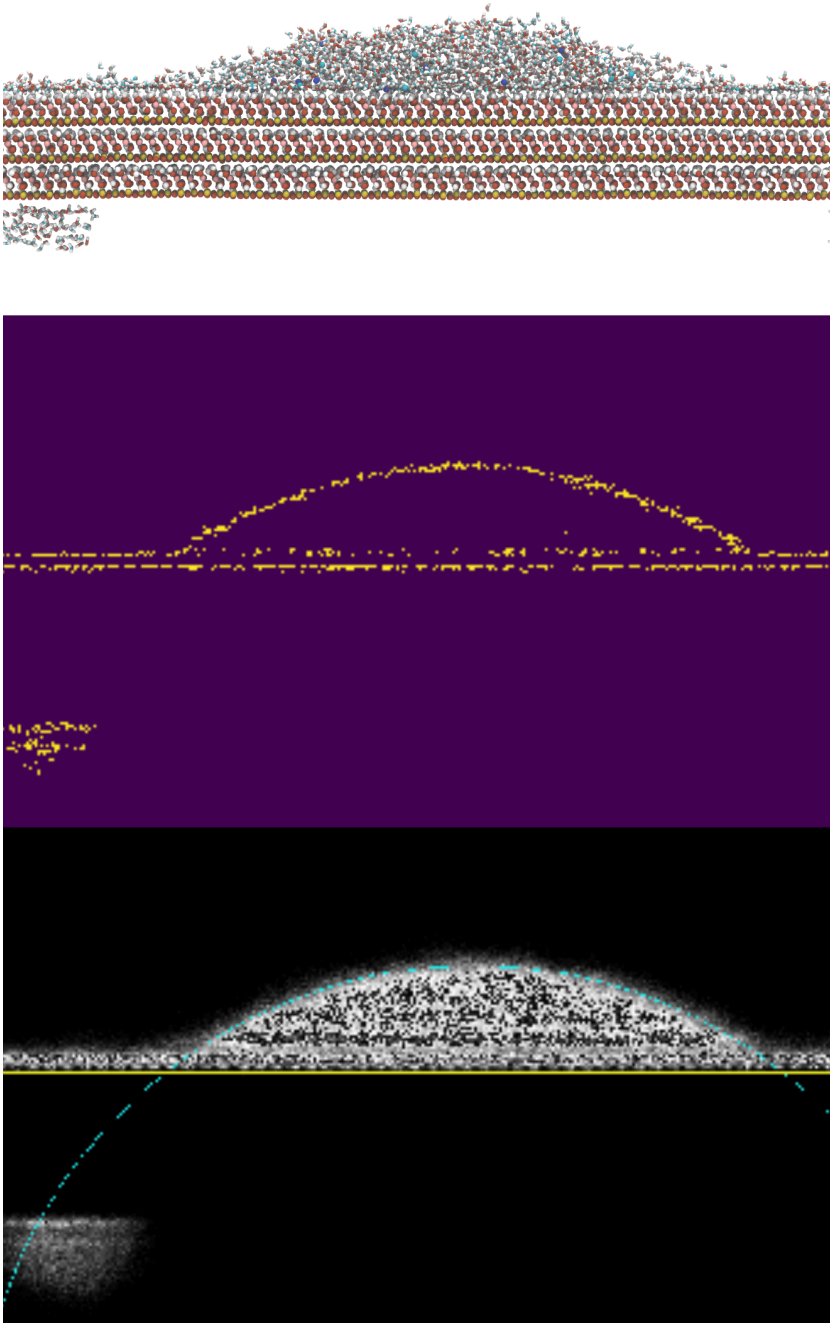

Figure 6.5: The protocol used to calculate the contact angle of a water droplet. The water density is calculated in 200 ps chunks over the entire trajectory (top). A contour is defined at the density half that of bulk water (middle). A circular Hough transform is used to automatically fit a circle to this contour (lower).

6.3 Results

6.3.1 Contact Angle Measurements

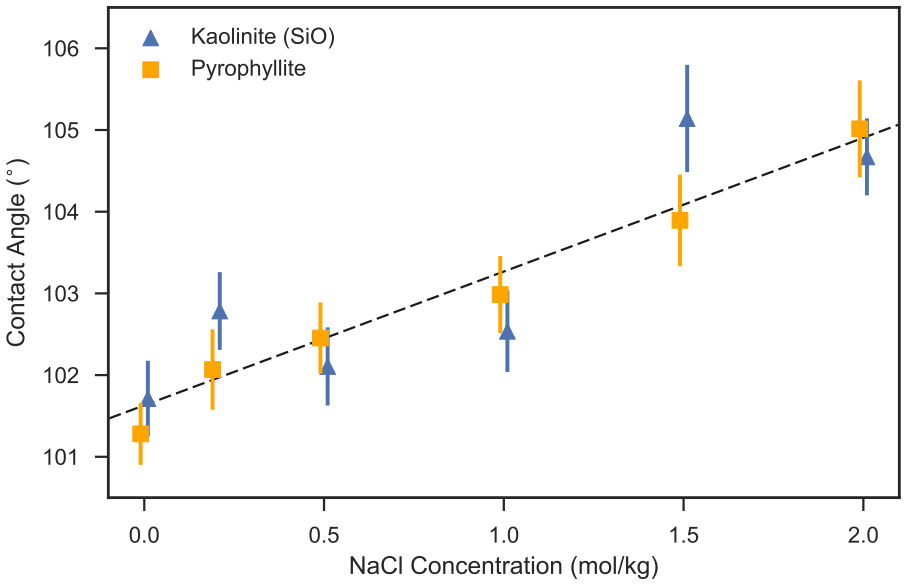

Figure 6.6: The contact angle variation of water as a function of NaCl concentration on the siloxane surface of kaolinite and pyrophyllite.

Figure 6.6 presents the salinity induced change in contact angle of a water droplet adsorbed to the siloxane surface of kaolinite. Also presented is the contact angle variation on the basal surface of pyrophyllite, which is chemically identical to the siloxane surface of kaolinite. We observe a linear trend of increasing contact angle with increasing NaCl concentration. Consequently, the siloxane surface becomes decreasingly water-wet at higher salinities, *viz.* the siloxane surface becomes *increasingly* water-wet at *lower* salinities. This has direct ramifications for low-salinity EOR, whereby we observe optimal water-wet siloxane surfaces at the lowest possible salt concentration, *i.e.* pure water. The result here presents a direct molecular description of the low-salinity effect. At lower salt concentrations, the wettability of a surface is increased. Consequently, the mineral surface is less oil-wet, and more oil can be recovered from a low-salinity water-flood. The same trend is observed for the hydroxylated aluminol surface of kaolinite, as is shown in Figure 6.7.

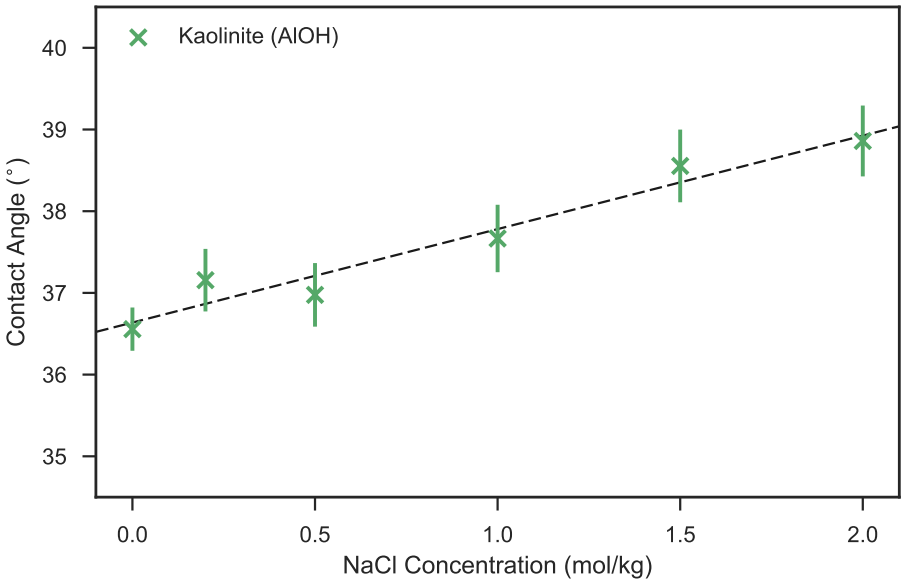

Figure 6.7: The contact angle variation of water as a function of NaCl concentration on the aluminol surface of kaolinite.

Table 6.3: The fresh water contact angles calculated in this study. Experimental data is from (a) Janczuk & Bialopiotrowicz[16], (b) Shang *et al.*[17] and (c) Wu[18].

	Siloxane(SiO)	Aluminol(AlOH)
This Study	101.7 ± 0.5	36.6 ± 0.3
Ŝolc *et al.*	105 ± 1	0
Experiment	17.4[a], 27.8[b], 46.1[c]	

Overall, our results concord with previous simulation and experimental results, as presented in Table 6.3. The wide variation in experimental data is likely due to the difficulty in producing pure crystalline surfaces of kaolinite, large enough to measure contact angles on. As a result, compacted pellets of kaolinite are frequently used as a substrate[16,18]. The amount of exposed siloxane and aluminol surface subsequently varies from study to study. Our results present that the aluminol surface is the major contributor to experimental contact angle studies. Our results imply that the aluminol surface of kaolinite is exposed in larger quantities compared to the siloxane surface.

In contrast to the simulation work of Ŝolc *et al.*[6], we observe a finite contact angle on the aluminol surface of kaolinite. Much like their work, we observe strong wetting behaviour between the hydroxyl groups of the aluminol surface and the water, causing the water to spread across the surface. We observe a monolayer of water forming at the aluminol surface of kaolinite, which remains present throughout the simulation. Ŝolc *et al.* did not see such behaviour, as their systems lacked the requisite amount of water molecules required to fully saturate the surface and create this monolayer. The formation of this monolayer is clear in Figure 6.8, which presents the post-simulation snapshot of the aluminol surface of kaolinite.

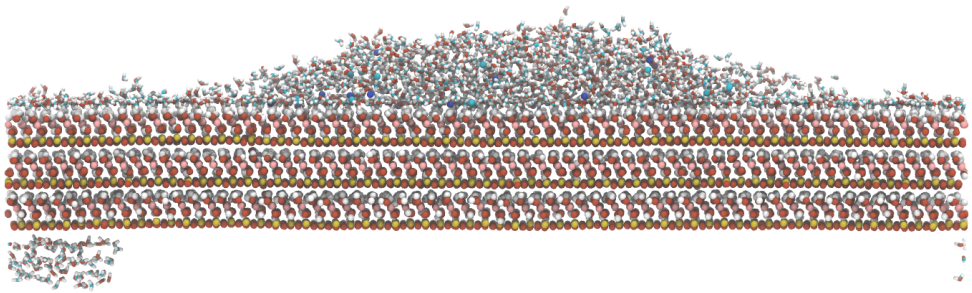

Figure 6.8: A post-simulation snapshot of a water droplet forming on the aluminol surface of kaolinite. The monolayer of water is present throughout the entire simulation trajectory of the water droplet on the aluminol surface.

6.3.2 Energy of Adhesion

To further examine the mechanisms driving the salinity induced wettability alteration, we have examined the energy of adhesion of water to the surfaces of kaolinite. The energy of adhesion is defined as the energy released upon forming the hydrated clay-water interface from its constituent parts, *i.e.* from individual interfaces of clay and water. The energy of adhesion has been calculated using the following equation:

$$W^{\text{adh}} = \frac{\langle E_{\text{clay-water}} \rangle - \langle E_{\text{clay}} \rangle - \langle E_{\text{water}} \rangle}{A} \tag{6.3.8}$$

where $E_{\text{clay-water}}$ is the potential energy of the simulation containing the interface between clay and water (as in Figure 6.4), E_{clay} is the potential energy of a simulation containing kaolinite solely, and E_{water} is the potential energy of a simulation containing water solely. A is the area of the interface within the simulations.

The energy of adhesion for both siloxane and aluminol surfaces is presented in Figure 6.9. We observe no salinity dependence on the adsorption energetics of water to either siloxane or aluminol surface of kaolinite. The experimental line averages over the work of Zoungrana *et al.*[19], Sakizci *et al.*[20] and Brooks *et al.*[21]. As with the contact angle results, we observe a larger contribution from the aluminol surface to the experimentally determined enthalpy of hydration.

The results suggest that the contact angle variation is an entropically driven process, rather than being driven solely by energetic changes. To examine this, we have examined the surface excess at both the clay-water and water-vapour interfaces.

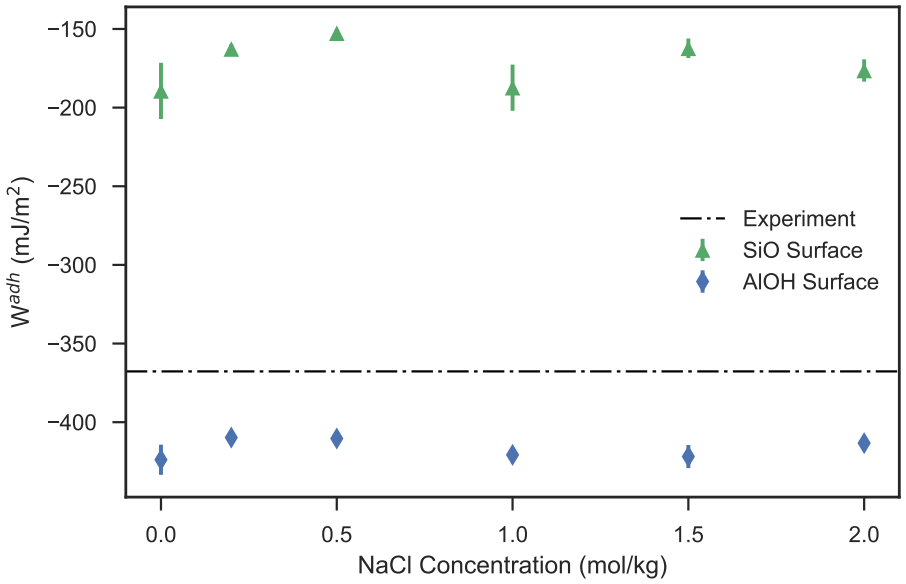

Figure 6.9: The energy of adsorption of water as a function of NaCl concentration on the siloxane and aluminol surfaces of kaolinite.

6.3.3 Surface Excess Measurements

Upon introducing inorganic salts to a solvent, the surface tension of the solution increases. This behaviour is explained due to an exclusion of ions from the liquid-vapour interface[22]. This directly alters the surface tension between the two phases as described by Gibb's adsorption isotherm:

$$d\gamma = -\Gamma_{\mathrm{Na}} d\mu_{\mathrm{Na}} - \Gamma_{\mathrm{Cl}} d\mu_{\mathrm{Cl}} \tag{6.3.9}$$

where Γ_i is the surface excess and μ_i is the chemical potential of species i.

In this study we have calculated the surface excess of sodium and chloride ions across the water-vapour interface as:

$$\Gamma_i = \int_{-\infty}^{z_{\mathrm{Gibbs}}} [\rho_i(z) - \rho_i^{\mathrm{liq}}] dz + \int_{z_{\mathrm{Gibbs}}}^{\infty} [\rho_i(z) - \rho_i^{\mathrm{vap}}] dz \tag{6.3.10}$$

where $\rho_i(z)$ is the non-intrinsic density profile of phase i across the interface, ρ_i^{liq} is the bulk liquid density of phase i, and ρ_i^{vap} is the bulk vapour density of phase i (typically $\rho_i^{\mathrm{vap}} = 0$ for ions in liquid-vapour simulations). z_{Gibbs} is the location of the Gibbs dividing plane, which is priorly calculated by minimising Γ_{water}, such that:

$$\Gamma_{\mathrm{water}} = \int_{-\infty}^{z_{\mathrm{Gibbs}}} [\rho_{\mathrm{water}}(z) - \rho_{\mathrm{water}}^{\mathrm{liq}}] dz + \int_{z_{\mathrm{Gibbs}}}^{\infty} [\rho_{\mathrm{water}}(z) - \rho_{\mathrm{water}}^{\mathrm{vap}}] dz = 0 \tag{6.3.11}$$

The surface excess of sodium and chloride ions at the clay-water interface has been calculated as:

$$\Gamma_i = \int_{z_{\mathrm{Clay}}}^{\infty} [\rho_i(z) - \rho_i^{\mathrm{liq}}] dz \tag{6.3.12}$$

where z_{Clay} is the location of the outermost atomic layer of clay.

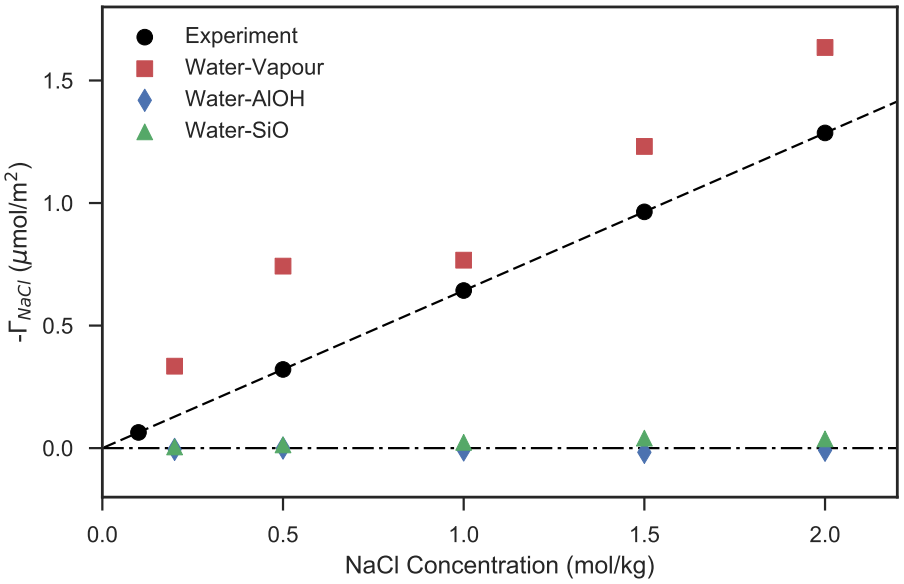

Figure 6.10: The surface excess of sodium and chloride ions at the water-vapour, water-siloxane, and water-aluminol interface.

The surface excess at the water-vapour interface, the siloxane-water interface, and the aluminol-water interface is presented in Figure 6.10. We note that the surface excess at the water-vapour interface agrees with the experimental work of Ali *et al.*[23], and depends on NaCl concentration. In contrast, we observe no salinity dependence in the surface excess of ions at the clay-water interface. Moreover, we observe the surface excess of ions at the clay-water interface to be several orders of magnitude lower compared to the water-vapour interface. This is further exemplified by examining the density profiles of sodium and chloride ions at the clay-water interface.

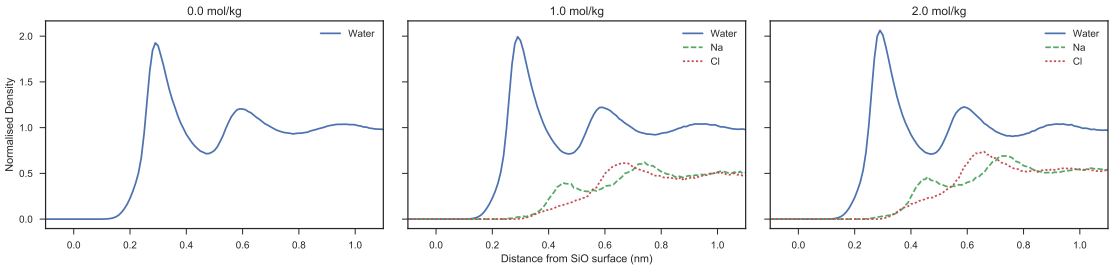

Figure 6.11: The normalised density distribution of water, sodium, and chloride about the siloxane-water interface at various NaCl concentrations.

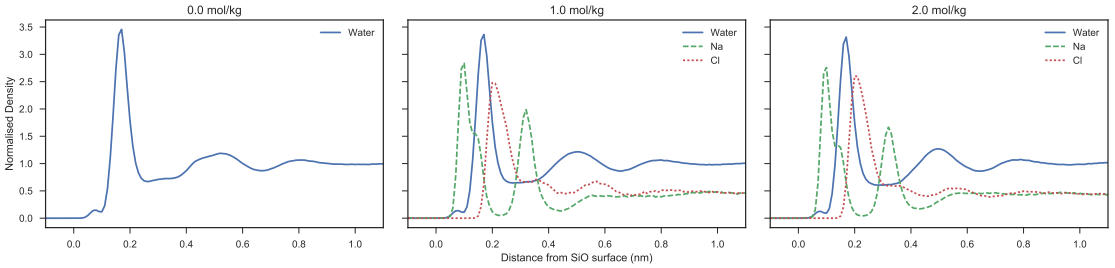

Figure 6.12: The normalised density distribution of water, sodium, and chloride about the aluminol-water interface at various NaCl concentrations.

Figure 6.11 and Figure 6.12 present the distribution of water molecules, sodium ions, and chloride ions, at the clay-water interface for the siloxane and aluminol surfaces of kaolinite respectively. Notably, we observe no change in the distributions of ions surrounding the clay at different NaCl concentrations, in keeping with our observations of the surface excess.

Overall, our results present an entropic reasoning for the salinity induced wettability changes at the surface of kaolinite. We observe an increased structuring at the water-vapour interface (an increased amount of ion exclusion), which, in turn, decreases the overall entropy of the system. Consequently, the surface tension associated with the liquid-vapour interface increases, causing the clay mineral to become decreasingly water-wet at higher NaCl concentrations. Recall that the contact angle scales with liquid-vapour interfacial tension as:

$$\cos(\theta) \propto \frac{1}{\gamma_{\mathrm{lv}}} \tag{6.3.13}$$

6.4 Conclusions

In this study we have used classical molecular dynamic simulations to examine salinity induced wettability changes at the basal surface of kaolinite. Our results help explain the phenomenon of low-salinity enhanced oil recovery. By understanding complex three-phase clay-oil-brine systems in terms of Young's equation, we have been able to interpret the underlying mechanisms driving low-salinity EOR using simpler two-phase simulations. Contact angle simulations clearly present a wettability alteration at low-salinities. We observe kaolinite to become increasingly water-wet at lower salinities, and therefore less oil-wet at lower salt concentrations. By examining the adsorption characteristics of water to kaolinite surfaces, we have been able to discern that this wettability change is an entropically driven process. In particular, our results imply that this change is due to the structural changes at the liquid-vapour interface. In the context of low-salinity EOR, this means that the primary wettability alterations will occur due to the changes in the oil-brine interfacial tension. This then raises the question: why does the efficacy of a low-salinity enhanced oil recovery water-flood depend on the clay mineral content of the reservoir?

Future work will examine this problem. Future work will examine charged clays and other mineral surfaces. Charged clays, such as smectites and illites, are well known to form salinity dependant electric double layers, regions where ionic distributions are perturbed. Consequently, one may find that the surface excess at the clay-water interface is concentration dependent for charged clays.

Bibliography

[1] JJ Sheng. Critical review of low-salinity waterflooding. *Journal of Petroleum Science and Engineering*, 120:216–224, 2014.

[2] Energy Information Administration (U.S.) and Government Publications Office. *International Energy Outlook: 2016 with Projections to 2040*. International Energy Outlook. U.S. Government Printing Office, 2016.

[3] MJ Wilson. The origin and formation of clay minerals in soils: Past, present and future perspectives. *Clay Minerals*, 34(1):7–25, 1999.

[4] J-L Bantignies, CCD Moulin, and H Dexpert. Wettability contrasts in kaolinite and illite clays: Characterization by infrared and x-ray absorption spectroscopies. *Clays and Clay Minerals*, 45(2):184–193, 1997.

[5] R Kareem. *Nano Geochemistry of Low Salinity Enhanced Oil Recovery*. PhD thesis, Durham University, 2016.

[6] R Šolc, MH Gerzabek, H Lischka, and D Tunega. Wettability of kaolinite (001) surfacesmolecular dynamic study. *Geoderma*, 169:47–54, 2011.

[7] CM Tenney and RT Cygan. Molecular simulation of carbon dioxide, brine, and clay mineral interactions and determination of contact angles. *Environmental Science and Technology*, 48(3):2035–2042, 2014.

[8] RT Downs and M Hall-Wallace. The american mineralogist crystal structure database. *American Mineralogist*, 88(1):247–250, 2003.

[9] DL Bish. Rietveld refinement of the kaolinite structure at 1.5 k. *Clays and Clay Minerals*, 41(6):738–744, 1993.

[10] L Martínez, R Andrade, EG Birgin, and JM Martínez. PACKMOL: a package for building initial configurations for molecular dynamics simulations. *Journal of Computational Chemistry*, 30(13):2157–2164, 2009.

[11] JH Weijs, A Marchand, B Andreotti, D Lohse, and JH Snoeijer. Origin of line tension for a lennard-jones nanodroplet. *Physics of Fluids*, 23(2):022001, 2011.

[12] RT Cygan, J-J Liang, and AG Kalinichev. Molecular models of hydroxide, oxyhydroxide, and clay phases and the development of a general force field. *Journal of Physical Chemistry B*, 108(4):1255–1266, 2004.

[13] C Vega and E De Miguel. Surface tension of the most popular models of water

by using the test-area simulation method. *The Journal of chemical physics*, 126(15):154707, 2007.

[14] DE Smith and LX Dang. Computer simulations of NaCl association in polarizable water. *The Journal of Chemical Physics*, 100(5):3757–3766, 1994.

[15] MJ Abraham, T Murtola, R Schulz, S Páll, JC Smith, B Hess, and E Lindahl. GROMACS: High performance molecular simulations through multi-level parallelism from laptops to supercomputers. *SoftwareX*, 1:19–25, 2015.

[16] B Janczuk and T Bialopiotrowicz. Components of surface free energy of some clay minerals. *Clays and Clay Minerals*, 36(3):243–248, 1988.

[17] J Shang, M Flury, JB Harsh, and RL Zollars. Comparison of different methods to measure contact angles of soil colloids. *Journal of Colloid and Interface Science*, 328(2):299–307, 2008.

[18] W Wu. Baseline studies of the clay minerals society source clays: colloid and surface phenomena. *Clays and Clay Minerals*, 49(5):446–452, 2001.

[19] T Zoungrana, A Berrada, J-M Douillard, and S Partyka. Competitive interactions between water and organic solvents onto mineral solid surfaces studied by calorimetry. *Langmuir*, 11(5):1760–1767, 1995.

[20] M Sakizci, BE Alver, and E Yörükoğullari. Thermal behavior and immersion heats of selected clays from turkey. *Journal of Thermal Analysis and Calorimetry*, 98(2):429, 2009.

[21] CS Brooks. Free energies of immersion for clay minerals in water, ethanol and n-heptane. *The Journal of Physical Chemistry*, 64(5):532–537, 1960.

[22] ML Schlossman. Liquid–liquid interfaces: studied by x-ray and neutron scattering. *Current opinion in colloid & interface science*, 7(3):235–243, 2002.

[23] K Ali and S Bilal. Surface tension, surface excess concentration, enthalpy and entropy of surface formation of aqueous salt solutions. *Colloids and Surfaces A: Physicochemical and Engineering Aspects*, 417:183–190, 2013.

Chapter 7

Thesis Conclusions

This thesis has been a study into the molecular mechanisms driving low-salinity enhanced oil recovery. Interactions between clay mineral surfaces, model oil compounds, and brine solutions have been successfully modelled using classical atomistic molecular dynamics.

In Chapter 1, several key aims were highlighted, to be examined by the MD simulations. They were:

1. To understand the role that clay particles play in low-salinity EOR at an atomic level, and to understand how different clays interact with oil.

2. To understand the role of salt concentration and ionic composition in low-salinity EOR. Whether the distinction between monovalent and divalent cation (primarily Na^+ or Ca^{2+}) is important in determining the oil-clay interactions.

3. To interpret the role of oil composition for oil-clay interactions. To understand how different functional groups (carboxylic acid, primary amines) alter the behaviour of alkanes at the oil-clay interface.

4. To probe how useful MD simulations can be to help us interpret surface wetting and wettability alterations at the atomic level.

Each of these aims have been tested and validated to varying success. The following pages discuss the successes of each chapter with respect to these aims.

Aim 1:

To understand the role that clay particles play in low-salinity EOR at an atomic level, and to understand how different clays interact with oil.

The three-phase clay-oil-brine interactions have been examined and discussed primarily in Chapters 3 and 5. These chapters focussed on two different clay minerals, montmorillonite and kaolinite respectively. Through both chapters, a diverse range of clay-oil-brine behaviours have been observed at the molecular level.

In Chapter 3, the interactions of montmorillonite with decane and decanoic acid have been modelled. The simulations present primarily that the wettability of the clay depends upon the nature of the charge balancing cation. The simulations show that divalent calcium ions increase oil-clay interactions, whilst monovalent sodium ions decrease oil-clay interactions.

In Chapter 5, the interactions between a range of organic molecules; including non-polar, polar, and ionic molecules, with the hydrated siloxane and hydroxyl surfaces of kaolinite were examined. The key result presents the formation of oil clusters upon the siloxane surface for decane, decanoic acid and decanamine.

Comparing both studies, one can formulate predictions regarding the role of clay minerals in low-salinity enhanced oil recovery. The siloxane surface of kaolinite appears oil-wetting in all simulations (a conclusion also presented in Chapter 6), and therefore is likely play an important role in oil recovery. In contrast, the siloxane surface of montmorillonite is primarily water-wetting. However, if divalent cations are present within the reservoir, then such clays must also be fully considered to truly understand low-salinity EOR.

The key difference between these two minerals is their apparent surface charge. Kaolinite is an uncharged clay, whilst montmorillonite contains a permanent negative surface charge. The results suggest that the properties of a mineral surface depends largely on its surface charge. Heterogeneities observed within experimental results (for example, varying contact angle measurements within local regions, see the PhD thesis by R. Kareem[1]) may be explained due to local domains of varying surface charge. The simulations present that clay minerals are likely to play an important role in low-salinity EOR.

Aim 2:

To understand the role of salt concentration and ionic composition in low-salinity EOR. Whether the distinction between monovalent and divalent cation (primarily Na^+ or Ca^{2+}) is important in determining the oil-clay interactions.

The role of salt *composition* was examined in Chapter 3. The chapter presented that by replacing divalent calcium ions with monovalent sodium cations, the clay surface became increasingly water-wet. It is therefore concluded that the distinction between monovalent and divalent cation is extremely important in determining the oil-clay interactions, and therefore determining overall oil recovery rates in low-salinity EOR.

This naturally led to the question: will monovalent sodium ions energetically replace divalent calcium ions? This was answered in Chapter 4, by examining the binding energy of charge-balancing cations to the basal surface of montmorillonite. Using the well-tempered metadynamics algorithm, it was shown that aqueous sodium ions would replace charge-balancing cations on the surface of montmorillonite. A Hofmeister-like series of cation-exchange was determined as:

$$K^+ > Na^+ > Ca^{2+} > Cs^+ > Ba^{2+}$$

This chapter focussed on the aqueous environment surrounding montmorillonite, and further work would be required to fully examine cation-exchange in the three-phase clay-oil-brine system.

The role of salt *concentration* was examined throughout the thesis, however, key results were observed in Chapters 2 and 6. Chapter 2 successfully tested that the atomistic MD simulations were capable of capturing the essential physics at liquid-liquid and liquid-vapour interfaces over a range of NaCl concentrations. In Chapter 6, kaolinite was observed to become increasingly water-wet, and therefore less oil-wet at lower salt concentrations. The apparent wettability change is deemed a potential mechanism for driving the low-salinity enhanced oil recovery phenomenon.

Aim 3:

To interpret the role of oil composition for oil-clay interactions. To understand how different functional groups (carboxylic acid, primary amines) alter the behaviour of saturated alkanes at the oil-clay interface.

The role of polar oil components have been examined upon the surfaces of montmorillonite and kaolinite in Chapters 3 and 5 respectively.

In Chapter 3 it was observed that the pH level surrounding the clay, and hence the protonation and charge of organic oil molecules plays an important role in the clay-oil interaction. Cation bridging is observed between initially oil-wet montmorillonite and oil containing polar functional groups.

In Chapter 5 it was observed that the decane molecules readily form droplets atop the siloxane surface of kaolinite, yet do not adsorb to the hydroxyl surface. The same behaviour was observed for protonated polar decanoic acids. In contrast, decanoate anions do not adsorb to the siloxane surface, but adsorb to the hydroxyl surface. Decanamine readily adsorbs to both silicate and hydroxyl surfaces. Once charged, the decanamine remains adsorbed to both surfaces.

In the context of low-salinity enhanced oil recovery, it appears that polar oil components play an important role, primarily dictating the oil-wettability at the surfaces of negatively charged clay minerals, *e.g.* montmorillonite. This is because divalent cations are capable of acting as ionic bridges between the clay and the oil. It is concluded, once again, that the ionic content of the low-salinity flood is important, especially when there is a large portion of polar functional groups in the oil.

Aim 4:

To probe how useful MD simulations can be to help us interpret surface wetting and wettability alterations at the atomic level.

Throughout this thesis, molecular dynamics simulations have been used to interpret the interfacial properties of liquid-liquid and liquid-solid interfaces. The work has highlighted several qualitative and quantitative techniques using classical MD that can help interpret the phenomenon of surface wetting and wettability alteration. One of the key advantages of computational techniques, such as atomistic molecular dynamics and density functional theory, is that they can provide both *quantitative* and *qualitative* results.

In Chapter 2, it was discussed that calculating properties directly at the low-salinity EOR regime was likely inaccessible. This was due to the margins of error within the simulations being much larger than the resolution required to resolve differences between pure water and 'low-salinity' water. These errors could be reduced by running larger simulations, with more atoms. This, however, requires more compute time, both in terms of resolving each time-step (there are more atoms to move per time-step), but also in terms of calculating thermodynamic properties (larger systems need more time to reach an equilibrated state). This double-hit of computational cost means that classical MD is unlikely to model the physical conditions of low-salinity EOR directly in the near future.

In contrast, Chapter 2 was very clear in being able to discern trends in thermodynamic quantities at various salt concentrations. Overall, the MD simulations provide useful insight into the overall trends of surface wetting, wettability alterations and low-salinity enhanced oil recovery at various salt concentrations.

7.1 Future Work

Throughout this thesis, atomistic molecular dynamics simulations have been used to help understand the phenomenon of low-salinity enhanced oil recovery at the molecular level. The primary aim of this study was to examine the interfaces between brine, oil and clay minerals. In this context, the study has been limited to examining two mineral surfaces (montmorillonite and kaolinite), several model oil compounds (decane, decanoic acid and decanamine) and brines containing solely NaCl or $CaCl_2$. A natural progression for further work would be to run similar studies on further minerals, illites or quartz for example; including more complex model oil compounds; and with various different inorganic salts and mixtures thereof.

Chronologically (throughout the period of supervised study), Chapters 3 and 5 were calculated first. Both chapters attempt to combine a mineral surface, model oil, and brine within the simulations. Such simulations return insightful qualitative results, but frequently fail to return as much useful quantitative and predictive results. Chapters 4 and 6 were an attempt to resolve this issue. By posing a very clear problem in the first instance, the MD simulations often return more fruitful results. Chapter 4 was successful in determining the adsorption characteristics of charge balancing cations on the mineral surface of montmorillonite. Chapter 6 was successful in modelling the salinity induced wettability changes at the surface of kaolinite. Both of these methodologies can be extended to examine further systems (minerals and brines) in future work.

Free energy methods, such as thermodynamic integration, umbrella sampling and metadynamics, provide a useful way of calculating quantities directly compatible with experiment. One may, in future, attempt to model the free energy of adsorption of a chemical 'tip' (a monolayer of decane for example) to a mineral surface. Such a calculation would be directly comparable to the force-distance curves generated using an atomic/chemical force microscope. Figure 7.1 presents an example of a chemical decane tip simulated using classical MD. The overlap between atomistic MD and experiment is an area filled with fruitful potential.

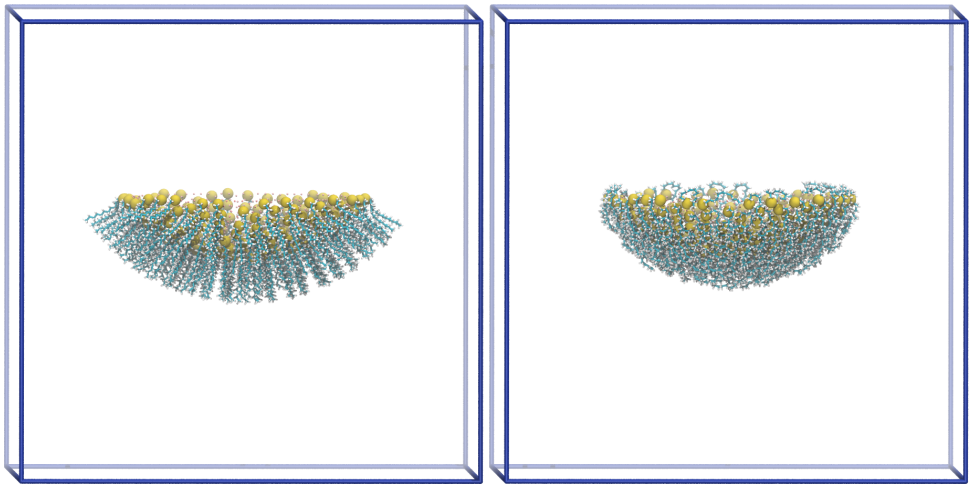

Figure 7.1: Snapshots of a chemical force microscope tip created and equilibrated using classical MD. (Left) presents the initial setup of decane molecules grafted upon an inert tip (yellow). Yellow atoms are chemically inert and would not interact with any substrate or solvent molecules. (Right) presents the equilibrated structure of a decane grafted chemical force microscope tip.

Another clear area of expansion is to study the salinity induced wettability alterations at the surfaces of charged clay minerals. As presented in Chapter 6, the surface excess of ions at the mineral surface was: (a) orders of magnitude lower than the surface excess at the water-vapour interface; (b) independent of salt concentration. This result may not be the case for charged clays, whereby a salinity dependent electric double layer can form. A natural progression would be to run the calculations present in Chapter 6, but for the charged clay montmorillonite, as in Figure 7.2.

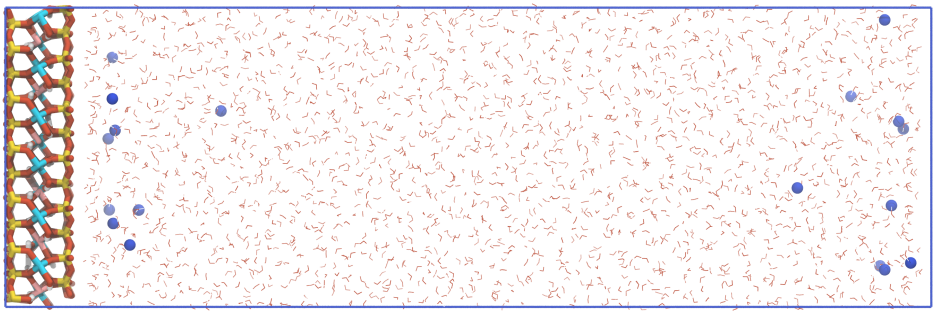

Figure 7.2: A snapshot of the supercell used to examine cation binding in Chapter 4. A similar setup could be used to examine the surface excess of ions at the mineral surface of montmorillonte.

7.2 Other Ventures

Throughout the period of supervised study, several further techniques were examined and shown (at least partially) to have some applicability to low-salinity EOR. These are listed in the following pages. Several of these techniques may be useful in interpreting the phenomenon of low-salinity enhanced oil recovery in the future.

7.2.1 A Theoretical Model of Low-Salinity Enhanced Oil Recovery

Following the work of Chapter 2 and Chapter 6, it was discerned that the change in surface tension at an interface could be described by Gibb's adsorption isotherm. Namely, the surface tension change could be expressed as:

$$d\gamma = -\Gamma_{\mathrm{Na}} d\mu_{\mathrm{Na}} - \Gamma_{\mathrm{Cl}} d\mu_{\mathrm{Cl}} \tag{7.2.1}$$

where Γ_i is the surface excess and μ_i is the chemical potential of species $i \in \{\mathrm{Na},\ \mathrm{Cl}\}$.

In principle, one could derive theoretical expressions for both the surface excess and chemical potential of NaCl at the brine-vapour, brine-oil and brine-clay interface. From which, the complete behaviour of the three-phase clay-oil-brine system could be derived.

Such calculations have previously been derived for the brine-vapour and brine-oil interfaces. The Onsager-Samaras theory describes how the surface tension varies with salt concentration at the liquid-vapour interface by the equation[2]:

$$\Delta\gamma = \frac{c_b \lambda_b}{2} k_B T \left[-\ln \frac{\kappa \lambda_b}{2} - 2\gamma_E + \frac{3}{2} \right] \tag{7.2.2}$$

where c_b is the bulk electrolyte concentration, γ_E is Euler's constant, λ_b is the Bjerrum length constant, and κ is the inverse Debye length, defined (for a 1:1 electrolyte) as:

$$\kappa = \sqrt{\frac{2 c_b e^2}{\epsilon_0 \epsilon_r k_B T}} \tag{7.2.3}$$

The Onsager-Samaras theory breaks down at salinities greater than 0.1 mol/L[3], however, the model should be sufficient to describe the effects of low-salinity EOR, where optimal salt concentrations operate on the milli-molar scale. Extensions to the theory have been developed to include liquid-liquid interfaces[4], and to include finite ion size effects[5].

A theoretical model of low-salinity EOR is currently being derived by combining the Onsager-Samaras theory for liquid-vapour/liquid-liquid interface with similar calculations for the liquid-mineral interface. This is being achieved by calculating the surface excess at the brine-mineral interface using the mean-field Gouy-Chapman model of the electric double layer[6,7]. The description of the electric double layer was calculated using the Poisson-Boltzmann equation, from which it can be shown that the surface excess at the brine-clay interface follows the expression:

$$\Gamma_{NaCl} = \frac{4c_b}{\kappa}\left\{\cosh\left(\frac{e\psi_0}{2k_BT}\right) - 1\right\} \tag{7.2.4}$$

where ψ_0 is the electrostatic potential of the charged surface.

This model is currently being finalised and is likely to lead to a theoretical explanation of salinity induced wettability changes at charged surfaces. Currently, the model determines the wettability of a surface solely on the salt concentration within the water phase, and the electrostatic surface potential of the mineral. The theory can be easily extended to include finite-ion size effects.

Similar thermodynamic models have been also been produced to examine the surface tension of oil-brine systems in the presence of dilute surfactants[8]. Upon introducing the surfactants to the model, a minimum was observed in the oil-brine interfacial tension. This was due to the partitioning of the surfactant between the oil and brine phases at the surfactant's critical micelle concentration. Such considerations may be implemented into the developing model, and the small presence of surfactant molecules may prove important to the phenomenon of low-salinity EOR.

7.2.2 Dissipative Particle Dynamics

Dissipative particle dynamics (DPD) is a computation technique, similar to atomistic molecular dynamics, used for simulating the properties of complex fluids. In this technique, each particle represents a region of bulk fluid, rather than a single atom. Subsequently, the length- and time-scales modelled by DPD can far exceed those of the all-atom classical MD simulations.

Dissipative particle dynamics simulations have been tested during the period of supervised study, and have shown promise in modelling the wettability alterations of the three-phase clay-oil-brine system (to be more general, the three-phase surface-liquid$_A$-liquid$_B$ system). Figure 7.3 presents one such simulation, whereby two types of liquid particles have been simulated interacting with a fixed surface. In this simulation, the fluid beads (red and pink) are presumed immiscible, and quickly phase separate. Both fluids possess the same interaction parameters with the wall (blue particles). As such, a contact angle of approximately 90° is observed. Introducing charges into beads of either phase would be an easy way to mimic the overall phenomenon of low-salinity enhanced oil recovery.

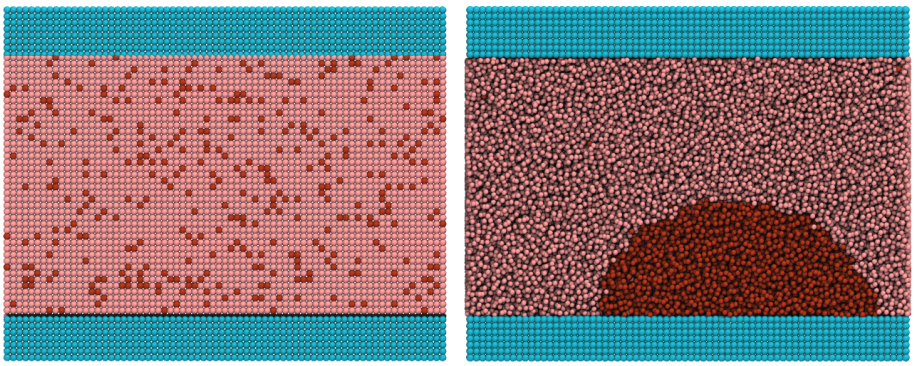

Figure 7.3: Snapshots of a DPD simulation used to probe three-phase wettability. (Left) presents the initial setup of a DPD simulation containing two fluid beads (red and pink) and a wall (blue). (Right) presents the final snapshot of the DPD simulation, whereby a fluid droplet has formed atop the surface.

The main disadvantage of DPD is in parameterising the interactions between fluid particles. The interaction parameters within DPD are difficult to compare against experimental or theoretical observables. This may cause a problem if one is interested in modelling low-salinity EOR as accurately as possible.

7.2.3 Classical/Fluid Density Functional Theory

Classical (also known as fluid) density functional theory (DFT) is a technique used to describe the equilibrium thermodynamic properties of complex fluids. It shares many similarities with the more familiar quantum mechanical density functional theory, however, rather than minimising the Hamiltonian with respect to the ground state electron density, one minimises the Grand Potential, Ω (the characteristic state function of the Grand Canonical ensemble - constant chemical potential μ, constant volume V, and constant temperature T), with respect to the average one-body particle density. The utility of classical DFT is large since the modelled 'particles' can represent atoms, ions, molecules, or even larger colloidal particles.

The formal definition of the Grand Potential functional used in classical DFT is given as:

$$\Omega[\rho(\mathbf{r})] = \mathcal{F}[\rho(\mathbf{r})] + \int \rho(\mathbf{r})(V_{ext}(\mathbf{r}) - \mu)dr \tag{7.2.5}$$

where $\mathcal{F}$ is the intrinsic Helmholtz free energy of the system, μ is the intrinsic chemical potential of the system, V_{ext} is the externally applied potential and $\rho(\mathbf{r})$ is the average one body fluid density.

The beauty of classical DFT is that the intrinsic Helmholtz free energy and chemical potential of a fluid is unique to that fluid. It is therefore independent of any applied external potential. The potential form of $\mathcal{F}$ and μ is typically broken down into a sum of linear contributions:

$$\mathcal{F}[\rho(\mathbf{r})] = \mathcal{F}_{id}[\rho(\mathbf{r})] + \mathcal{F}_{hs}[\rho(\mathbf{r})] + ... \tag{7.2.6}$$

$$\mu = \mu_{id} + \mu_{hs} + ... \tag{7.2.7}$$

In this example, id and hs represent the ideal gas and hard-sphere contributions to the Grand Potential functional respectively. It is simple to add additional physics to the system by introducing more terms into equations 7.2.6 and 7.2.7.

Ultimately, one can derive a functional form of $\mathcal{F}$ and μ for a fluid independent of any mineral/surface, then apply a wall potential (for example, a 10-4 or 10-3 Lennard-Jones potential) to model the fluid interactions with said mineral surface. Figure 7.4 presents an example of the classical density functional theory applied to a hard sphere fluid in 1D. In the presented figure, a repulsive external wall potential is applied at $z = 0$ and $z = 10$. The hard spheres are of radius $r = 1$. The packing fraction of system 1 (left) is 50%, whilst the packing fraction of system 2 (right) is 75%.

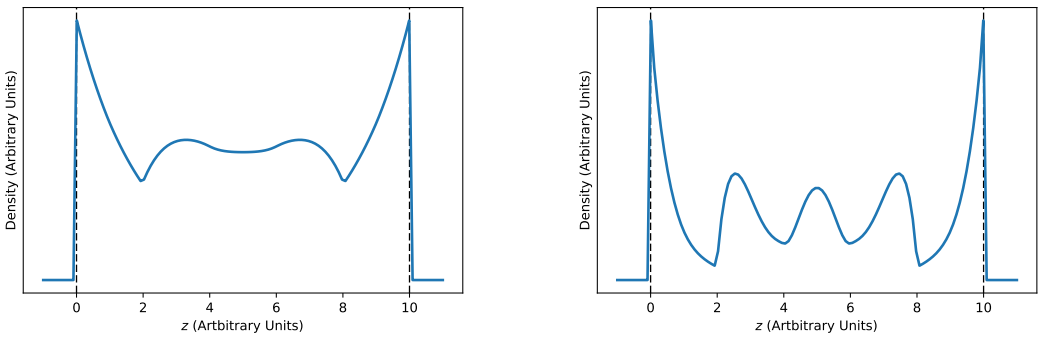

Figure 7.4: The density profiles of a hard sphere fluid calculated using 1D classical density functional theory. Hard spheres are of radius $r = 1$, (left) presents the density profile with a packing fraction of 50%, (right) presents the density profile with a packing fraction of 75%.

Many advancements have already been progressed in developing accurate intrinsic Helmholtz and chemical potentials functionals for hydrocarbons and ions, for example, the SAFT model (statistical associating fluid theory)[9,10]. The applicability of classical DFT to low-salinity enhanced oil recovery will be determined by the availability of accurate representative functionals for the oil and brine phases. The technique appears to offer an exciting opportunity to unravel the mechanisms driving surface wettability over a variety of length-scales, and to unravel the mysteries of low-salinity enhanced oil recovery.

7.3 Concluding Remarks

Overall, this thesis has successfully described some of the key mechanisms driving low-salinity enhanced oil recovery at the molecular level using atomistic classical molecular dynamics.

The cation-exchange phenomenon, whereby divalent cations are replaced by monovalent cations at a negatively charged mineral surface, is deemed to be one of the more important mechanisms driving the low-salinity effect. This phenomenon is observed at the basal surface of montmorillonite, whereby replacing calcium ions with sodium ions drastically alters the mineral surface to overwhelmingly water-wet.

The salinity component of low-salinity EOR remains rather elusive. It has been discerned that the wettability of the clay-oil-brine system varies due to the changes at the oil-brine interface. If this were strictly true, then the phenomenon of low-salinity EOR would be mineral independent. Work is currently being undertaken to further examine the role of the mineral surface on altering the salinity-induced wettability changes.

Whilst a complete picture of low-salinity enhanced oil recovery remains incomplete, the simulations presented in this thesis have helped form a more coherent picture of the phenomenon.

Bibliography

[1] R Kareem. *Nano Geochemistry of Low Salinity Enhanced Oil Recovery*. PhD thesis, Durham University, 2016.

[2] L Onsager and NNT Samaras. The surface tension of Debye-Hückel electrolytes. *Journal of Chemical Physics*, 2(8):528–536, 1934.

[3] C-H Ho, H-K Tsao, and Y-J Sheng. Interfacial tension of a salty droplet: Monte Carlo study. *Journal of Chemical Physics*, 119(4):2369–2375, 2003.

[4] A Bellemans. The surface tension of ionic solutions: I. derivation of the limiting law at infinite dilution from the Poisson-Boltzmann equation. *Physica*, 30(4):924–930, 1964.

[5] AP dos Santos and Y Levin. Ions at the water-oil interface: interfacial tension of electrolyte solutions. *Langmuir*, 28(2):1304–1308, 2011.

[6] RJ Hunter and LR White. *Foundations of colloid science*. Number v. 1 in Oxford science publications. Clarendon Press, 1987.

[7] JN Israelachvili. *Intermolecular and Surface Forces: With Applications to Colloidal and Biological Systems*. Colloid Science Series. Academic Press, 1985.

[8] R Aveyard and TA Lawless. Interfacial tension minima in oil-water-surfactant systems. systems containing pure non-ionic surfactants, alkanes and inorganic salts. *Journal of the Chemical Society, Faraday Transactions 1: Physical Chemistry in Condensed Phases*, 82:2951–2963, 1986.

[9] WG Chapman, KE Gubbins, G Jackson, and M Radosz. New reference equation of state for associating liquids. *Industrial & Engineering Chemistry Research*, 29(8):1709–1721, 1990.

[10] C McCabe and A Galindo. Saft associating fluids and fluid mixtures. *Applied Thermodynamics of Fluids*, pages 215–279, 2010.

Appendix A

Supplementary Information

A.1 Chapter 3: Supplementary Information

Further analyses calculated for Chapter 3 are presented in the following pages. Radial distribution functions have been used to determine cut-offs for cation bridging events. Additional density profiles, dynamic clustering and dynamic cation bridging figures are presented.

RDF profiles between clay surface and ions

Note that in all simulations, the Stern layer and first hydration shell are within 5Å of the clay basal surface. This has been used as the cut-off value for potential cation bridges.

Colors given in legends.

	Na-MMT	Ca-MMT
Fresh water	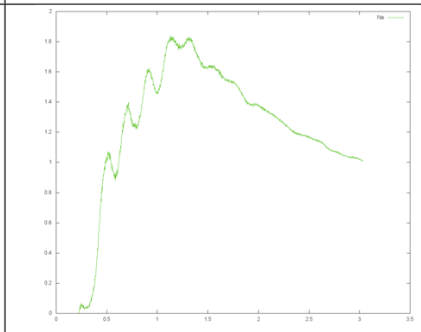	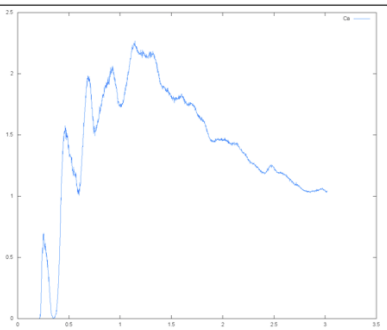
Low salinity (0 ppt)	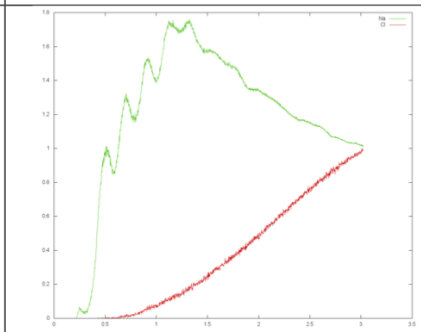	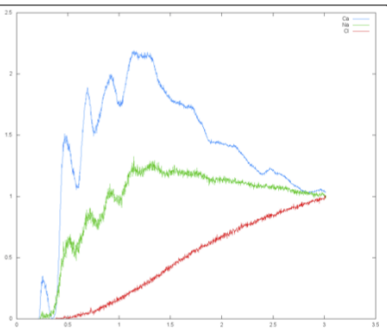
High salinity (5 ppt)	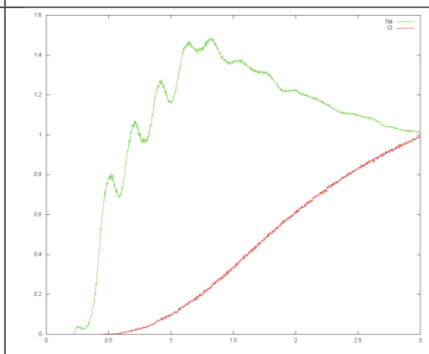	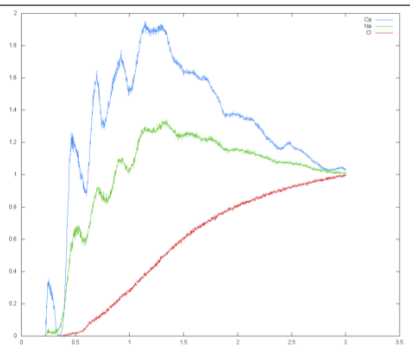
Sea water (35ppt)	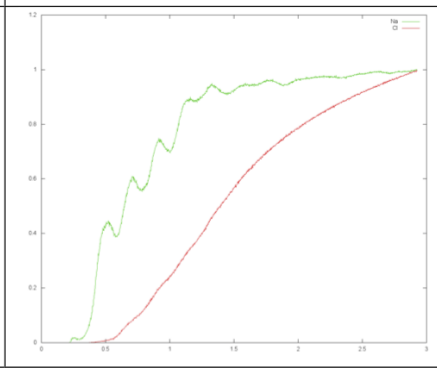	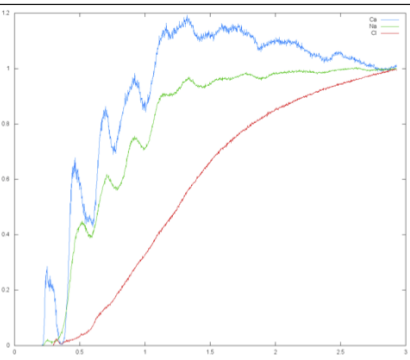

Water-wet density profiles.

NaMMT left, CaMMT right. Plots for decane are given in the paper, decanoic acid presented here: top, Na-decanoate: bottom. Salt concentration along z-axis. Colors are: organics (black), sodiums (green), chlorides (red) and calciums (blue)

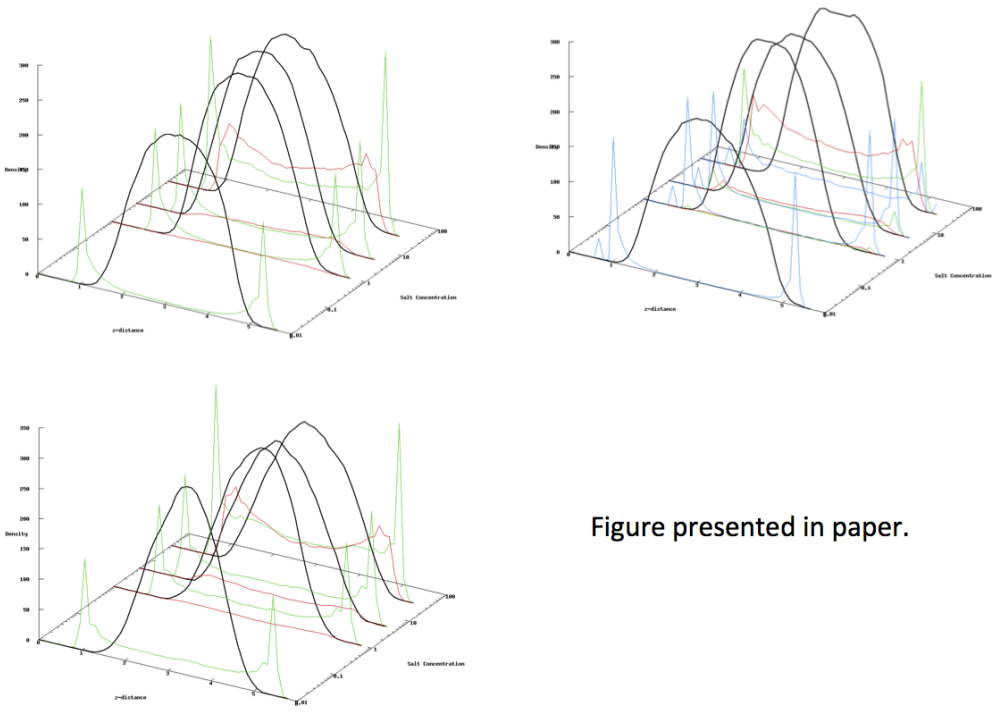

Figure presented in paper.

Oil-wet density profiles.

NaMMT left, CaMMT right. Plots for decane are presented here: top, decanoic acid: middle, Na-decanoate: bottom. Salt concentration along z-axis. Colors are: organics (black), sodiums (green), chlorides (red) and calciums (blue)

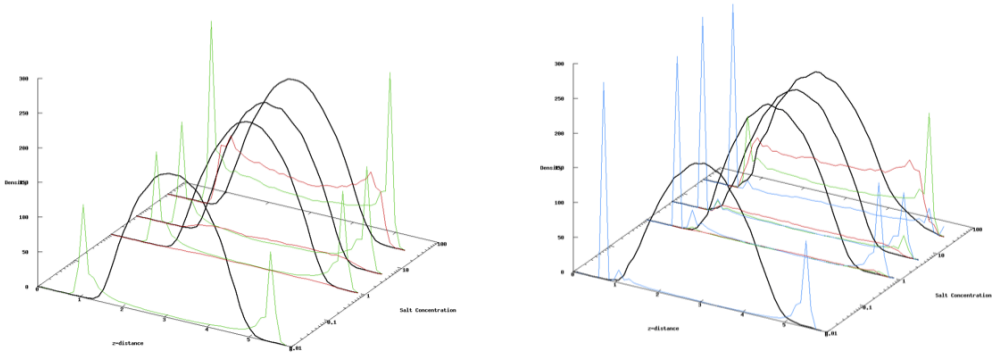

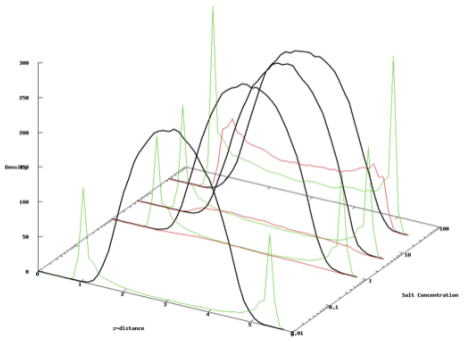

Figure presented in paper.

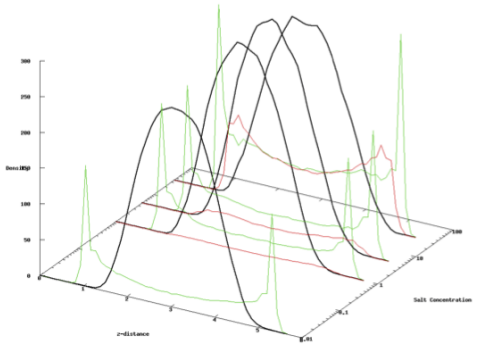

Figure presented in paper.

Cluster analysis of organic molecules

All colors defined in keys.

Water-wet simulations:

	Na-MMT	Ca-MMT
Decane	Figure presented in paper.	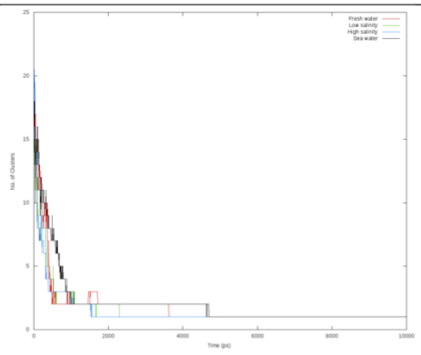
Dec_a	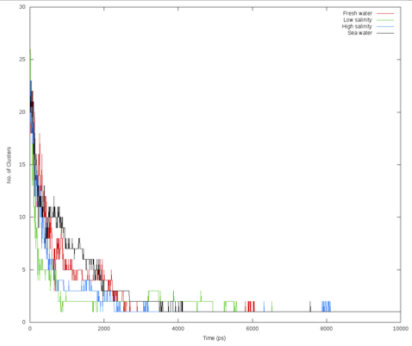	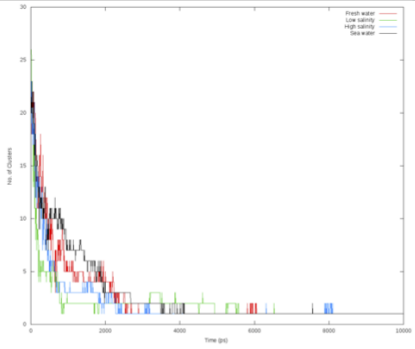
Dec_ad	Figure presented in paper	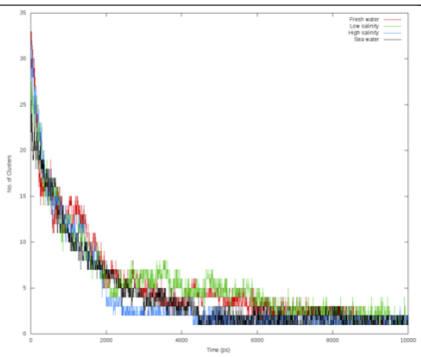

Oil-wet simulations:

	Na-MMT	Ca-MMT
Decane	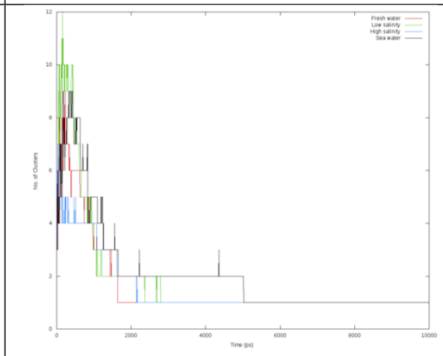	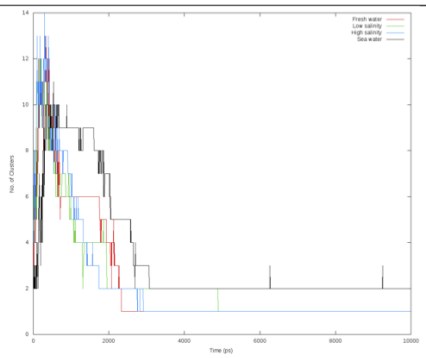
Dec_a	Figure presented in paper.	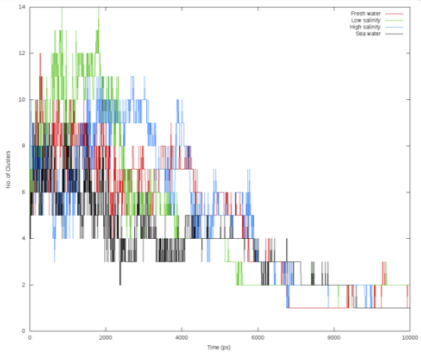
Dec_ad	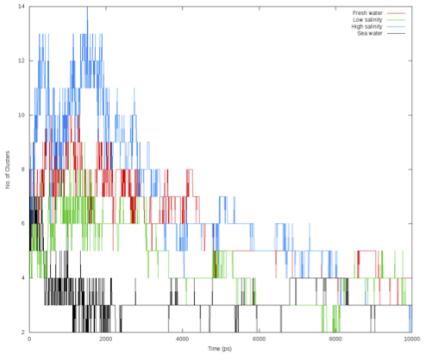	Figure presented in paper.

A.2 Chapter 5: Supplementary Information

Further details on the computational models and parameterisations used in Chapter 5 are presented in the following pages.

Force Fields

The total energy of the system is calculated as:

$$E_{total} = E_{bonded} + E_{non-bonded}$$

whereby ClayFF utilises the following bonded and non-bonded functional forms:

$$E_{bond} = k(r_{ij} - r_o)^2$$

$$E_{non-bonded} = E_{Coul} + E_{VDW}$$

$$E_{Coul} = \frac{e^2}{4\pi\epsilon_0} \sum_{i \neq j} \frac{q_i q_j}{r_{ij}}$$

$$E_{VDW} = \sum_{i \neq j} D_{0,ij} \left[\left(\frac{R_{0,ij}}{r_{ij}} \right)^{12} - 2 \left(\frac{R_{0,ij}}{r_{ij}} \right)^{6} \right]$$

The non-bonding cross terms are calculated using the following mixing rules:

$$R_{0,ij} = \frac{1}{2}(R_{0,i} + R_{0,j})$$
$$D_{0,ij} = \sqrt{D_{0,i} D_{0,j}}$$

The atom types used in this simulation are as follows:

Species	**Atom type**	**Charge, e**	R_0, **nm**	D_0, **kJ/mol**
Tetrahedral Si	st	2.1000	3.3020E-01	7.701E-06
Octahedral Al	ao	1.5750	4.2712E-01	5.564E-06
Hydrohyl H	ho	0.4250	0.00	0.00
Hydroxyl O	oh	-0.9500	3.1655E-01	6.502E-01
Sodium ion	Na	1.00	2.3500E-01	5.443E-01
Chloride ion	Cl	-1.00	4.4000E-01	4.188E-01

The hydroxyl groups are bonded with the following parameters:

Type	r_0, **nm**	k, **kJ/mol nm²**
Hydroxyl bond	0.1	463532.8

The CHARMM36 force field has been utilised to model the oil constituents within the system. Again, the non-bonded parameters are calculated as:

$$E_{non-bonded} = E_{Coul} + E_{VDW}$$

whereby...

$$E_{Coul} = \frac{e^2}{4\pi\epsilon_0}\sum_{i\neq j}\frac{q_i q_j}{r_{ij}}$$

$$E_{VDW} = \sum_{i\neq j} D_{0,ij}\left[\left(\frac{R_{0,ij}}{r_{ij}}\right)^{12} - 2\left(\frac{R_{0,ij}}{r_{ij}}\right)^{6}\right]$$

and the non-bonding cross terms are again calculated using the following mixing rules:

$$R_{0,ij} = \frac{1}{2}\left(R_{0,i} + R_{0,j}\right)$$

$$D_{0,ij} = \sqrt{D_{0,i}D_{0,j}}$$

The bonded interactions in CHARMM36 are sufficiently more complex than those of ClayFF and follow the form:

$$E_{bonded} = E_{bond\ stretch} + E_{angle\ bend} + E_{UB} + E_{dihedral} + E_{improper} + E_{CMAP}$$

$$E_{bond} = k\left(r_{ij} - r_o\right)^2$$

$$E_{angle} = k\left(\theta_{ij} - \theta_o\right)^2$$

$$E_{UB} = k(b^{1-3} - b^{1-3,0})^2$$

$$E_{dihedral} = k\left(1 + cos(n\varphi - \delta)\right)$$

$$E_{improper} = k(\omega + \omega^0)^2$$

$$E_{CMAP} = \upsilon_{CMAP}(\Phi, \Psi)$$

The following is a list of atom types assigned to the organic oil molecules of the system. The non-bonded and bonded parameters for each atom type can be freely found at: http://mackerell.umaryland.edu/charmm_ff.shtml

Species	**Atom type**
Aliphatic CH_3	CG331
Aliphatic CH_2	CG321
Aliphatic H	HGA3
Carbonyl C	CG2O3
Carbonyl O(1)	OG2D2
Carbonyl O(2)	OG2D1
Aliphatic CH_2 adjacent to N	CG324
Polar H	HGP2
Primary NH3+	NG3P3
Neutral methylamine N	NG321
Polar H (neutral methylamine)	HGPAM2
Water O	OT
Water H	HT

The TIP3P-derived CHARMM water model was used to model the solvent in the system. The model had the following non-bonded parameters:

Species	**Atom type**	**Charge, e**	**R_0, nm**	**D_0, kJ/mol**
Oxygen	OT	-0.834	0.315057422683	0.63639
Hydrogen	HT	0.417	0.192464	0.0400013524445

With harmonic bonds for the O-H intramolecular interaction described by:

$$E_{bond} = k(r_{ij} - r_o)^2$$

Type	**r_0, nm**	**k, kJ/mol nm²**
OH bond	0.09572	502416.0

And a harmonic angle term given as:

$$E_{angle} = k(\theta_{ij} - \theta_o)^2$$

Type	θ_o	**k, kJ/mol rad²**
HOH angle	104.52	460.24